

# **Tandem Organic Photovoltaics**

**by**

**Brian E. Lassiter**

**A dissertation submitted in partial fulfillment  
of the degree requirements for the degree of  
Doctor of Philosophy  
(Materials Science and Engineering)  
in The University of Michigan  
2013**

**Doctoral Committee:**

**Professor Stephen R. Forrest, Chair  
Professor L. Jay Guo  
Professor Robert Krasny  
Professor Joanna M. Millunchick**

© Brian E. Lassiter

---

All Rights Reserved  
2013

*There is a single light of science,  
and to brighten it anywhere  
is to brighten it everywhere.*

— Isaac Asimov

# Acknowledgments

Not long ago, I knew next to nothing of organic electronics and the scientific process. My progress towards understanding the field since then has largely been due to the generous guidance of others.

First and foremost is that of my advisor, Prof. Stephen Forrest. His insatiable hunger for science and discovery, along with his understanding of science from the nitty-gritty to the big picture of “why?” was what drew me into this field. The combination of freedom and guidance and the constant demand for scientific rigor have pushed me to places further than I knew how to go.

I am also indebted to Mary Ellen Zvanut for my summer spent working in her lab. Experimental research is a unique art which cannot be understood without getting your hands dirty. Her guidance in measurement and data analysis showed me the wonders of the scientific process and ultimately put me on the path I am still on today.

My deepest appreciation also goes out to my fellow OCM members, as they are the ones who truly make things happen on a day-to-day basis. In the early days, the most influential was Richard “Johnny-no-longer” Lunt. His enthusiastic assistance on experimental methods, guidance on figuring out what data actually means, and general encouragement were indispensable in the process of getting my feet wet in science, along with the efforts of Ning

Li, Guodan Wei, Stephane Kena-Cohen, and Chris Giebink. My appreciation also goes to my contemporaries here at OCM, Jeramy Zimmerman, Xiaoran Tong, Kyle Renshaw, Michael Slootsky, Eva Ruff, and the rest of OCM for their positive influence on my life at Michigan. And, last but not least, my thanks to Anurag Panda for asking so many questions this last year. Being a mentor for younger students balances things out by making me think that, just maybe, I've learned some things over the last five years.

I am profoundly indebted to Richard Hubbard, who did not disregard a naive young college freshman who, though having never played the instrument, dared to pursue a degree in saxophone performance. His jovial encouragement has led me to a lifelong skill with I which to create joy for myself and others.

Outside of work, I have performed with innumerable outstanding musicians in Ann Arbor, Detroit, and the surrounding areas. My most common partners in crime have been Ryan Dolan and Alec Cooper, whom with me form the Rampage Horns. In addition to being the basis for the Third Coast Kings (and subsequently Rampage Swing), some of my favorite times during grad school have been jamming in the basement to whatever music suited our fancy. Of everyone I've met during grad school, I will miss them the most.

Thankfully, the most important person I've met in Ann Arbor will be continuing the journey with me. Robin, you make every day better. Marrying you was the easiest, best decision I've ever made.

Lastly, my most fundamental gratitude goes to my parents. Their lifelong encouragement has provided me a foundation for all that I hope to achieve. I am fortunate to have had their support in finding my own, unique path in this world.

Brian Einstein Lassiter

Ypsilanti, MI

May, 2013

# Table of Contents

<b>Acknowledgments</b> . . . . .	ii
<b>List of Tables</b> . . . . .	x
<b>List of Figures</b> . . . . .	xi
<b>Abstract</b> . . . . .	xvi
<b>Chapter 1 Motivation</b> . . . . .	1
1.1 Terminology . . . . .	2
1.2 Current status . . . . .	4
1.3 Low-carbon energy generation . . . . .	5
1.4 Practical consideration of photovoltaics . . . . .	7
1.5 The cost of PV . . . . .	9
1.6 Photovoltaic state of the art . . . . .	10
1.7 This work . . . . .	12
<b>Chapter 2 Introduction to organic electronics</b> . . . . .	14
2.1 Background . . . . .	14
2.2 Energy levels . . . . .	17
2.3 Excitons . . . . .	18
2.4 Heterojunctions . . . . .	20
2.5 Principles of OPV . . . . .	21
2.5.1 Dark Current . . . . .	22
2.5.2 Photocurrent . . . . .	24
2.6 Photocurrent measurements . . . . .	26
2.7 Thin film characterization . . . . .	30

2.7.1	X-ray diffraction	31
2.7.2	Photoelectron Spectroscopy	32
2.7.3	Atomic force microscopy	35
2.8	Modeling the external quantum efficiency	37
<b>Chapter 3 Scaling organic vapor phase deposition</b>		41
3.1	Background	43
3.1.1	Organic Light Emitting Diodes	43
3.1.2	Organic Transistors	44
3.1.3	Organic Photovoltaics	44
3.1.4	Crystalline growth	47
3.2	Scaling	49
3.2.1	Previous work	49
3.2.2	Model	51
3.2.3	Results	53
3.2.4	Discussion	57
3.3	Future work	58
3.3.1	Crystalline film growth	58
3.3.2	Graded HJ	60
3.4	Conclusions	60
<b>Chapter 4 Inverted OPV</b>		61
4.1	Background	61
4.1.1	Overview	61
4.1.2	Polymer devices	63
4.1.3	Small molecule devices	64
4.1.4	This work	65
4.2	Theory	66
4.3	Experiment	68
4.4	Results	69
4.4.1	Conventional devices	69
4.4.2	Devices without BCP	70
4.4.3	Inverted devices	74
4.5	Future work	80
4.5.1	Origin of the Open Circuit Voltage	80
4.5.2	Parallel tandem devices	80
4.5.3	Capping layer	82
4.5.4	Flexible substrates	82



4.5.5	Lifetime testing . . . . .	83
4.6	Conclusions . . . . .	84
<b>Chapter 5 Structural templating of multiple polycrystalline layers in organic photovoltaic cells . . . . .</b>		
		85
5.1	Background . . . . .	86
5.2	Experiment . . . . .	89
5.3	Results . . . . .	91
5.4	Discussion . . . . .	97
5.5	Conclusions . . . . .	97
<b>Chapter 6 Organic photovoltaics incorporating electron conducting buffer layers . . . . .</b>		
		99
6.1	Background . . . . .	100
6.1.1	Buffer layers in organic photovoltaics . . . . .	100
6.1.2	Functionalized squaraines . . . . .	103
6.2	Experiment . . . . .	106
6.3	Results . . . . .	107
6.4	Discussion . . . . .	110
6.5	Future work . . . . .	112
6.6	Conclusions . . . . .	112
<b>Chapter 7 Understanding tandem organic photovoltaic cell performance . . . . .</b>		
		114
7.1	Introduction . . . . .	114
7.2	Theory . . . . .	118
7.3	Results . . . . .	122
7.4	Discussion . . . . .	130
7.5	Conclusions . . . . .	131
7.6	Future work . . . . .	132
<b>Chapter 8 Tandem small molecule organic photovoltaics incorporating solution- and vacuum-processed donor materials . . . . .</b>		
		133
8.1	Background . . . . .	133
8.1.1	Tandems incorporating phthalocyanines and perylene derivatives . . . . .	133
8.1.2	Tandems incorporating phthalocyanines and fullerenes . . . . .	136
8.1.3	Tandems incorporating non-phthalocyanine donor materials . . . . .	141
8.1.4	Tandems incorporating doped, transparent transport layers . . . . .	143
8.2	Modeling tandem current-voltage characteristics . . . . .	146

8.3	Tandem organic photovoltaics incorporating SubPc and DPSQ as donor materials . . . . .	150
8.3.1	Experiment . . . . .	150
8.3.2	Single-cell results . . . . .	152
8.3.3	Tandem results . . . . .	155
8.3.4	Discussion . . . . .	157
8.3.5	Conclusions . . . . .	159
8.4	Tandem organic photovoltaics incorporating DBP and blended squaraines as donor materials . . . . .	160
8.4.1	Experiment . . . . .	160
8.4.2	Single-cell results . . . . .	162
8.4.3	Tandem results . . . . .	164
8.4.4	Discussion . . . . .	165
8.4.5	Conclusions . . . . .	166
8.5	Future work . . . . .	166
<b>Chapter 9 Tandem organic photovoltaics incorporating two solution-processed small molecule donor layers . . . . .</b>		<b>169</b>
9.1	Background . . . . .	169
9.2	Experiment . . . . .	171
9.3	Results and Discussion . . . . .	173
9.4	Conclusions . . . . .	179
<b>Chapter 10 Additional work on buffer layers . . . . .</b>		<b>180</b>
10.1	Organic electronics with symmetric electrodes . . . . .	180
10.1.1	Background . . . . .	180
10.1.2	Experiment . . . . .	181
10.1.3	Results and Discussion . . . . .	182
10.1.4	Conclusions . . . . .	186
10.2	Doping of metal oxide charge transport layers with organic molecules . . . . .	186
10.2.1	Experimental Method . . . . .	187
10.2.2	Results . . . . .	188
10.2.3	Discussion . . . . .	193
10.2.4	Conclusions . . . . .	195
10.3	Mixed buffer layers . . . . .	195
10.3.1	Background . . . . .	195
10.3.2	Theory . . . . .	195
10.3.3	Experiment . . . . .	196

10.3.4 Results . . . . .	197
10.3.5 Discussion . . . . .	201
10.3.6 Conclusions . . . . .	204
<b>Chapter 11 Conclusions . . . . .</b>	<b>206</b>
<b>Appendix . . . . .</b>	<b>211</b>
<b>Bibliography . . . . .</b>	<b>216</b>

# List of Tables

<b>Table</b>		
1.1	Lifecycle greenhouse gas emissions by electricity source. . . . .	4
4.1	Fitted parameters for conventional devices without BCP . . . . .	72
4.2	Fitted parameters for conventional devices with BCP . . . . .	74
4.3	Effect of different cathode materials on the $V_{OC}$ . . . . .	76
4.4	Comparison of conventional and inverted devices . . . . .	79
5.1	Device performance of templated OPVs . . . . .	95
6.1	Device performance of OPVs with different buffer layers . . . . .	109
7.1	Device structures and performance parameters for archetype single-cell devices. . . . .	123
7.2	Fitting parameters from archetype single-cell devices. . . . .	123
8.1	Organic photovoltaic performance. . . . .	153
8.2	Organic photovoltaic performance under simulated 1 sun AM1.5G illumination, corrected for spectral mismatch. . . . .	164
9.1	Organic photovoltaic performance. . . . .	175
10.1	Device performance with different electrodes. . . . .	184
10.2	Comparison of the series resistance for OPVs with different buffer layers. . . . .	191
10.3	Organic photovoltaic performance for devices with various buffer layers. . . . .	199

# List of Figures

Figure		
1.1	Sources of world electricity production. . . . .	5
1.2	Area required to produce 3 TW of photovoltaic power . . . . .	6
1.3	Electricity generation in Germany for two days in May of 2012. . . . .	8
1.4	Organic solar cell costs . . . . .	11
1.5	Best research-cell efficiencies as of early 2013. . . . .	12
2.1	OLED television . . . . .	15
2.2	Common organic semiconductors . . . . .	16
2.3	Fullerene C <sub>60</sub> . . . . .	16
2.4	Examples of flexible OPV cells . . . . .	17
2.5	The three types of excitons . . . . .	19
2.6	Organic heterojunctions . . . . .	21
2.7	Schematic diagram of dark processes in OPVs. . . . .	23
2.8	Dark Current Fits . . . . .	23
2.9	Processes inside an OPV cell . . . . .	25
2.10	A schematic diagram of various heterojunction morphologies . . . . .	26
2.11	International standard solar spectra . . . . .	27
2.12	Parameters of the <i>J-V</i> curve from an OPV device . . . . .	28
2.13	Schematic of the OPV test setup . . . . .	29
2.14	Spectra and responsivities necessary for spectral mismatch correction. . .	30
2.15	Schematic of a fixed source Bragg-Brentano conventional powder x-ray diffractometer. . . . .	31
2.16	Diagram of the Bragg condition in x-ray diffraction. . . . .	32
2.17	Schematic representation of photoemission spectroscopy. . . . .	33
2.18	Typical UPS data. . . . .	34
2.19	Experimental setup for force derivative measurement as a function of tip-sample spacing. . . . .	36

2.20	Typical AFM data. . . . .	36
2.21	Geometry of the multilayer stack used in the optical electric field calculations. . . . .	38
2.22	Calculated absorbed spectral power and external quantum efficiency. . . . .	40
3.1	Schematic of the VTE process . . . . .	42
3.2	Schematic of the OVPD process . . . . .	43
3.3	OVPD deposition of pentacene . . . . .	44
3.4	Comparison of VTE and OVPD growth . . . . .	45
3.5	Micrographs demonstrating growth regimes of CuPc in OVPD . . . . .	46
3.6	Nanocrystalline network growth by OVPD . . . . .	47
3.7	Changes in exciton diffusion length as a function of crystal size in PTCDA . . . . .	48
3.8	Schematic for an early large-area OVPD design . . . . .	50
3.9	Deposition profile for Gen. 6 substrates . . . . .	51
3.10	Schematic for a new large-area OVPD design . . . . .	54
3.11	Simulated and experimental data for OVPD deposition uniformity . . . . .	55
3.12	Simulated and experimental data for OVPD material utilization efficiency . . . . .	56
3.13	Reactor design for Gen. 6 substrates . . . . .	57
3.14	Modeled uniformity for Gen. 6 substrates as a function of reactor height . . . . .	58
3.15	Deposition profile for Gen. 6 substrates . . . . .	59
4.1	Comparison of conventional and inverted devices . . . . .	62
4.2	Schematic diagram of the structure of a top-illuminated OPV . . . . .	65
4.3	Energy levels in a OPV device . . . . .	66
4.4	Equivalent-circuit diagram of a solar cell . . . . .	66
4.5	Performance of a conventional SubPc/C <sub>60</sub> device . . . . .	71
4.6	Performance conventional devices with and without BCP . . . . .	72
4.7	Fitting parameters of devices with and without BCP . . . . .	73
4.8	Performance of the initial inverted device . . . . .	75
4.9	Effect of different electrodes on $V_{OC}$ . . . . .	77
4.10	Inverted devices' $V_{OC}$ as a function of $\Delta\Phi$ . . . . .	77
4.11	Performance of the optimized inverted device . . . . .	78
4.12	Comparison of conventional and inverted devices . . . . .	79
4.13	Parallel tandem device geometries . . . . .	81
4.14	Contour plot of photocurrent as a function of buffer and capping layer thicknesses. . . . .	83
5.1	Cartoon depicting two different molecular orientations . . . . .	86
5.2	X-ray diffraction patterns of templated molecules . . . . .	87
5.3	Characteristics of a templated OPV. . . . .	88
5.4	X-ray diffraction patterns of templated molecules . . . . .	90
5.5	Absorption coefficient of templated CuPc . . . . .	92

5.6	Ultraviolet photoelectron spectroscopy spectra of templated materials . . .	93
5.7	Atomic force micrographs of templated materials . . . . .	94
5.8	Current-voltage characteristics of devices with various templating layers .	96
5.9	Quantum efficiencies and absorptions of templated devices . . . . .	98
6.1	Energy levels of cathode-side buffer layers . . . . .	101
6.2	Comparisons of neat and doped BPhen layers. . . . .	102
6.3	Comparison of devices with BCP or a ruthenium complex as a buffer layer.	102
6.4	Energy levels and absorption coefficients for various buffer layers . . . .	103
6.5	Functionalized squaraine molecules . . . . .	104
6.6	Qualitative summary of the structural and performance outcomes . . . . .	105
6.7	Fill factor of devices with various cathode-side buffer layers . . . . .	107
6.8	Short-circuit current of devices with various cathode-side buffer layers . .	109
6.9	Series resistances of devices with various buffer layers . . . . .	111
6.10	Current-voltage characteristics of devices with various buffer layers . . .	111
7.1	Schematic diagram of thermalization losses in photovoltaics. . . . .	115
7.2	Schematic diagram of a tandem cell incorporating sub-cells stacked in series.	117
7.3	Dark and illuminated current-voltage characteristics for single-cell devices.	122
7.4	Contour plots of simulated tandem device performance characteristics. . .	124
7.5	Current-voltage characteristics of three example tandem devices. . . . .	125
7.6	Contour plots of simulated tandem device performance characteristics. . .	127
7.7	Current-voltage characteristics of three example tandem devices. . . . .	128
8.1	Hiramoto et al's tandem structure . . . . .	134
8.2	Performance of Yakimov et al's tandem device . . . . .	135
8.3	Enhancement in the optical field due to surface plasmons and the effect on CuPc absorption . . . . .	136
8.4	A tandem device incorporating two CuPc/C <sub>60</sub> planar-mixed heterojunctions.	137
8.5	A tandem device incorporating polymer- and small molecule-based sub-cells.	138
8.6	Schematic architectures of the tandem devices with different recombination layers. . . . .	139
8.7	Energy level diagram of an inverted tandem OPV. . . . .	140
8.8	Current density-voltage characteristics of the tandem cells with all-organic tunnel junctions. . . . .	141
8.9	External quantum efficiencies and extinction coefficients related to tandem OPVs. . . . .	142
8.10	Structure of the tandem configuration utilizing SubPc and SubNc. . . . .	143
8.11	Chemical structure of a merocyanine dye and device performance. . . . .	144
8.12	TAPC:fullerene device structure and performance. . . . .	145
8.13	Tandem OPV cell incorporating transparent, doped transport layers. . . .	146

8.14	Chemical structures for active materials incorporated in to a tandem cell. .	147
8.15	Process flow diagram for the modeling of tandem OPVs. . . . .	148
8.16	Extinction coefficients for the active materials used in the organic photo-voltaic cells . . . . .	152
8.17	Experimental current density vs. voltage characteristics for single-cell and tandems . . . . .	154
8.18	Calculated optical-electric field strength and absorbed spectral power . . .	155
8.19	Calculation of the power conversion efficiency of tandem devices . . . . .	156
8.20	Equilibrium energy level diagram of the tandem device . . . . .	158
8.21	Experimental external quantum efficiency spectra . . . . .	159
8.22	Extinction coefficients for the active materials used in the organic photo-voltaic cells . . . . .	162
8.23	Experimental current density vs. voltage characteristics for single-cell and tandem devices . . . . .	163
8.24	Experimental external quantum efficiency spectra . . . . .	165
9.1	Performance of $fSQ/C_{60}$ devices from various solvents . . . . .	173
9.2	Optical and atomic force micrographs for samples exposed to solvents . .	174
9.3	Device performance as a function of protective layer thickness and annealing conditions . . . . .	176
9.4	Performance of $fSQ/C_{60}$ tandem device . . . . .	178
10.1	Schematic diagram of the symmetric-electrode device. . . . .	183
10.2	Energy level diagram for the symmetric-contact device. . . . .	183
10.3	$J-V$ characteristic of devices with various electrodes. . . . .	184
10.4	External quantum efficiencies for devices with various electrodes. . . . .	185
10.5	Open-circuit voltage vs. short-circuit current for devices with various electrodes. . . . .	186
10.6	Resistivity of doped $MoO_3$ films. . . . .	189
10.7	Absorption coefficient of doped $MoO_3$ films. . . . .	190
10.8	$J-V$ characteristics of OPVs with doped $MoO_3$ layers. . . . .	190
10.9	$J-V$ characteristics of OPVs with AOB-doped $MoO_3$ layers. . . . .	191
10.10	$J-V$ characteristics and series resistance of OPVs with doped $MoO_3$ layers. .	192
10.11	$J-V$ characteristics and series resistance of OPVs with doped $MoO_3$ layers. .	192
10.12	Schematic of energy levels necessary for n- and p-type doping. . . . .	194
10.13	Proposed equilibrium energy level diagram for different buffer layers. . .	197
10.14	Normalized photoluminescence spectra of fullerene with various test layers. .	198
10.15	Extinction coefficients for thin films of fullerene, BCP, and mixtures thereof. .	198
10.16	Characterization of devices with various buffer layers. . . . .	200



10.17	Voltage-biased, normalized external quantum efficiency spectra for devices with various buffer layers. . . . .	200
10.18	Characterization of devices, varying the fullerene:BCP buffer layer mixing ratio. . . . .	201
10.19	Characterization of devices, varying the fullerene:BCP buffer layer position.	202
10.20	External quantum efficiency spectra. . . . .	202

# Abstract

The unique properties of organic semiconductors have led to significant scientific and commercial interest in organic electronics over the last ten years. During that time, these devices have gone from being a laboratory curiosity to being in hundreds of millions of pockets around the world. Going forward, there are opportunities for organic photovoltaics (OPVs) to provide carbon-neutral energy production due to the potential for flexible, low-cost, and large-scale production. In the first part of this thesis, we demonstrate techniques for depositing and controlling the morphologies of organic thin films. Organic vapor phase deposition (OVPD) is utilized to demonstrate a method to deposit organic thin films efficiently over large areas. An inverted architecture for OPVs is presented, which presents the possibility of depositing devices directly onto low-cost metal foils. We also explore the mechanisms and effects of structural templating in OPVs, where the molecular orientation of the active materials is controlled. This results in an improvement in power conversion efficiency of over 50% compared to untemplated devices. Additionally, we introduce new buffer layers in OPVs which lead to significant improvements in the device fill factor, resulting in

an increase in power conversion efficiency of more than 25%. In the second part of this thesis, we present developments in tandem OPVs for high-efficiency photovoltaics. By incorporating multiple sub-cells into a multi-junction OPVs architecture, the losses inherent in all OPV devices can be reduced significantly. Two of the works presented incorporate one solution-processed and one vacuum-processed sub-cell, resulting in efficiencies as high as  $8.3 \pm 0.3\%$  power conversion efficiency. We have also developed new techniques to utilize two solution-processed sub-cells into a monolithic tandem architecture, leading to a  $> 10\%$  increase in power conversion efficiency compared to an optimized single-cell device.

# Chapter 1

## Motivation

With concern for global warming mounting, one of the most important scientific problems of our time is how to produce clean and renewable energy. The International Governmental Panel on Climate Change (IPCC) recently stated that there is a more than 90% scientific certainty that trends in global warming are caused by human activity.<sup>1</sup> The primary source of global warming is the release of carbon dioxide (CO<sub>2</sub>), most of which comes from the burning of fossil fuels (coal, gasoline, natural gas, etc). Because of the relatively long lifetime of CO<sub>2</sub> in the atmosphere (approximately 300 years), much of the CO<sub>2</sub> emitted since the beginning of the industrial revolution is still present in the atmosphere. The IPCC predicts that, over the course of the 21st century, there will be an increase in global temperatures of 1.1 to 6.4 °C (3.2 to 11.5 °F) and a sea level rise of 18 to 59 cm (7 to 23 inches), depending on the amount of greenhouse gas emissions during that time.<sup>1</sup> The likely results of these changes includes coastal flooding, reduction in water supplies, loss of agricultural land, and increased severe weather activity.<sup>1</sup>

To minimize global warming, the IPCC has proposed carbon emission cuts of approximately 50% (compared to levels in the year 2000) by 2050.<sup>1</sup> These cuts are in direct conflict

with historical growth in total global energy use due to population and economic growth, as world-wide energy usage is predicted to triple by the year 2050.<sup>1</sup> There are three principal areas being explored to achieve the ambitious goal of reduced carbon emissions: natural resource management, including a reduction of deforestation and increase of protected lands; reduced energy usage, including increased transportation, lighting, and heating efficiency; and a shift to low-carbon energy production. In the short-term, all three of these are equally important; however, there are physical limits on how much land can be protected, and improvements in energy efficiency is not likely to lead to more than 50% reduction in usage.<sup>2</sup> In the long-term, generation of large amounts of low-carbon energy is essential to limit global warming.

At its most fundamental level, the main issue of low-carbon energy production is to develop technologies which can scale to a level that satisfies future energy demands. Carbon-emitting fossil fuel consumption has proven easily scalable, resulting in their use for 80% of the electricity currently consumed on the planet. It has also been shown that there are sufficient reserves of oil, natural gas, and coal to last hundreds of years.<sup>3</sup> The problem then is to shift to develop low-carbon energy sources which can scale to similar levels as fossil fuels with competitive pricing.

## **1.1 Terminology**

First, a brief overview of terminology used in this chapter. Electricity usage is measured in watts (W), which is a unit of power. A compact fluorescent light bulb might use 10 watts (W), and a microwave oven might use 1000 W. The watt is also used to measure

generation, such as a 500 megawatt (MW)<sup>†</sup> coal-fired power plant or a 4 MW wind turbine. For non-continuous power sources, this can present a problem when trying to compare numbers to more traditional, continuous power sources such as coal, natural gas, or nuclear: while a 100 MW coal plant will generate 100 MW continuously, a 100 MW wind farm will sometimes operate at 100 MW during optimum wind speed or 10 MW at low wind speeds. Wind power is typically rated by the “name-plate” power, while solar cells are rated by the “watts peak”, both of which represent the power generated under ideal circumstances. The ratio of the average power and the ideal power is known as the capacity factor (CF), which is typically 30 - 40% for wind and 10 - 20% for solar.<sup>‡</sup> Because of this variability, here we will discuss energy production in terms of the energy generated, in units of watt-hours (Wh), which takes into account the total electricity generated. For example, using a 10 W light bulb for 24 h uses  $10 \text{ W} \times 24 \text{ h} = 240 \text{ Wh}$  of energy, while a 1 kW photovoltaic\* installation with a CF of 10% would generate  $1 \text{ kW} \times 24 \text{ h} \times 10\% = 2.4 \text{ kWh}$  over the course of a day. The cost of electric energy is then measured in dollars per kilowatt-hour (\$/kWh), with typical rates in the U.S. ranging from \$0.08 - 0.17/kWh. For reference, the average U.S. household electricity usage per year is 11.5 MWh.

---

<sup>†</sup>A reminder of how the metric system prefixes work: k = kilo = 1,000 =  $10^3$ , M = mega =  $10^6$ , G = giga =  $10^9$ , T = tera =  $10^{12}$ . For example, 1 MW = 1,000 kW = 1,000,000 W.

<sup>‡</sup>This is dependent on factors such as temperature, latitude, cloud cover, etc.

\*The word “photovoltaics”, also known as solar cells, refers to technologies which convert sunlight directly into electricity. There are also other “solar thermal” forms of production which use light to generate heat.

## 1.2 Current status

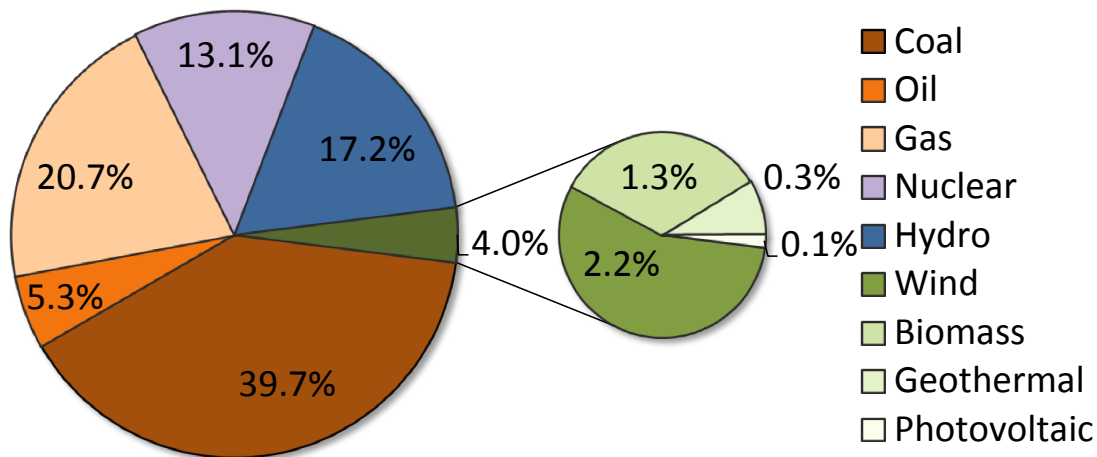
World electricity production in 2012 is estimated to have been 21,900 TWh. Figure 1.1 shows the sources of production, with coal as the largest source (40%), followed by natural gas (21%), hydroelectric (17%), nuclear (13%),<sup>†</sup> and oil (5%). Excluding hydroelectric, the remaining renewable sources account for only 4.0% of production: wind (2.2%), biomass (1.3%), geothermal (0.3%) and photovoltaic (0.1%). Table 1.1 shows the IPCC's calculations of the median lifecycle greenhouse gas emissions for these sources.<sup>4</sup> These values take into account all emissions during the construction, installation, operation, and disposal of each technology. From this table, it is apparent that the majority of today's electricity is generated from sources which produce large amounts of greenhouse gases. Although the recent shift in U.S. production from coal to natural gas has the potential to reduce emissions by half, these are still nearly ten times the emissions created by renewable technologies.

---

<sup>†</sup>Note that while nuclear is a low-carbon source, it is not "renewable" since it consumes fuel that exists in finite amounts in the earth's crust.

**Table 1.1** Lifecycle greenhouse gas emissions by electricity source, in median g(CO<sub>2</sub>)/kWh. From Ref. 4.

Source	Emissions (median, g(CO <sub>2</sub> )/kWh)
Hydroelectric	4
Wind (onshore)	12
Nuclear (Gen. II)	16
Biomass	18
Solar thermal	22
Geothermal	45
Solar PV (poly-Si)	46
Natural gas	469
Coal	1001



**Figure 1.1** Sources of world electric power in 2012, totaling 21,900 TWh. The pie on the right shows the distribution of non-hydroelectric renewable sources, which total 4.0% of total generation. From Ref. 5.

### 1.3 Low-carbon energy generation

The principal candidates for low-carbon energy generation are geothermal, tidal, wind, biomass, hydroelectric, carbon sequestration, nuclear, and solar. The first two can be ignored in this case because they simply cannot scale to the multi-1,000 TWhr/year level of energy production.<sup>3</sup> Although wind power is likely to be a significant portion of global energy production, realistic estimates predict a maximum of 3,000 to 5,000 TWh/year.<sup>§3</sup> Biomass too has an inherent scaling problem, because most land utilized for energy production would either take away from global food production or encourage further deforestation. Hydroelectric power also cannot scale further, as more than one half of the estimated 7,000 TWh easily dammable sites are already utilized. Carbon sequestration is a proposed

<sup>§</sup>Realistic estimates of potential U.S. wind power production are around 700 TWh/year. Although some have estimated world-wide potential wind power production at 9,000-14,000 TWh/year, these numbers ignore reduction in wind velocity when large numbers of turbines are present.<sup>3</sup>



technology where carbon emissions from burning coal are permanently stored underground. While this is conceptually convenient, it has not been sufficiently demonstrated on even a small scale. The current technology of nuclear fission based on uranium can be scaled significantly, but known ore reserves would only provide approximately 900,000 TWh, or less than 40 years of energy at current usage levels.<sup>3</sup> Developing “breeder” reactors which reprocess uranium’s nuclear waste into plutonium would greatly extend the lifetime of uranium as a fuel, but distributing large amounts of high-grade plutonium to thousands of reactors around the world has grave implications for global security. Research on other nuclear technologies such as a thorium fuel cycle or fusion have not yet approached practical viability.



**Figure 1.2** Map of the United States depicting the area (red box) necessary for 10% efficient solar cells to generate the 3 TW currently consumed nationwide. From Ref. 3.

The remaining option for low-carbon energy generation is solar power. The sun provides the earth with  $1.0 \times 10^9$  TWh/year, which is enough energy in one hour to power the entire

planet for a year. To produce the annual energy which is currently consumed in the United States would require an area  $300 \times 300 \text{ km}^2$  covered with 10% efficient photovoltaic cells, as shown in Fig. 1.2.<sup>3</sup> This is not a trivial amount of land, but it comprises only 1.7% of the total area of the U.S., equivalent to the land covered up by the national highway system. The problem then becomes one of cost; however, unlike the problem of limited supply, this is one which can be solved by science. It is essential, therefore, that new technologies be developed for low-cost photovoltaic power production.

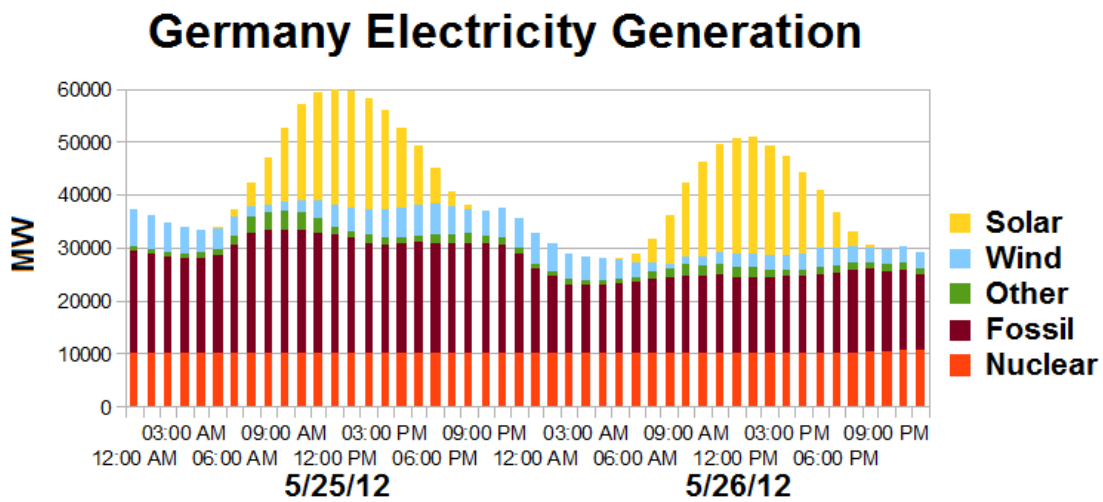
## 1.4 Practical consideration of photovoltaics

While photovoltaics (PVs) are a promising option for low-carbon energy production, they are by no means an ideal source of energy. Sunlight is not continuous throughout the day, limiting the amount of energy which can be harvested. The duration of sunlight is not constant throughout the year, and cloud cover can significantly reduce generation. In many places, the capacity factor is approximately 10%, meaning that the average daily power produced by a PV module is one tenth of the its power rating.<sup>6</sup>

Nevertheless, Germany is currently a test case which shows that PV can be a significant source of electricity. In 2012, 5.8% of Germany's electricity was generated by PV, totaling 28.5 TWh.<sup>6</sup> Figure 1.3 shows electricity generation data for two days in 2012. The baseline generation by nuclear and fossil fuel sources can be seen at the bottom of the graph in orange and red. Peak power consumption during daylight hours is provided by PV. The change in generation throughout the day reflects the typical daily usage cycle: energy usage is higher during the day, when offices and manufacturing are most active, and when air

conditioning is in use. These two days reflect a best-case scenario, where 17% of Germany’s total electricity was provided by PV, including 35% of the peak usage.

The German data indicate an initial application for PVs: to generate peak power during the day. The most viable regions for PVs are those with more solar flux (e.g. those close to the equator, with low cloud cover); where electricity is more expensive; and those with large daytime energy demands (e.g. air conditioning). In the near future, it is feasible to provide at least 10% of global energy demand using PV; however, exceeding this value will require some form of energy storage. This could take the form of conventional lead-acid, nickel-metal, or lithium-ion batteries, molten-salt batteries, or some other technology; however, it will add substantially to the cost of the hybrid PV/storage system.



**Figure 1.3** Electricity generation in Germany for two days in May of 2012. Values are averaged over each hour. From Ref. 6.

## 1.5 The cost of PV

Even considering PV systems without energy storage capabilities, cost is still a primary limitation of current photovoltaic technologies. Two useful measures of cost are module cost per area ( $\$/\text{m}^2$ ), where the module is what the reader may know as the “solar panel”) and levelized energy cost (LEC). LEC incorporates module costs (including materials, process, manufacturing), balance of systems (inverters, structural materials, wiring), amortization, lifetime, and efficiency. This, in effect, estimates the total-cost-in versus total-energy-out for sources of energy. Silicon (Si)-based modules currently account for more than 80% of the PV market, with costs currently  $\sim \$150/\text{m}^2$  with an LEC of  $\sim \$0.25/\text{kWh}$ , which compares unfavorably to coal ( $\sim \$0.10/\text{kWh}$ ), natural gas ( $\sim \$0.07/\text{kWh}$ ), and uranium ( $\sim \$0.11/\text{kWh}$ ).<sup>7</sup> Although prices have decreased more than 90% over the last 30 years, it may be necessary to move to a materials system which is cheaper and better lends itself to large area production.

Organic photovoltaics (OPVs) are a promising technology for large-scale, low-cost energy production. Current inorganic PV technologies require fabrication on an expensive crystalline substrate (e.g. Si or GaAs) or a glass substrate which can withstand high temperatures (e.g. CdTe). Because organic materials are processed at lower temperatures than traditional semiconductors, they can be deposited on a wide variety of low-cost substrates such as plastics and metal foils. Additionally, it may be possible to deposit organic films via a roll-to-roll production process, reducing costs by increasing production speed in a process similar to the printing of newspapers.<sup>†</sup> Although fabricating OPVs is much more

---

<sup>†</sup>United States production of newspapers was once greater than 10,000  $\text{km}^2$  per year, showing that roll-to-roll processes are scalable to the magnitude necessary.

complicated than putting ink on paper, the technology has the potential to dramatically reduce the cost of PVs.

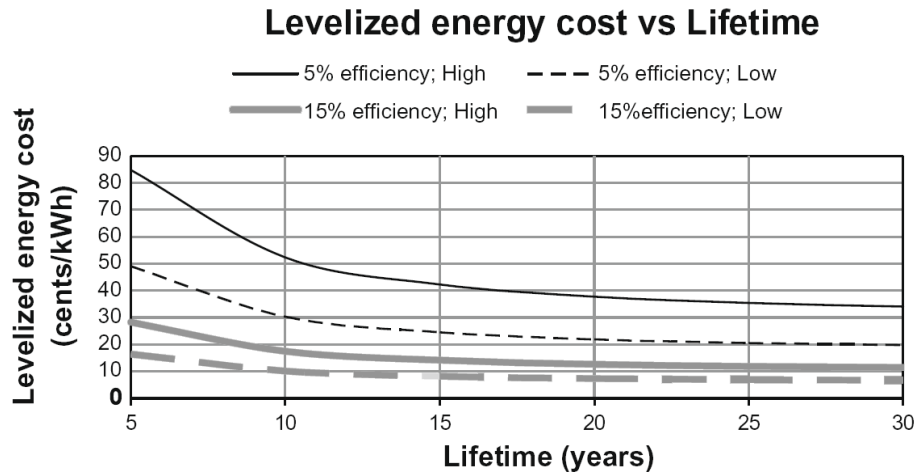
A 2009 study predicted an OPV module cost of \$50-\$140/m<sup>2</sup> and an LEC of \$0.07-\$0.13/kWh.<sup>7</sup> The wide range calculated is due to the uncertainty in production methods. For more traditional manufacturing processes, these costs are similar to estimates for commercially available CdTe modules (\$130/m<sup>2</sup>);<sup>7</sup> however, if less expensive deposition methods are utilized, OPV may become competitive with other low-carbon sources of energy. It is important to note that these estimates make many assumptions. Figure 1.4 shows the effect of variations in lifetime on the LEC for OPVs on the upper and lower end of manufacturing cost and at 5% and 15% efficiency. A more recent study calculates that with a 5 year lifetime, the cost of OPV modules will need to be approximately \$45/m<sup>2</sup> to compete with current inorganic PV technologies;<sup>8</sup> nevertheless, these calculations support the notion that OPV can be a practical and cost-effective means of power generation on a large scale if problems with efficiency, lifetime, and production cost are addressed. Although the investigations into the maximum possible lifetime of OPVs have only recently begun, there has been significant process recently with the power conversion efficiency.<sup>†</sup>

## 1.6 Photovoltaic state of the art

Progress in the power conversion efficiency ( $\eta_P$ ) of PV cells has increased steadily over the past four decades. Figure 1.5 shows measurements collected by the National Renewable Energy Laboratory (NREL) as of early 2013. The reader can see that, even for mature

---

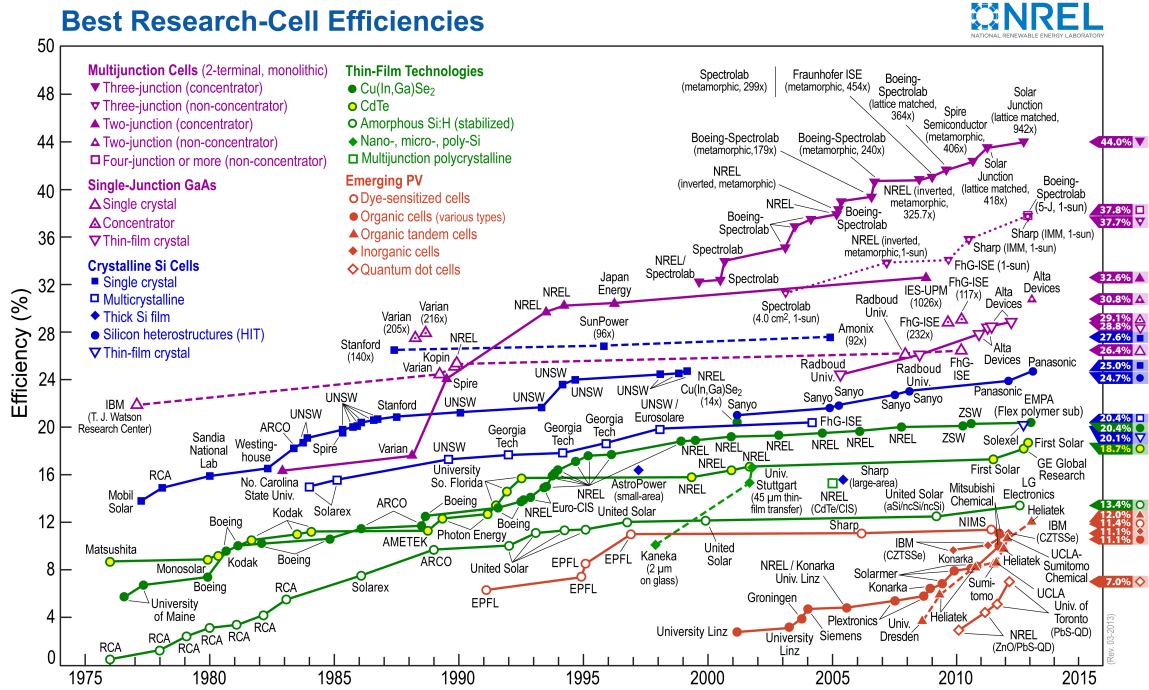
<sup>†</sup>Power conversion efficiency is defined as the total power in vs. the total power out. In the case of PVs, this is the amount of light on the solar cell divided by the electrical power that is output.



**Figure 1.4** Comparison of levelized energy costs for organic solar cells as a function of cell lifetime. Calculations are shown assuming 5% efficiency (black lines), 15% efficiency (gray lines), high production costs (solid lines) and low production costs (dashed lines). From Ref. 7.

technologies such as CdTe and GaAs, there have been substantial improvements over the last 5 years: specifically, new techniques in thin-film GaAs cells based on the epitaxial liftoff process<sup>9-11</sup> have been demonstrated with  $\eta_P = 28.8\%$ , which is approaching the theoretical maximum of 30% for a single-junction cell.<sup>12</sup> The field of OPVs has also shown significant improvements over the last 10 years, improving from  $\eta_P = 3\%$  to a recent record above 11%. Recent work by Giebink et al. has calculated that values of 22% are possible for OPVs.<sup>13</sup>

With the vast scientific, industrial, and consumer interest, it is an exciting time to be part of the photovoltaic community.



**Figure 1.5** Progress in the best research-cell efficiencies of various PV technologies. Courtesy of NREL.

## 1.7 This work

This thesis is organized as follows: Chapter 2 gives a background into the physical processes in organic electronics, along with an overview of measurement techniques used in this work. This is followed in Chapter 3 by an investigation into the performance and scalability of large-area organic vapor phase deposition systems. The remainder of this work involves OPV devices, beginning in Chapter 4 with work on inverted devices. Chapter 5 investigates the effects of controlling the molecular orientation via structural templating. In Chapter 6 electron conducting buffer layers are developed for OPVs which significantly increase their

fill factor, leading to significantly improved power conversion efficiency. These results are subsequently used in tandem OPV cells, where in Chapter 8 two donor-acceptor pairs are incorporated monolithically to increase the power conversion efficiency. This also includes an analytical model of these devices, through which we develop the criteria to minimize electrical losses in tandem OPV. Chapter 10 contains additional work on anode- and cathode-side buffer layers in OPVs.



# Chapter 2

## Introduction to organic electronics

### 2.1 Background

Organic semiconductors have recently gained considerable attention both scientifically and commercially due to their potential for novel and low-cost electronic devices. Organic light emitting diodes (OLEDs) have been commercially available since 2004, when small, monochrome OLED displays were incorporated into portable devices. In 2008, Sony released the world's first OLED TV, shown in Fig. 2.1. Although the widespread production of large OLED displays has had a number of setbacks since 2008, OLEDs have become one of the primary technologies for mobile phone displays, earning \$4.2 billion in 2011.<sup>14</sup> In the future, organic electronic devices are a promising technology for the production of low-cost, light-weight, and flexible applications such as roll-up displays, wearable electronics, and energy-generating paint.

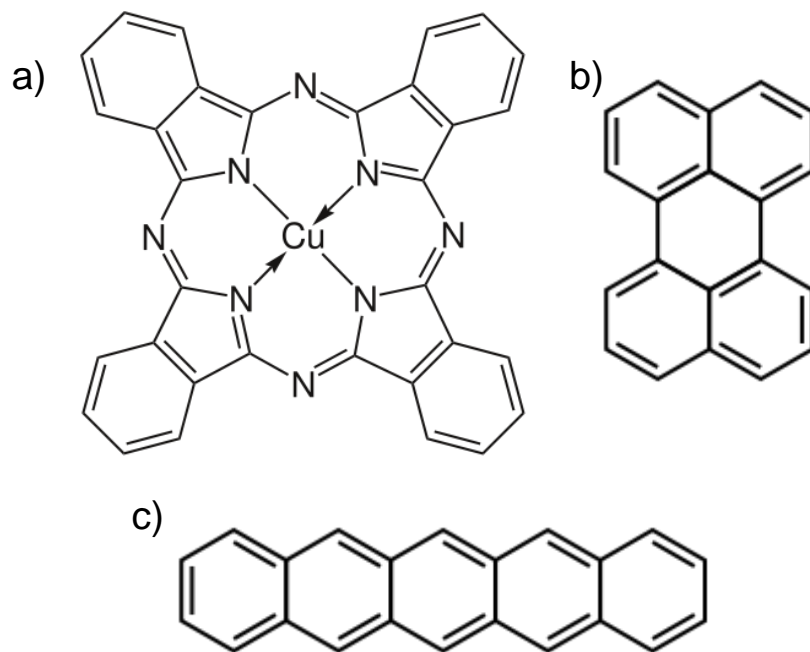
Organic semiconductors can be divided into two primary categories: small molecules and polymers. Small molecules are molecules with a definite molecular weight. Intramolecularly, atoms are covalently bonded, typically consisting of carbon, nitrogen and hydrogen.



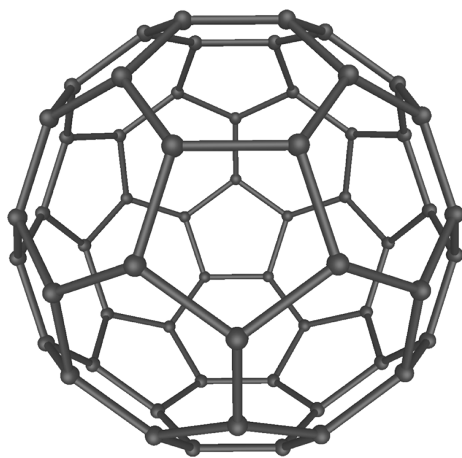
**Figure 2.1** The world's first OLED television, featuring a 3 mm thick display. Courtesy of Wikimedia commons.

Intermolecularly, they interact weakly with other molecules primarily via van der Waals interactions. Polymers consist of chains of repeating molecular segments connected via covalent bonds, with van der Waals interactions occurring between the chains. This work will mainly focus on small molecule-based devices. Archetypical molecules copper phthalocyanine (CuPc), perylene, and pentacene are shown in Fig. 2.2. A characteristic of these materials is the formation of a delocalized, pi-conjugated system within each molecule, giving rise to its electronic properties. For this reason, fullerenes such as C<sub>60</sub> (Fig. 2.3) are typically referred to as "organic," even though they do not have the C-H bonds characteristic of organic molecules.

Research on organic photovoltaic (OPV) cells started to gain attention in the early 1960s.<sup>15,16</sup> Until the mid-1970s power conversion efficiencies were very low, on the order of 10<sup>-5</sup>%. By the early 1980s, devices primarily consisted of relatively thick Schottky diodes and achieved around 0.1% efficiency.<sup>17</sup> In 1986, the field was revolutionized with



**Figure 2.2** Chemical structures of three common organic semiconductors: a) copper phthalocyanine (CuPc), b) perylene, and c) pentacene.

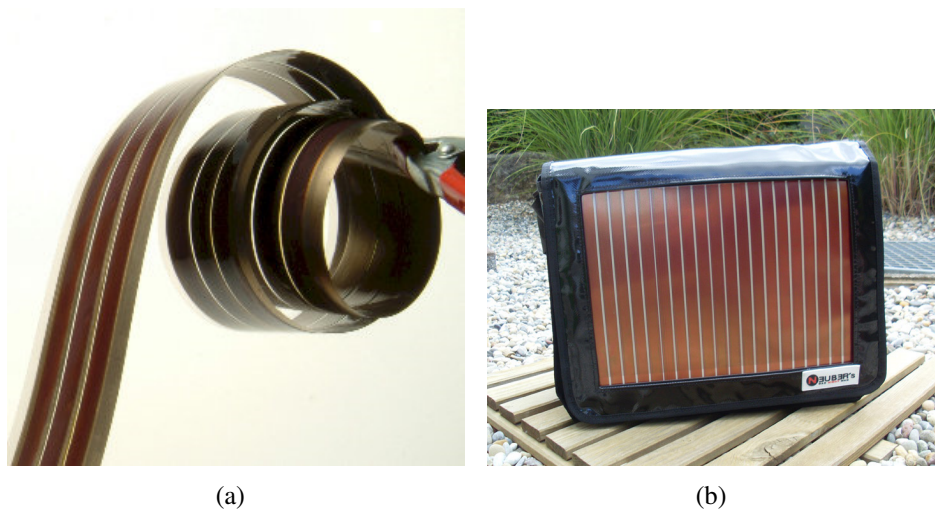


**Figure 2.3** Chemical structure of fullerene (C<sub>60</sub>).

C. W. Tang's invention of the donor-acceptor (D-A) heterojunction (HJ). By utilizing two layers, one electron donating and one electron accepting, a 1.0% efficient device was demonstrated.<sup>18</sup> The D-A HJ continues to be fundamental to OPV design to this day, driving progress over the last 25 years in materials and architecture to increase cell power conversion efficiency  $> 9\%$ .<sup>19,20</sup> In the 4th quarter of 2009, Konarka released its first line of commercial OPV cells, including a solar-powered shoulder bag (Fig. 2.4). Although Konarka has subsequently gone bankrupt, there are a multitude of other corporations bringing organic electronics to the marketplace.

## 2.2 Energy levels

Electronic processes in organic semiconductors are substantially different than their inorganic counterparts. For inorganic materials, the conduction and valence bands are



**Figure 2.4** Flexible OPVs (a) on a roll and (b) in a commercially available shoulder bag.

fundamental to understanding carrier transport; however, these bands arise from the existence of a periodic lattice structure, with strong inter-atomic interactions. While it is possible to grow organic single crystals, most organic electronic devices consist of amorphous or polycrystalline films, where long-range order is absent. The van der Waals bonds create poor intermolecular coupling, so energy bands typically do not exist as they do in inorganic materials. Instead, we refer to the highest-occupied molecular orbital (HOMO) and lowest-occupied molecular orbital (LUMO) energies. Neutral electronic excitations can promote electrons from the HOMO to the LUMO, whereupon they can migrate from molecule to molecule by thermally-activated hopping.<sup>21</sup> Because of the significant energy barriers that must be overcome for each hop, carrier mobility in organic materials is typically on the order of  $10^{-5}$  to  $1 \text{ cm}^2/\text{V}\cdot\text{s}$ ,<sup>22</sup> compared to  $10$  to  $10^5 \text{ cm}^2/\text{V}\cdot\text{s}$  for inorganic semiconductors.

## 2.3 Excitons

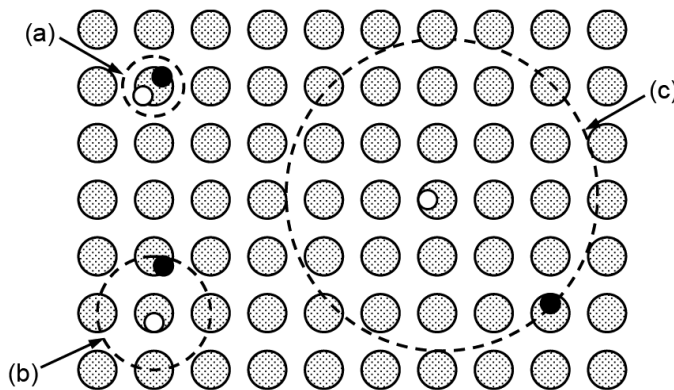
Another difference between inorganic and organic optoelectronic devices is the excitonic nature of organic thin films. An exciton is a bound electron-hole pair that is created when the molecule is optically excited. The exciton binding energy ( $E_{binding}$ ) can be described by

$$E_{binding} = \frac{q^2}{4\pi\epsilon_0\epsilon_r r}, \quad (2.1)$$

where  $q$  is the elementary charge,  $\epsilon_0$  is the vacuum permittivity,  $\epsilon_r$  is the relative permittivity (or dielectric constant), and  $r$  is the exciton radius.

There are three types of excitons: Frenkel, charge transfer (CT), and Wannier-Mott,

which are shown schematically in Fig. 2.5. Frenkel excitons reside on a single molecule and have a small radius and high binding energy, while CT excitons reside on adjacent molecules and have a slightly larger radius and slightly smaller binding energy. Wannier-Mott excitons have a large radius, typically many times the intermolecular distance, and correspondingly lower binding energy. For typical inorganic semiconductors such as silicon,  $\epsilon_r \geq 12$ . This leads to an exciton binding energy on the order of 5 meV, creating Wannier-Mott excitons that can be thermally dissociated at room temperature ( $kT \approx 26$  meV). These excitons are typically only observable at low temperature in inorganic crystalline semiconductors. Because of the low relative dielectric constant of organic materials ( $\sim 3$ ), exciton binding energies are on the order of 0.1 to 1 eV. This leads to the presence of a stable Frenkel state at room temperature.



**Figure 2.5** A schematic representation of the three types of excitons: (a) Frenkel, (b) charge transfer, and (c) Wannier-Mott. From Ref. 21.

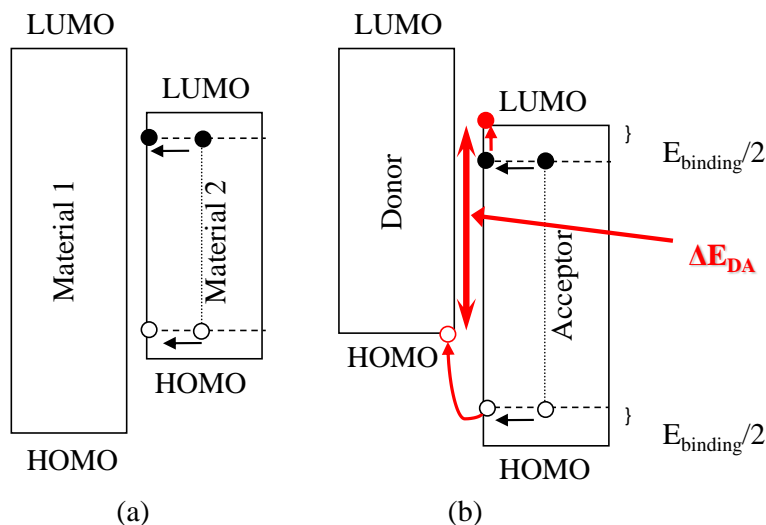
## 2.4 Heterojunctions

The presence of tightly-bound excitons leads to a fundamental difference in device design when compared to those consisting of inorganic materials, as excitons must first be dissociated before charge collection can occur. Electric field-dissociation of excitons is impractical, as fields as high as  $10^6$  V/cm<sup>†</sup> dissociate < 10 % of excitons.<sup>23</sup> A strategy that has proven successful for exciton dissociation at low applied fields is the donor-acceptor heterojunction.<sup>18</sup>

There are two types of heterojunctions discussed here. For a type-I heterojunction, material 1 has a smaller LUMO and a larger HOMO than material 2, as shown in Fig. 2.6(a). Excitons in material 2 do not have equal- or lower-energy states to transfer to in material 1, so the excitons are effectively 'blocked'. In a type-II heterojunction, the HOMOs and LUMOs of two materials are offset in a staggered fashion, as in Fig. 2.6(b). In this case, the hole from an exciton in the acceptor material which reaches the interface can transfer to a deep state in the donor material and gain energy to be promoted into the LUMO. Charge transfer occurs, and the resulting free carriers can then be transported by field-induced drift. For a type-II heterojunction, the maximum theoretical potential that can be extracted from the carriers is the difference between the HOMO of the donor and the LUMO of the acceptor ( $\Delta E_{DA}$ ), as shown in red in Fig. 2.6(b). This is the limiting factor of the open-circuit voltage ( $V_{OC}$ ) of OPV devices, as we will discuss in subsequent chapters.

---

<sup>†</sup>For a typical organic device with an active layer of 100 nm, this would be equivalent to applying > 10 V, which is greater than the breakdown voltage.



**Figure 2.6** Energy diagram of organic heterojunctions. Electrons and holes are represented by filled and open circles, respectively. Bound electron-hole pairs are in black, while free carriers are in red. Type-I (a) and type-II (b) heterojunctions are shown.

## 2.5 Principles of OPV

Organic photovoltaic devices typically have a number of commonly used components: an anode, where holes are collected; a donor material that transports holes; an acceptor material that transports electrons; and a cathode where electrons are collected. In this section, we will discuss photonic, electronic, and excitonic processes which occur inside these devices.



## 2.5.1 Dark Current

In the absence of light, OPVs typically behave similarly to a diode. Device current-voltage ( $J$ - $V$ ) characteristics have often been fit using the Shockley equation:

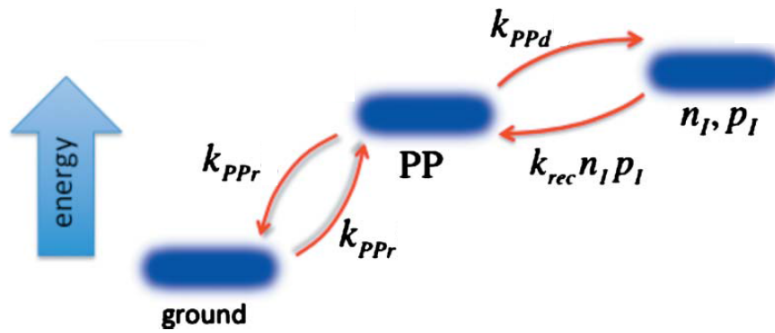
$$J_{dark}(V_a) = J_s \left[ \exp \left( \frac{V_a - JR_s}{nk_B T/q} \right) - 1 \right], \quad (2.2)$$

where  $J_s$  is the reverse saturation current,  $n$  is the ideality factor,  $k_B T$  is the Boltzmann constant-temperature product,  $q$  is the electronic charge, and  $R_s$  is the cell series resistance; however, many organic devices deviate significantly from this model, especially at low temperature. Recently, an ideal diode equation for organics was developed by Giebink et al., which can be used to simulate the dark current at equilibrium:<sup>24</sup>

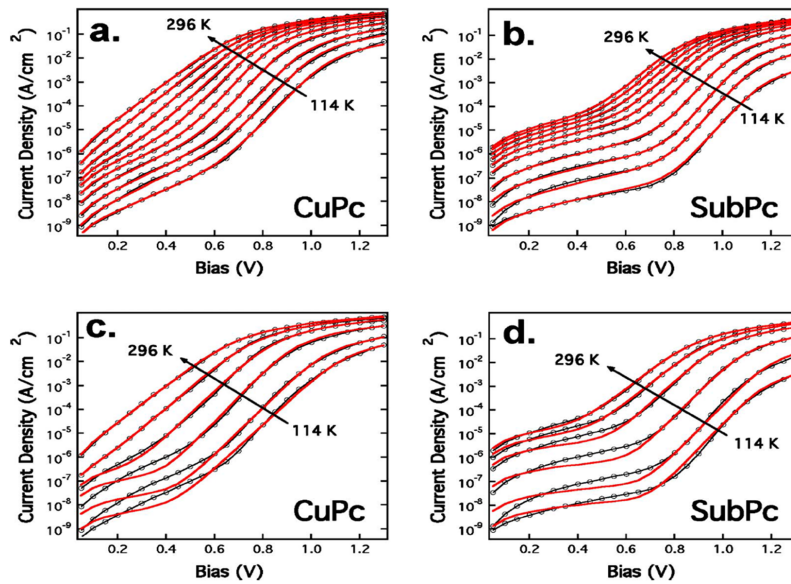
$$J_{dark}(V_a) = J_{sD} \left[ \exp \left( \frac{V_a - JR_s}{n_D k_B T/q} \right) - \frac{k_{PPd}}{k_{kPPd,eq}} \right] + J_{sA} \left[ \exp \left( \frac{V_a - JR_s}{n_A k_B T/q} \right) - \frac{k_{PPd}}{k_{kPPd,eq}} \right], \quad (2.3)$$

where  $J_{sD}$  and  $J_{sA}$  are saturation currents,  $k_{PPd}$  is the polaron pair dissociation rate,  $k_{kPPd}$  is the polaron pair dissociation rate at equilibrium, and  $n_D$  and  $n_A$  are ideality factors due to trap-limited recombination in the donor and acceptor, respectively. In this case, generation and recombination take place via a polaron pair (PP) state at the DA interface, as shown schematically in Fig. 2.7.

As seen in Fig. 2.8(c) and (d), although Eq. (2.2) fits well near room temperature, Eq. (2.3) provides better fits over a wide range of bias and temperature.



**Figure 2.7** Schematic diagram of dark processes in OPVs. Injected carriers (right) or generated carriers (left) must go through an intermediate polaron pair (PP) state before either recombining or being extracted, respectively. Adapted from Ref. 24.



**Figure 2.8** Dark current density vs forward voltage for (a) CuPc/C<sub>60</sub> and (b) SubPc/C<sub>60</sub> devices recorded for  $T = 296, 275, 247, 218, 193, 171, 155, 145, 128,$  and  $114$  K. Bold (red) lines indicate fits to Eq. (2.3) in the text. Thin (black) lines connect the data points and serve as a guide to the eyes. Both data sets are refit using the generalized Shockley equation in (c) and (d), where the difference between data and theory is most pronounced at low voltage and temperature. From Ref. 24.

## 2.5.2 Photocurrent

Generation of current from an OPV is a four step process: First, a photon is absorbed, creating an exciton. The exciton moves by diffusion and has a probability of encountering a heterojunction interface. At the interface, charge transfer may occur, dissociating the exciton into a free electron and hole. Finally, these carriers are transported towards the electrodes and collected. The external quantum efficiency ( $EQE$ ) is defined as the product of the efficiencies of each of these processes (Fig. 2.9):

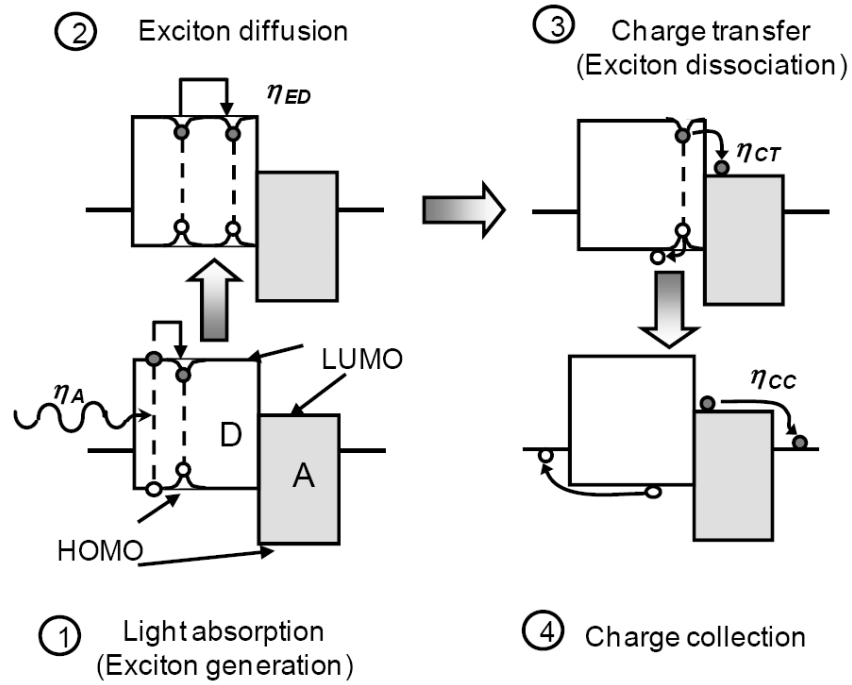
$$EQE = \eta_A \eta_{ED} \eta_{CT} \eta_{CC} \quad (2.4)$$

where  $\eta_A$  is the absorption efficiency,  $\eta_{ED}$  is the exciton diffusion efficiency,  $\eta_{CT}$  is the charge transfer efficiency, and  $\eta_{CC}$  is the charge collection efficiency. For a bilayer OPV,  $\eta_{CT}$  and  $\eta_{CC}$  are  $\approx 1$ , while  $\eta_A$  is a function of layer thickness and absorption length ( $L_A$ ), and  $\eta_{ED}$  is a function of layer thickness and exciton diffusion length ( $L_D$ ).  $L_A$  for these materials is on the order of 100 nm, but  $L_D$  is on the order of 10 nm, creating a competition between  $\eta_A$  and  $\eta_{ED}$ . This problem has been addressed by device geometries with increased donor-acceptor surface areas such as mixed heterojunctions,<sup>25,26</sup> planar-mixed heterojunctions,<sup>27</sup> and controlled bulk heterojunctions,<sup>28</sup> as shown in Fig. 2.10. Light trapping schemes have also been employed to increase absorption.<sup>29-36</sup>

The short-circuit current of the device ( $J_{SC}$ ) can be calculated by integrating the  $EQE$ :

$$J_{SC} = \int \frac{q\lambda}{hc} EQE(\lambda) S(\lambda) d\lambda, \quad (2.5)$$

where  $\lambda$  is the photon wavelength,  $q$  is the elementary charge,  $h$  is Planck's constant,  $c$  is



**Figure 2.9** A schematic diagram of excitonic and electronic processes within an OPV device. Courtesy of Fan Yang.

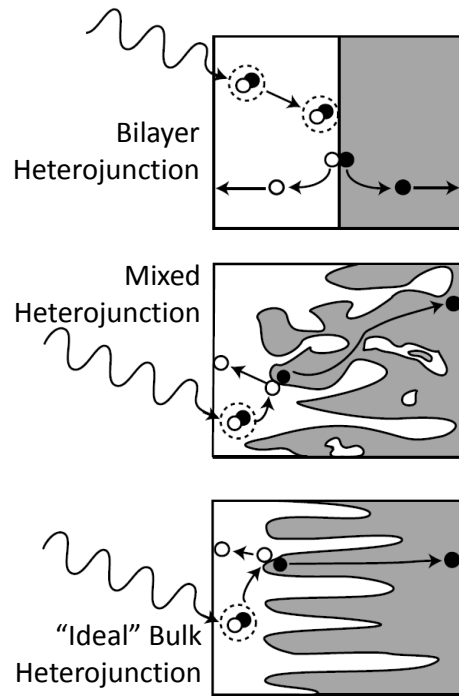
the speed of light, and  $S(\lambda)$  is the illumination spectral irradiance. The standard AM1.5G solar spectrum is typically used for terrestrial purposes, as shown in Fig. 2.11.

The power conversion efficiency ( $\eta_P$ ) is defined as the maximum power point divided by the incident light power ( $P_0$ ):

$$\eta_P = \frac{(J \cdot V)_{max}}{P_0}, \quad (2.6)$$

The fill factor ( $FF$ ), is defined as follows and illustrated in Fig. 2.12:

$$FF = \frac{(J \cdot V)_{max}}{J_{SC} V_{OC}}. \quad (2.7)$$



**Figure 2.10** A schematic diagram of various heterojunction morphologies within an OPV device. Courtesy of Fan Yang.

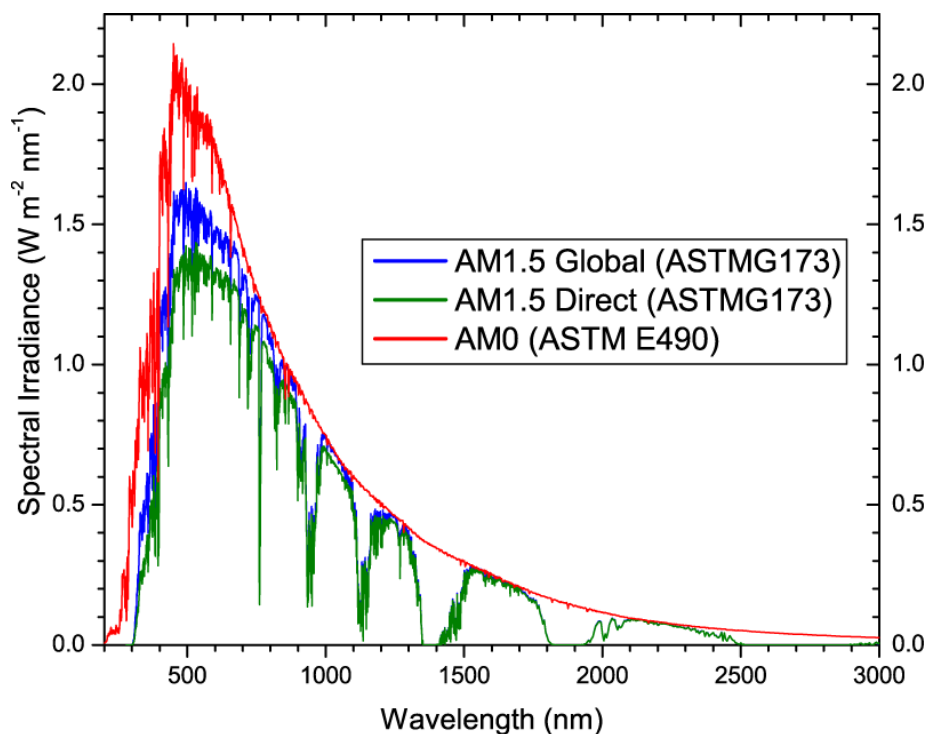
Substituting this into Eq. (2.6), we are left with the commonly used form:

$$\eta_P = \frac{V_{OC} J_{SC} FF}{P_0}. \quad (2.8)$$

## 2.6 Photocurrent measurements

To measure the performance of a solar cell, we measure the  $J$ - $V$  characteristics under simulated solar illumination and the  $EQE$ .

A schematic of an OPV testing station is shown in Fig. 2.13. A filtered Xe lamp is used as the solar simulating illumination source, and the intensity is varied by the use of

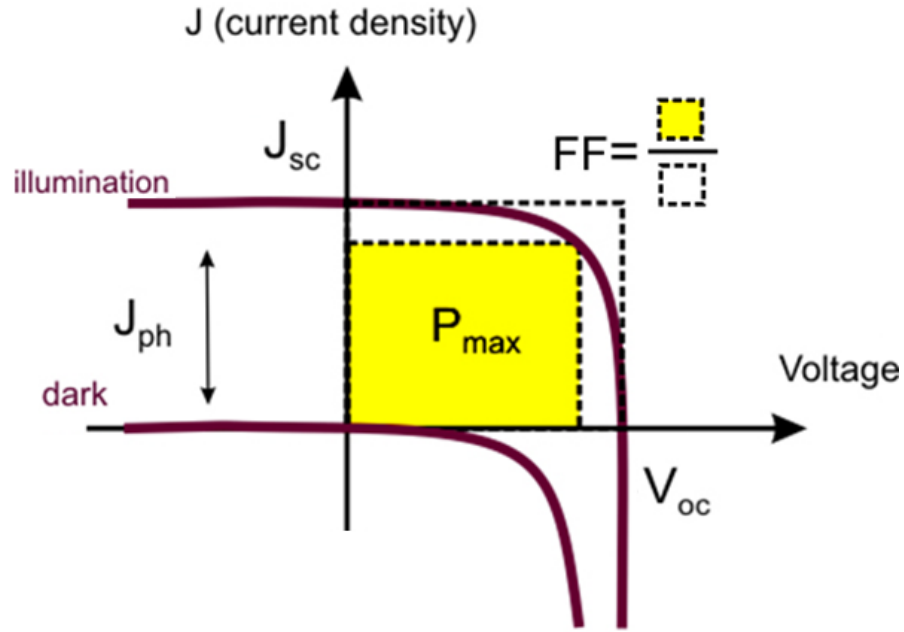


**Figure 2.11** International standard solar spectra AM0 (red), AM1.5D (green) and AM1.5G (blue). AM0 is used for space-based applications, while AM1.5G is typically used for terrestrial applications.

neutral density filters. The incident light intensity is measured using an NREL-traceable Si detector.<sup>37</sup> Probes contact the anode and cathode of the OPV cell, which are connected to a semiconductor parameter analyzer that sweeps voltage and measures the current.

The probes are then connected to a lock-in amplifier that measures current from the device. Light from another Xe lamp is collimated into a monochromator and chopped before being focused into a fiber. As the beam exits the fiber, it is collimated and focused to an area smaller than the device. The input intensity is subsequently calibrated with a NIST-traceable Si detector.

To more accurately represent the data for 1-sun intensity calculations, they must be

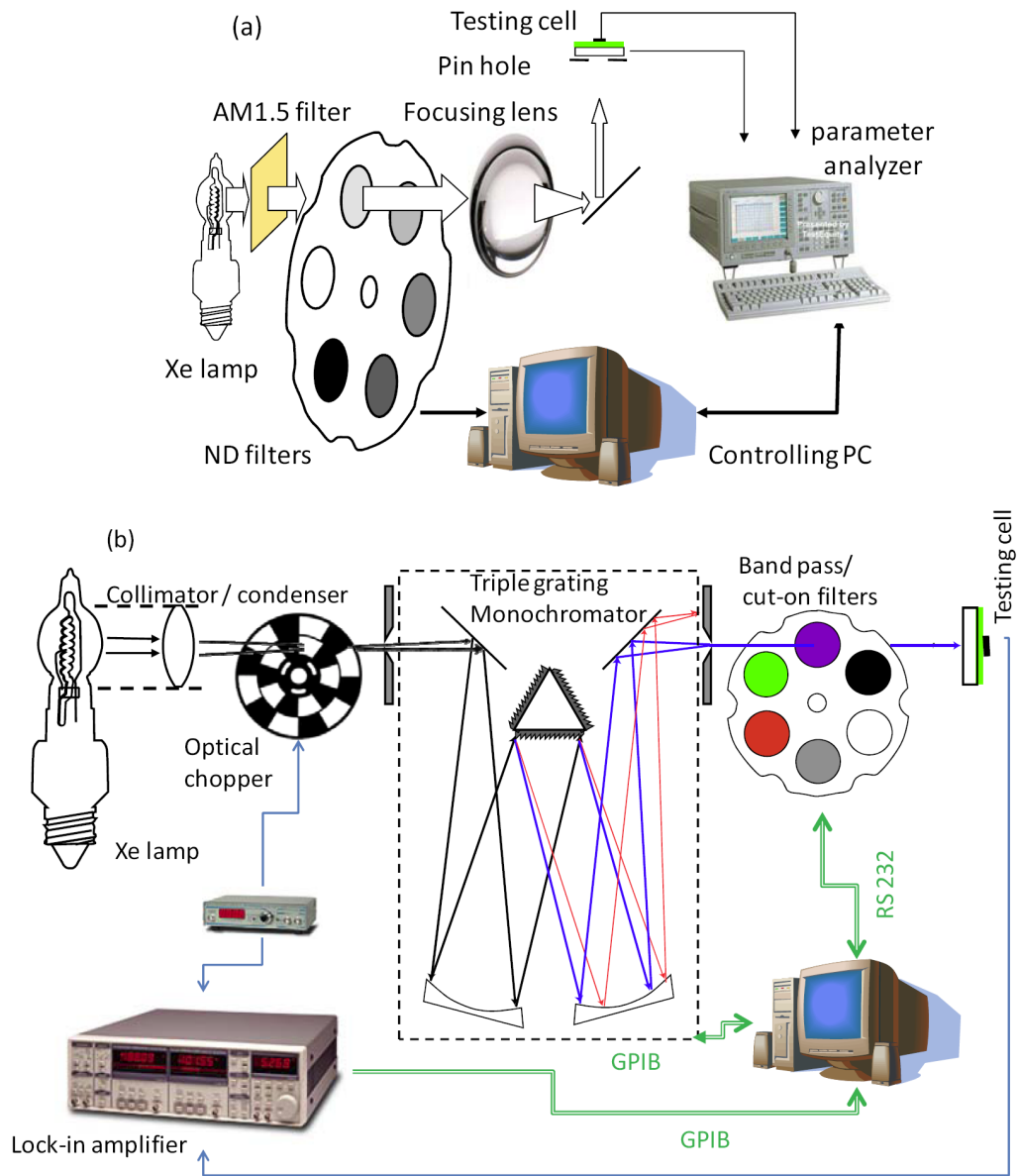


**Figure 2.12** A generalized  $J$ - $V$  curve typical of an OPV device showing the important performance parameters. Courtesy of Mark Thompson.

corrected for spectral mismatch.<sup>38</sup> This accounts for differences between the AM1.5G and simulated solar spectra, along with the spectral response of the test device and the reference device used to calibrate the lamp intensity. The  $J_{SC}$  is divided by the spectral mismatch factor,  $M$ , which is calculated as follows:

$$M = \frac{\int_{\lambda_1}^{\lambda_2} E_{Ref}(\lambda) S_R(\lambda) d\lambda \int_{\lambda_1}^{\lambda_2} E_S(\lambda) S_T(\lambda) d\lambda}{\int_{\lambda_1}^{\lambda_2} E_{Ref}(\lambda) S_T(\lambda) d\lambda \int_{\lambda_1}^{\lambda_2} E_S(\lambda) S_R(\lambda) d\lambda}, \quad (2.9)$$

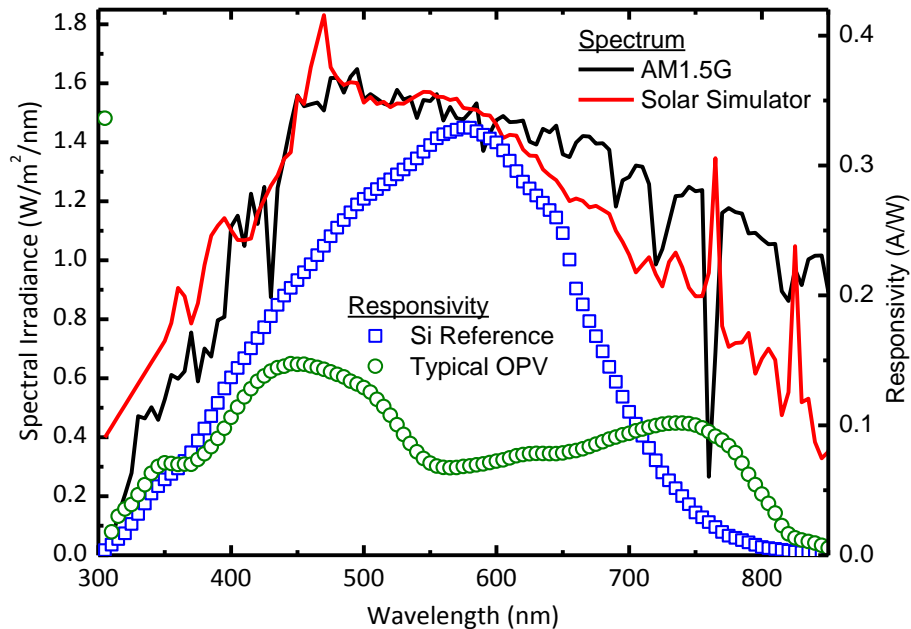
where  $E_{Ref}(\lambda)$  is the reference spectral irradiance,  $E_S(\lambda)$  is the source spectral irradiance,  $S_R(\lambda)$  is the spectral responsivity of the reference cell, and  $S_T(\lambda)$  is the spectral responsivity of the test cell, and  $\lambda_1$  and  $\lambda_2$  should encompass the spectral responses of both cells.



**Figure 2.13** A schematic of the testing setup used for OPV devices. Courtesy of Fan Yang.



These spectra and responsivities are shown in Fig. 2.14.



**Figure 2.14** Spectra (lines) and responsivities (symbols) necessary for spectral mismatch correction.

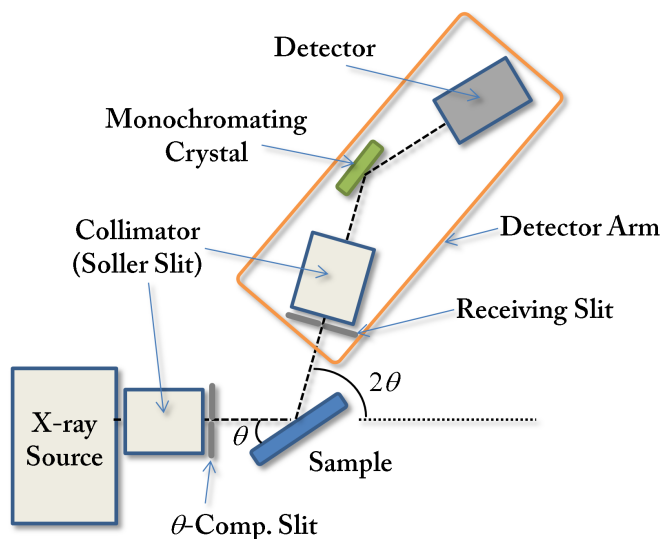
## 2.7 Thin film characterization

Thin film characterization provides additional information about film morphology, which can lead to greater understanding of the materials properties and the effects of process conditions. Three techniques used in this work are x-ray diffraction (XRD), ultraviolet photoelectron spectroscopy (UPS), and atomic force microscopy (AFM).

## 2.7.1 X-ray diffraction

X-ray diffraction was presented as a technique for probing atomic spacing by William Lawrence Bragg in 1912.<sup>39,40</sup> Fig. 2.15 shows a schematic of the experimental setup, where a collimated x-ray beam is incident on the sample. X-rays are then scattered with constructive interference that is a function of the incident angle, the crystal spacing, and the wavelength of the x-rays according to the Bragg relation:

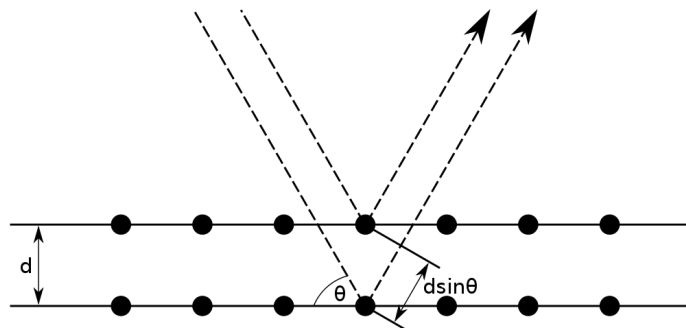
$$n\lambda = 2d \sin(\theta) \quad (2.10)$$



**Figure 2.15** Schematic of a fixed source Bragg-Brentano conventional powder x-ray diffractometer. Courtesy of Richard Lunt.

where  $n$  is the diffraction order,  $\lambda$  is the photon wavelength,  $d$  is the crystal spacing, and  $\theta$  is the angle between the sample plane and the incident beam. This relation is shown schematically in Fig. 2.16. From these measurements, information about the crystal structure,

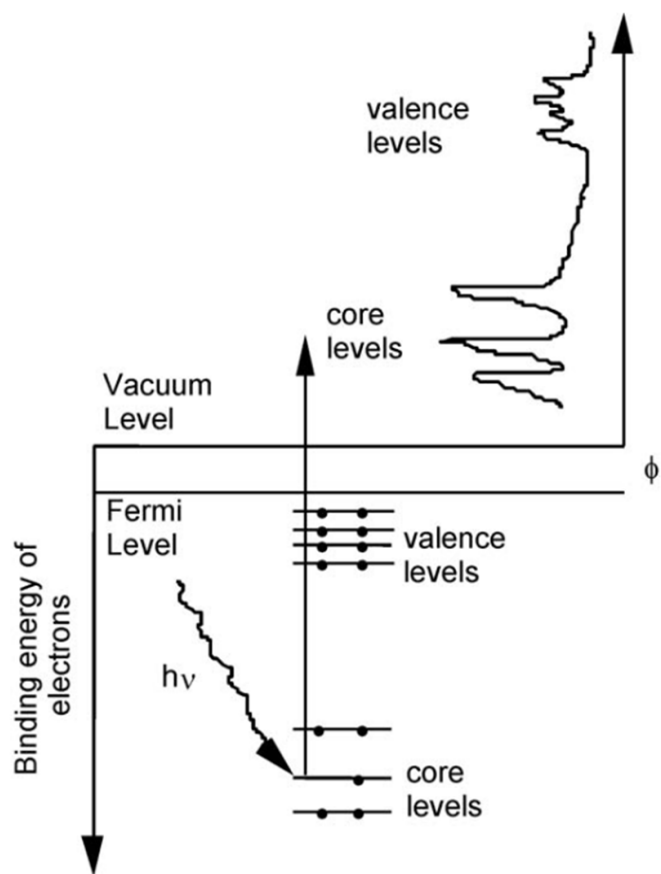
crystalline domain size, and orientation can be calculated.



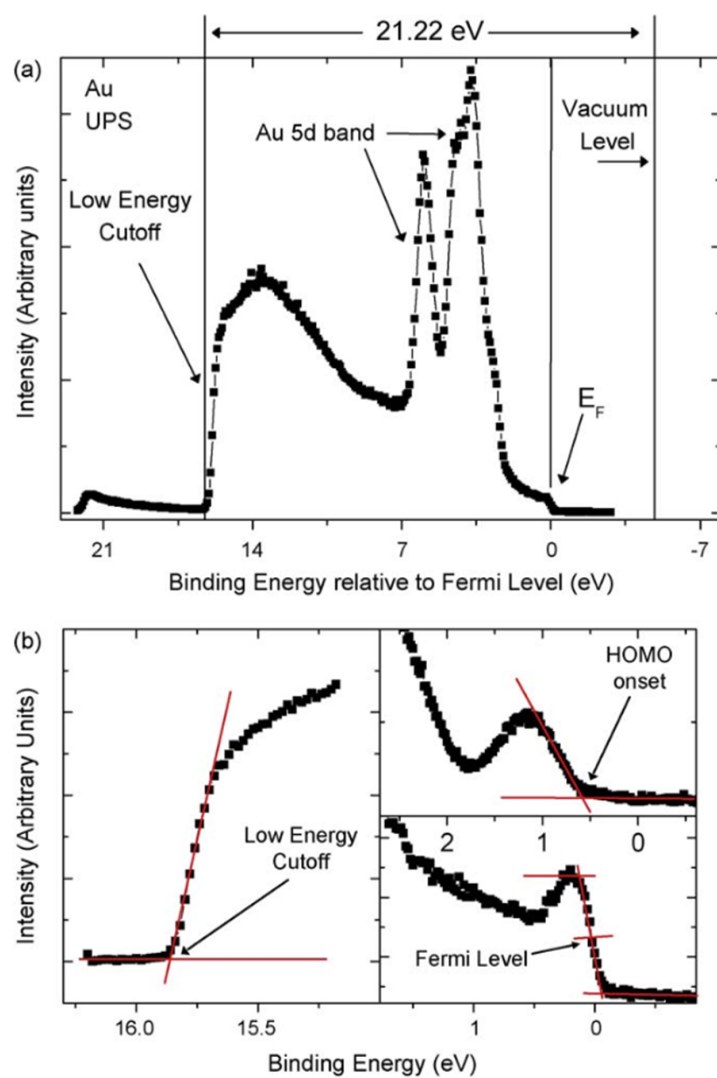
**Figure 2.16** Diagram of the Bragg condition in x-ray diffraction. Courtesy of Wikimedia Commons.

## 2.7.2 Photoelectron Spectroscopy

Photoelectron spectroscopy (PES) takes advantage of the photoelectric effect, which was described by Einstein in 1905.<sup>41</sup> Incident photons interact with the electrons in occupied energy levels, as shown in Fig. 2.17. According to the incident photon energy, valence- or core-level electrons can be ejected. In 1962, Turner et al. introduced a method now known as ultraviolet photoelectron spectroscopy, where high intensity UV light from a He source ejects valence-level electrons.<sup>42</sup> The kinetic energy of these electrons is measured, providing information about the energy levels in a material, and is commonly used to measure the work function and HOMO energy level in organic semiconductors. Figure 2.18 shows a typical UPS spectrum for Au, along with closeups of the low energy cutoff, HOMO onset, and Fermi level.



**Figure 2.17** A schematic representation of photoemission spectroscopy. Photoelectrons originate from energy levels occupied by electrons, including the valence as well as the core-level states. From Ref. 43.



**Figure 2.18** (a) UPS spectra of a clean Au surface; (b) UPS feature position determination, including the low energy cutoff (left), the HOMO onset of a semiconductor (top right), or the Fermi level of a metal (bottom right). From Ref. 43.

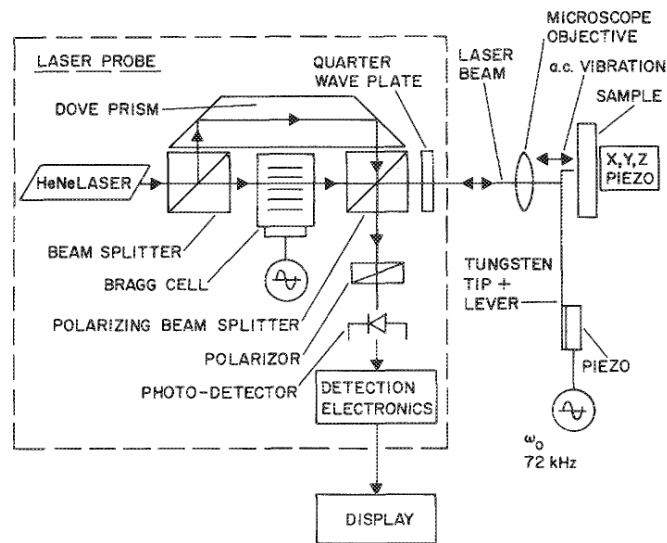
The HOMO energy ( $E_{HOMO}$ ) can be calculated as follows:

$$E_{HOMO} = E_{He1} + E_{cutoff} - E_{onset} \quad (2.11)$$

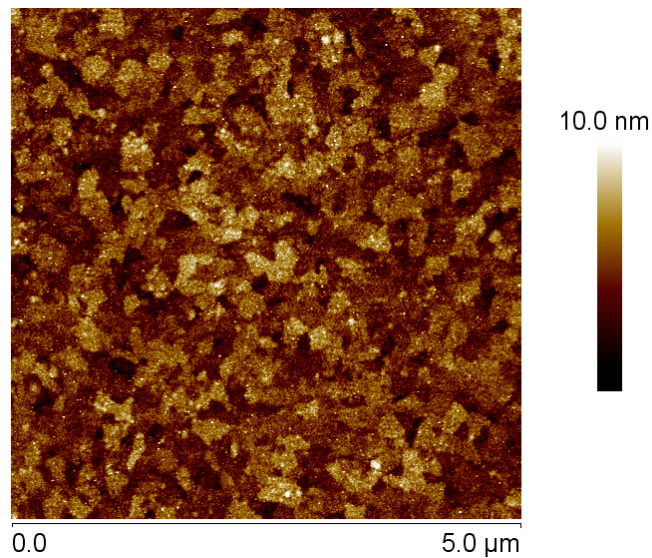
where  $E_{HeI}$  is the illumination energy,  $E_{cutoff}$  is the cutoff energy, and  $E_{onset}$  is the onset energy, as defined in Fig. 2.18. These measurements typically have a resolution of  $\pm 0.1$  eV. UPS data can provide useful information about energy levels in materials and the type of heterojunction they form when combined with another semiconductor.

### 2.7.3 Atomic force microscopy

Atomic force microscopy was introduced in 1986 by Binnig et al. as a method to measure surface contours at a scale below the optical diffraction limit.<sup>44-46</sup> The basic experimental setup is shown in Fig. 2.19, where a cantilever tip is brought within close proximity of the surface. The cantilever tip is driven at its resonant frequency, and the force on the tip is measured to determine the proximity to the sample. Thus, surface contours can be measured with a near-atomic level resolution. State-of-the art AFMs today typically have a vertical resolution on the order of 30 pm. Figure 2.20 shows an example of typical AFM data obtained from on a sample consisting of glass/100 nm In:SnO<sub>2</sub>/15 nm blended squaraine. Measurements by AFM can provide useful information for the characterization of surface roughness and nanoscale features.



**Figure 2.19** Experimental setup for force derivative measurement as a function of tip-sample spacing. From Ref. 45.



**Figure 2.20** Typical AFM data. The sample consists of glass/100 nm In:SnO<sub>2</sub> (ITO)/15 nm blended squaraine.

## 2.8 Modeling the external quantum efficiency

It is desirable to be able to predict device  $EQE$ , both to increase understanding and to optimize device design. Because the cathode material is typically reflective and the active layer thicknesses are  $< 100$  nm, optical interference effects caused by incident and reflected waves are important. Pettersson et al. introduced a formalism in 1999 to calculate the optical electric field in each layer, along with the absorption and exciton profile.<sup>47</sup> The optical electric field amplitude  $\bar{E}(x)$  is calculated as a function of wavelength and position ( $x$ ) throughout the layers.\* Light propagation is described by  $2 \times 2$  matrices, with continuity present in the tangential component of the electric field throughout the structure. As shown in Fig. 2.21, it is assumed that the first layer (the substrate,  $j = 0$ ) is semi-infinite, followed by the thin film layers ( $j = 1, 2, \dots, m$ ) with thicknesses  $d_j$  and wavelength-dependent complex indices of refraction,  $\bar{n}_j = n_j + i \cdot k_j$ . The layer stack is illuminated along the direction  $x$ .

The propagation of the optical field at the interface between layer  $j$  and  $k$  is described by the interface matrix  $I_{jk}$ :

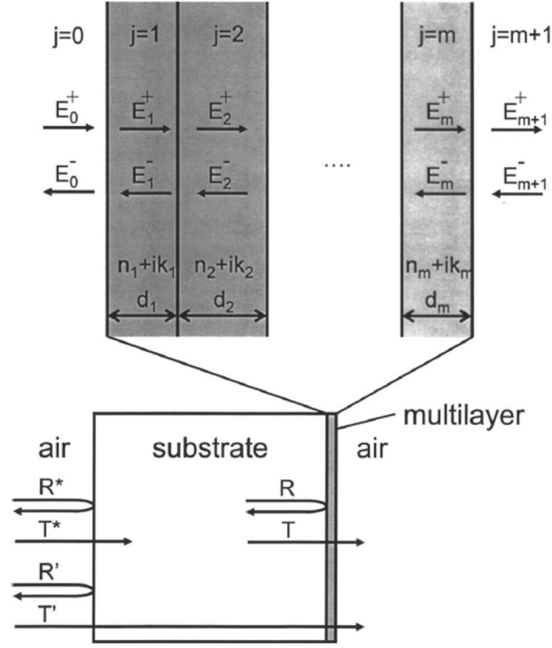
$$\begin{bmatrix} \bar{E}_j^+ \\ \bar{E}_j^- \end{bmatrix} = I_{jk} \begin{bmatrix} \bar{E}_k^+ \\ \bar{E}_k^- \end{bmatrix} = \begin{bmatrix} \frac{1}{t_{jk}} & \frac{r_{jk}}{t_{jk}} \\ \frac{r_{jk}}{t_{jk}} & \frac{1}{t_{jk}} \end{bmatrix} \begin{bmatrix} \bar{E}_k^+ \\ \bar{E}_k^- \end{bmatrix}, \quad (2.12)$$

where  $\bar{E}_j^\pm$  and  $\bar{E}_k^\pm$  are the components of the optical electric field propagating in the positive (+) and negative (−) directions in adjacent layers  $j$  and  $k$ , respectively, while the Fresnel complex reflection and transmission coefficients are  $r_{jk} = (\bar{n}_j - \bar{n}_k) / (\bar{n}_j + \bar{n}_k)$  and

---

\*Since this is a 1-D model, it is assumed that illumination is at normal incidence, all layers are flat compared to the wavelengths considered, and layers are optically homogeneous and isotropic.





**Figure 2.21** Geometry of the multilayer stack used in the optical electric field calculations. Layers 0 and  $m + 1$  are the transparent substrate and air, respectively. All calculated properties of this multilayer system are corrected for the air/glass reflections at the back side of the transparent substrate. From Ref. 23.

$t_{jk} = 2\bar{n}_j / (\bar{n}_j + \bar{n}_k)$ , respectively. The absorption matrix is

$$L_j = \begin{bmatrix} e^{-i\xi_j d_j} & 0 \\ 0 & e^{i\xi_j d_j} \end{bmatrix}, \quad (2.13)$$

where  $\xi_j = (2\pi/\lambda)\bar{n}_j$ .

The total electric field throughout the device can then be described by

$$\bar{E}_j(x) = \bar{E}_j^+(x) + \bar{E}_j^-(x) = (t_j^+ e^{i\xi_j x} + t_j^- e^{-i\xi_j x})\bar{E}_0^+, \quad (2.14)$$

and the time-averaged absorbed power is described by

$$Q_j(x) = \frac{4\pi c \epsilon_0 k_j n_j}{2\lambda} |\overline{E}_j(x)|^2, \quad (2.15)$$

where  $c$  is the speed of light and  $\epsilon_0$  is the permittivity of free space.

Next, the exciton generation rate,  $G_j(x) = (\lambda/hc)Q_j(x)$ , is used to calculate the exciton population within the active layers:

$$L_D^j \frac{\partial^2 p}{\partial x^2} - p + \tau_j G_j = 0, \quad (2.16)$$

where  $p$  is the exciton density,  $L_D^j = \sqrt{D_j \tau_j}$  is the exciton diffusion length of the material layer  $j$ ,  $D_j$  is the exciton diffusivity, and  $\tau_j$  is the exciton lifetime. Equation (2.16) is then solved using two boundary conditions: (1) ideal non-quenching (i.e. 'blocking') interfaces with  $\delta p / \delta x = 0$ ; and (2) quenching interfaces with  $p = 0$ . The photocurrent density contribution at the D-A interface is then given by the following relation:

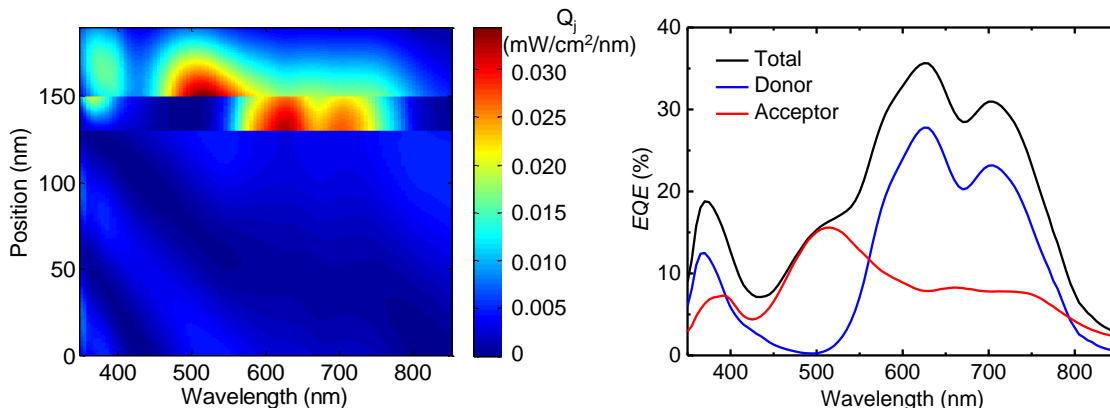
$$J_j = q \frac{L_D^j{}^2}{\tau_j} \left. \frac{\delta p}{\delta x} \right|_{x=x_{DA}}, \quad (2.17)$$

where  $x_{DA}$  is the position of the D-A HJ. Finally, the  $EQE$  for each active layer can be calculated:

$$EQE_j = \frac{2J_j/q}{c\epsilon_0 |\overline{E}_0^+|^2}, \quad (2.18)$$

assuming that  $\eta_{CT} = \eta_{CC} = 1$ .

Figure 2.22 shows an example of data calculated by the model, including  $Q_j$  and  $EQE$



**Figure 2.22** Calculated (left) absorbed spectral power and (right) external quantum efficiency for an archetypal bilayer donor-acceptor heterojunction device consisting of 130 nm In:Sn<sub>2</sub> (ITO)/20 nm CuPc/40 nm PTCBI/Ag. Position is with reference to the glass/ITO interface.

for an archetypal bilayer HJ device consisting of glass/130 nm ITO/20 nm CuPc/40 nm PTCBI/Ag, where  $L_D = 10$  nm and 5 nm for the donor and acceptor, respectively. This model allows for the optimization of layer structures prior to device growth, requiring only  $\bar{n}$  and  $L_D$  as input parameters, which can be measured by variable-angle spectroscopic ellipsometry and photoluminescence quenching,<sup>48</sup> respectively.

## Chapter 3

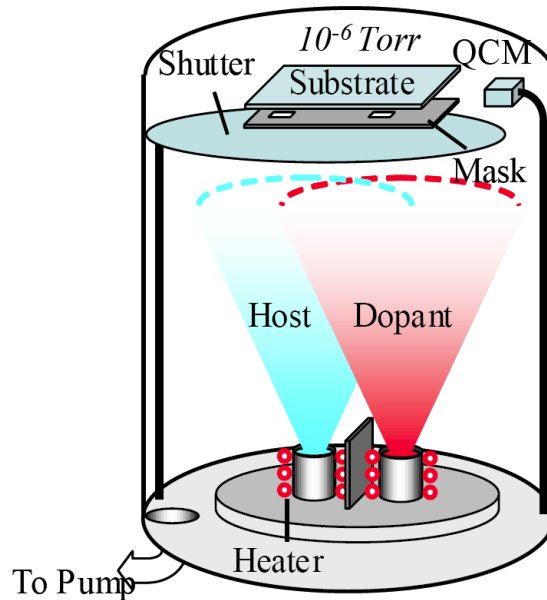
# Scaling organic vapor phase deposition

Organic vapor phase deposition (OVPD) was introduced as a technique for the growth of organic thin films in 1995.<sup>49</sup> It was developed to overcome fundamental limitations of standard vacuum thermal evaporation (VTE) techniques: low material utilization efficiency, limited morphology control, poor thickness uniformity, and poor doping control. OVPD allows greater control over film growth by decoupling the evaporation and deposition events. In this chapter, we give an overview of basic operation of OVPD, followed by a brief discussion of the theoretical principles behind OVPD growth. Subsequently, we will review previous OVPD results, followed by current work on scaling and directions for future OVPD work.

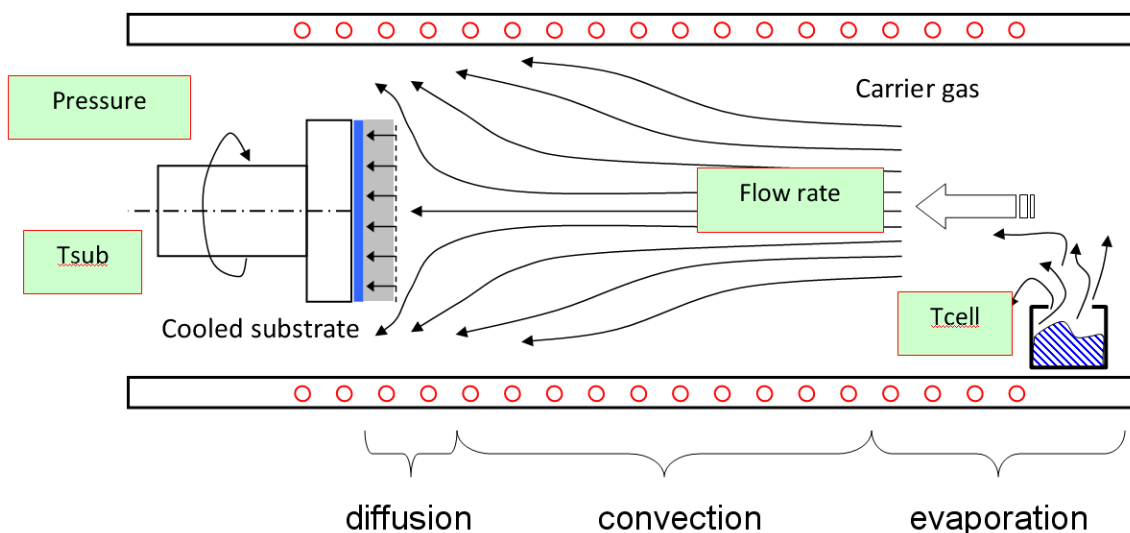
First, we present a brief comparison of VTE and OVPD. VTE occurs at high vacuum ( $< 10^{-6}$  Torr), where material is heated resistively in a boat or crucible and transported ballistically towards the substrate (Fig. 3.1). Typically, the only control typically available is the source temperature, which determines the deposition rate. To achieve uniform films and uniform codeposition, there must be a substantial distance between the source and substrate. This, in turn, reduces the material utilization efficiency, typically  $\sim 3\%$  in research-scale

systems.

OVPD occurs in a hot-walled reactor at low vacuum ( $\sim 1$  Torr). Material is heated in a crucible and is transported convectively by an inert carrier gas (Fig. 3.2). When the material arrives at the substrate, it encounters a boundary layer. At this point, the transport changes from a convective regime to a diffusive regime. Once the materials diffuse through the boundary layer, they adsorb onto a cooled substrate. In OVPD there are four control parameters: source temperature, carrier gas flow rate, pressure, and substrate temperature. By varying these four parameters, unique film morphologies can be achieved.



**Figure 3.1** Schematic of the VTE process. Courtesy of Fan Yang.



**Figure 3.2** Schematic of the OVPD process. Courtesy of Richard Lunt.

## 3.1 Background

The unique abilities of the OVPD process have previously been utilized for the growth of films and devices, including OLEDs, transistors, OPVs, and the growth of crystalline films.

### 3.1.1 Organic Light Emitting Diodes

The first devices grown in OVPD were fluorescent OLEDs.<sup>50</sup> In this work, N'-diphenyl-N,N'-bis (3-methylphenyl)1-1'biphenyl1-4-4' diamine (TPD)/tris-(8-hydroxyquinoline) aluminum (Alq<sub>3</sub>) devices grown by OVPD and VTE both exhibited a peak *EQE* of  $0.40 \pm 0.05\%$ . This was followed by a phosphorescent device based on a guest/host system of fac-tris(2-phenylpyridine)iridium (Ir(ppy)<sub>3</sub>)/4,4'-bis(N-carbazolyl)biphenyl (CBP) which exhibited a peak *EQE* of  $7.0 \pm 0.1\%$  from both VTE and OVPD.<sup>51</sup> Operation lifetime of these devices was also shown to be equivalent. Recently, an OLED structure which

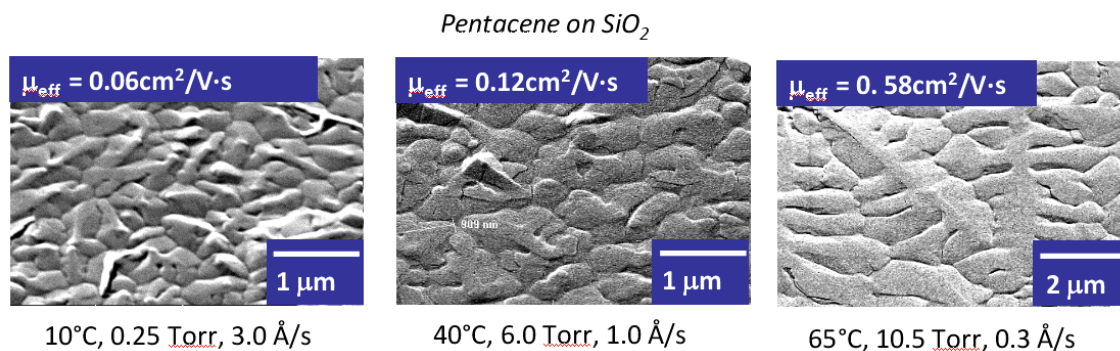
incorporated graded recombination zones was grown by OVPD. These devices showed both increased peak  $EQE$  from 9 to 18% and decreased roll-off at high light intensities.<sup>52,53</sup>

### 3.1.2 Organic Transistors

Thin-film transistors (TFTs) have also been grown via OVPD. An initial study on pentacene TFTs found that OVPD growth conditions could influence the morphology of the pentacene films (Fig. 3.3).<sup>54</sup> At high substrate temperature and low growth rate, large crystal domains resulted in a high field effect mobility ( $\mu_{eff}$ ); however, due to fractures and voids along the grain boundaries, these films had a significantly reduced on-off ratio. More recent work on pentacene-based devices have seen further improvement in performance.<sup>55,56</sup>

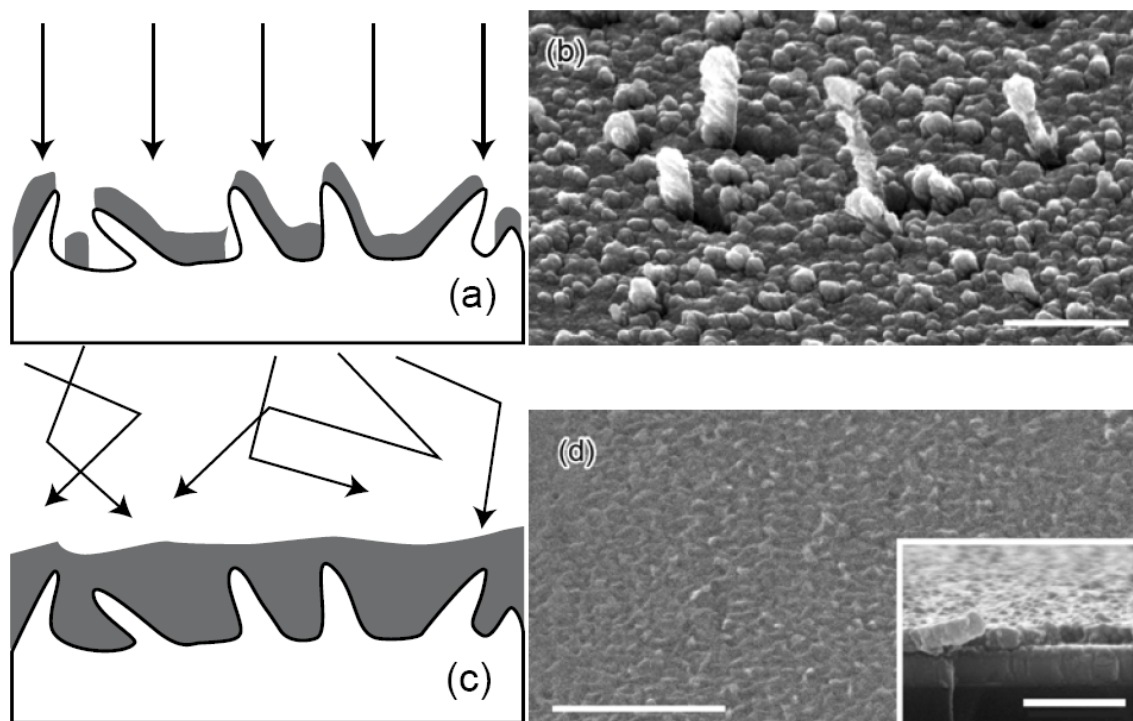
### 3.1.3 Organic Photovoltaics

Since 2005, there have been significant advances in OPV devices grown by OVPD. One advantage of OVPD is the ability to conformally coat rough surfaces. Because the molecules have numerous collisions when diffusing through the boundary layer, molecular motion



**Figure 3.3** Scanning electron microscope images of pentacene deposited by OVPD on SiO<sub>2</sub> under different conditions. From Ref. 54.

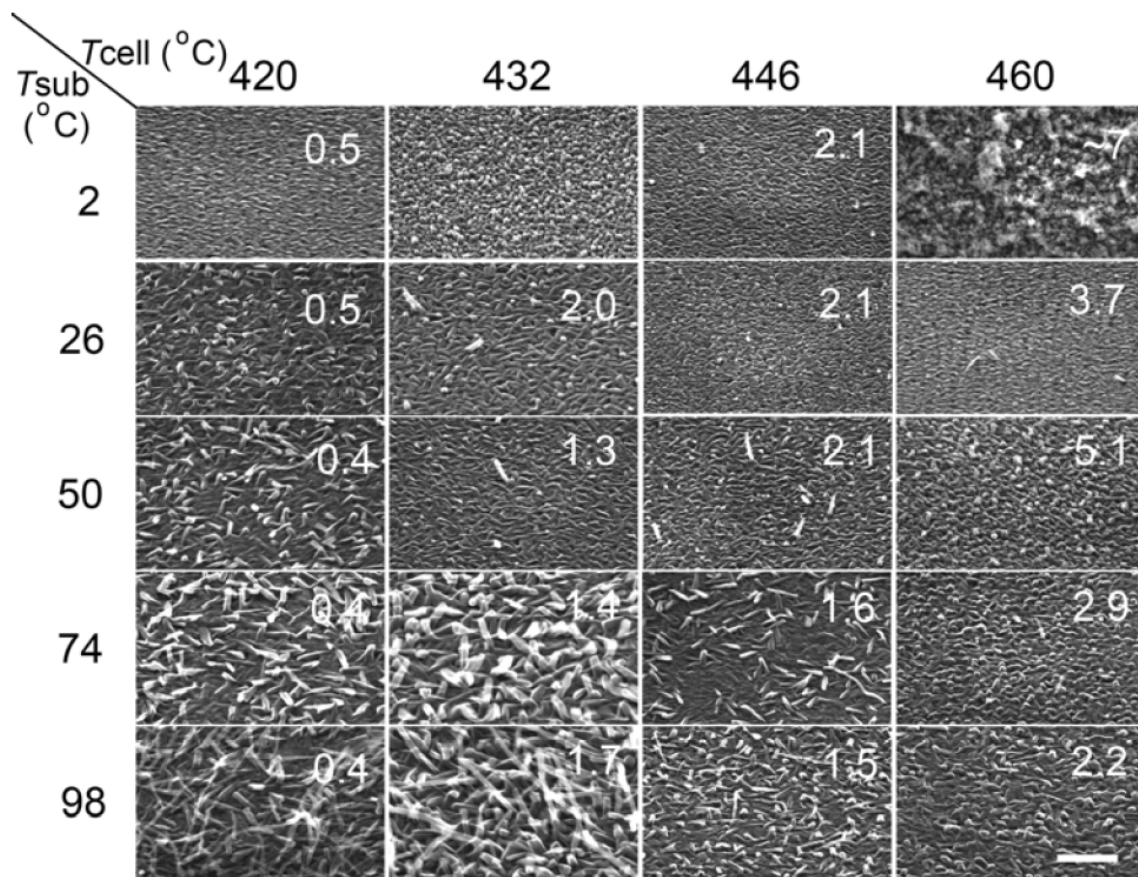
becomes anisotropic. This has the effect of filling in gaps on the substrate, as seen in Fig. 3.4. This was shown to be advantageous for OPVs grown on low-cost, rough substrates such as SnO<sub>2</sub>:F.<sup>58</sup> It was also demonstrated that by changing the growth conditions of the donor CuPc, a wide variety of morphologies can be achieved, including smooth, rough, and nanowire morphologies (Fig. 3.5).<sup>57,59,60</sup> It was then shown that by growing a layer of CuPc nanowires and then conformally covering it with an acceptor (C<sub>60</sub>), device performance was improved 40% compared to an analogous bilayer control device.<sup>57,59,61</sup> This technique was extended by depositing alternating ultrathin layers of CuPc and C<sub>60</sub>.<sup>28</sup> Due to differences in surface energy, the materials preferentially deposit on similar molecules, forming



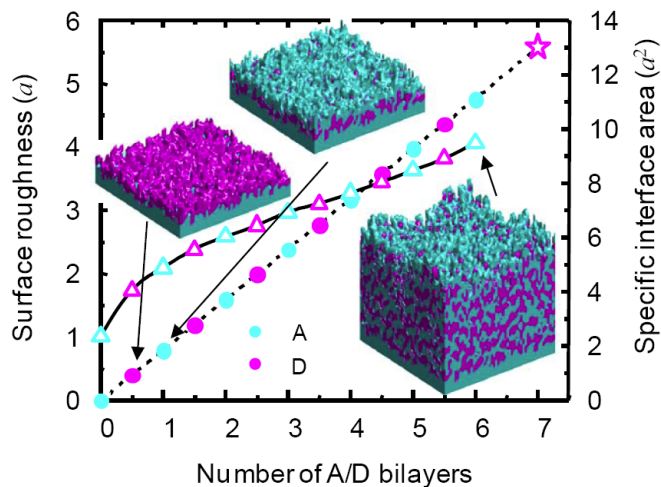
**Figure 3.4** Comparison of growth by VTE and OVPD onto a folded surface. Schematic representations of (a) VTE and (c) OVPD and scanning electron microscope images of C<sub>60</sub> grown on CuPc by (b) VTE and (d) OVPD. Scale bars are 500 nm. From Ref. 57.



nanocrystalline islands. By alternating multiple periods of donor/acceptor growth, an interpenetrating network was formed (Fig. 3.6). As a result of the increased donor/acceptor interface area and increased thickness possible in a nanocrystalline film, this device tripled the efficiency compared to a bilayer control device. It was later demonstrated that this technique could be extended to a simultaneous heterojunction with two donors and one acceptor.<sup>62</sup>



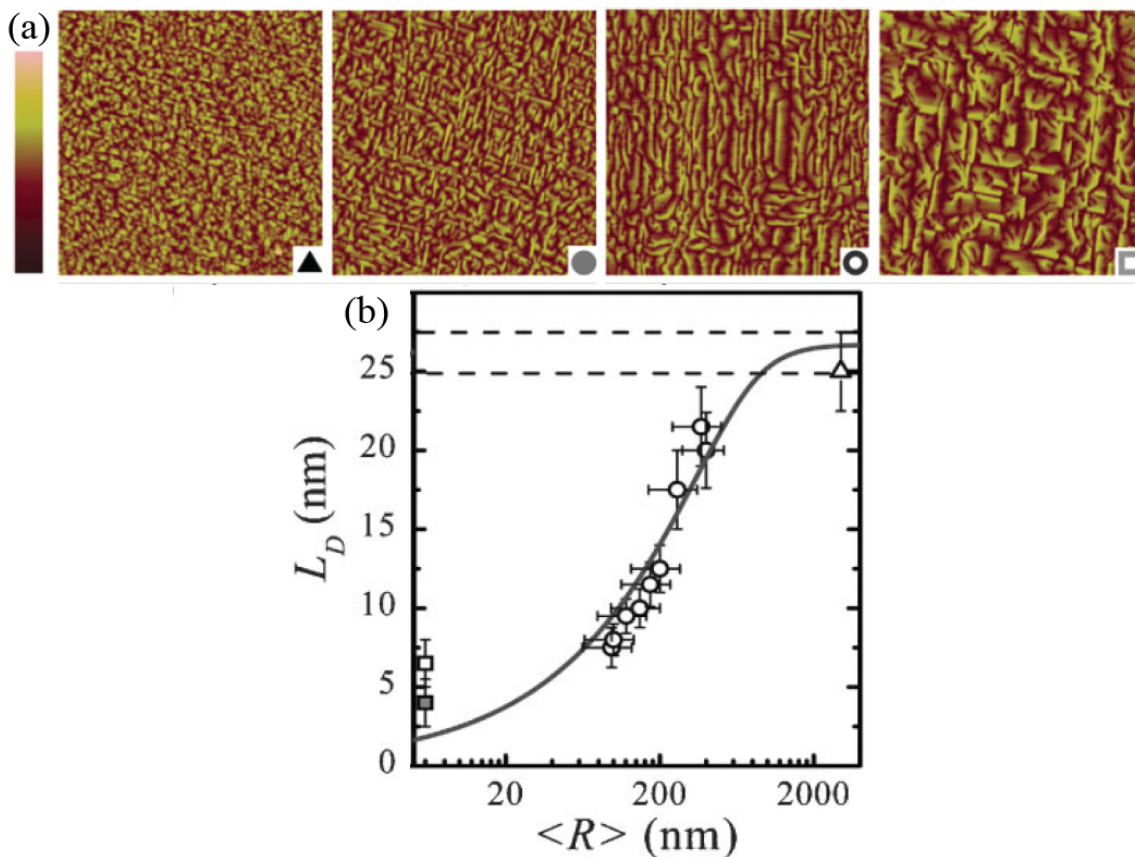
**Figure 3.5** Scanning electron microscope images of CuPc growth in OVPD under different conditions. The scale bar is 500 nm. From Ref. 59.



**Figure 3.6** Modeling of the growth of a nanocrystalline network by OVPD. Growth occurs by alternating thin layers of the donor (magenta) and acceptor (cyan). The specific interface area (solid circles) and surface roughness (open triangles) are shown. From Ref. 28

### 3.1.4 Crystalline growth

As can be seen from the previous two sections, control over morphology and crystallinity is an important feature of OVPD. To better quantify these features, an OVPD system was constructed with in-situ high-pressure reflection high-energy electron diffraction (HP-RHEED).<sup>63</sup> Using HP-RHEED, crystal ordering was monitored during deposition. By this technique, the exciton diffusion length ( $L_D$ ) in 3,4,9,10-perylenetetracarboxylic dianhydride (PTCDA) was measured using spectrally resolved photoluminescence quenching<sup>48</sup> as a function of mean crystal diameter ( $\langle R \rangle$ ) (Fig. 3.7).<sup>64</sup> This presents a new avenue for improving OPV performance, as one of the main limiting factors is low  $L_D$ . Preliminary work on ordered crystalline heterojunctions has been also reported on KBr substrates.<sup>65</sup>



**Figure 3.7** (a) Atomic force micrographs of thin (350 nm) PTCDA films grown under various conditions. The image widths and heights are 5  $\mu\text{m}$  and 50 nm respectively. The root-mean-square surface roughness values from left to right are 7.0, 7.6, 8.0, and 8.2 nm. (b) Measured exciton diffusion length ( $L_D$ ) and mean crystal diameter ( $\langle R \rangle$ ). The single-crystalline limit is indicated by dashed lines. The diffusion length varies as a function of grain size due to nonradiative quenching at grain boundaries. From Ref. 64

## 3.2 Scaling

Scaling to large substrate sizes is essential to reduce the cost of organic electronic devices. Twenty years ago, commercial liquid crystal displays (LCDs) were first deposited onto 300 x 400 mm<sup>2</sup> (Gen. 1) glass substrates. Recently, Sharp began producing displays on 2.9 x 3.1 m<sup>2</sup> (Gen. 10) substrates.<sup>66</sup> The reason for the continual move to larger substrate sizes is simple: cost. By making a large number of devices on a single substrate, production costs are decreased accordingly. Scaling is also essential for solar cell production, as large areas are required to generate power.

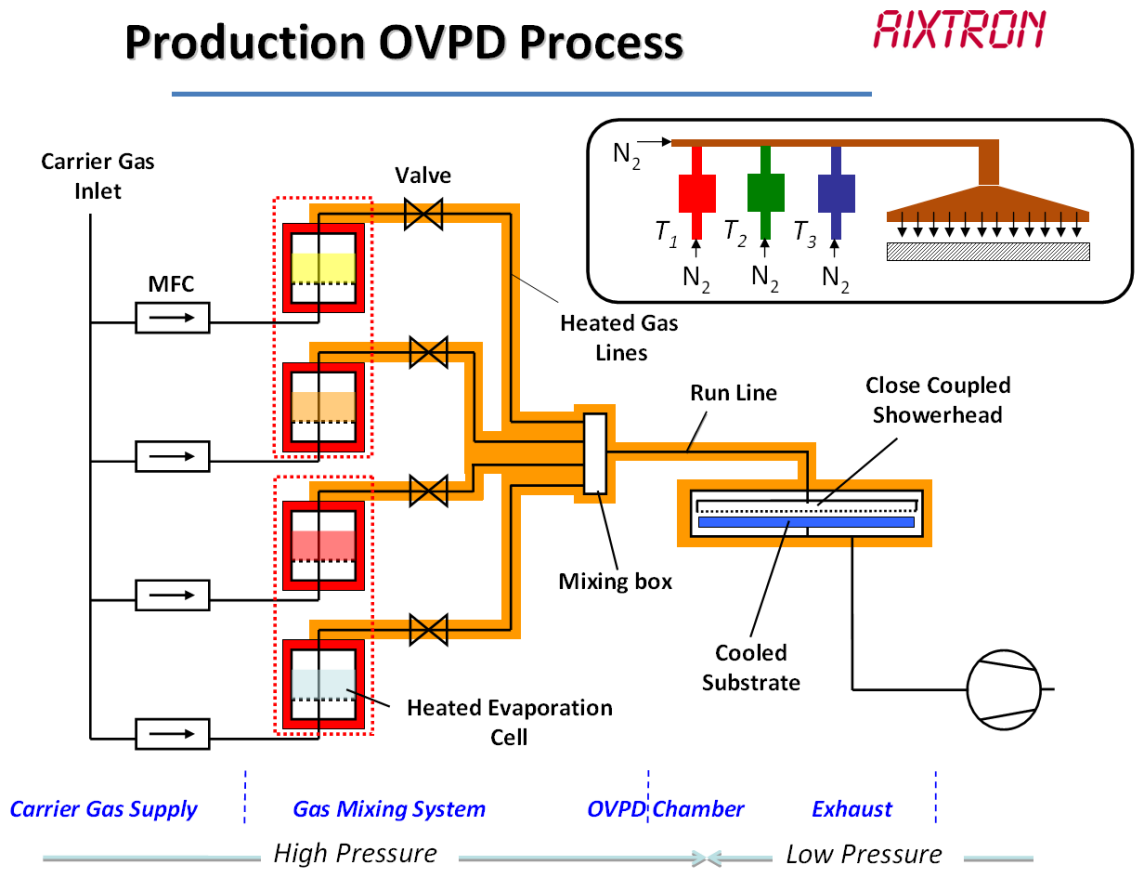
With this in mind, this section will explore the use of OVPD as a method for deposition of large-area organic thin films. First, we will discuss previous large-area OVPD designs and address their limitations. Second, we present and test a model for calculating the deposition characteristics of an OVPD system. Third, we will compare the data from a 200 mm diameter demonstration system with the modeled results. Lastly, we will extend our model to commercial-size substrates, demonstrating that OVPD is a promising technology for large-area deposition.

### 3.2.1 Previous work

A large-area OVPD system was previously constructed that incorporated a close-coupled showerhead (Fig. 3.8).<sup>67,68</sup> In that design, sources are heated individually and then transported via small-diameter run-lines. Material deposition is controlled by hot-valves. For codeposition, gases homogenize in a central mixing box, followed by another small diameter run-line. The material then reaches the showerhead, where it is dispersed over the

substrate area.

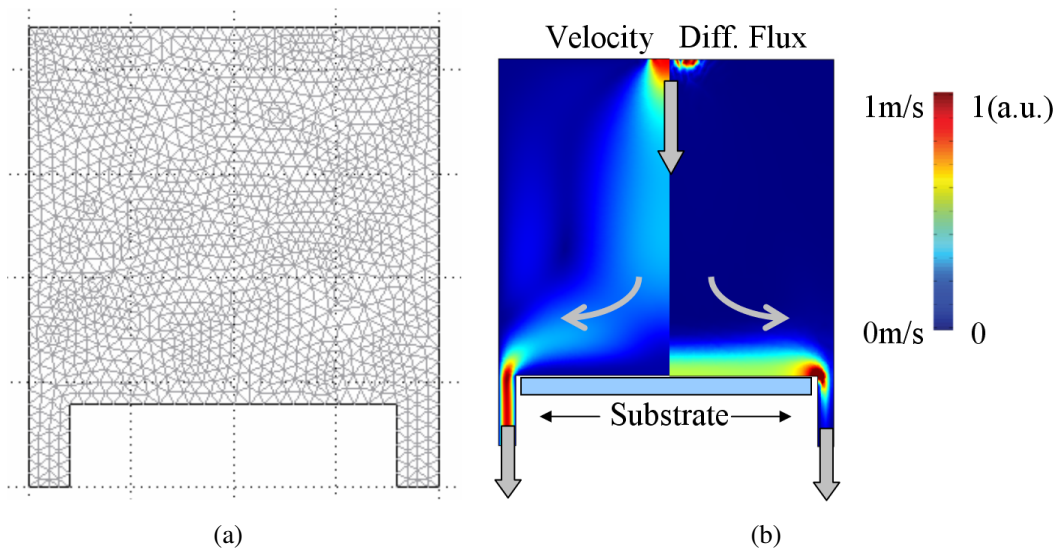
The complexity of this design has some inherent limitations: first, the use of high pressure, small diameter run lines creates a large number of molecule-wall collisions. This magnifies trapping by cold spots that are present and generally increases the residence time of the molecules. Second, the close-coupled showerhead is expensive and adds complexity to the system. Lastly, the presence of large pressure drops complicates scaling, as higher and higher flow rates and pressures are necessary as the substrate size is increased.



**Figure 3.8** Process schematic for an early large-area OVPD design. From Aixtron.

### 3.2.2 Model

To eliminate the problems encountered in the previous system, we returned to the original OVPD design: a single, large-diameter gas transport tube for all materials. We implemented the finite element method<sup>69</sup> (FEM) to explore the scaling of this design by simulating conditions inside the reactor. In the FEM, a mesh is created representing conditions at selected points in the system. A set of coupled partial differential equations is then numerically solved at each point in the mesh. Once a stable solution is iteratively achieved, properties can be extracted and analyzed. An example of the mesh used and a contour plot of properties are shown in Fig. 3.9. In this case, the left half of the output shows the velocity of gas in the reactor, while the right half shows the diffusive flux. These data are then used to calculate the deposition profile (flux across the substrate surface), material utilization efficiency (flux in versus flux out), and other parameters.



**Figure 3.9** (a) Example of a mesh used in finite element modeling of the OVPD process. (b) Contour plot of velocity and diffusive flux obtained from finite element modeling.

In our system, we incorporated the 2D continuum equations for mass, energy, and momentum using a pseudo-compressible gas\*:

$$\begin{aligned}
\nabla \cdot (-D\nabla C + C\mathbf{U}) &= 0 \\
\nabla \cdot (-k\nabla T + \rho C_p T\mathbf{U}) &= Q \\
-\nabla \cdot \mu(\nabla\mathbf{U} + (\nabla\mathbf{U})^T) + \rho(\mathbf{U} \cdot \nabla)\mathbf{U} + \nabla P &= \mathbf{F} \\
\nabla \cdot \mathbf{U} &= 0,
\end{aligned} \tag{3.1}$$

where  $D$  is the diffusivity,  $C$  is the concentration,  $\mathbf{U}$  is velocity,  $k$  is the Boltzmann constant,  $\rho$  is density,  $C_p$  is the specific heat capacity,  $T$  is temperature,  $Q$  is heat,  $\mu$  is viscosity,  $P$  is pressure, and  $\mathbf{F}$  is the external force. These coupled continuum (Navier-Stokes) equations were used to solve the velocity, temperature, concentration (flux), and pressure fields. The temperature dependent viscosity and thermal conductivity of the nitrogen carrier gas used were  $\mu = 1.73 \times 10^{-5} \times (T / 300) \text{ kg/m}\cdot\text{s}$  and  $k = 0.025 \times (T / 300) \text{ W/m}\cdot\text{K}$ , respectively,<sup>70</sup> where  $T$  is the local temperature in K. The diffusivity was calculated<sup>71</sup> according to  $D = D_0(T^{3/2}/P)$ , where  $D_0 = 5.2 \times 10^{-5} \text{ m}^2\cdot\text{Pa/s}\cdot\text{K}^{3/2}$  was calculated using the kinetic theory of gases. The organic concentration at the inlet was fixed, and the concentration at the cooled substrate was assumed to be 0, corresponding to a molecular sticking coefficient of 1.

---

\*We chose a pseudo-compressible gas due to constraints in an older version of Femlab; however, a more recent test-run with a fully-compressible gas showed similar results.

### 3.2.3 Results

To demonstrate the scalability of OVPD, we designed a system with a 200mm diameter stage, shown in Fig. 3.10(a).<sup>†</sup> It consists of 10 source cells arranged radially along a heated stainless steel gas transport tube. Each cell has three main components: a crucible, a gradient heater, and a plug valve (Fig. 3.10(b)). The material is heated to evaporation temperature by translating the crucible through the thermal gradient inside of the source cell. Materials are carried by nitrogen gas flow to a cooled stage which can be raised and lowered for transfer in vacuum.

By using a large-diameter gas transport tube for this system, we eliminate the high-pressure run lines and pressure drops of the previous system. The gas transport tube allows thermal mixing of the material prior to deposition, making a close-coupled showerhead unnecessary for uniform deposition.

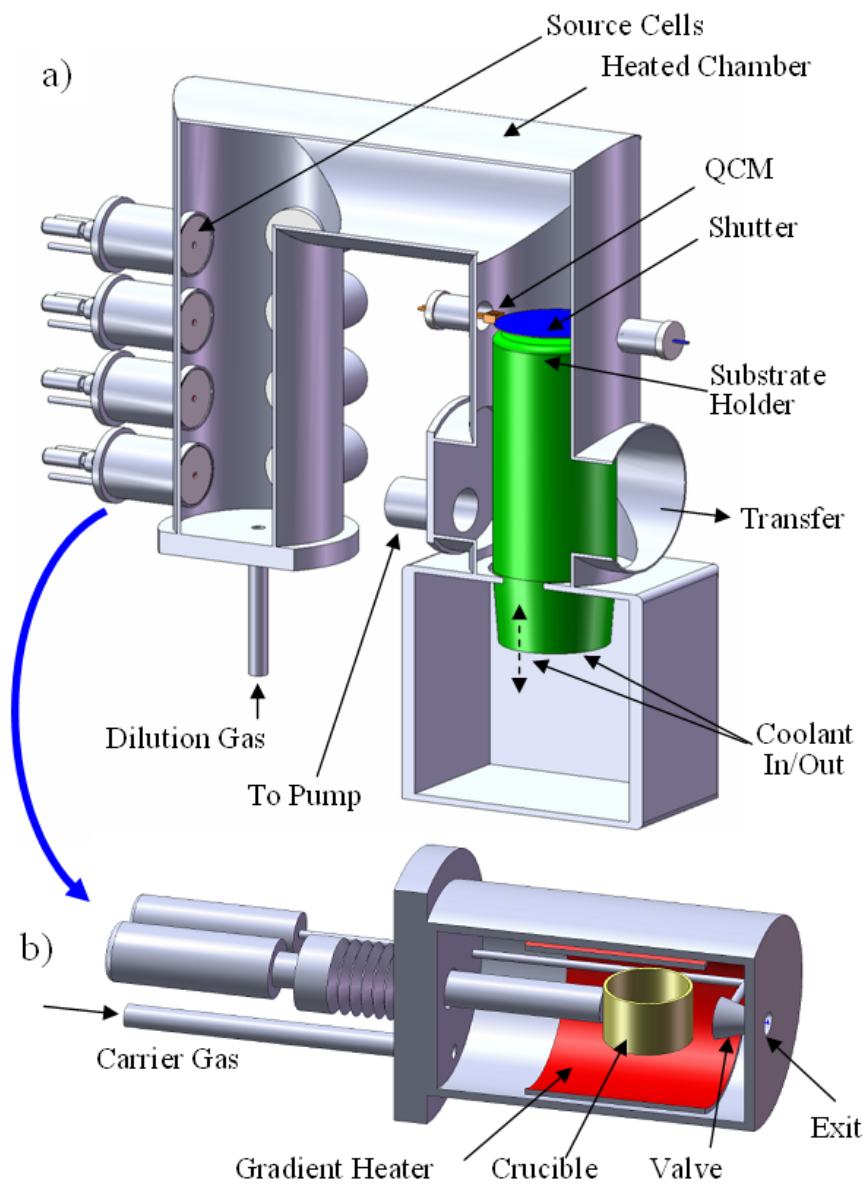
We measured the film uniformity in the system by depositing  $\sim 100$  nm of the archetypical organic material Alq<sub>3</sub> onto a 200mm diameter silicon wafer. Thicknesses were measured by variable-angle spectroscopy ellipsometry (VASE) at 14 points across the wafer. For this study, we define uniformity as the maximum deviation from the mean, excluding 20 mm from each edge.

For optimized conditions of 100 sccm flow and 300 mTorr pressure, we achieved  $\pm 6.0\%$  uniformity without rotation, shown in the open squares in Fig. 3.11. An almost identical profile was predicted by the model, with a uniformity of  $\pm 6.1\%$ . With rotation, uniformity improved to  $\pm 1.6\%$ . As can be seen from the inset photograph of a wafer, the majority of the non-uniformity is from increased deposition at the edges due to boundary layer thinning.

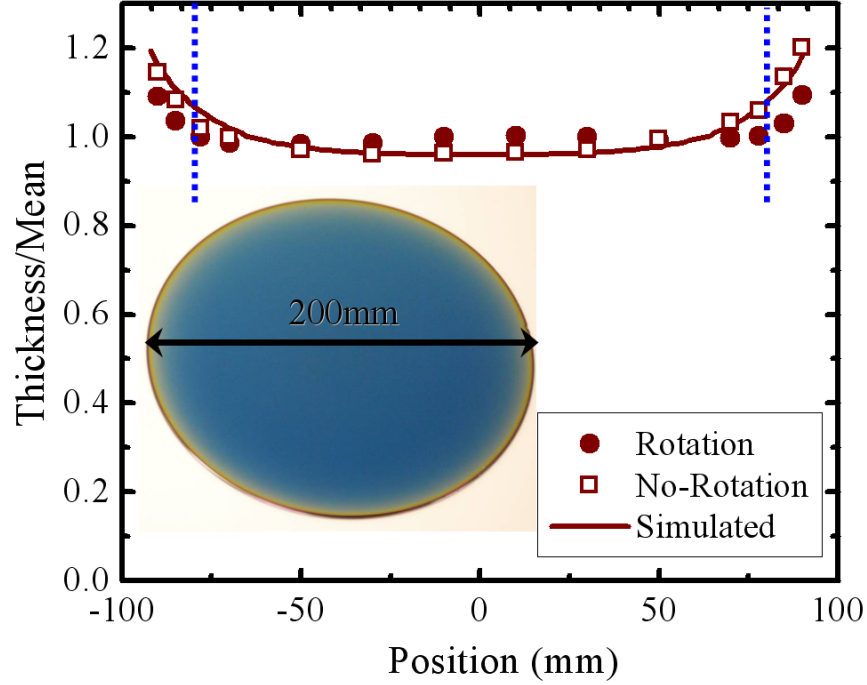
---

<sup>†</sup>Assembled by Angstrom Engineering, Ontario, Canada





**Figure 3.10** Schematic for a new large-area OVPD design. a) shows the entire system, consisting of a 250 mm stainless steel gas transport tube with 12 source cells arranged radially, while b) shows an individual source cell.<sup>72</sup>



**Figure 3.11** A comparison of deposition uniformity for simulated deposition (solid line), deposition with rotation (solid circles) and deposition without rotation (open squares). Inset: image of a 200 mm Si wafer with a 100 nm film of Alq<sub>3</sub>.<sup>72</sup>

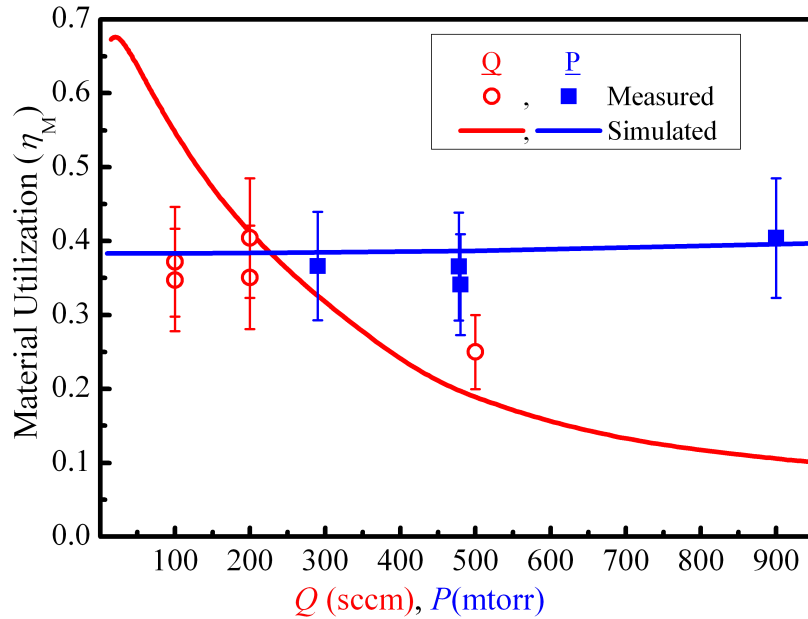
Next, we measured the material utilization efficiency in the system, defined as the amount of material used divided by the amount of material deposited. This was measured by loading a known amount of material ( $m_{loaded}$ ), typically 25 mg, into the crucible. The OVPD shutter was then opened, and the source was heated to deposition temperature. A deposition rate of 0.3 nm/s was maintained until all material was evaporated. The thickness ( $t$ ) of the sample was then measured by VASE. We then calculated the material utilization efficiency ( $\eta_M$ ):

$$\eta_M = \frac{m_{deposited}}{m_{loaded}} = \rho_{Alq_3} V = \rho_{Alq_3} t A_{Si}, \quad (3.2)$$

where  $m_{deposited}$  is the calculated mass deposited,  $\rho_{Alq_3}$  is the density of Alq<sub>3</sub> (1.1 g/cm<sup>3</sup>),

and  $A_{S_i}$  is the area of the substrate.

Because OVPD takes place in a hot-walled reactor, it is capable of very high material utilization. In this case greater than 40% has been achieved. In blue, we have plotted material utilization as a function of pressure at constant flow rate (Fig. 3.12). In agreement with our model, it is largely invariant, as flow patterns only vary slightly over this pressure range. In red, we plot material utilization as a function of source flow rate at constant pressure. As the flow rate increases, convective transport increases, decreasing the amount of material to reach the substrate. In the low flow regime, the data diverges from the model, likely due to condensation of material on the cooled back flange of the source cell. This design aspect is important for research purposes, as it minimizes thermal degradation of



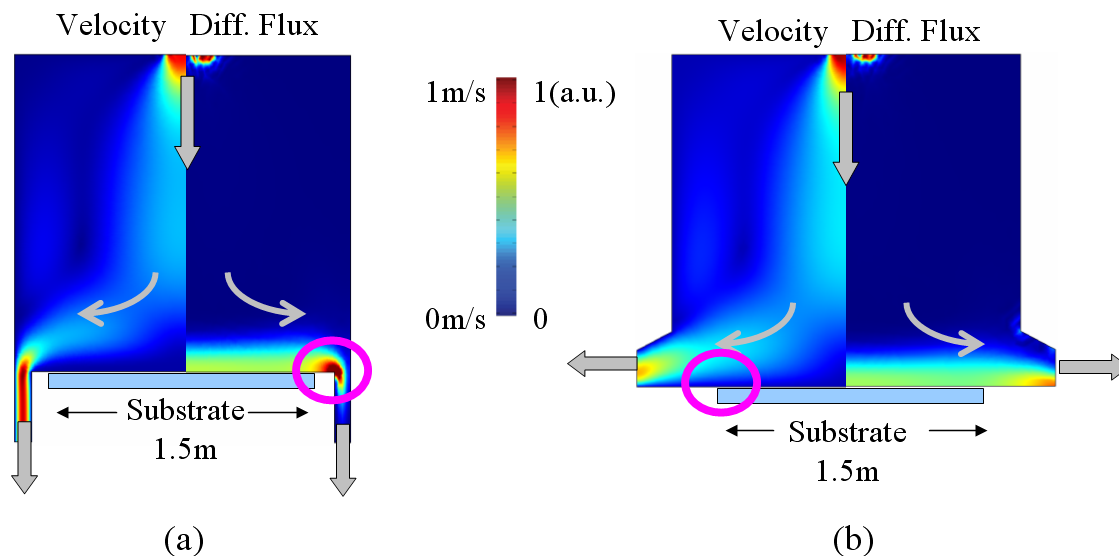
**Figure 3.12** A comparison of material utilization efficiency for varying source flow rate (red) and chamber pressure (blue). Simulated (lines) and experimental (symbols) data are shown.<sup>72</sup>

materials but is not essential in a production-scale reactor.

### 3.2.4 Discussion

We have further extended our model to larger, Gen. 6 systems ( $1.5 \times 1.8 \text{ m}^2$ ). To mitigate the edge effects seen previously, two designs are considered: one similar to previous designs with the substrate flush with the stage (Fig. 3.13(a)), and the other where the system is laterally pumped, eliminating the sharp edge (Fig. 3.13(b)).

For practical reasons, it is essential that uniform deposition is possible for reactors that will fit inside standard industrial buildings. We found that for a height-width ratio of one-to-one, very uniform films can be grown. The standard design can achieve uniformities  $\sim 2\%$  for optimized conditions, but the alternative design provides more design flexibility



**Figure 3.13** Contour plot of modeled velocity and diffusive flux for two Gen. 6 reactor designs. The pink circle notes the area of the edge effects.<sup>72</sup>

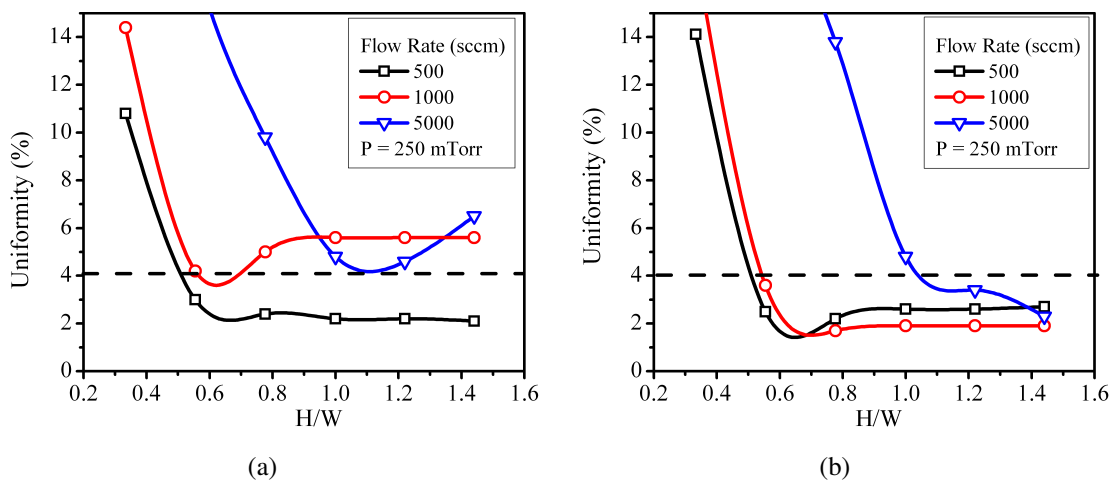
while achieving similar performance (Fig. 3.14).

Choosing a reactor height of 1.8m, we then modeled the uniformity across a 1.5 m substrate at different conditions. The plot shows deposition flux as a function of position across the stage (Fig. 3.15). The dotted lines denote the substrate width. The standard design has moved the edge effects outside of the substrate area, while the laterally pumped design has reduced edge effects.

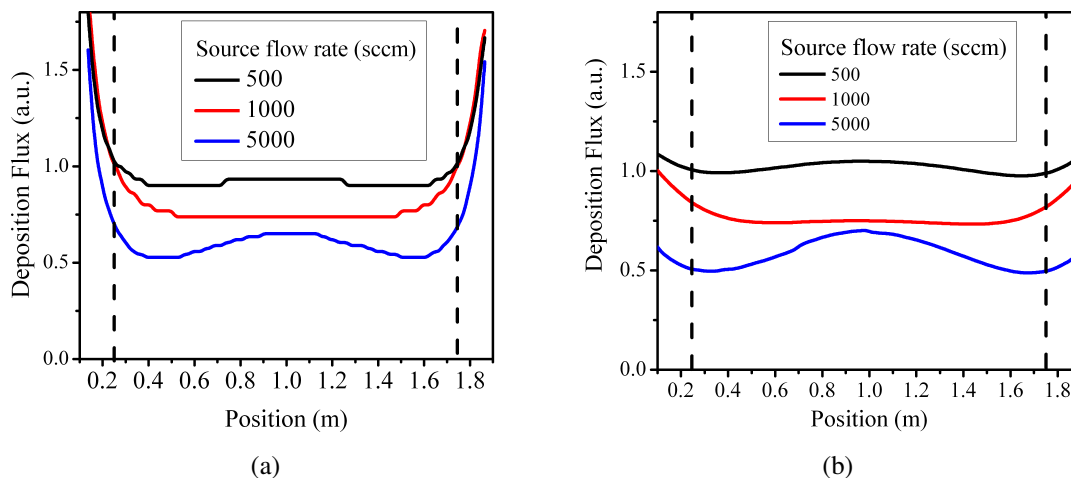
### 3.3 Future work

#### 3.3.1 Crystalline film growth

Recently, new donor materials such as chloro-aluminum phthalocyanine,<sup>73</sup> subphthalocyanines,<sup>74,75</sup> squaraines,<sup>76</sup> and other materials have shown improved performance in bilayer OPV devices via enhanced open-circuit voltage and/or increased absorption spectrum;



**Figure 3.14** Modeled uniformity for a Gen. 6 substrate as a function of reactor height for (a) standard and (b) alternative geometries at various source flow rates. Lines are guide to the eye.<sup>72</sup>



**Figure 3.15** Deposition profiles for a Gen. 6 substrate for (a) standard and (b) alternative geometries at various source flow rates.<sup>72</sup>

however, when these materials are grown in VTE, the films are typically amorphous and have low exciton diffusion lengths. By using OVPD and the methods of Lunt et al.,<sup>48</sup> it may be possible to grow crystalline films of useful OPV materials with increased exciton diffusion length and carrier mobility.<sup>64</sup> This would allow the use of thicker films in OPVs, leading to increased efficiency.

Crystalline growth of new donor materials is also applicable to extend previous work on nanocrystalline networks. OPVs based on nanocrystalline networks<sup>28</sup> demonstrated dramatic improvement in power conversion efficiency over bilayer or bulk devices. The challenge in this case is to learn how to grow crystalline islands from materials which typically grow in smooth, amorphous films.

### **3.3.2 Graded HJ**

The ability of OVPD to precisely vary doping concentrations can be extended to create a graded-heterojunction (GHJ) OPV. Use of this technique to increase the charge recombination zone in OLEDs showed substantial increases in performance.<sup>52,53</sup> In an OPV, the purpose of a GHJ would be twofold: first, increase the donor-acceptor interface area, thereby increasing exciton dissociation and photocurrent; second, maintain percolation pathways through the mixed region so that carriers are not lost to recombination. This approach could be based on amorphous or nanocrystalline films.

## **3.4 Conclusions**

We have demonstrated the capabilities demonstrated for organic thin film growth by OVPD. In this work, we have presented a simple OVPD system scaled to a substrate size of 200 mm. The design uses a large gas transport tube for all materials, eliminating the problems with pressure drops and cold spots experienced in previous designs. Using this system, we have demonstrated a uniformity of  $\pm 1.6\%$  over a 200 mm wafer and a material utilization exceeding 40%. Our simulations have shown the potential adaptability of this approach to large scale deposition of organic films, taking us one step closer towards the goal of low-cost organic photovoltaic devices.

# Chapter 4

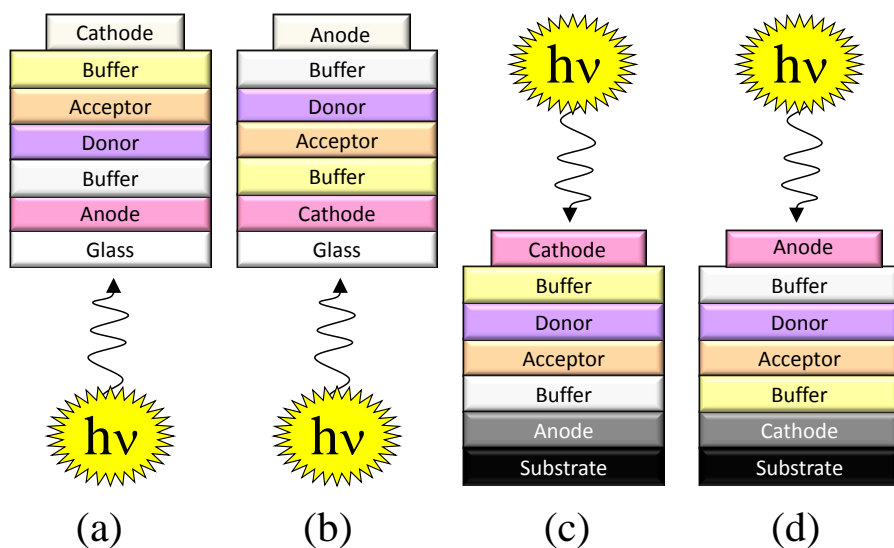
## Inverted OPV

### 4.1 Background

#### 4.1.1 Overview

In 2004, an inverted device architecture was introduced which has the potential to reduce the cost of OPVs.<sup>77</sup> To eliminate confusion on the meaning of the word "inverted" as used in the literature, I will define two different parameters: electrode sequence and illumination incidence direction. Conventional devices are bottom-illuminated (through the substrate) and have the transparent anode lying directly on the substrate. An inverted device is one where the deposition order is reversed, placing the cathode directly on the substrate. A top-illuminated device (sometimes referred to as "inverted" in the literature) is one where a reflective anode is deposited on the substrate, and illumination occurs through the cathode. Another possibility is to have an inverted device where a reflective cathode is deposited on the substrate and a transparent anode is deposited last, which we will refer to as "fully-inverted." These geometries are shown schematically in Fig. 4.1.





**Figure 4.1** Schematic drawings comparing (a) conventional, (b) inverted, (c) top-illuminated, and (d) fully-inverted device geometries.

Top-illuminated and inverted devices have the potential for reducing the cost of OPVs in a number of ways. Conventional devices are typically deposited onto In:SnO<sub>2</sub> (ITO)-coated glass. Both of these materials are expensive in comparison to the organic materials being used, but the glass is necessary to anneal the ITO at high temperature and achieve a highly conductive film. By first depositing a metal layer, a wide range of flexible, light-weight, and opaque substrate choices becomes available. The use of plastic or thin metal foils as substrates has the promise of decreasing device cost both in materials and by its applicability to roll-to-roll processing, reducing module costs. A top-illuminated architecture also lends itself to devices that eliminate ITO altogether, reducing materials and processing costs. Another advantage is the ability to use external dielectric capping layers to reduce reflection of light at the surface of the device. It has been shown that by varying the thickness and refractive index of the capping material, absorbed light can be substantially increased, espe-

cially when using a thin metal film as an anode.<sup>78</sup> Lastly, some work has shown increased lifetime in inverted devices.<sup>79,80</sup> Details of these advantages will be discussed below.

### 4.1.2 Polymer devices

The first inverted OPV device was published in 2004. Nyberg<sup>77</sup> demonstrated a fully-inverted device with the structure Bi/C<sub>60</sub>/poly(3-(4',-1",4",7"-trioxaoctyl)phenyl)thiophene) (PEOPT)/poly(3,4-ethylenedioxythiophene) poly(styrenesulfonate) (PEDOT:PSS); however, performance was poor. This was followed by another fully-inverted device consisting of glass/Al/Ti/poly(3-hexylthiophene) (P3HT):[6,6]-phenyl C61-butyric acid methyl ester (PCBM)/PEDOT/Au grid device by Glatthaar et al. which achieved an efficiency of 1.4%.<sup>81</sup> Since then, ~40 papers have been published on similar polymer-based devices. The trend of this work has been to incorporate carrier selective transport layers. Materials such as TiO<sub>x</sub> and ZnO have been used as electron transporting layers, while materials such as MoO<sub>3</sub> and WO<sub>3</sub> have been used as hole transporting layers.<sup>†</sup> These layers are necessary to reduce leakage current because of the anisotropic nature of the bulk heterojunction morphology.<sup>25</sup> One report incorporated both TiO<sub>x</sub> and MoO<sub>3</sub>.<sup>83</sup> Without the MoO<sub>3</sub> layer, the open circuit voltage ( $V_{OC}$ ) was dependent on the cathode metal, changing from 0.09 V for Ag, 0.30 V for Al, and 0.46 V for Au. This is expected, as an increase in the cathode work function should increase the built-in field; however, when incorporating MoO<sub>3</sub> on the cathode side, the  $V_{OC}$  was invariant with cathode metal (0.63, 0.61, and 0.61 V, respectively).<sup>83</sup>

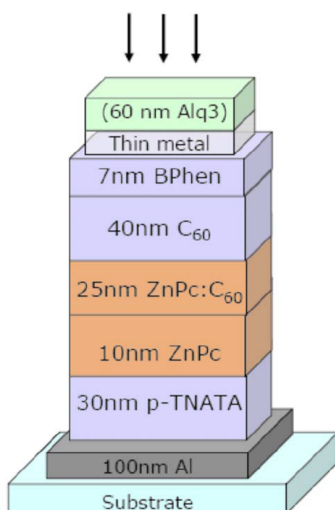
---

<sup>†</sup>It has recently been shown that these are electron transport layers.<sup>82</sup> More details are in Appendix 10.1

### 4.1.3 Small molecule devices

A number of small molecule inverted devices have also been reported. There have been CuPc-based top-illuminated devices using Ni,<sup>78,84</sup> NiO,<sup>85</sup> and MoO<sub>3</sub><sup>86</sup> as hole transport layers; however, all of these devices have suffered due to poor optical field placement inside of the cell. Optical interference effects from the reflective electrode create a periodic intensity of the optical field which is proportional to its wavelength. Shorter wavelengths (typically absorbed by the acceptor, C<sub>60</sub>) are enhanced close to the reflector (~20-40nm), while longer wavelengths (typically absorbed by the donor) are enhanced further from the reflector (40-70nm). For top-illuminated devices, this places the optical field maxima in the wrong materials, significantly decreasing  $J_{SC}$ . Meiss et al.<sup>87-89</sup> have addressed this problem in a top-illuminated device by incorporating doped transport layers and a planar-mixed heterojunction (PMHJ) architecture, shown in Fig. 4.2. The PMHJ increases the vertical area of the heterojunction, decreasing the importance of optical field maximum;<sup>27</sup> additionally, the optical field placement can be tuned by varying the thickness of the transparent doped transport layer. Their device achieved an efficiency of 2.2%. Although this is the highest efficiency found in the literature for small molecule top-illuminated or inverted devices, it is still significantly lower than their best conventional device (~2.8%).<sup>90</sup>

One reason why few high-efficiency inverted small molecule devices have been demonstrated is related to bathocuproine (BCP), which is typically deposited as a buffer layer between the acceptor and cathode. The role of BCP has been described in terms of exciton blocking,<sup>79,91-96</sup> damage blocking,<sup>91,95,96</sup> and contact improvement.<sup>93,97-99</sup> When incorporating BCP as a buffer layer, substantial increases in  $FF$ ,  $J_{SC}$ , and  $V_{OC}$  have been demonstrated. Because BCP forms a type-I heterojunction with C<sub>60</sub> (due to its large optical

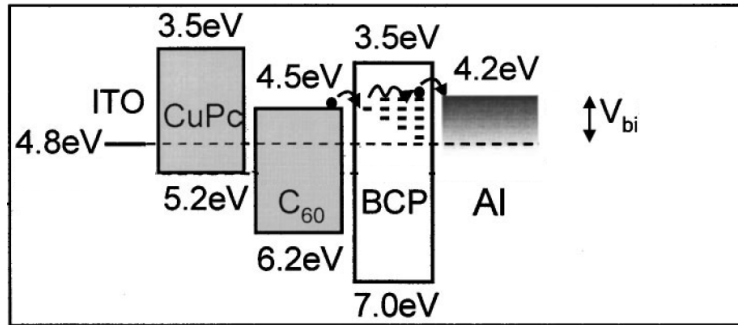


**Figure 4.2** Structure of a top-illuminated device from Meiss et al.<sup>87</sup>

gap), one might expect it to block electrons rather than transport them; however, it has been shown that evaporation of metals directly onto BCP damages the material, creating defects that allow electron transport via mid-gap states (Fig. 4.3).<sup>96</sup> The damage is limited in depth, which makes BCP films thicker than 10 nm unsuitable.<sup>91</sup> For an inverted device, BCP would be deposited onto the metal, and no defect states would be created. This results in resistive, poorly rectifying devices. Groups have attempted to replace BCP with other electron transporting materials such as Alq<sub>3</sub><sup>79</sup> or ZnO,<sup>100</sup> but these have shown poor performance.

#### 4.1.4 This work

Here, we demonstrate a fully-inverted OPV device based on a simple SubPc/C<sub>60</sub> bilayer structure with an efficiency of 2.5%. We do this by eliminating the BCP layer entirely and varying the cathode metal and anode buffer layer to achieve an efficiency comparable to

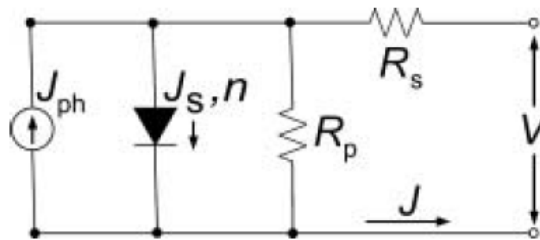


**Figure 4.3** Energy levels in a standard CuPc/C<sub>60</sub> OPV cell. Electron transport through the BCP is possible due to defect states caused by metal deposition.<sup>96</sup>

our conventional device. By doing so, we are able to achieve similar performance to that of a conventional device.

## 4.2 Theory

To understand the operating characteristics of OPVs, a modified version of the Giebink equation can be applied.<sup>24,101</sup> Specifically, we assume that  $n_D \approx n_A$  and  $J_{sA} \gg J_{sD}$ , allowing us to use a single ideality factor ( $n$ ) and a single reverse saturation current ( $J_s$ ). A parallel resistance ( $R_p$ ) is then added to account for leakage across the device, resulting in the following equation:



**Figure 4.4** A schematic of the equivalent-circuit diagram for an OPV device.

$$J_{dark}(V) = \frac{R_P}{R_S + R_P} J_S \left\{ \exp \left( \frac{q(V - J(V)R_S)}{nkT} \right) - 1 \right\} - \frac{k_{PPd}}{k_{kPPd,eq}} + \frac{V - J(V)R_S}{R_P}, \quad (4.1)$$

An equivalent circuit model is shown in Fig. 4.4).  $J_{ph}$  is defined as the difference between the illuminated and dark currents,  $J_{ph} = J_{light} - J_{dark}$ . For our purposes, we assume that  $k_{PPd} \approx k_{kPPd,eq}$  and  $R_P \gg R_S$ , and the form then simplifies to the following\*:

$$J_{dark}(V) = J_S \left\{ \exp \left( \frac{q(V - J(V)R_S)}{nkT} \right) - 1 \right\} + \frac{V - J(V)R_S}{R_P}, \quad (4.2)$$

From §2.4, the maximum  $V_{OC}$  in an OPV device is defined by the energy difference between donor and acceptor frontier orbitals ( $\Delta E_{DA}$ ); however, there are several physical processes which can reduce this value. By setting  $J_{light} = 0$  and  $V = V_{OC}$  in Eq. (4.2), we can then calculate the  $V_{OC}$  based on the previously determined fit parameters:

$$V_{oc} = \frac{nkT}{q} \ln \left( \frac{J_{ph}(V_{oc})}{J_S} - \frac{V_{oc}}{J_S R_P} + 1 \right), \quad (4.3)$$

Typically  $J_{ph} \gg J_S - V_{OC} / R_P$ , leading to a simplified, linear form:

$$V_{oc} = \frac{nkT}{q} \ln \left( \frac{J_{ph}(V_{oc})}{J_S} \right), \quad (4.4)$$

However, for the case of  $J_{ph} \cong J_S$  or  $J_{ph} \cong 1/R_P$ , the full equation should be used and must be solved numerically.

---

\*Note that we do not assume  $R_P \approx \infty$ , as this can be an important factor for devices with very low  $J_S$ .

We can now treat  $J_S$  explicitly,<sup>102</sup>

$$J_S = J_{S0} \exp\left(\frac{-\Delta E_{DA}}{2nkT}\right), \quad (4.5)$$

where  $J_{S0}$  is a temperature-independent prefactor.

Substituting Eq. (4.5) into Eq. (4.3) and rearranging terms, we find:

$$V_{oc} = \frac{\Delta E_{DA}}{2q} + \frac{nkT}{q} \ln \left[ \frac{1}{J_{S0}} \left( J_{ph}(V_{oc}) - \frac{V_{oc}}{R_P} \right) \right], \quad (4.6)$$

Hence,  $V_{OC}$  has a linear dependence on  $\Delta E_{DA}$  and a logarithmic dependence on the photocurrent. It can also be seen that the second term is negative (because  $J_{ph} \ll J_{S0}$ ), so  $V_{OC}$  can only be reduced from the theoretical maximum. Therefore, to maximize  $V_{OC}$  for a given donor and acceptor combination, it is important to have low  $J_{S0}$  and high  $R_P$ .

### 4.3 Experiment

All substrates were first cleaned by the standard cleaning process of surfactant, deionized water, and solvents. Glass and ITO-coated glass substrates were subsequently treated with UV-ozone before transfer into a nitrogen glovebox ( $< 1$  ppm  $H_2O$  and  $O_2$ ). SubPc (Aldrich, 85%) and  $C_{60}$  (Alfa Aesar, 99.92% sublimed) were purified three times and one time, respectively, by vacuum thermal gradient sublimation.<sup>23</sup> BCP (LumTec),  $MoO_3$  (Aldrich, 99.99%) and metals were used as purchased. Organic and metal films were grown by vacuum thermal evaporation (VTE) at a base pressure  $< 10^{-6}$  Torr. SubPc,  $C_{60}$ ,  $MoO_3$ , and metal films were grown at 0.10, 0.15, 0.05, and 0.2 nm/s, respectively. For inverted devices, ITO films were sputter-deposited by Ar plasma at 2 mTorr at powers

ranging from 20-100 W (0.01 to 0.08 nm/s). All rates were measured by a quartz crystal microbalance and calibrated by VASE. Top electrodes were patterned by a shadow mask with 1 mm diameter circular openings. Samples were transferred between gloveboxes in an o-ring-sealed container.

All sample measurements were performed in air. Current-voltage ( $I$ - $V$ ) data was measured by an Agilent semiconductor parameter analyzer. Solar cells were illuminated by a 150 W Xe lamp with AM1.5G filters (Oriel). Light intensity was varied using neutral density filters and calibrated by an NREL-calibrated silicon reference cell.  $EQE$  measurements were illuminated by an unfiltered 150 W Xe lamp passed through a monochromator. A chopper operating at 300 Hz was connected to a lock-in amplifier, which measured the device current. The lamp spectrum was measured by an NREL-calibrated silicon detector. A schematic of the testing setup is shown in Fig. 2.13. Optical constants were measured by VASE. An  $L_D$  of 8 nm for SubPc was measured using photoluminescence quenching by the method of Lunt et al.,<sup>48</sup> while an  $L_D$  of 20 nm for C<sub>60</sub> was estimated from  $EQE$  measurements.<sup>23</sup>

## 4.4 Results

### 4.4.1 Conventional devices

Conventional SubPc/C<sub>60</sub> OPVs have previously been shown to achieve 3.0% efficiency.<sup>75</sup> Devices grown in our lab were typically in the range of 2.8 to 3.0%; however, occasionally efficiencies as high as 3.8% were measured. This is likely due to variations in material purity, as has been shown previously for CuPc/C<sub>60</sub> devices.<sup>103</sup> For this work, I have cho-



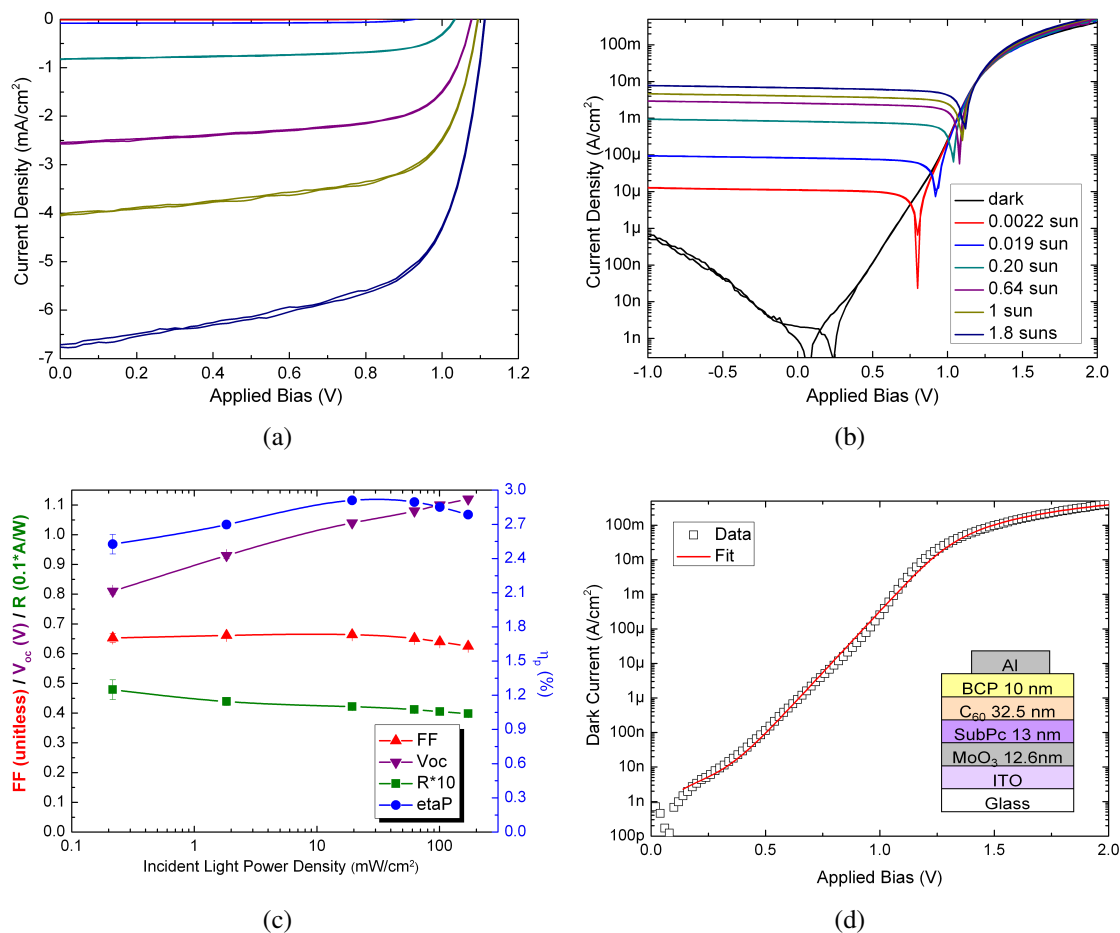
sen a control device for comparison that was grown in a similar time frame to the other devices under study. For a structure of glass/ITO/12.6 nm MoO<sub>3</sub>/13 nm SubPc/32.5 nm C<sub>60</sub>/10 nm BCP/100 nm Al, the  $FF$ ,  $V_{OC}$ ,  $J_{SC}$ , and  $\eta_P$  were 0.64, 1.10 V, 4.1 mA/cm<sup>2</sup>, and  $2.85 \pm 0.02\%$ , respectively (Fig. 4.5).

#### 4.4.2 Devices without BCP

High efficiency SubPc-based devices are fabricated without the use of BCP by optimization of the C<sub>60</sub> thickness. This is in contrast to previous work that showed a decrease from 3.0% to 0.1% when the BCP was eliminated.<sup>94</sup> The structure of the devices was glass/ITO/11 nm SubPc/ $x$  nm C<sub>60</sub>/ $y$  nm BCP/100 nm Al, where  $x$  was varied from 10 to 60 and  $y$  was 0 or 10. In Fig. 4.6, device performance is plotted as a function of the sum of BCP and C<sub>60</sub> thicknesses to compare devices with similar optical field distributions. Optimized devices without BCP perform nearly as well as those with BCP,  $3.00 \pm 0.04\%$  and  $3.21 \pm 0.02\%$  respectively, while for non-optimum thicknesses the devices without BCP had efficiencies reduced  $\sim 50\%$ .

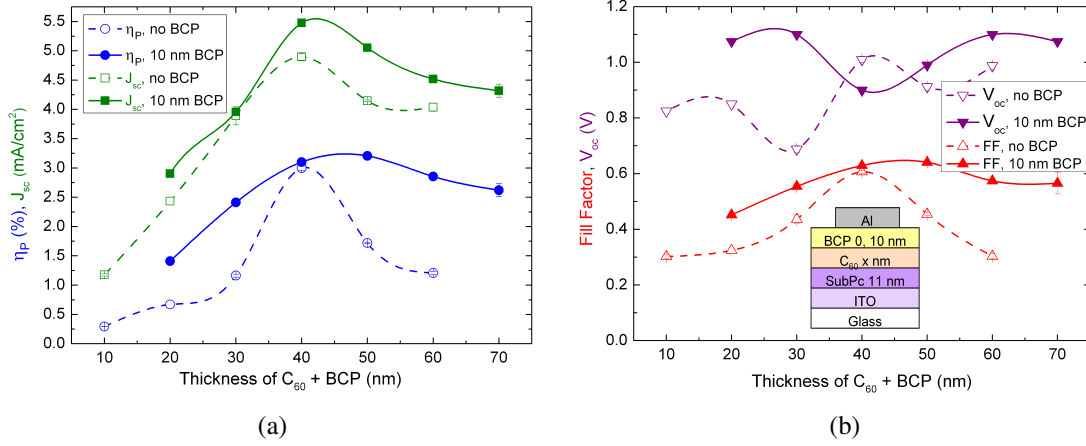
By fitting the dark  $J$ - $V$  curves according to Eq. (4.2), we can compare their characteristics (Fig. 4.7, Table 4.1, and Table 4.2). For thinner devices,  $R_P$  is much lower than those with BCP. This leads to higher leakage current, lowering the  $V_{OC}$  and  $FF$  of these devices. On the other hand, for thicker devices without BCP,  $n$  and  $R_S$  increase at the expense of  $FF$ . We can then input  $n$ ,  $J_{S0}$ ,  $R_S$ ,  $R_P$ , and  $J_{ph}$  into Eq. (4.6) to calculate the  $V_{OC}$  (Fig. 4.7(c)). The agreement between the measured and calculated values shows that these devices are adequately described according to our model.

By modeling the  $J_{SC}$  of these devices according to the transfer matrix method described



**Figure 4.5** Device performance for the a conventional SubPc/C<sub>60</sub> bilayer device with a MoO<sub>3</sub> buffer layer including (a) linear and (b) semilog J-V curves at varying light intensities, (c) performance parameters as a function of light intensity, and (d) fitting of the dark current (device structure inset). For (c), lines are a guide to the eye.

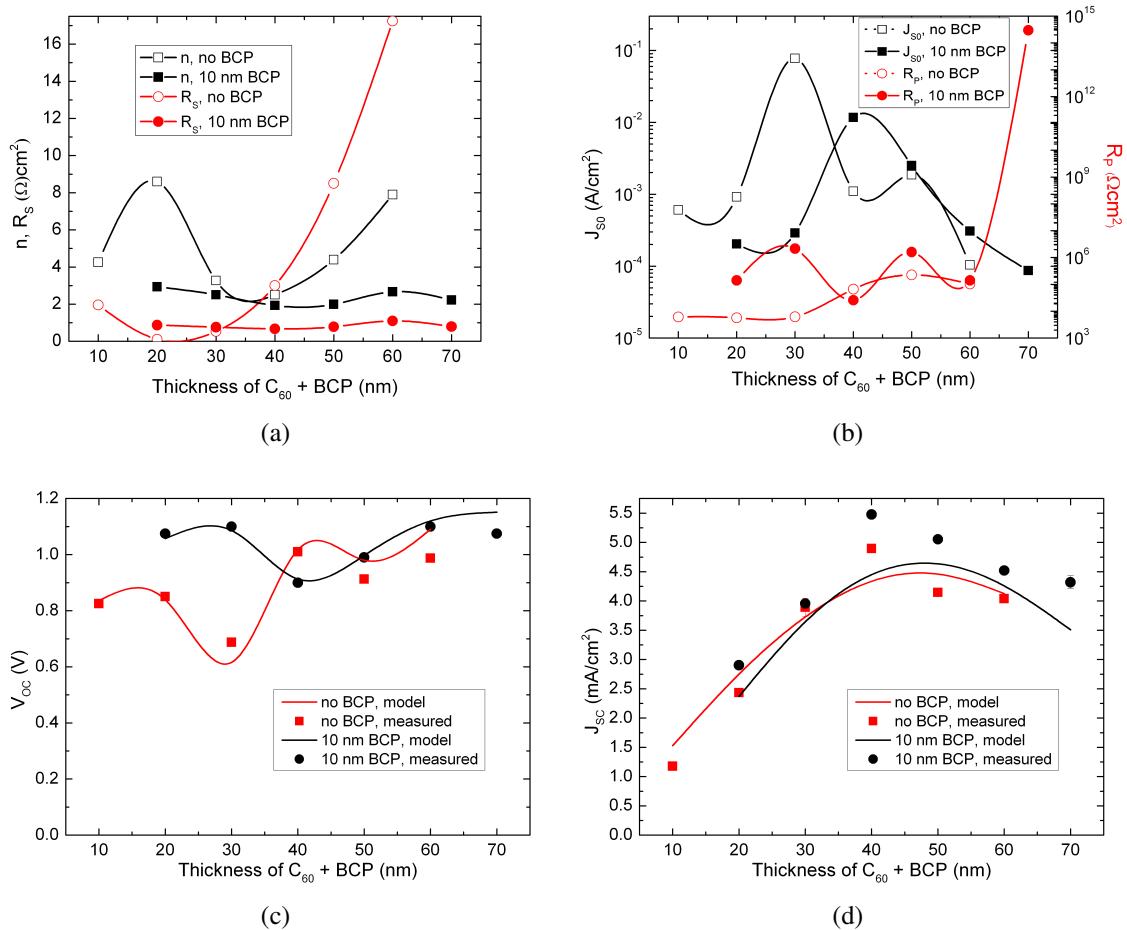
earlier, we can see that there is close agreement between the devices with and without BCP and reasonable agreement between the measurement and model (Fig. 4.7(d)). Thinner devices without BCP show  $J_{SC}$  slightly lower than the model. This could be due to exciton quenching at the C<sub>60</sub>/metal interface, but it is a relatively small effect. This suggests that BCP does indeed serve as an exciton blocking layer.



**Figure 4.6** Comparison of device performance parameters (a)  $\eta_P$  and  $J_{SC}$  and (b)  $FF$  and  $V_{OC}$  (device structure inset) for SubPc/C<sub>60</sub> devices with (filled symbols, solid lines) and without (open symbols, dashed lines) a BCP layer as a function of the sum of the C<sub>60</sub> and BCP thicknesses. Lines are a guide to the eye.

**Table 4.1** Fitted parameters to  $J$ - $V$  curves for varying thicknesses of C<sub>60</sub> for conventional devices without BCP according to Eq. (4.2). These parameters are then used to calculate  $V_{OC}$  (in V) using Eq. (4.3).  $J_{SC}$  (in mA/cm<sup>2</sup>) is calculated via the transfer matrix method.

Thick. (nm)	$n$	$J_S$ (A/cm <sup>2</sup> )	$R_S$ ( $\Omega$ cm <sup>2</sup> )	$R_P$ ( $\Omega$ cm <sup>2</sup> )	$V_{OC}$ Meas.	$V_{OC}$ Calc.	$J_{SC}$ Meas.	$J_{SC}$ Calc.
10	4.25	$6.04 \times 10^{-4}$	1.96	$6.10 \times 10^3$	0.825	0.836	1.18	1.53
20	8.60	$9.15 \times 10^{-4}$	0.112	$5.70 \times 10^3$	0.850	0.839	2.43	2.80
30	3.27	$7.75 \times 10^{-2}$	0.535	$6.20 \times 10^3$	0.688	0.616	3.89	3.79
40	2.50	$1.10 \times 10^{-3}$	3.00	$6.66 \times 10^5$	1.01	1.02	4.90	4.42
50	4.39	$1.86 \times 10^{-3}$	8.51	$2.25 \times 10^6$	0.913	0.980	4.15	4.55
60	7.90	$1.04 \times 10^{-4}$	17.2	$1.04 \times 10^6$	0.988	0.836	4.04	4.13



**Figure 4.7** Analysis of the equivalent-circuit fitting parameters (a)  $n$  (black) and  $R_S$  (red) and (b)  $J_{S0}$  (black) and  $R_P$  (red) for SubPc/C<sub>60</sub> devices with (filled symbols) and without (open symbols) a BCP layer as a function of the sum of the C<sub>60</sub> and BCP thicknesses. Lines are a guide to the eye. The  $V_{OC}$  is plotted as a function of the sum of the C<sub>60</sub> and BCP thicknesses (c) for experimental data (symbols) and calculated according to Eq. (4.6) (lines) for devices with BCP (black) and without BCP (red). (d) The experimental and modeled data for the  $J_{SC}$  is presented in a similar fashion.

**Table 4.2** Fitted parameters to  $J$ - $V$  curves for varying thicknesses of  $C_{60}$  for conventional devices with BCP according to Eq. (4.2) (thicknesses are the sum of  $C_{60}$  plus BCP). These parameters are then used to calculate  $V_{OC}$  (in V) using Eq. (4.6).  $J_{SC}$  (in mA/cm<sup>2</sup>) is calculated via the transfer matrix method.

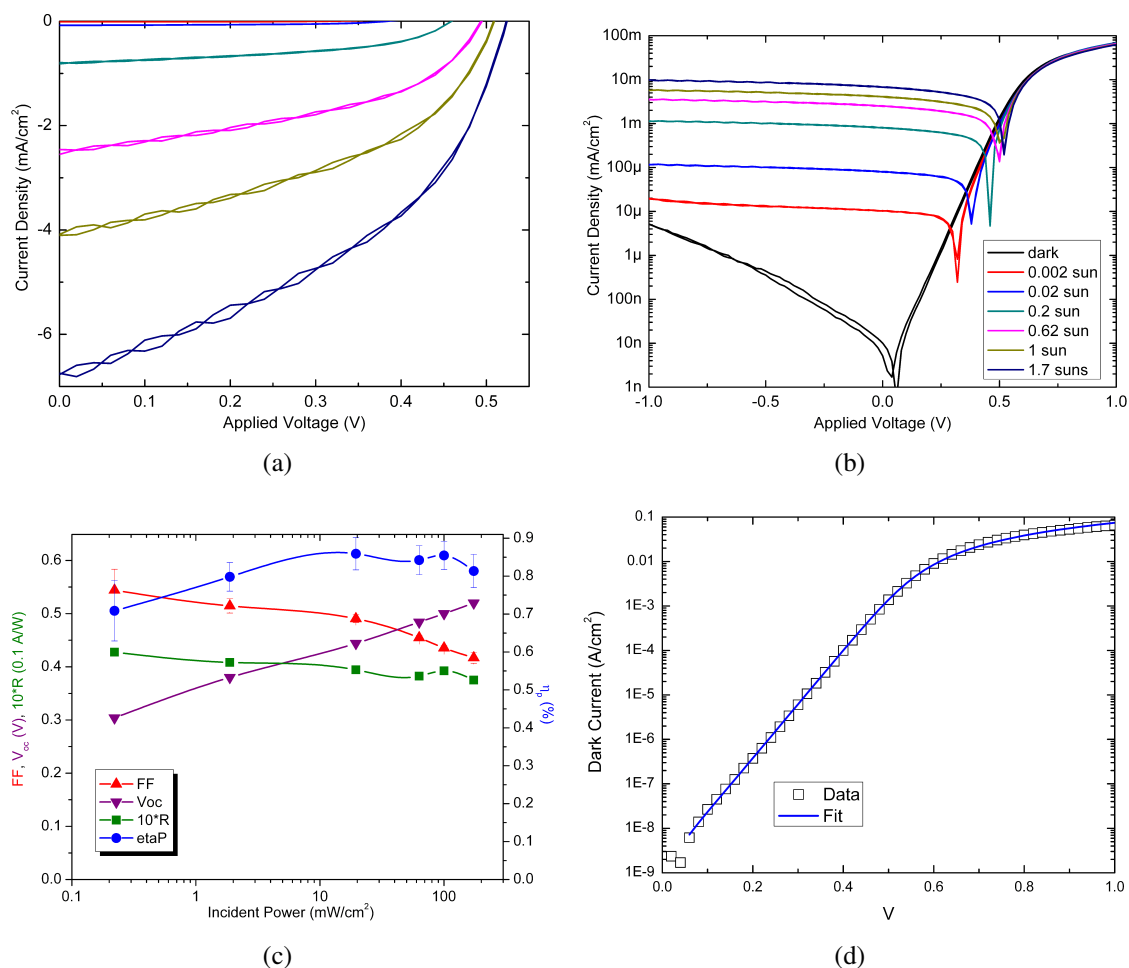
Thick. (nm)	$n$	$J_{S0}$ (A/cm <sup>2</sup> )	$R_S$ ( $\Omega$ cm <sup>2</sup> )	$R_P$ ( $\Omega$ cm <sup>2</sup> )	$V_{OC}$ Meas.	$V_{OC}$ Calc.	$J_{SC}$ Meas.	$J_{SC}$ Calc.
20	2.93	$2.03 \times 10^{-4}$	0.874	$1.41 \times 10^5$	1.01	1.06	2.90	2.37
30	2.50	$2.89 \times 10^{-4}$	0.763	$2.15 \times 10^6$	1.10	1.09	3.96	3.73
40	1.92	$1.17 \times 10^{-2}$	0.669	$2.57 \times 10^4$	0.900	0.913	5.48	4.56
50	1.99	$2.50 \times 10^{-3}$	0.783	$1.59 \times 10^6$	0.990	0.997	5.05	4.73
60	2.67	$3.07 \times 10^{-4}$	1.09	$1.42 \times 10^5$	1.10	1.12	4.52	4.33
70	2.22	$8.68 \times 10^{-5}$	0.794	$2.95 \times 10^{14}$	1.08	1.06	4.32	3.51

### 4.4.3 Inverted devices

The ability to fabricate high efficiency SubPc/ $C_{60}$  devices without BCP presented a new architecture for inverted devices. By reversing the deposition order, we were able to fabricate fully-inverted devices. The structure glass/100 nm Al/50 nm  $C_{60}$ /13 nm SubPc/10 nm MoO<sub>3</sub>/40 nm sputtered ITO (sITO), resulted in  $FF$ ,  $J_{SC}$ ,  $V_{OC}$ , and  $\eta_P$  of 0.44, 4.1 mA/cm<sup>2</sup>, 0.50 V, and  $0.85 \pm 0.04\%$  respectively (Fig. 4.8).

Since the optical field was similar to that of the conventional device, the  $J_{SC}$  was nearly identical to that of the conventional; however, overall efficiency was decreased substantially because the  $V_{OC}$  was reduced by half. By fitting the  $J$ - $V$  curve according to Eq. (4.2), we see that  $n$  decreases from 2.36 to 1.37 and  $J_{S0}$  increases substantially from  $3.27 \times 10^{-4}$  to  $2.02 \times 10^3$ , leading to a concomitant reduction in  $V_{OC}$  according to Eq. (4.6).

One physical explanation for the reduction of  $V_{OC}$  is a change in the built-in field. Although it is commonly thought that OPVs are insensitive to the electrode work functions,<sup>104</sup> for materials with high  $V_{OC}$  it has been shown that the electrode work function difference



**Figure 4.8** Device performance for the initial fully-inverted SubPc/C<sub>60</sub> bilayer device including (a) linear and (b) semilog J-V curves at varying light intensities, (c) performance parameters as a function of light intensity, and (d) fitting of the dark current (device structure inset). For (a), (b), and (c), lines are a guide to the eye.<sup>‡</sup>

( $\Delta\Phi$ ) plays an important role in determining the  $V_{OC}$ ,<sup>105</sup> mostly likely by influencing the built-in field. It has been shown previously that sITO ( $\Phi_{sITO} = 4.1$  eV) has a smaller  $\Phi$  than commercial ITO ( $\Phi_{ITO} = 4.8$  eV),<sup>106</sup> which could be a factor in the reduced  $V_{OC}$ . To test this hypothesis, we used different metals as the cathode and found that the  $V_{OC}$  changed as

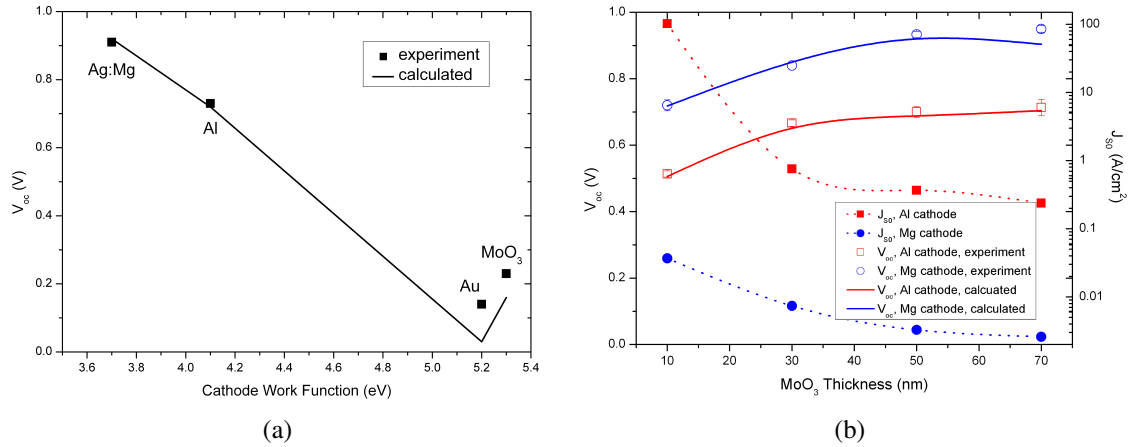
a function of the metal work function. Comparing Au ( $\Phi_{Au} = 5.2$  eV) to Al ( $\Phi_{Al} = 4.1$  eV) to Mg doped with 5 wt% Ag ( $\Phi_{Mg} = 3.7$  eV), the  $V_{OC}$  increased from 0.14 to 0.72 to 0.92 V (Fig. 4.9(a), Table 4.3).

We also incorporated Au between the MoO<sub>3</sub> and sITO layers, which we expected to have a similar effect due to an increase in  $\Delta\Phi$ ; however, in this case the  $V_{OC}$  only increased slightly, from 0.64 to 0.71 V. Recently Kinoshita, et al. showed that by increasing the thickness of MoO<sub>3</sub> from 0 to 50 nm on ITO,  $\Phi_{MoO_3}$  increased from 4.9 to 5.9 eV, resulting in a  $V_{OC}$  increase from 0.57 to 0.97 V.<sup>105</sup> By increasing the thickness of MoO<sub>3</sub> from 10 to 70 nm, we found a similar trend in  $V_{OC}$  for both Al ( $0.51 \pm 0.01$  to  $0.71 \pm 0.02$  V) and Ag:Mg ( $0.72 \pm 0.02$  to  $0.95 \pm 0.01$  V) cathodes, as shown in Fig. 4.9(b). From this, it was clear that the  $V_{OC}$  was based primarily on  $\Phi_{MoO_3}$ . By taking the data from Kinoshita<sup>105</sup> for  $\Phi_{MoO_3}$  as a function of thickness, we plot  $V_{OC}$  as a function of  $\Delta\Phi$ , as shown in Fig. 4.10.  $V_{OC}$  shows a roughly linear rise with increasing  $\Delta\Phi$ , with values saturating at around 1 V.<sup>†</sup> At this point, the  $V_{OC}$  has been maximized to the same level as for the conventional device, which is limited by  $\Delta E_{DA}$ .

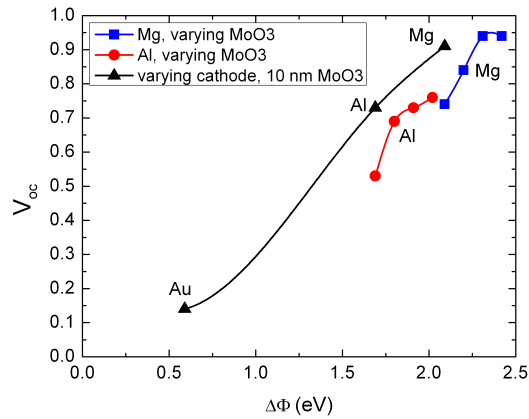
<sup>†</sup>The reader may note that the  $V_{OC}$  from experiment to experiment for a single cathode metal is not consistent (e.g. Al devices at 0.50, 0.73, and 0.64 V). This is due to different thicknesses of the organic and sITO layers and conditions being used to optimize the devices; nevertheless, for experiments that have been compared directly, these layers are typically grown simultaneously, so the trends are valid.

**Table 4.3** Fitted parameters to  $J$ - $V$  curves for inverted devices with varying cathode materials according to Eq. (4.2). These parameters are then used to calculate  $V_{OC}$  (in V) using Eq. (4.3).

Cathode	$\Phi$ (eV)	$V_{OC}$ Meas.	$V_{OC}$ Calc.	$n$	$J_{S0}$ (A/cm <sup>2</sup> )	$R_S$ ( $\Omega$ cm <sup>2</sup> )	$R_P$ ( $\Omega$ cm <sup>2</sup> )
Ag:Mg	3.7	$0.92 \pm 0.01$	0.92	3.05	$3.49 \times 10^{-3}$	1.99	$3.06 \times 10^4$
Al	4.1	$0.72 \pm 0.01$	0.72	1.51	$1.79 \times 10^0$	8.87	$6.73 \times 10^7$
Au	5.2	$0.14 \pm 0.01$	0.03	11.0	$4.28 \times 10^{-1}$	59.6	$1.10 \times 10^3$
MoO <sub>3</sub>	5.3	$0.23 \pm 0.01$	0.16	5.94	$2.77 \times 10^{-1}$	90.6	$5.64 \times 10^4$



**Figure 4.9** Experimental data (open symbols) and calculated values (lines) of the  $V_{OC}$  and the fitted  $J_{S0}$  (dashed lines, closed symbols) of inverted SubPc/C<sub>60</sub> devices as a function of (a) cathode work function and (b) MoO<sub>3</sub> thickness.

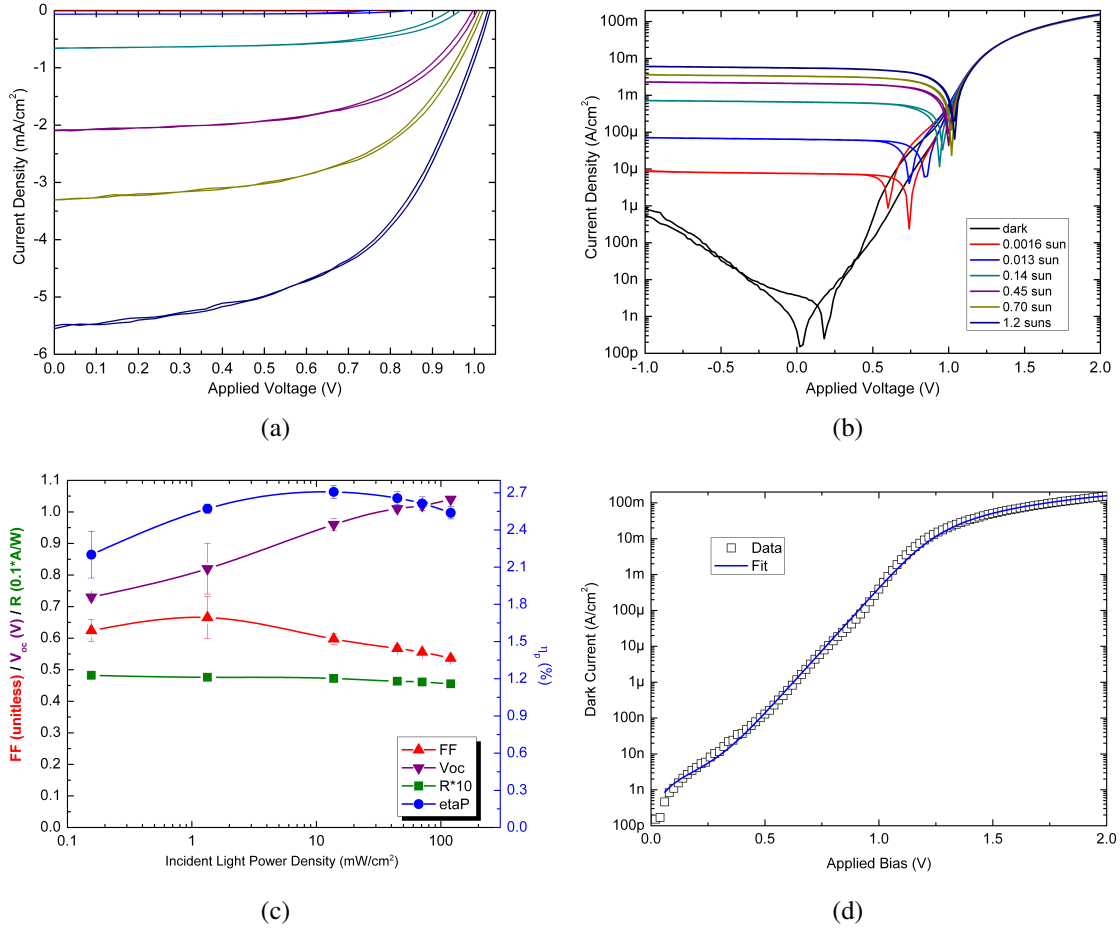


**Figure 4.10** Plot of  $V_{OC}$  as a function of electrode work function difference for varying cathode and 10 nm MoO<sub>3</sub> (black triangles) and Al cathode (red circles) or Ag:Mg cathode (blue squares) with 10, 30, 50, and 70 nm of MoO<sub>3</sub>. Lines are a guide to the eye.

An optimized device was then fabricated with the structure glass/30 nm Ag:Mg/50 nm C<sub>60</sub>/12 nm SubPc/50 nm MoO<sub>3</sub>/40 nm sITO, where  $FF$ ,  $J_{SC}$ , and  $V_{OC}$  were 0.54, 4.6 mA/cm<sup>2</sup>, and 1.04 V, respectively, resulting in an  $\eta_P$  of  $2.54 \pm 0.05\%$  (Fig. 4.11). By comparing the performance and fitting parameters for this device and the control from



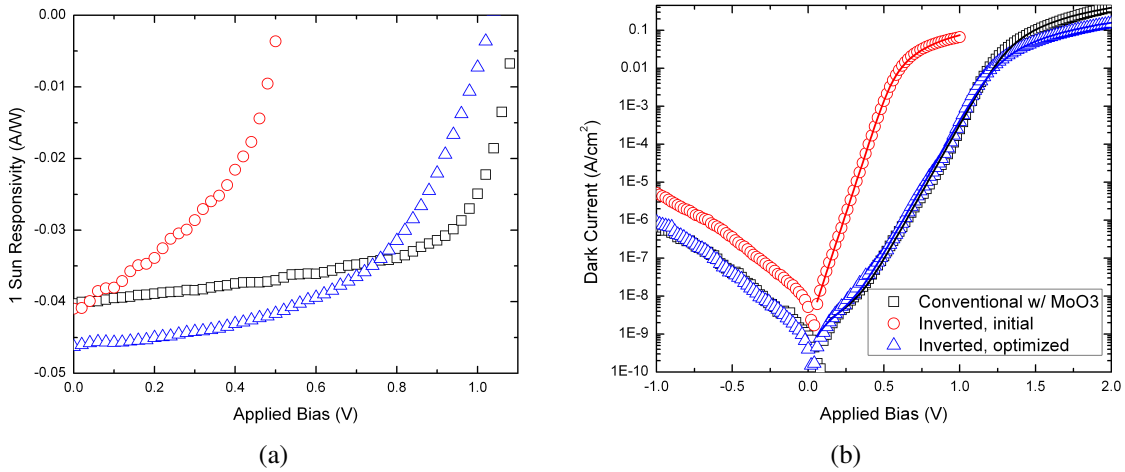
Fig. 4.5, we can see that  $V_{OC}$ ,  $R$ ,  $n$ ,  $J_{S0}$ ,  $R_S$ , and  $R_P$  are nearly identical.  $FF$  is slightly lower, leading to a lower  $\eta_P$  (Fig. 4.12, Table 4.4); nevertheless, we demonstrated that by tuning the properties of the cathode metal and anode buffer layer, an inverted device can be comparable to a conventional one.



**Figure 4.11** Device performance for an optimized fully-inverted SubPc/C<sub>60</sub> bilayer device including (a) linear and (b) semilog  $J$ - $V$  curves at varying light intensities, (c) performance parameters as a function of light intensity, and (d) fitting of the dark current (device structure inset). For (a), (b), and (c), lines are a guide to the eye.

**Table 4.4** Device performance and fitted parameters to  $J$ - $V$  curves for conventional and inverted devices according to Eq. (4.2)

Device	$V_{OC}$ V	$FF$	$R$ mA/W	$\eta_P$ %	$n$	$J_{S0}$ A/cm <sup>2</sup>	$R_S$ $\Omega$ cm <sup>2</sup>	$R_P$ $\Omega$ cm <sup>2</sup>
Control, w/ MoO <sub>3</sub>	1.10	0.64	40.5	2.85±0.02	2.36	3.27x10 <sup>-4</sup>	1.46	6.69x <sup>7</sup>
Inverted, initial	0.50	0.44	39.3	0.85±0.04	1.38	2.02x10 <sup>3</sup>	4.91	5.17x <sup>7</sup>
Inverted, optimized	1.04	0.54	45.5	2.54±0.05	2.42	4.22x10 <sup>-4</sup>	4.02	7.60x <sup>7</sup>



**Figure 4.12** Comparison of the (a) 1 sun responsivity and (b) dark current for conventional (black squares), initial inverted (red circles), and optimized inverted devices (blue triangles). Solid lines represent the dark current fits according to Eq.(4.2).

## 4.5 Future work

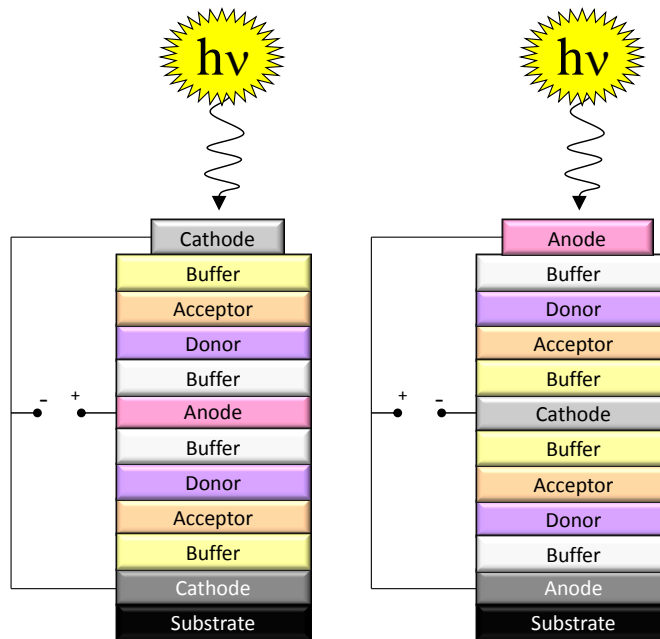
### 4.5.1 Origin of the Open Circuit Voltage

There are still questions remaining as to why the  $V_{OC}$  of inverted devices is often much lower than for conventional devices. Many of the previous works have used non-standard contacts for inverted devices without providing insight into the physical origin of this effect.<sup>77,81</sup> For the case of our inverted structure, there are a number of possibilities. First, the formation of a native oxide on the cathode may act as a thin insulating layer. This could play a role in the increase in  $R_S$  for inverted devices with Al as the cathode, as Al forms a native oxide layer even at high vacuum. This oxide layer could also create an interface dipole, thereby changing the work function and opposing the built-in field.<sup>107</sup> A further possibility is a difference in stacking between the donor and acceptor. It was recently shown that CuPc grown on C<sub>60</sub> had different energy level alignment than C<sub>60</sub> grown on CuPc, which could affect the interface gap and therefore  $V_{OC}$ .<sup>108</sup> Another consideration is a difference between the energetics of a metal-on-organic interface versus an organic-on-metal interface. Some insight into this question may be gained from the use of ultraviolet photoelectron spectroscopy (UPS) and inverse photoemission spectroscopy (IPES).

### 4.5.2 Parallel tandem devices

The ability to fabricate fully-inverted OPVs creates new possibilities for stacking devices in tandem. The standard tandem consists of two OPVs stacked in series.<sup>109</sup> Series tandems have demonstrated moderate increases in efficiency over a single cell.<sup>110,111</sup> From basic circuit analysis, we know that for two diodes in series, the voltage is the sum of the sub-

cells; however, a drawback of this design is that the photocurrent from the sub-cells must be matched to achieve charge balance. This is a limiting factor when designing a tandem structure, as layer thicknesses must be carefully tuned to achieve a balanced photocurrent; however, in a parallel tandem configuration, current-matching is unnecessary.<sup>112–115</sup> In this case, the voltage between the sub-cells must be matched, which is not a limiting factor if appropriate materials are chosen for each sub-cell. In one possible parallel configuration, a conventional device is first deposited on a glass/ITO substrate. A thin, transparent electrode material is then deposited which acts as the cathode for both sub-cells. An inverted device is then deposited and capped with a reflective anode. Alternatively, a fully-inverted device could be deposited first, followed by a transparent anode, followed by a conventional device with a reflective cathode. These geometries are shown schematically in Fig. 4.13.



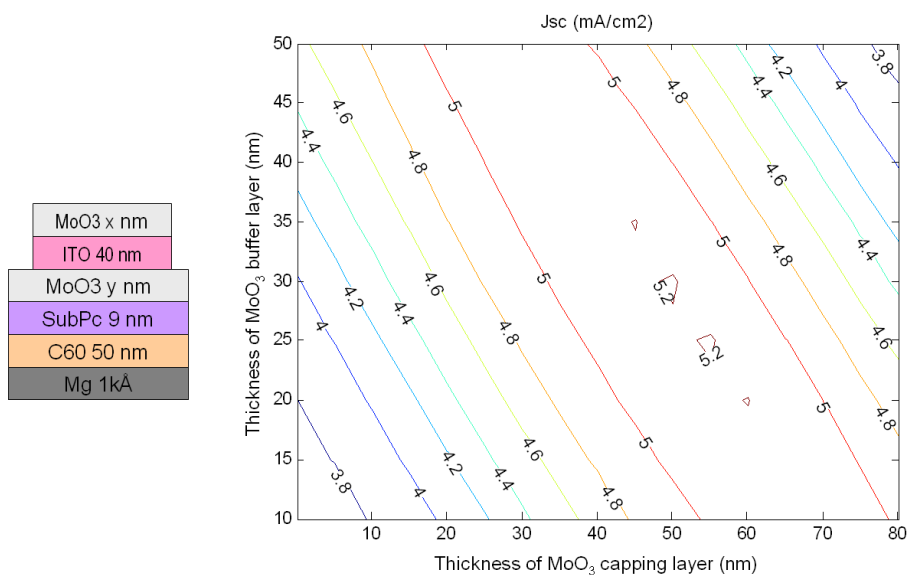
**Figure 4.13** Schematic drawings depicting two possible geometries for parallel tandem devices.

### 4.5.3 Capping layer

One advantage of a top-illuminated structure is the ability to incorporate a capping layer on top of the anode. It has been shown previously that by tuning the thickness and  $n_R$  of the capping material, incoupling of light into the cell can be increased.<sup>78</sup> For this study, we have chosen  $\text{MoO}_3$  as our capping layer for three reasons: it is transparent over the solar spectrum, it has a suitable  $n_R$  ( $\sim 2$ ), and it is convenient to use since it is already incorporated into our device structure. A similar  $\text{MoO}_3$ /thin Ag/ $\text{MoO}_3$  compound anode has previously been demonstrated by Tao et al.<sup>83</sup> Using the aforementioned transfer matrix formalism, we have modeled a device with the structure 100 nm Ag:Mg/50 nm  $\text{C}_{60}$ /9 nm SubPc/ $y$  nm  $\text{MoO}_3$ /40 nm sITO/ $x$  nm  $\text{MoO}_3$ , where  $x$  is varied from 0 to 80 and  $y$  is varied from 10 to 50. The modeled  $J_{SC}$  is shown as a contour plot in Fig. 4.14. It can be seen that our fabricated device ( $x = 0, y = 50$ ) can be improved from  $4.6\text{mA}/\text{cm}^2$  to  $5.2\text{mA}/\text{cm}^2$  by adding a 30 nm capping layer.

### 4.5.4 Flexible substrates

Because this inverted structure is grown metal-first, it is a natural candidate for growth on low-cost, flexible substrates. Eliminating glass as a substrate is essential to reducing the cost of OPVs in addition to allowing for OPVs in novel, flexible devices. Low-cost metal foils and plastics such as polypropylene show promise for these applications, as long as the surface roughness does not significantly degrade device performance. To further decrease cost and increase flexibility, sITO can be replaced with a compound thin metal anode.<sup>78,83</sup> Fabrication of these devices would be an important step in demonstrating the practicality of this design.



**Figure 4.14** Contour plot of the modeled  $J_{SC}$  as a function of MoO<sub>3</sub> capping layer (x-axis) and buffer layer (y-axis) thicknesses.

## 4.5.5 Lifetime testing

Another important topic of OPV research is lifetime. The lifetime\* of our unpackaged conventional devices is typically around 10 h. Previous research has suggested that three possible mechanisms for degradation are oxidation of the low work function cathode,<sup>116</sup> O<sub>2</sub> and H<sub>2</sub>O diffusion into the C<sub>60</sub> layer,<sup>117,118</sup> and crystallization and roughening of the BCP layer.<sup>79</sup> Our inverted device structure has the potential to eliminate these issues because the cathode and C<sub>60</sub> layers are protected by numerous layers, and BCP is absent. Previous work showed an improvement in lifetime from 61 to 1500 h by using an inverted structure.<sup>79</sup> By comparing the lifetime of conventional and inverted devices, we may be able to gain insight into the degradation mechanism in these devices. These tests could then be extended to longer time scales by incorporating an appropriate encapsulant.<sup>118–120</sup>

\*Lifetime is typically defined as the time until performance degrades to 80% of the post burn-in value.

## 4.6 Conclusions

Here, we have demonstrated a fully-inverted OPV device based on a simple SubPc/C<sub>60</sub> bilayer structure with an efficiency of 2.5%. We have done this by eliminating the cathode buffer layer entirely and varying the cathode metal and anode buffer layer work function to maximize the open-circuit voltage. By doing so, we are able to achieve similar performance to that of a conventional device.

## Chapter 5

# Structural templating of multiple polycrystalline layers in organic photovoltaic cells

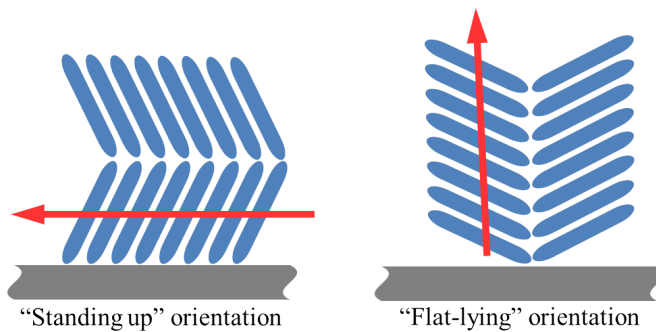
Organic photovoltaics (OPVs) offer the possibility for creating low-cost, lightweight, and flexible renewable energy sources;<sup>121</sup> however, further improvements are required to reach commercial viability. One limitation of OPVs is their low open-circuit voltage ( $V_{OC}$ ), which is typically three to four times lower than the optical energy gap of the materials employed.<sup>122</sup> Low short-circuit current ( $J_{SC}$ ) is also typically observed due to the trade-off between the relatively long optical absorption length and the short exciton diffusion length.<sup>48</sup> One means to improve solar cell performance is to control crystalline ordering.<sup>123,124</sup> In past work, for example, we have shown that the exciton diffusion length is significantly increased with structural order.<sup>64</sup> Furthermore, anisotropies native to the structure of many organic crystals can result in control over both the optical absorption and charge transport properties of the resulting film (Fig. 5.1). Hence, considerable work has been focused on controlling crystal structure used in the active region of organic solar



cells to result in an improvement of its several operating parameters. In this work, 3,4,9,10-perylenetetracarboxylic dianhydride (PTCDA) is used as a self-organizing template<sup>48,125–128</sup> for the growth of subsequent layers. The addition of a diindenoperylene (DIP) layer on the PTCDA serves three purposes: propagating the templating effect of PTCDA, acting as an exciton blocking layer (EBL),<sup>95</sup> and influencing the surface morphology of subsequently deposited films. As a result, we observe an increase in *both*  $J_{SC}$  and  $V_{OC}$  due to control of molecular crystalline orientation, leading to a concomitant increase in  $\eta_p$ .

## 5.1 Background

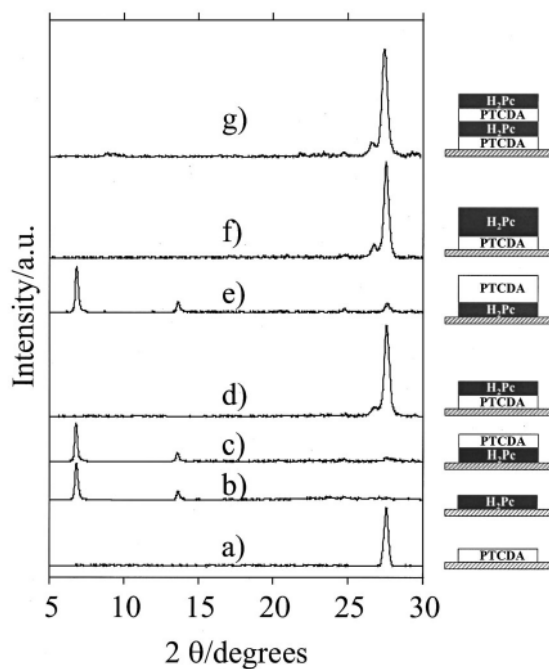
PTCDA has a number of properties which make it unique among organic semiconductors. It is one of the few materials that typically organizes into a relatively flat-lying state on non-interacting substrates such as  $\text{SiO}_2$ , glass, or ITO-coated glass.<sup>129–134</sup> In 2000, Heutz et al. discovered that some organic molecules that are subsequently deposited onto a thin film of PTCDA will also take a more flat-lying orientation, in a process known as structural



**Figure 5.1** Cartoons of (left) "Standing up" and "Flat-lying" molecular orientations. The arrow shows the favored direction for charge transport.

templating.<sup>126</sup> In this case, they employed free-base phthalocyanine ( $H_2Pc$ ), with an intermolecular plane spacing of 1.3 nm, that appears in the XRD data at  $6.8^\circ$  in Fig. 5.2. PTCDA itself has an interplanar spacing of 0.32 nm, which appears as a peak at  $27.6^\circ$ . When the  $H_2Pc$  is evaporated onto a pre-deposited layer of PTCDA, the peak at  $6.8^\circ$  completely disappears, and a new peak appears at  $26.8^\circ$ , indicating that  $H_2Pc$  has taken a flat-lying orientation. Later work confirmed this orientation, adding detail about the physical and optical properties of the films.<sup>127,135–137</sup>

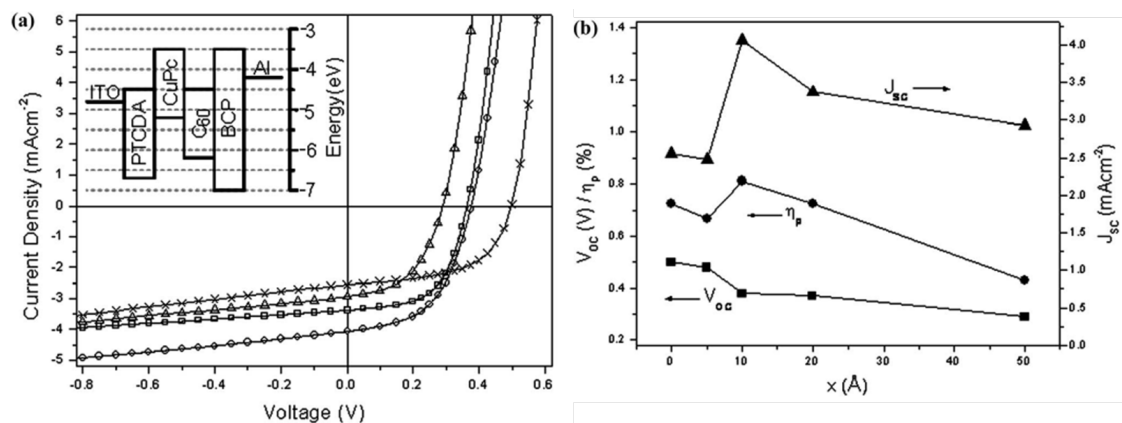
In 2005, Sakurai et al. showed similar templating behavior of copper phthalocyanine



**Figure 5.2** X-ray powder diffraction scans for (a) a reference PTCDA single layer, (b) a reference  $H_2Pc$  single layer, the double layer structures, (c)  $H_2Pc/PTCDA$ , (d)  $PTCDA/H_2Pc$ , (e)  $H_2Pc/PTCDA$  (300 nm), (f)  $PTCDA/H_2Pc$  (380 nm) and the four layer structure (g)  $PTCDA/H_2Pc/PTCDA/H_2Pc$ . The thicknesses of the layers are 150 and 190 nm for PTCDA and  $H_2Pc$ , unless otherwise stated. From Ref. 126.

(CuPc) on PTCDA,<sup>128</sup> (Fig. 5.3) followed by the demonstration of a single crystal hetero-junction of PTCDA/CuPc on KBr by Lunt et al.<sup>65</sup> OPVs utilizing templated CuPc soon followed, showing a 60% increase in  $J_{SC}$  compared to untemplated devices; however, there was a concomitant decrease in  $V_{OC}$ , leading to a negligible increase in  $\eta_p$ .<sup>138</sup>

Since the publication of this work, a number of other templated materials have been utilized in OPVs, including chloroaluminum phthalocyanine (ClAlPc),<sup>125,139–141</sup> diindenoperylene (DIP),<sup>48,142,143</sup> copper hexadecafluorophthalocyanine (F<sub>16</sub>CuPc),<sup>144–147</sup> zinc phthalocyanine (ZnPc),<sup>148</sup> and lead phthalocyanine (PbPc).<sup>149,150</sup> Additionally, CuI has been introduced as a templating material which has superior templating and electrical properties compared to PTCDA.<sup>148,151</sup>



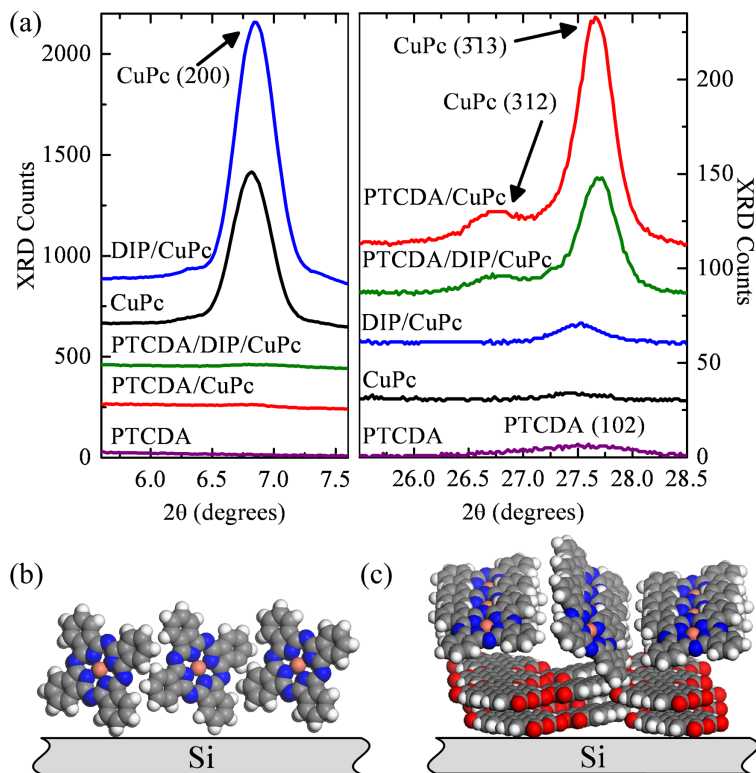
**Figure 5.3** (a)  $J$ - $V$  curves for a series of ITO/ $x$  Å PTCDA/30 nm CuPc/40 nm C<sub>60</sub>/10 nm BCP/Al devices,  $x = 0$  Å (crosses), 10 Å (circles), 20 Å (squares), and 50 Å (triangles), (inset) an energy level diagram for the devices, and (b) device parameters for the series. From Ref. 138.

## 5.2 Experiment

Organic thin films were grown on 100 nm thick layers of ITO pre-coated onto glass substrates. Prior to deposition, the ITO/glass substrates were cleaned in surfactant and a series of solvents,<sup>28</sup> and then exposed to ultraviolet-ozone for 10 min before loading into a high vacuum chamber (base pressure  $< 10^{-6}$  Torr). First purified by thermal gradient sublimation in vacuum,<sup>152</sup> PTCDA, DIP, CuPc, C<sub>60</sub>, and bathocuproine (BCP) were then thermally evaporated at 0.2, 0.05, 0.1, 0.15, and 0.1 nm/s, respectively, followed by a 100nm thick Al cathode deposited through a shadow mask with an array of 1 mm diameter openings. For each experiment, CuPc, C<sub>60</sub>, BCP, and Al were simultaneously grown with and without structural templating layers, the latter for control purposes.

Ultraviolet photoelectron spectroscopy (UPS) was used to measure the film ionization energies relative to vacuum. For UPS, the samples were transferred in nitrogen from the growth chamber to an ultrahigh vacuum system (base pressure  $< 5 \times 10^{-9}$  Torr) where they were illuminated with the He I source. X-ray diffraction (XRD) was performed using a rotating anode Rigaku Cu-K $\alpha$  diffractometer in the Bragg-Brentano configuration, and atomic force microscope (AFM) images were obtained in the tapping mode. Active region absorption was calculated from measurement of the device reflectivity ( $R$ ) obtained at 6° (near-normal) incidence after subtracting the loss measured for an ITO/BCP/Al reference. The active layer absorption is then equal to  $(1 - R)$ . Internal quantum efficiency ( $IQE$ ) was obtained from the ratio of the external quantum efficiency ( $EQE$ ) to the absorption. Current density versus voltage ( $J$ - $V$ ) characteristics were measured in the dark and under simulated AM1.5G solar illumination. The illumination intensity and quantum efficiency measurements were referenced using an NREL-calibrated Si detector.<sup>37</sup> Errors quoted

correspond to the standard deviation in values determined by measuring three positions on the same substrate.



**Figure 5.4** (a) X-ray diffraction patterns of PTCDA, CuPc, DIP, and combinations of these layers on Si. The standing-up CuPc (200) orientation (b) disappears when CuPc is grown on a pre-deposited PTCDA template layer. This orientation is then replaced by the (c) flat-lying orientations as evidenced by the appearance of the (312) and (313) diffraction peaks.

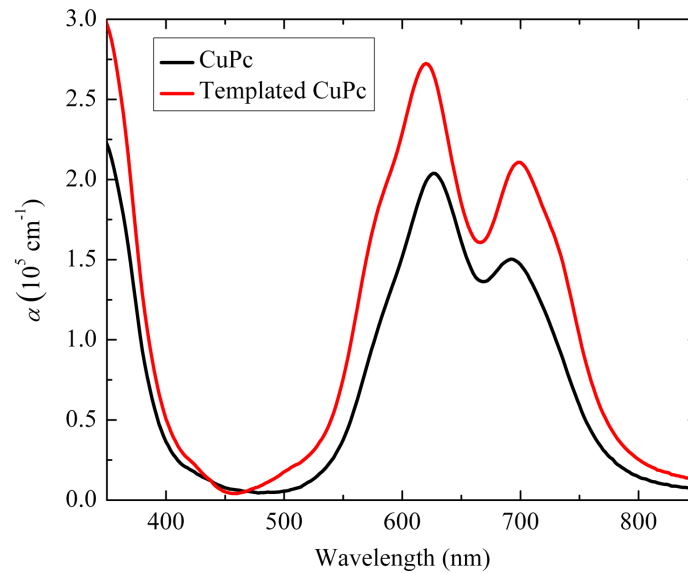
## 5.3 Results

Figure 5.4 shows the XRD patterns for films grown on oxidized Si substrates.<sup>†</sup> A weak diffraction peak at  $2\theta=27.5^\circ$  is observed for a 1.5 nm thick layer of PTCDA, indicating the existence of the "flat-lying"  $\alpha$ -phase (102) orientation. For a 25 nm thick layer of CuPc, the "standing-up" (molecular normal parallel to the substrate plane, as seen in Fig. 5.4(b))  $\alpha$ -phase (200) orientation is inferred from the peak at  $2\theta=6.8^\circ$ . When a 25 nm thick layer of CuPc is grown on a 1.5 nm thick DIP layer, the CuPc orientation is largely unchanged, whereas, when grown on 1.5 nm thick PTCDA, there is a nearly complete disappearance of the (200) orientation along with the appearance of peaks at  $2\theta=26.7^\circ$  and  $27.7^\circ$ , corresponding to the flat-lying CuPc (312) and ( $\bar{3}$ 13) orientations as shown in Fig. 5.4(c). When a 25 nm thick CuPc layer is grown on a bilayer of 1.5 nm thick DIP on 1.5 nm PTCDA, we see similar changes in CuPc orientation to that grown directly on PTCDA. These data suggest that by using PTCDA as a templating layer, the orientation of DIP changes from (001)  $\beta$ -phase on glass, to the (020)  $\beta$ -phase on PTCDA,<sup>48,153</sup> which in turn orients the CuPc molecules for maximum out-of-substrate-plane conductivity. This orientation also increases the absorption coefficient by approximately 30%, as shown in Fig. 5.5

It has also been found that the energies of the frontier orbitals of organic materials are influenced by their crystalline structure. For example, an increase in highest occupied molecular orbital (HOMO) energy was previously reported for CuPc lying flat on highly-oriented pyrolytic graphite.<sup>154</sup> Figure 5.6(a) shows the UPS data for PTCDA, CuPc, templated CuPc, and templated DIP, where dashed lines indicate the intercepts. Comparing CuPc (black/circle) to templated CuPc (red/diamond), we measure a shift in the highest

---

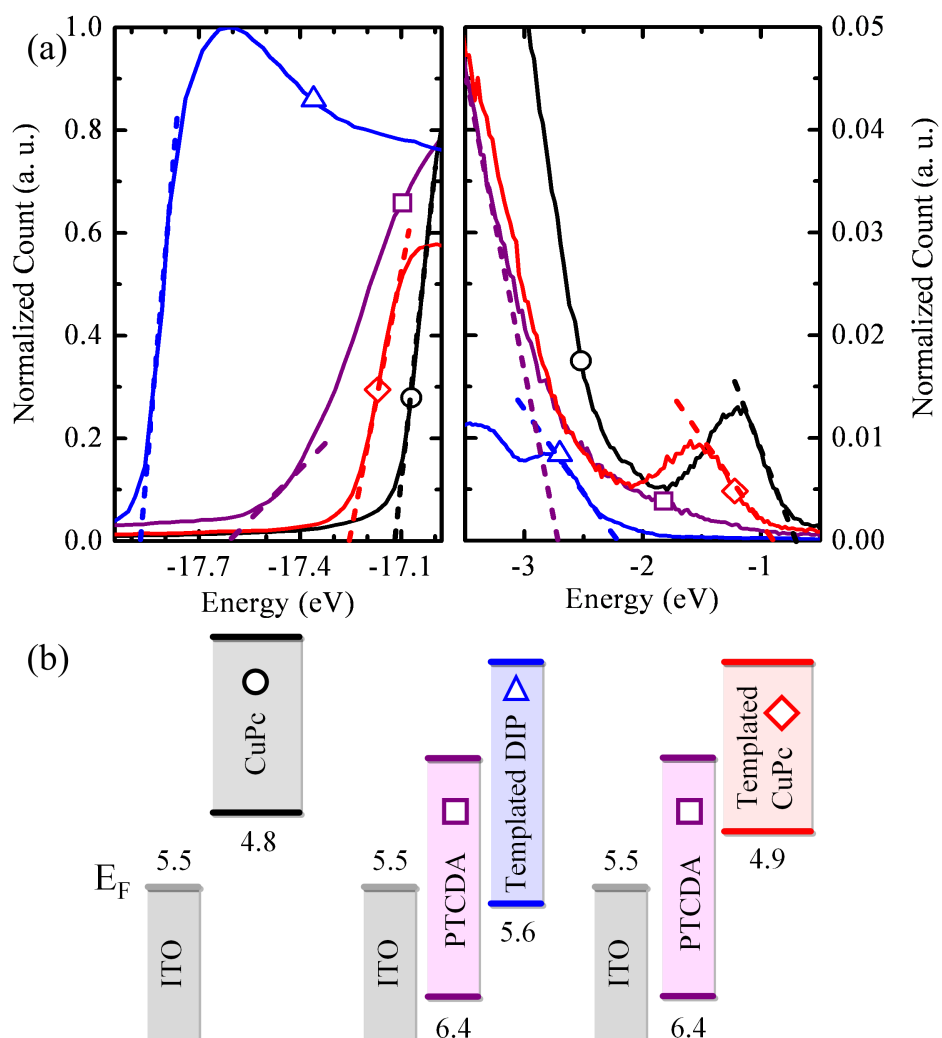
<sup>†</sup>XRD data on ITO substrates was similar, but Si is shown here due to the lower noise floor.



**Figure 5.5** Absorption coefficient measurements showing an increase in absorption for templated CuPc compare to untemplated CuPc.

energy cutoff from  $-0.93 \pm 0.01$  eV to  $-0.70 \pm 0.01$  eV (a difference of  $-0.23$  eV) below the Fermi level upon templating. We also see a vacuum level shift of  $0.15 \pm 0.01$  eV, as indicated by the change in low-energy cutoff. Adding these values, we infer that the HOMO energy of CuPc (measured for 5.0 nm thick films deposited on ITO) is increased by  $-0.08 \pm 0.02$  eV when a 1.5 nm thick layer of PTCDA is used for templating the CuPc. The relative positions of the HOMO levels for PTCDA, DIP, and CuPc taken from UPS measurements are shown schematically in Fig. 5.6(b) assuming vacuum level alignment. It is apparent that the PTCDA/CuPc interface acts as a type-II (staggered) heterojunction,<sup>131</sup> and DIP can function as an EBL in a type-I (nested) heterojunction with CuPc.

Finally, the surface morphology of the CuPc layer changes from a root mean square (RMS) roughness of 1.8 nm when grown directly on ITO (Fig. 5.7(a)), to a roughness of 3.9 nm when grown on either PTCDA or DIP (Figs. 5.7(b) and 5.7(c)). In the latter two cases,

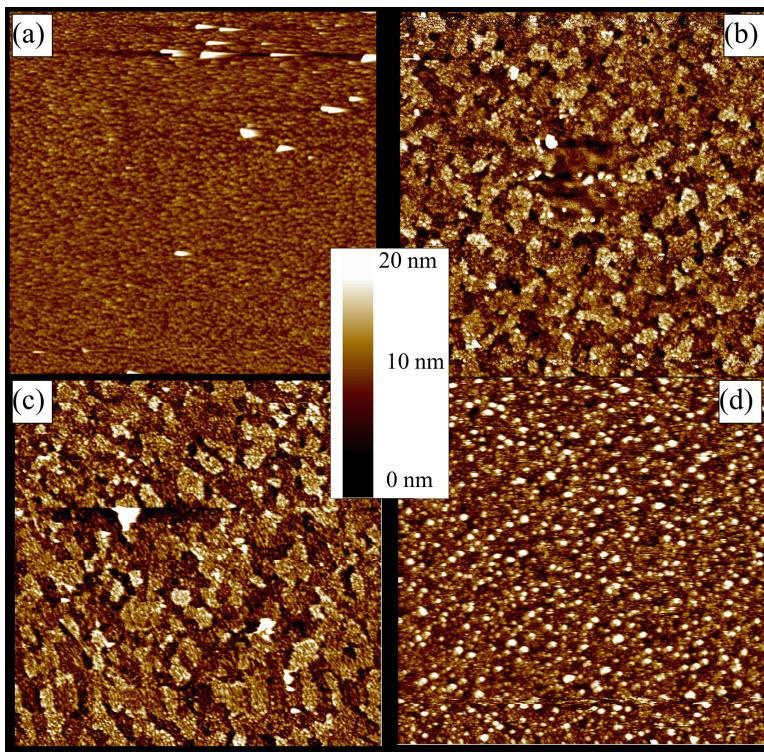


**Figure 5.6** (a) Ultraviolet photoelectron spectroscopy data for 1.5 nm thick PTCDA, 5.0 nm thick CuPc, and 5.0 nm thick templated films of DIP and CuPc on indium tin oxide (ITO). The high energy cutoff of CuPc shifts  $\sim 0.2$  eV when templated on PTCDA compared to films on ITO. Dashed lines show extrapolations of the data to the energy axis. (b) Energy level diagrams inferred from the measured highest occupied molecular orbital energies CuPc and PTCDA (units of eV). Symbols and colors in (a) correspond to those in (b).



the underlying grain structure of ITO becomes apparent. When crystalline DIP is grown on top of PTCDA, a CuPc roughness of 6.8 nm and an island size of  $\sim 100$  nm results, as shown in Fig. 5.7(d). The surface area ratio (compared to a perfectly planar junction) of these morphologies is 1.01, 1.05, 1.03, and 1.12, respectively.

Device performances under one sun, AM1.5G illumination for the structures glass/ITO/(0, 1.5 nm) PTCDA/(0, 1.5 nm) DIP/25 nm CuPc/40 nm C<sub>60</sub>/10 nm BCP/Al are shown in Fig. 5.8 and summarized in Table 5.1. In this case, the templating layers consist of Device (I) none (control), (II) 1.5 nm DIP, (III) 1.5 nm PTCDA/0 nm DIP, and (IV) 1.5 nm PTCDA/1.5 nm



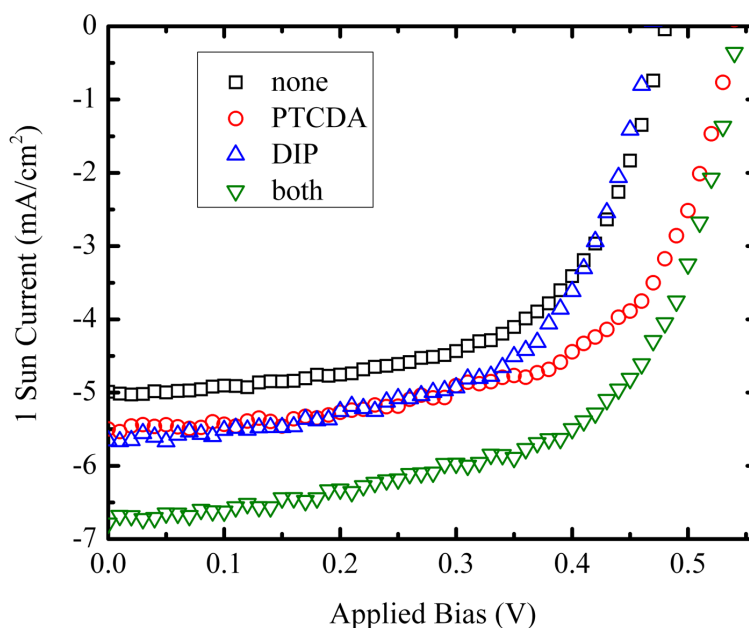
**Figure 5.7** Atomic force microscope images of (a) 25 nm thick CuPc, (b) 1.5 nm thick PTCDA/25 nm thick CuPc, (c) 1.5 nm thick DIP/25 nm thick CuPc, and (d) 1.5 nm thick PTCDA/1.5 nm thick DIP/25 nm CuPc. Lateral spans of each image are  $5 \mu\text{m}$ . The cluster-like morphology of (d) suggests a bulk heterojunction interface between CuPc and C<sub>60</sub>.

DIP EBL. The efficiency of the control ( $1.42 \pm 0.04\%$ ) is similar to recently published data,<sup>28,152</sup> although it is below the highest efficiencies reported for this material combination.<sup>155</sup> Device II performs similarly to the un-templated structure, while for Device III, structural templating leads to an increase of 0.06 V in  $V_{OC}$  and a small increase in  $J_{SC}$ , resulting in  $\eta_p = 1.76 \pm 0.04\%$ . This increase in  $V_{OC}$  is due to the increase in the HOMO energy of CuPc as shown in Fig. 5.6(b). This is consistent with previous work suggesting that  $V_{OC}$  is proportional to the interface energy gap, which is defined as the difference between the donor HOMO and acceptor lowest unoccupied molecular orbital energy.<sup>24,101,122</sup> Incorporating both PTCDA and DIP in Device IV shows the same  $V_{OC}$  as for Device III, while  $J_{SC}$  is substantially increased, leading to  $\eta_p = 2.19 \pm 0.05\%$ . The  $FF$  for all devices is  $\approx 0.60$ , indicating that they have similar diode characteristics and shunt resistances under illumination.<sup>156</sup>

Devices incorporating a planar-mixed heterojunction (PMHJ)<sup>27</sup> were also fabricated with the structure glass/ITO/(0, 1.5nm) PTCDA/(0, 1.5 nm) DIP/15 nm CuPc/10 nm CuPc:C<sub>60</sub> (1:1)/35 nm C<sub>60</sub>/10 nm BCP/Al. As shown in Table 5.1, there is a similar in-

**Table 5.1** OPV performance for planar heterojunction (PHJ) and planar-mixed heterojunction (PMHJ) devices under simulated 1 sun, AM1.5G illumination.

Architecture	Templating Layer	$V_{OC}$ (V)	$FF$	$J_{SC}$ (mA/cm <sup>2</sup> )	$\eta_p$ (%)
PHJ	None	0.48	0.60	4.9	$1.42 \pm 0.04$
PHJ	DIP	0.47	0.60	5.0	$1.42 \pm 0.19$
PHJ	PTCDA	0.54	0.61	5.4	$1.76 \pm 0.04$
PHJ+EBL	PTCDA	0.54	0.62	6.6	$2.19 \pm 0.05$
PMHJ	None	0.50	0.61	6.2	$1.89 \pm 0.05$
PMHJ	DIP	0.51	0.62	6.4	$2.02 \pm 0.06$
PMHJ	PTCDA	0.48	0.59	7.1	$1.99 \pm 0.05$
PMHJ+EBL	PTCDA	0.50	0.63	8.1	$2.49 \pm 0.03$



**Figure 5.8** Current-voltage characteristics of devices with various templating layers: none (squares), PTCDA (triangles), DIP (upwards triangles), or PTCDA and DIP (downwards triangles) under one-sun illumination.

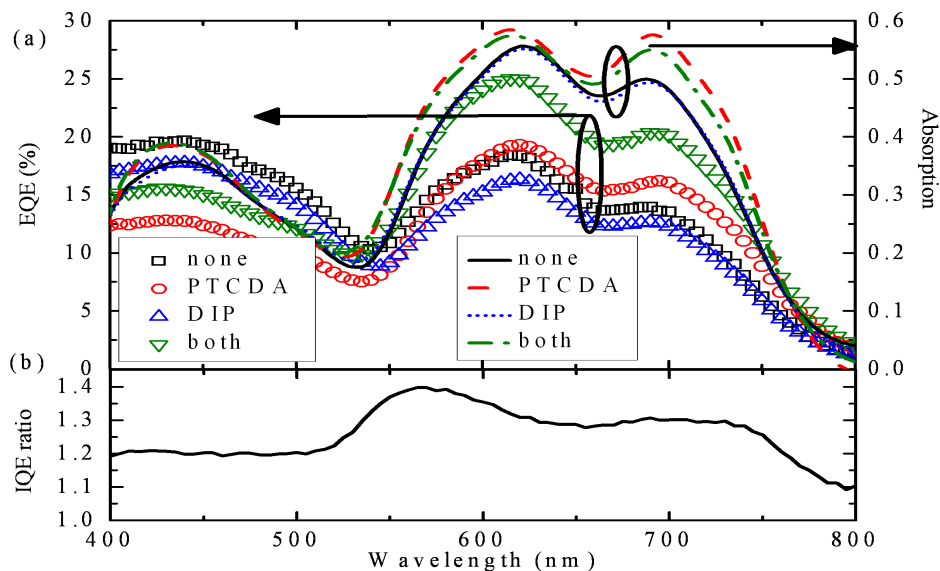
crease in  $J_{SC}$  from 6.2 to 8.1 mA/cm<sup>2</sup> when incorporating both the PTCDA and DIP layers due to the increase in absorption coefficient due to a more advantageous orientation of the initial CuPc donor region. However, this is accompanied by a decrease in  $V_{OC}$  from 0.50 to 0.48 V. This is due to a previously reported frustration of crystallinity in co-evaporated CuPc:C<sub>60</sub> films.<sup>27,28</sup> The resulting amorphous film does not have the preferred stacking, which results in the deeper CuPc HOMO in Fig. 5.6(b). Nevertheless, the combination of a templating layer and an EBL, the efficiency increases to  $2.49 \pm 0.03\%$ , or nearly double that of the planar control.

## 5.4 Discussion

The mechanisms for OPV efficiency enhancement are further understood by comparing the internal (*IQE*) and external quantum efficiencies (*EQE*) of the cells. Figure 5.9(a) shows *EQE* (symbols) and absorption (lines) for the approximately planar heterojunction (PHJ) devices. For Device III, which employs a PTCDA template, the absorption (corresponding to  $1-R$ ) of CuPc at  $\lambda = 690$  nm is increased from 0.50 to 0.58. This leads to an increase in *EQE* from 14 to 16% in the same spectral region, accompanied by a decrease in *EQE* at shorter wavelengths. This decrease could arise from a decrease in the exciton diffusion length due to morphology changes. Integrating across the solar spectrum, Devices I, II, and III have comparable photocurrent, while Device IV is 25% higher. The ratio of the *IQE* of Device IV to Device III is  $>1$  across the spectrum, shown in Figure 5.9(b). The 10% increase in surface area accounts for an increase in *IQE* across the spectrum (see Fig. 5.7). The additional increase in the spectral region from  $\lambda = 550$  nm to 750 nm (where CuPc absorbs) is attributed to exciton blocking by DIP. Whereas in Device III, excitons generated in CuPc can quench at the PTCDA/CuPc interface, by incorporating DIP in Device IV the contribution of CuPc to the *IQE* is increased approximately 20% according to optical models utilizing the transfer matrix approach.<sup>47</sup>

## 5.5 Conclusions

In summary, we have demonstrated improved OPV performance resulting from a change in crystalline orientation achieved via structural templating of subsequently deposited layers of DIP and CuPc. Using PTCDA as a crystalline template, the DIP and CuPc molecular



**Figure 5.9** (a) External quantum efficiency (*EQE*) and absorption measured for Devices I - IV. (b) Ratio of the internal quantum efficiencies (*IQE*) of Device IV to Device III.

stacking were modified from a standing-up to a flat-lying orientation relative to the substrate plane. For CuPc, this leads to improvement in orbital overlap between adjacent molecules, and hence changes in frontier energy levels and absorption coefficient that combine to substantially increase the power conversion efficiency. In addition, DIP propagates the structural templating, changes CuPc film morphology, and serves as an EBL between PTCDA and CuPc. The OPV efficiency increases from  $1.42 \pm 0.04\%$  to  $2.19 \pm 0.05\%$  for a PHJ, and from  $1.89 \pm 0.05\%$  to  $2.49 \pm 0.03\%$  for a PMHJ by the improved stacking arrangements of CuPc in a CuPc/C<sub>60</sub> OPV cell. Our results show the impact of controlling the crystalline morphology and orientation on organic optoelectronic properties.

## Chapter 6

# Organic photovoltaics incorporating electron conducting buffer layers

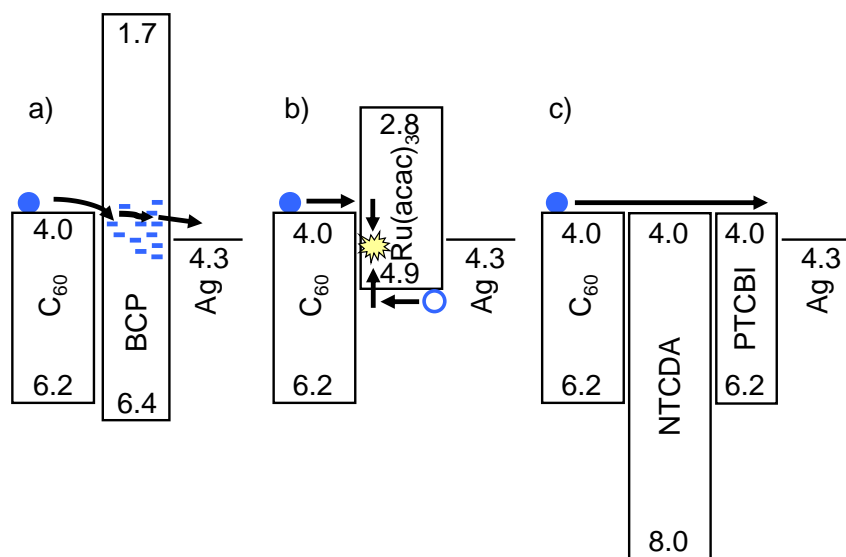
An important milestone to increased efficiency in OPVs was the introduction of a buffer layer interposed between the acceptor layer and cathode contact, forming a so-called double heterojunction solar cell.<sup>95,96</sup> The first material introduced as a cathode buffer layer in small molecule OPVs was bathocuproine (BCP). Since then, it has become an archetypal material, being utilized in well over 100 publications,<sup>149,150,157–170</sup> including the closely related material, bathophenanthroline (BPhen).<sup>87–89,161,162,171–181</sup> The ideal buffer serves multiple purposes: to protect the underlying acceptor material (e.g. C<sub>60</sub>) from damage due to the evaporation of hot cathode metal atoms, to provide efficient electron transport to the cathode, to serve as an exciton blocking layer (EBL) that prevents excitons generated in the acceptor from quenching at the cathode, and to act as a spacer that maximizes the optical field at the active donor-acceptor heterojunction. The most commonly used EBLs are wide energy gap (and hence transparent) semiconductors, such as BCP and BPhen, that transport carriers via cathode metal-deposition-induced damage that results in a high density of conducting trap states (Fig. 6.1 a).<sup>95,96</sup> However, as the layer is conductive only

in the presence of traps, the thickness is limited by the depth of damage ( $\sim 10$  nm), which may not be optimal for achieving a maximum optical field intensity in the active region of the device. In this chapter, we utilize another type of buffer layer, where the lowest occupied molecular orbital (LUMO) is aligned with that of the acceptor, allowing for low-resistance transport of electrons directly from acceptor to cathode.<sup>182</sup> We show that 3,4,9,10 perylenetetracarboxylic bisbenzimidazole (PTCBI) serves as a trap-free, efficient electron conductor and forms a low energy barrier contact with the Ag cathode. This leads to an increased fill factor from  $FF = 0.60$  typical of analogous BCP-based devices, to  $FF = 0.70$ . Additionally, 1,4,5,8-naphthalene-tetracarboxylic-dianhydride (NTCDA) is shown to function as a wide-gap electron-conducting EBL. By using both NTCDA and PTCBI in a compound blocking layer structure as in Fig. 6.1c, we obtain optimal optical spacing, leading to increased photocurrent. This results in a spectrally corrected power conversion efficiency of  $\eta_p = 5.1 \pm 0.1\%$  under 1 sun, AM1.5G simulated solar illumination, an improvement of  $>25\%$  compared to a conventional device with a BCP blocker.

## 6.1 Background

### 6.1.1 Buffer layers in organic photovoltaics

A number of alternatives to cathode-damaged BCP have been explored. Doping of BPhen by coevaporation has been demonstrated with Mg,<sup>168</sup> or Yb,<sup>183</sup> increasing the conductivity and allowing films as thick as 40 nm to be utilized without a significant increase in series resistance or absorption, as shown in Fig. 6.2. Figure 6.2 also shows that the mid-gap transport states in BPhen deepen with Yb doping, which decreases the barrier electrons



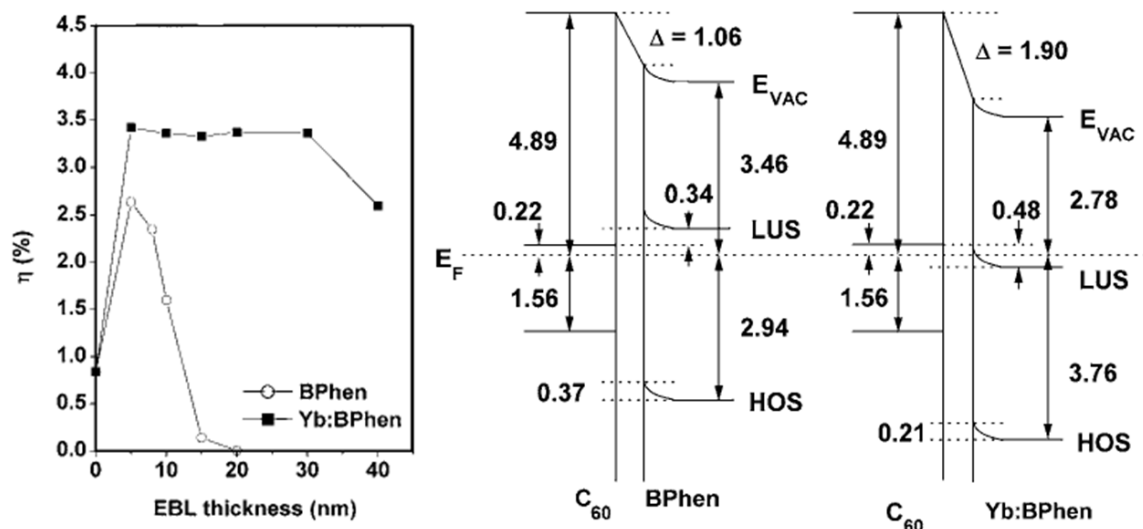
**Figure 6.1** Energy level diagrams of exciton blocking layers that transport charge via a) damage-induced trap states, b) electron-hole recombination, and c) electron transport through the lowest unoccupied molecular orbital.

encounter at the C<sub>60</sub>/BPhen interface.

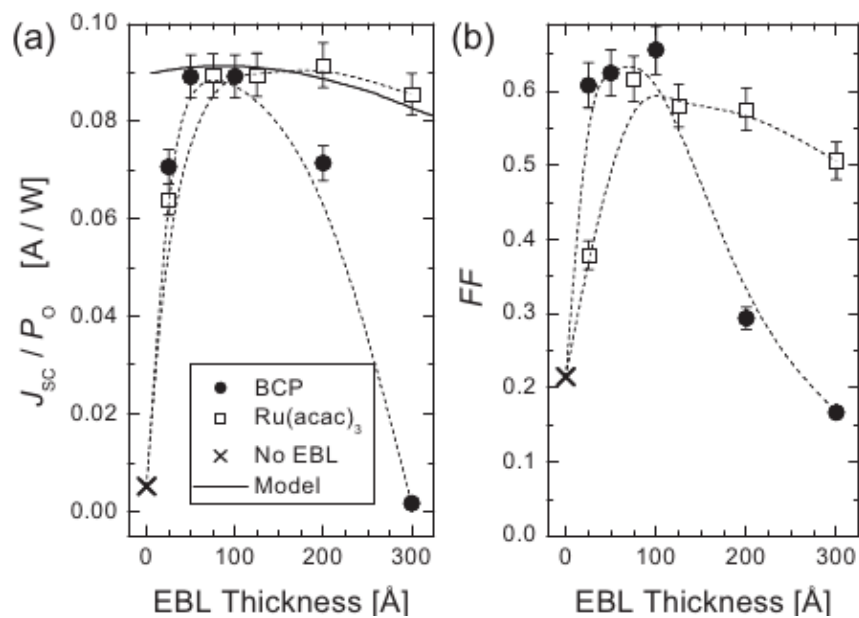
Other doped EBLs have been demonstrated, notably by Maennig et al.<sup>184,185</sup> On the cathode side, n-doped C<sub>60</sub> is utilized to decrease the energy barrier created at the C<sub>60</sub>/Ag interface.

A second type of EBL was introduced based on tris-(acetylacetonato) ruthenium(III) (Ru(acac)<sub>3</sub>) and related compounds that have a small highest occupied molecular orbital (HOMO) energy. In this case, holes from the cathode are transported along the HOMO of Ru(acac)<sub>3</sub> and recombine with electrons at the acceptor/EBL interface, as shown in Fig. 6.1b.<sup>92,186</sup> Figure 6.3 shows Ru(acac)<sub>3</sub> layers as thick as 30 nm can be used, with minimal loss of performance.

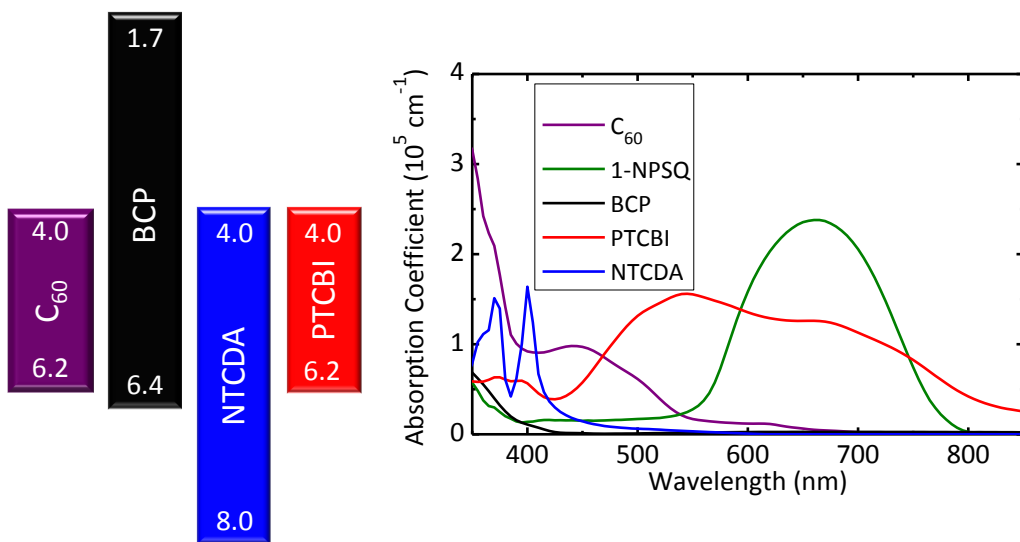




**Figure 6.2** (left) Photovoltaic response of devices with structure of ITO/CuPc/ $C_{60}$ /EBL/Al as functions of EBL thickness, where EBL is either BPhen or Yb:BPhen. (right) Energy level diagram for the  $C_{60}$ /BPhen and the  $C_{60}$ /Yb:BPhen contacts. From Ref. 183.



**Figure 6.3** a) Responsivity ( $J_{sc}/P_0$ ) and b) fill factor  $FF$  of devices where the EBL thickness is varied from 0 to 300 Å. The device with no EBL is marked by an X. The solid line in (a) is the calculated responsivity, and the dashed lines serve as guides to the eye. From Ref. 92.

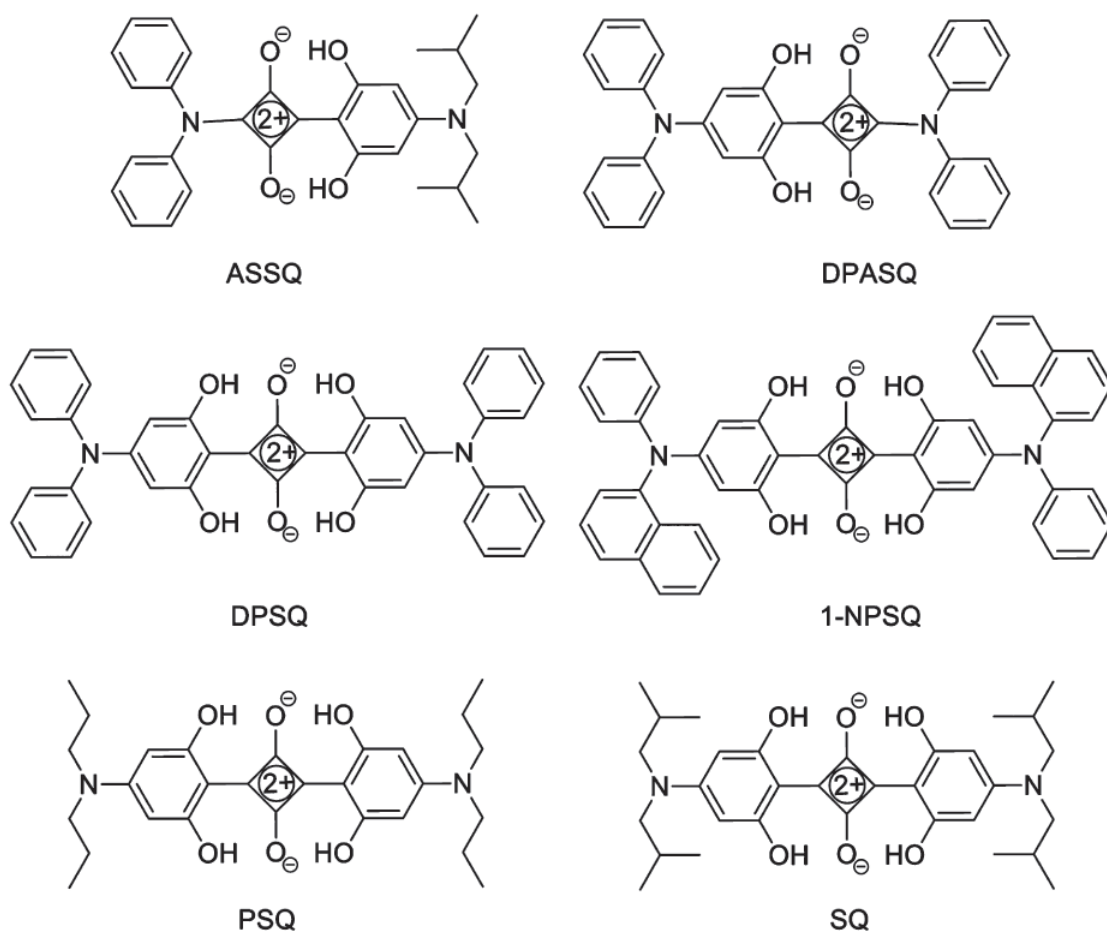


**Figure 6.4** Left: energy levels of C<sub>60</sub>, BCP, NTCDA, and PTCBI.<sup>74,187</sup> Right: Measured absorption coefficients of the same materials.

## 6.1.2 Functionalized squaraines

The remainder of this work will utilize functionalized squaraine (*fSQ*) molecules as donors. These materials have previously been used in optical recording, dye-sensitized solar cells, and fluorescence imaging due to their strong optical properties.<sup>188</sup> In 2009, Wang et al. utilized diisobutyl squaraine (dibSQ) in a bilayer HJ OPV, resulting in  $\eta_P = 3.2\%$ .<sup>76</sup> This was followed by improved performance with dibSQ by incorporating thermal annealing<sup>189</sup> and in a bulk HJ architecture.<sup>124,164,190</sup> A number of other *fSQs* have also been synthesized and successfully utilized in OPVs, as shown in Fig. reffig:SQs.<sup>191–193</sup>

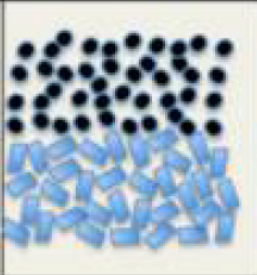

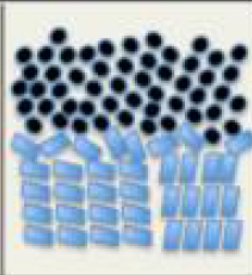
The highest performing of these molecules are not sublimable, necessitating the use of solution-processed deposition. The *fSQs* are soluble in common organic solvents such as chloroform, dichlorobenzene, dichloromethane (DCM), and tetrahydrofuran, and thin films can be deposited from solution by spin coating. The as-cast films tend to be amorphous, but



**Figure 6.5** Molecular structural formulas of functionalized squaraine donors. From Ref. 193.

crystallization can be induced by post-processing such as thermal or solvent vapor annealing (SVA).<sup>194</sup> In SVA, the films are exposed to the saturated vapors of a solvent, typically DCM, until the molecules reorganize into nanocrystalline domains. Zimmerman et al. recent found a strong dependence of the  $J_{SC}$  and  $V_{OC}$  on different processing conditions.<sup>194</sup> As-cast films were amorphous, with low  $J_{SC}$  and high  $V_{OC}$ . Films which had SVA after the  $fSQ$  but before  $C_{60}$  had high  $J_{SC}$  but low  $V_{OC}$ ; however, if SVA was applied after the  $C_{60}$  layer, both high  $J_{SC}$  and  $V_{OC}$  were achieved, as summarized in Fig. 6.6. This is due to

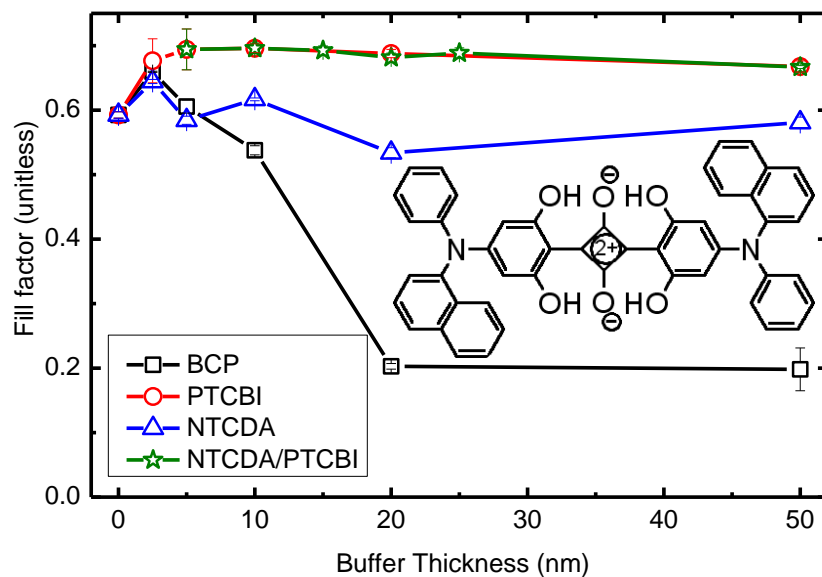
the difference in requirements of ordering in the bulk vs. at the interface. Crystallinity in the bulk of the active materials leads to higher exciton diffusion lengths, increasing  $J_{SC}$ , whereas crystallinity (i.e. tight packing) at the donor-acceptor interface increases the rate of polaron pair recombination, decreasing the  $V_{OC}$  (see Eq. (6.1)). By applying SVA after both donor and acceptor materials have been deposited, the bulk of each material increases in crystallinity, while the interface remains disordered, resulting in high  $J_{SC}$  and  $V_{OC}$ .

$C_{60}$			
DPSQ			
	<b>As-Cast</b>	<b>Pre-<math>C_{60}</math></b>	<b>Post-<math>C_{60}</math></b>
Bulk DPSQ	Amorphous	Ordered	Mod. Order
Bulk $C_{60}$	Weak Order	Ordered	Weak Order
Interface	Disordered	Ordered	Disordered
Surface	Smooth	Rough	Smooth
$k_{ppr}$	Low	High	Low
$V_{OC}$	High	Low	High
$J_{SC}$	Low	Moderate	High

**Figure 6.6** Qualitative summary of the structural and performance outcomes induced by the processing conditions. From Ref. 194.

## 6.2 Experiment

Devices were grown on 100 nm thick layers of indium tin oxide (ITO) pre-coated onto glass substrates. Prior to deposition, the ITO surface was cleaned in a surfactant and a series of solvents,<sup>28</sup> and then exposed to ultraviolet-ozone for 10 min before loading into a high vacuum chamber (base pressure  $< 10^{-7}$  Torr) where MoO<sub>3</sub> was thermally evaporated at  $\sim 0.1$  nm/s. Substrates were then transferred to a N<sub>2</sub> glovebox where 2,4-bis[4-(N-Phenyl-1-naphthylamino)-2,6-dihydroxyphenyl] squaraine<sup>192</sup> (1-NPSQ, see molecular structural formula in Fig. 6.7, inset) films were spin-coated from heated 6.5 mg/ml solutions in 1,2-dichlorobenzene, and thermally annealed on a hot plate at 110 °C for 5 min to promote the growth of a nanocrystalline morphology.<sup>189</sup> Substrates were once again transferred into the high vacuum chamber for deposition of purified organics at 0.1 nm/s, followed by a 100nm thick Ag cathode deposited at 0.1 nm/s through a shadow mask with an array of 1 mm diameter openings. Current density versus voltage (*J-V*) characteristics were measured in an ultra-pure N<sub>2</sub> ambient, in the dark and under simulated AM1.5G solar illumination from a filtered 150 W Xe lamp. Lamp intensity was varied using neutral density filters. Optical intensities were referenced using an NREL-calibrated Si detector,<sup>37</sup> and photocurrent measurements were corrected for spectral mismatch.<sup>195</sup> Errors quoted correspond to the deviation from the average value of three or more devices on the same substrate.



**Figure 6.7** Fill factor ( $FF$ ) under spectrally corrected 1 sun, AM1.5G illumination for devices with BCP buffer layers (squares), PTCBI (circles), NTCDA (triangles), and compound NTCDA/PTCBI (stars) as functions of thickness. Lines are a guide to the eye. Inset: the molecular structure of 1-NPSQ.

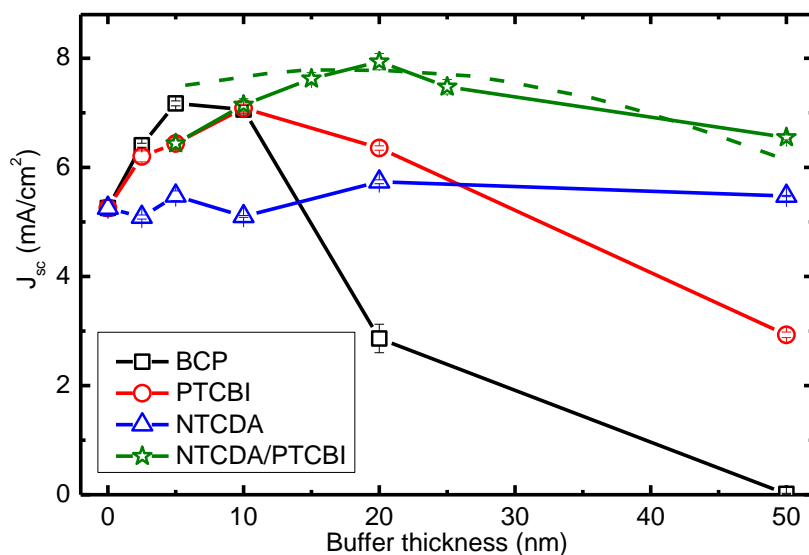
## 6.3 Results

The HOMO and LUMO energies of  $C_{60}$  are 6.2 and 4.0 eV, respectively,<sup>74</sup> while BCP has corresponding energies of 6.4 and 1.7 eV,<sup>187</sup> as shown in Figs 6.1 and 6.4. Because the PTCBI and NTCDA LUMOs approximately align with that of  $C_{60}$ ,<sup>187</sup> electron transport can occur between these materials in the absence of damage.

Devices were fabricated with the following structure: glass/100 nm ITO/8 nm  $MoO_3$ /15 nm 1-NPSQ/40 nm  $C_{60}$ /buffer(s)/100 nm Ag. The open-circuit voltage depends on the interfacial energy gap between the donor and acceptor,<sup>24,122</sup> and is  $V_{oc} = 0.90$  to  $0.96 \pm 0.01$  V, independent of buffer layer composition. Figure 6.7 shows  $FF$  as a function of buffer layer thickness  $x$  for BCP, PTCBI, NTCDA, and compound buffers consisting of  $(x-5)$  nm

NTCDA/5 nm PTCBI. Optimal performance for devices with BCP occurs at a thickness of 5 nm, with  $FF = 0.60 \pm 0.01$ , beyond which there is sharp drop in efficiency due to the limited depth of damage-induced transport states extending into the film from the surface.<sup>95,96</sup> In contrast, devices with PTCBI exhibit  $FF = 0.70 \pm 0.01$ , with only a small reduction as  $x \rightarrow 50$  nm, confirming the low resistance transport in this material. The optimum thickness for PTCBI is 10 nm, where  $\eta_p$  decreases for thicker films due to a decrease in short-circuit photocurrent ( $J_{sc}$ ), since PTCBI absorption overlaps with that of the active acceptor and donor layers. Devices with NTCDA buffer layers show  $FF = 0.62 \pm 0.01$ . In contrast, devices with a compound 15 nm NTCDA/5 nm PTCBI buffer have  $FF = 0.68 \pm 0.01$ , which is similar to that of PTCBI alone.

The compound NTCDA/PTCBI buffer layer leads to increases in  $J_{sc}$  compared to PTCBI alone. Unlike PTCBI, the wide energy gap NTCDA is transparent across the visible spectrum (Fig. 6.4). Hence, the PTCBI is kept sufficiently thin (5 nm) to provide a low-barrier cathode contact without introducing excessive optical absorption. At the same time, the NTCDA thickness is adjusted to maximize the optical field at the donor-acceptor junction without increasing series resistance, contrary to the case with BCP. The trend in  $J_{sc}$  as a function of buffer layer agrees with optical modeling using the transfer-matrix approach,<sup>47</sup> shown by the dashed line in Fig. 6.8. Optimized devices employing compound buffers achieve  $J_{sc} = 8.0 \pm 0.1$  mA/cm<sup>2</sup> compared to  $7.2 \pm 0.1$  mA/cm<sup>2</sup> for BCP and  $7.1 \pm 0.1$  mA/cm<sup>2</sup> for PTCBI, as seen in Fig. 6.8. For devices without a buffer and with BCP, PTCBI, NTCDA, and PTCBI/NTCDA buffers, we measure  $\eta_p = 2.8 \pm 0.1$ ,  $4.0 \pm 0.1$ ,  $4.6 \pm 0.1$ ,  $3.2 \pm 0.1$ , and  $5.1 \pm 0.1\%$ , respectively. These results are summarized in Table 6.1.



**Figure 6.8** Spectrally corrected short-circuit current ( $J_{SC}$ ) under 1 sun, AM1.5G illumination for devices with BCP buffer layers (squares), PTCBI (circles), NTCDA (triangles), and compound NTCDA/PTCBI (stars) as a function of thickness. Solid lines are a guide to the eye. The dashed line is  $J_{SC}$  modeled based on the optical intensity in the device for the case of the NTCDA/PTCBI buffer.

**Table 6.1** OPV performance for devices with different buffer layers under simulated 1 sun (mismatch corrected), AM1.5G illumination.

Buffer Layer	Thickness(nm)	$V_{oc}$ (V)	$FF$	$J_{sc}$ (mA/cm <sup>2</sup> )	$\eta_p$ (%)
none	0	0.90	0.59	5.3	$2.8 \pm 0.1$
BCP	5	0.93	0.60	7.2	$4.0 \pm 0.1$
PTCBI	10	0.94	0.70	7.1	$4.6 \pm 0.1$
NTCDA	10	0.94	0.62	5.6	$3.2 \pm 0.1$
NTCDA/PTCBI	15/5	0.945	0.68	8.0	$5.1 \pm 0.1$

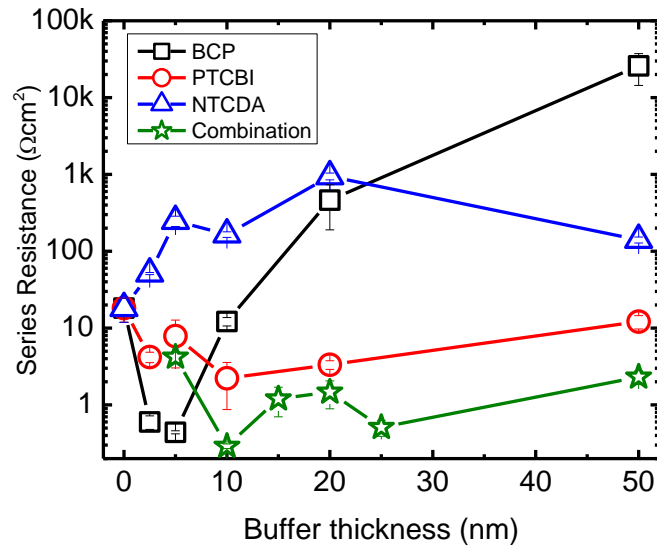


## 6.4 Discussion

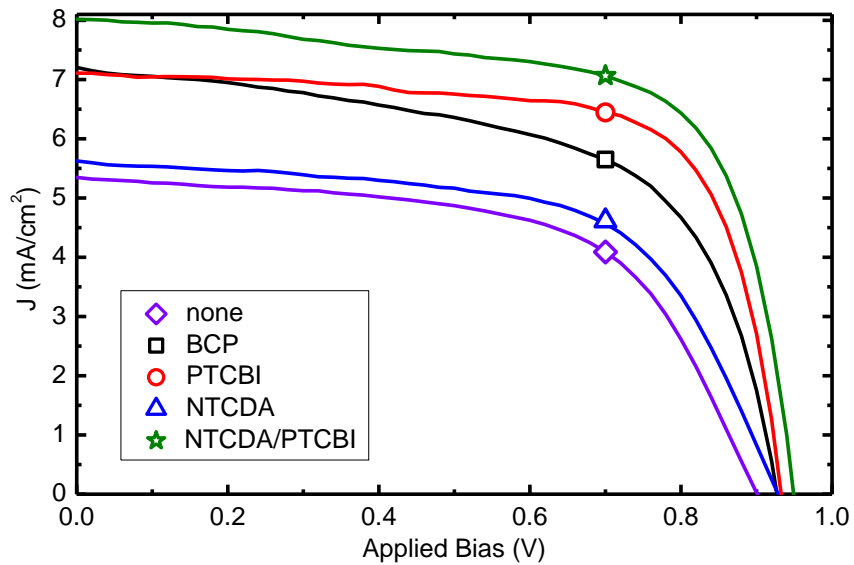
To understand the differences in  $FF$  between the several buffer layer combinations explored, we describe the current density using the ideal diode equation:<sup>24</sup>

$$J = J_s \left\{ \exp[q(V_a - JR_s)/nk_bT] - \frac{k_{ppd}}{k_{kppd,eq}} \right\} - q\eta_{PPd}(V_a)J_X, \quad (6.1)$$

where  $J_s$  is the reverse saturation current,  $q$  is the electron charge,  $V_a$  is the applied voltage,  $R_s$  is the series resistance,  $n$  is the ideality factor,  $T$  is temperature,  $k_{ppd}$  is the polaron pair dissociation rate,  $k_{kppd,eq}$  is the equilibrium polaron pair dissociation rate,  $\eta_{PPd}(V_a)$  is the field-dependent polaron pair dissociation efficiency, and  $J_X$  is the exciton current reaching the heterojunction.  $k_{ppd}/k_{kppd}$  is taken to be  $\sim 1$  in this case. For optimized BCP, PTCBI, and NTCDA/PTCBI buffer layer devices,  $R_s < 10 \Omega\text{-cm}^2$  (Fig. 6.9), indicating efficient transport of electrons to the cathode. With layers as thick as 50 nm,  $R_s$  for PTCBI and compound buffers does not change appreciably, while for BCP it increases to  $> 10 \text{ k}\Omega\text{-cm}^2$  for  $x = 50 \text{ nm}$ . Devices with NTCDA-only buffers have  $R_s > 100 \Omega\text{-cm}^2$  for all thicknesses, due to an electron extraction barrier formed at the NTCDA/Ag interface, which has been reported to be  $> 1 \text{ eV}$ .<sup>90</sup> However, NTCDA-based devices that include a 5 nm thick layer of PTCBI have a similar  $R_s$  to that of PTCBI alone, in good agreement with the previous reports of a 0.1 eV barrier at the PTCBI/Ag interface.<sup>196,197</sup>



**Figure 6.9** Series resistances, obtained by fits of the dark current at forward bias to the to Eq. (6.1), for devices with BCP (squares), PTCBI (circles), NTCDA (triangles), and compound NTCDA/PTCBI buffers (stars).



**Figure 6.10** Spectrally corrected current density vs. voltage characteristics in the 4<sup>th</sup> quadrant under 1 sun, AM1.5G illumination for optimized devices with no buffer (diamond), 5 nm BCP (square), 10 nm PTCBI (circle), 10 nm NTCDA (triangle), and compound 15 nm NTCDA/5 nm PTCBI buffers (star).

## 6.5 Future work

The physical origin of the  $FF$  improvement is still unclear. One possible mechanism for the difference in  $FF$  for devices with BCP or PTCBI is the effect of trapped charges on the internal electric field. From Eq. (6.1), the current density for a device under illumination is determined by the field-dependence of  $\eta_{PPd}$ .<sup>24</sup> Because electron transport in BCP occurs through damage-induced traps, their residence in these deep levels induces an electric field that is opposite to the field induced by  $V_a$ , resulting in increased recombination at the heterojunction. This appears in the  $J$ - $V$  characteristic as an increased slope at zero bias (see Fig. 6.10), leading to a decrease in  $FF$ . There is also recent evidence that the slope at reverse bias in OPVs is due to either photoconductivity<sup>198,199</sup> or exciton-polaron quenching.<sup>200</sup> This is explored further in Chapter 10.3.

Our recent work suggests that excitons are efficiently quenched at the  $C_{60}$ /PTCBI interface. The preliminary results are discussed further in Chapter 10.3.

## 6.6 Conclusions

In summary, we have demonstrated the use of electron conducting EBLs in OPVs. Here, electrons are transported via the LUMO states directly from that of the acceptor to the cathode. By using PTCBI as a buffer layer, we find  $FF = 0.70 \pm 0.01$ , compared to  $FF = 0.60 \pm 0.01$  for conventional BCP-based devices. Adding an NTCDA electron-conducting EBL in combination with PTCBI allows for optimized optical spacing and efficient exciton blocking, leading to an increase in  $\eta_p$  that is  $>25\%$  for an analogous squaraine/ $C_{60}$ /BCP OPV. The increased stability of PTCBI compared to BCP may also potentially extend the

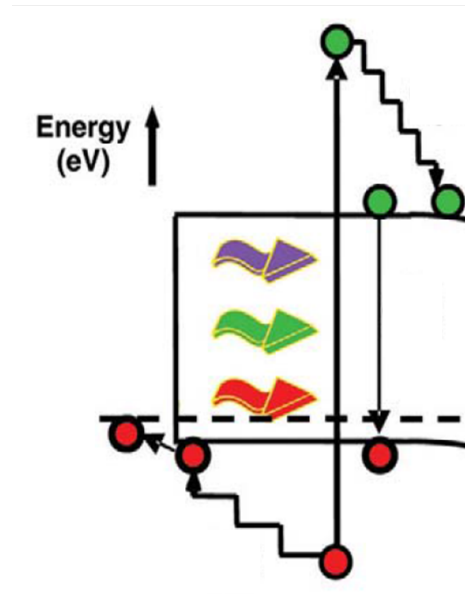
operational lifetime of OPVs employing blocking layers.

# Chapter 7

## Understanding tandem organic photovoltaic cell performance

### 7.1 Introduction

For the single-junction PV cells considered thus far, there are fundamental limits to  $\eta_P$  that can be achieved at 1-sun standard illumination. In 1961, Shockley and Queisser calculated the ultimate limit for a single-junction cell at 30%, with the optimum optical gap energy  $E_{op} = 1.3$  eV.<sup>12</sup> This work was recently generalized to the case of excitonic PVs, predicting a maximum  $\eta_P$  between 22 and 27% (depending on the energy loss at the donor-acceptor interface).<sup>13</sup> One of the main factors in these calculations is the relationship between  $E_{op}$ ,  $V_{OC}$ , and photon absorption coefficient ( $\alpha$ ). For single crystal materials,  $\alpha$  drops off rapidly for photons with energy  $< E_{op}$ , while polycrystalline and amorphous films have a significant sub-gap absorption tail. As shown previously in Fig. 2.11, the solar spectrum has photon energies spanning  $0.5 < E < 4.1$  eV. To absorb the maximum number of photons,  $E_{op}$  should be as small as possible; however,  $V_{OC}$  is inversely related to  $E_{op}$ . This tradeoff between the number of photons absorbed and the  $V_{OC}$  is the origin of the optimum  $\eta_P$  and  $E_{op}$ .



**Figure 7.1** Schematic diagram of thermalization losses in photovoltaics. Adapted from Ref. 201.

When photons with  $E > E_{op}$  are absorbed they lose energy through lattice phonons in a process called thermalization, which is shown schematically in Fig. 7.1. One method to reduce thermalization losses is the use of multi-junction cells, where multiple sub-cells with different  $E_{op}$  are monolithically stacked. The sub-cell with larger  $E_{op}$  will then absorb the high-energy photons, decreasing thermalization losses, while the sub-cell with the smaller  $E_{op}$  will allow the absorption of additional, low-energy photons. According to the work of Vos, a so-called 'tandem' architecture incorporating two sub-cells can achieve  $\eta_P = 42\%$  with  $E_{op} = 1.0$  and  $1.9$  eV.<sup>202</sup> It is also possible to incorporate more than two sub-cells, increasing the maximum  $\eta_P$  to 49%, 53%, and 68% for 3, 4, and an infinite number of sub-cells, respectively. As a rule of thumb, it is possible to increase the efficiency of a single-cell device by  $\sim 40\%$  by incorporating a two-sub-cell tandem architecture.<sup>203</sup>

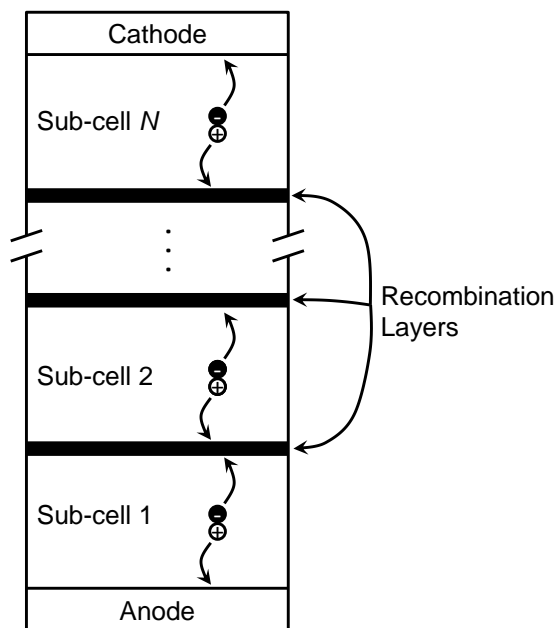
Understanding the operation of tandem OPVs is significantly more complex than that of

a single-cell device due to the inability to directly contact and measure its constituent sub-cell characteristics, a consequence of the low lateral conductivity of the interconnect layers between sub-cells. Previous theoretical investigations into tandem OPVs have considered optical absorption,<sup>204,205</sup> dependence on donor-acceptor (D-A) heterojunction (HJ) energy offsets,<sup>203</sup> and the relationship between the sub-cell and tandem current density-vs.-voltage ( $J$ - $V$ ) characteristics.<sup>112,206</sup>

In this section, we develop a framework to understand the operating characteristics of tandem OPVs consisting of an arbitrary number of sub-cells. Tandem performance is quantified in terms of the power conversion efficiency penalty,  $\Delta\eta$ , which is the loss incurred when one or more sub-cells are not operating at their maximum power points (MPPTs) when the tandem cell is at its MPPT. To minimize  $\Delta\eta$ , the currents at the MPPTs for each sub-cell must be equal. We also provide means to accurately calculate the tandem spectral mismatch factor ( $M_T$ ) and fill factor ( $FF_T$ ), which are functions of both the  $FF$  and short circuit current density,  $J_{SC}$ , of the constituent sub-cells. An analytical model is then developed that can be used to calculate the  $J$ - $V$  characteristics of both bilayer and mixed-layer OPVs used in a tandem cell. The model includes the effects of dark current, exciton dissociation at the D-A HJ, and parasitic photoconductivity by direct exciton dissociation in the sub-cell active region bulk,<sup>198,199</sup> along with current losses due to polaron-pair recombination and bimolecular recombination. We utilize this model to understand and optimize tandem cell operation. The dependence of tandem performance on the  $FF$  and  $J_{SC}$  of the constituent sub-cells is then determined based experimental data in Chapter 8.

This chapter is organized as follows: First, we describe a theory of tandem OPV performance and develop a model for the  $J$ - $V$  characteristics of bilayer and mixed-layer OPVs

used as sub-cells in archetype small molecular weight tandem structures. Next, experimental device data are fit to theory to extract physical parameters that are subsequently used to model tandem device operation under a variety of conditions. This is followed by a generalization to tandems consisting of an arbitrary number of sub-cells, followed by conclusions.



**Figure 7.2** Schematic diagram of a tandem cell incorporating  $N$  sub-cells stacked in series. Incident photons are absorbed, generating excitons, which are subsequently dissociated into free carriers. Holes (open circles) in the first sub-cell are collected at the anode, while electrons (closed circles) in the  $N$ th sub-cell are collected at the cathode. All other carriers recombine with opposite charges at the transparent recombination layers between the sub-cells.



## 7.2 Theory

To analyze performance, we begin by assuming that the tandem cell consists of  $N$  series-connected sub-cells, with each sub-cell separated by a charge recombination layer<sup>110,207</sup> as shown schematically in Fig. 7.2. Continuity requires that the current through each cell in the stack is equal, and that the total voltage across the stack is the sum of the voltages across the  $N$  sub-cells and their intervening layers (if any). We define  $\Delta\eta$  as the power conversion efficiency penalty at the tandem cell MPPT relative to its value if each individual sub-cell in the stack were operating at its own MPPT. That is,

$$\Delta\eta = 1 - J_{M-T}V_{M-T} / \sum_{i=1}^N J_{M-i}V_{M-i}, \quad (7.1)$$

where  $J_{M-i}$  is the current density at the maximum power point of sub-cell  $i = 1, 2, \dots, N$  (as numbered from the transparent anode contact), and  $V_{M-i}$  is the voltage at the maximum power point of the  $i$ th sub-cell. Also, the subscript 'T' refers to the value of a parameter for the complete tandem device. Here, the MPPT of the  $i$ th sub-cell is defined as follows:

$$MPPT_i = J_{M-i}V_{M-i} = FF_i J_{SC-i} V_{OC-i}, \quad (7.2)$$

where  $V_{OC}$  is the open circuit voltage. Setting  $\Delta\eta = 0$  and taking the tandem cell at its MPPT, we substitute  $J_{M-i} = J_{M-T}$ , obtaining  $V_{M-T} = \sum_{i=1}^N V_{M-i}$ . That is, to minimize  $\Delta\eta$ , all sub-cells in the tandem must be simultaneously operating at their respective MPPTs. It follows that a criterion to achieve the maximum power conversion efficiency,  $\eta_{P-T}$ , for a tandem cell is to match  $J_{M-i}$  for each sub-cell. In the case that the ratio  $J_{SC-i}/J_{M-i}$  is equal for each sub-cell, then an equivalent condition is that  $J_{SC}$  of each sub-cell be equal;

however, for OPVs this is not always the case as shown later in this section.

Now, for a single-junction OPV, the spectral mismatch factor is defined as the following: <sup>38,195</sup>

$$M_i = \frac{\int_{\lambda_1}^{\lambda_2} E_{Ref}(\lambda) S_R(\lambda) d\lambda \int_{\lambda_1}^{\lambda_2} E_S(\lambda) S_T(\lambda) d\lambda}{\int_{\lambda_1}^{\lambda_2} E_{Ref}(\lambda) S_T(\lambda) d\lambda \int_{\lambda_1}^{\lambda_2} E_S(\lambda) S_R(\lambda) d\lambda}, \quad (7.3)$$

where  $E_{Ref}(\lambda)$  is the solar reference spectral irradiance,  $E_S(\lambda)$  is the source lamp spectral irradiance,  $S_R(\lambda)$  is the spectral responsivity of the reference cell,  $S_T(\lambda)$  is the spectral responsivity of the test cell, and wavelengths  $[\lambda_1, \lambda_2]$  span the response spectral domain of both the reference and the device under test.

Calculating spectral mismatch for a tandem device requires quantitative knowledge of the  $J$ - $V$  characteristics and spectral mismatch factors of each sub-cell as they operate in the tandem. Since it is generally not possible to extract the  $J$ - $V$  data for the sub-cells in the tandem stack, a formalism is required to accurately simulate the individual device performances. For this purpose, the current density at applied voltage,  $V_a$ , is written as follows: <sup>24,198,199</sup>

$$J(V_a) = J_{dark}(V_a) + J_{jxn}(V_a) + J_{pc}(V_a), \quad (7.4)$$

where  $J_{dark}$  is the dark current density,  $J_{jxn}$  is the current from dissociation of excitons at the D-A HJ, and  $J_{pc}$  is the photoconductive current density from excitons that dissociate in the bulk photoactive regions (i.e. away from the active D-A HJ). The dark current for an

organic heterojunction is<sup>24</sup>

$$J_{dark}(V_a) = J_{sD} \left[ \exp \left( \frac{V_a - JR_S}{n_D k_B T / q} \right) - \chi \right] + J_{sA} \left[ \exp \left( \frac{V_a - JR_S}{n_A k_B T / q} \right) - \chi \right] \quad (7.5)$$

where  $J_{sD}$  and  $J_{sA}$  are the saturation currents,  $n_D$  and  $n_A$  are the ideality factors that depend on charge recombination at traps in the donor and acceptor layers, respectively,  $k_B T$  is the Boltzmann constant-temperature product,  $q$  is the electronic charge,  $R_S$  is the cell series resistance, and  $\chi$  is the ratio of the polaron pair dissociation rate ( $k_{PPd}$ ) at  $V_a$ , to its equilibrium value at  $V_a = 0$ . We assume that  $\chi \approx 1$  at low  $V_a$ , characteristic of operation at or near the MPPT.

The junction photocurrent is given as follows:

$$J_{jxn}(V_a) = -q J_X \eta_{CC}(V_a) \eta_{PPd}(V_a) \quad (7.6)$$

where  $J_X$  is the exciton current density reaching the D-A interface,  $\eta_{CC}$  is the charge collection efficiency,<sup>27</sup> and  $\eta_{PPd}$  is the interfacial polaron pair dissociation efficiency.<sup>24</sup> The former is used to determine the losses due to recombination of free carriers in devices containing a mixed D-A layer, viz.:<sup>27</sup>

$$\eta_{CC}(V_a) = \frac{L_{c0}(V_{bi} - V_a)}{V_{bi} d_m} \left[ 1 - \exp \left( - \frac{V_{bi} d_m}{L_{c0}(V_{bi} - V_a)} \right) \right] \quad (7.7)$$

where  $L_{c0}$  is the charge collection length at  $V_a = 0$ ,  $d_m$  is the mixed layer thickness, and  $V_{bi}$  is the built-in potential. Note that when  $d_m/L_{c0} \rightarrow 0$ , then  $\eta_{CC} \rightarrow 1$ , as expected for a simple bilayer device which is the 'limit' of a planar-mixed HJ.<sup>27</sup> On the other hand,  $\eta_{PPd}$

accounts for dissociation of polaron pairs at the DA interface in a bilayer OPV:

$$\eta_{PPd}(V_a) = \frac{k_{PPd}(V_a)}{k_{PPr}(V_a) + k_{PPd}(V_a)} \quad (7.8)$$

where  $k_{PPr}$  is the polaron pair recombination rate. Next, the layer photoconductive current density is as follows:

$$J_{pc}(V) = S_{pc}(V - JR_S - V_{bi}) \quad (7.9)$$

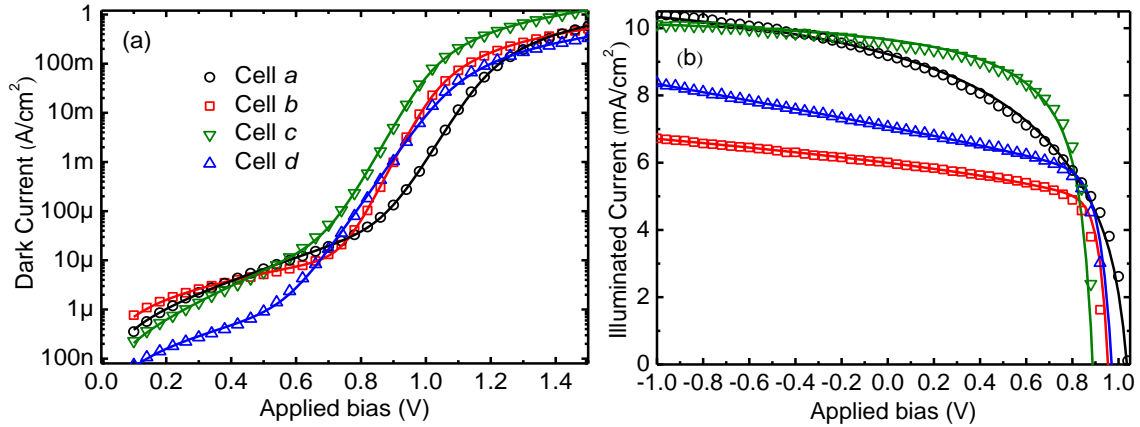
where  $S_{pc}$  is the photoconductance which is a linear function of incident light power intensity,<sup>198</sup> and hence  $J_X$ . Finally, to correct for mismatch between the reference lamp and the solar spectra, the measured  $J_X$  is replaced with  $MJ_X$ . By fitting both the dark and illuminated  $J$ - $V$  characteristics of the discrete cells, we obtain the parameters required to calculate Eq. (7.4) that can ultimately be used to simulate the tandem cell characteristics. For mixed-layer devices,  $S_{pc} = 0$  and  $\eta_{PPd} = 1$ , since all excitons are dissociated almost immediately after generation.<sup>208</sup> This leaves  $J_X$ ,  $L_{c0}$ , and  $V_{bi}$  as fitting parameters. Conversely, for bilayer devices,  $\eta_{CC} \approx 1$ , and  $S_{pc}$  can be obtained from the slope of the reverse illuminated  $J$ - $V$  characteristics, requiring that we obtain  $J_X$ ,  $\eta_{PPd}$  and  $V_{bi}$  from the fits. Optical absorption and exciton diffusion within the discrete and tandem cells can be modeled using the transfer matrix approach<sup>47</sup> to determine  $J_X$ . Once the sub-cell  $J$ - $V$  characteristics have been obtained, the tandem  $J$ - $V$  characteristic is calculated by summing voltages at each value of current, from which the uncorrected power conversion efficiency ( $\eta_P^{uncor}$ ) is obtained. The sub-cell  $J$ - $V$  characteristics are then corrected for spectral mismatch, from which the corrected tandem  $J$ - $V$  characteristic and power conversion efficiency ( $\eta_P^{cor}$ )

are calculated, along with  $J_{SC-T}$ ,  $V_{OC-T}$ ,  $FF_T$ , and  $\Delta\eta$ . From these results we obtain the tandem spectral mismatch factor,  $M_T = \eta_P^{uncor} / \eta_P^{cor}$ .

## 7.3 Results

### Fits to theory

We compare the data from four archetype devices that have been incorporated into binary-sub-cell tandem devices in Chapter 8. Here, single-cell devices are identified by lower case letters (e.g. Cell *a*), tandem devices with upper case letters (e.g. Tandem *A*), and tandem sub-cells are indexed by numbers that begin with the sub-cell nearest to the anode (e.g. Sub-cell 1, see Fig. 7.2), sometimes referred to as the 'front cell'. In Table reftable:tandemM1, we provide experimental results for Cell *a* consisting of a SubPc:C<sub>70</sub> graded HJ active region, Cell *b* employing a 2,4-bis[4-(N,N-diphenylamino)-2,6-dihydroxyphenyl]



**Figure 7.3** a) Dark and b) illuminated current-voltage characteristics for single-cell devices used in this work. Experimental data are represented by symbols, while the fits are represented by solid lines. Parameters used in these fits are found in Table 7.2.

**Table 7.1** Device structures and performance parameters for archetype single-cell devices.

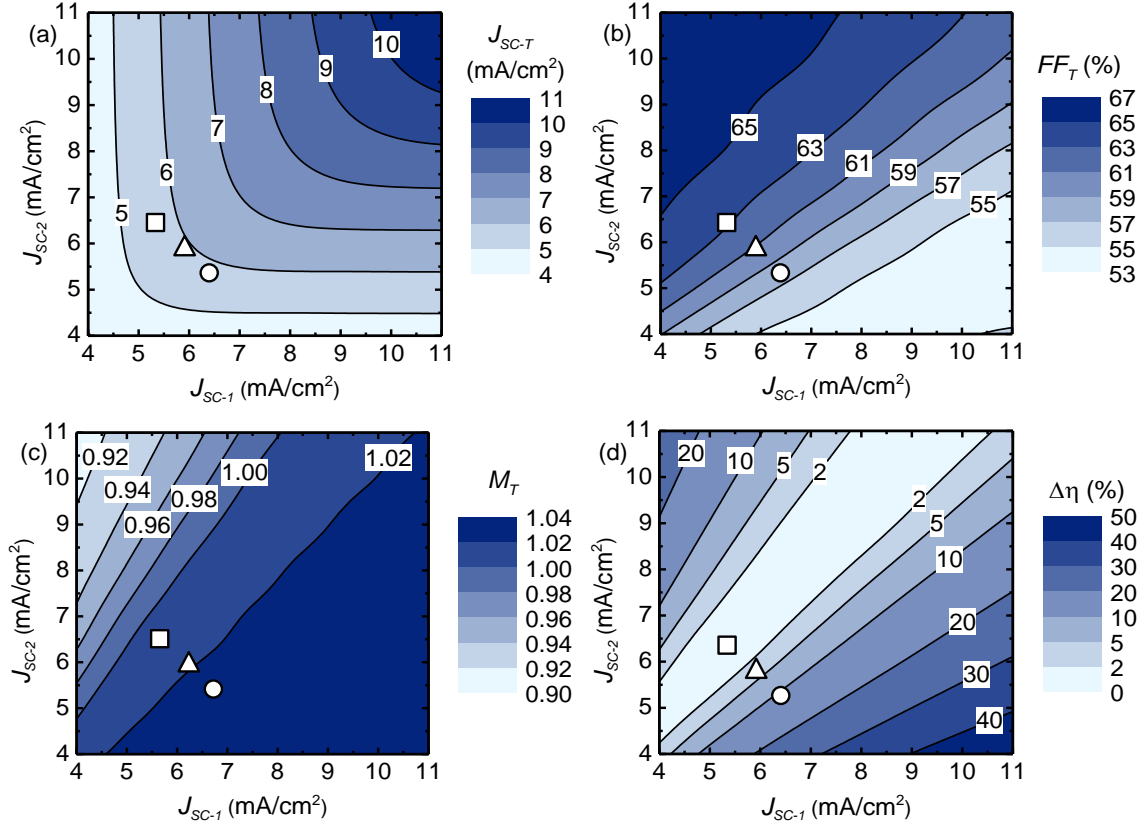
Parameter	Cell <i>a</i>	Cell <i>b</i>	Cell <i>c</i>	Cell <i>d</i>	Unit
Donor	SubPc	DPSQ	DBP	DPASQ:DPSQ	
Acceptor	C <sub>70</sub>	C <sub>70</sub>	C <sub>70</sub>	C <sub>70</sub>	
HJ Type	Graded	Bilayer	Planar-mixed	Bilayer	
$V_{OC}$	1.04 ± 0.01	0.94 ± 0.01	0.89 ± 0.01	0.96 ± 0.01	V
$FF$	48 ± 1	71 ±	61 ± 1	66 ± 1	%
$J_{SC}$	8.5 ± 0.1	6.1 ± 0.1	9.4 ± 0.1	7.7 ± 0.1	mA cm <sup>-2</sup>
$\eta_P$	4.3 ± 0.1	4.1 ± 0.1	5.0 ± 0.1	4.9 ± 0.1	%

**Table 7.2** Fitting parameters from archetype single-cell devices in Table 7.1.

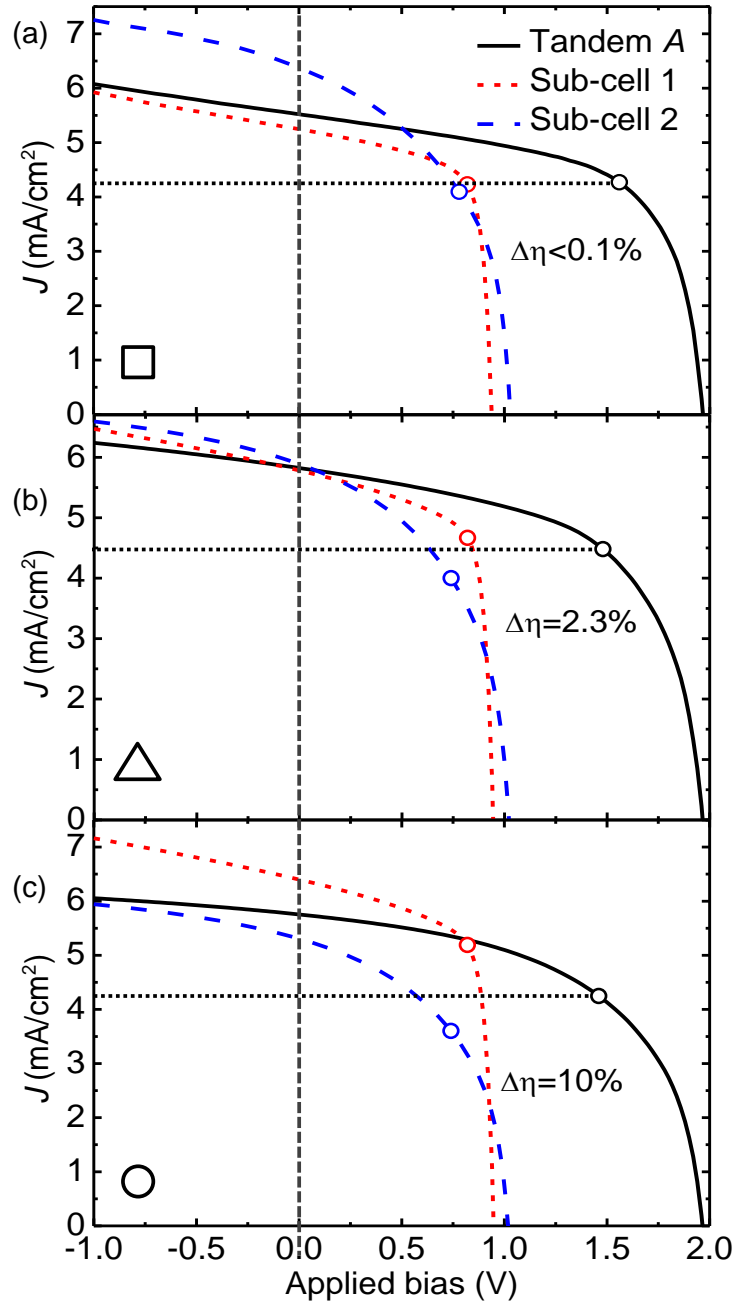
Parameter	Cell <i>a</i>	Cell <i>b</i>	Cell <i>c</i>	Cell <i>d</i>	Unit
$J_{sD}$	2.1 x 10 <sup>-6</sup>	2.1 x 10 <sup>-7</sup>	2.1 x 10 <sup>-7</sup>	1.6 x 10 <sup>-7</sup>	A cm <sup>2</sup>
$n_D$	7.8	19.3	5.7	12.2	–
$J_{sA}$	3.2 x 10 <sup>-15</sup>	1.6 x 10 <sup>-14</sup>	1.3 x 10 <sup>-13</sup>	4.0 x 10 <sup>-12</sup>	A cm <sup>2</sup>
$n_A$	1.56	1.31	1.42	1.78	–
$R_s$	0.41	0.67	0.33	0.96	ωcm <sup>2</sup>
$J_{X0}$	12.2	6.1	11.0	6.4	cm <sup>-2</sup> s <sup>-1</sup>
$L_{c0}/d_m$	1.9	–	5.5	–	–
$k_{PPd}/k_{PPr}$	–	40	–	2000	–
$V_{bi}$	1.17	1.00	0.96	1.01	V
$S_{pc0}$	–	0.72	–	1.10	mA cm <sup>-2</sup> V <sup>-1</sup>
$M_{single-cell}$	1.04	0.94	1.04	0.96	–
$M_{sub-cell}$	1.03	0.90	1.03	0.93	–

squaraine<sup>193</sup> (DPSQ)/C<sub>70</sub> bilayer HJ, Cell *c* with a tetraphenyldibenzoperiflanthene<sup>209</sup> (DBP):C<sub>70</sub> planar-mixed HJ, and Cell *d* consisting of a blended squaraine/C<sub>70</sub> bilayer HJ, where the squaraine blend consists of DPSQ and [2-[4-(N,N-diphenylamino)-2,6-dihydroxyphenyl]-4-[4-diphenyliminio] squaraine] (DPASQ). More details for the first two materials combinations are in Chapter 8.3, while the latter two can be found in Chapter 8.4. Figure 7.3 shows the dark and illuminated  $J$ - $V$  characteristics for these four devices, with experimental data indicated by symbols, and fits to Eq. (7.4) represented by solid lines. The

fitting parameters obtained are listed in Table reftable:tandemM2. The data taken under illumination in Fig. 7.3(b), are fit to voltages up to  $V_a = -1$  V, as required for modeling tandem performance. Comparing fits to the data, we find the theory accurately predicts both bilayer and mixed small molecule OPV performance.



**Figure 7.4** Contour plots of simulated device performance characteristics of Tandem A using Cell *a* as Sub-cell 1 and Cell *b* as Sub-cell 2. The short-circuit current ( $J_{SC}$ ) of each sub-cell is varied by changing the exciton flux at the heterojunction ( $J_X$ ). The square, triangle, and circle in the plots denote data points corresponding to example devices used in Fig. 7.5.



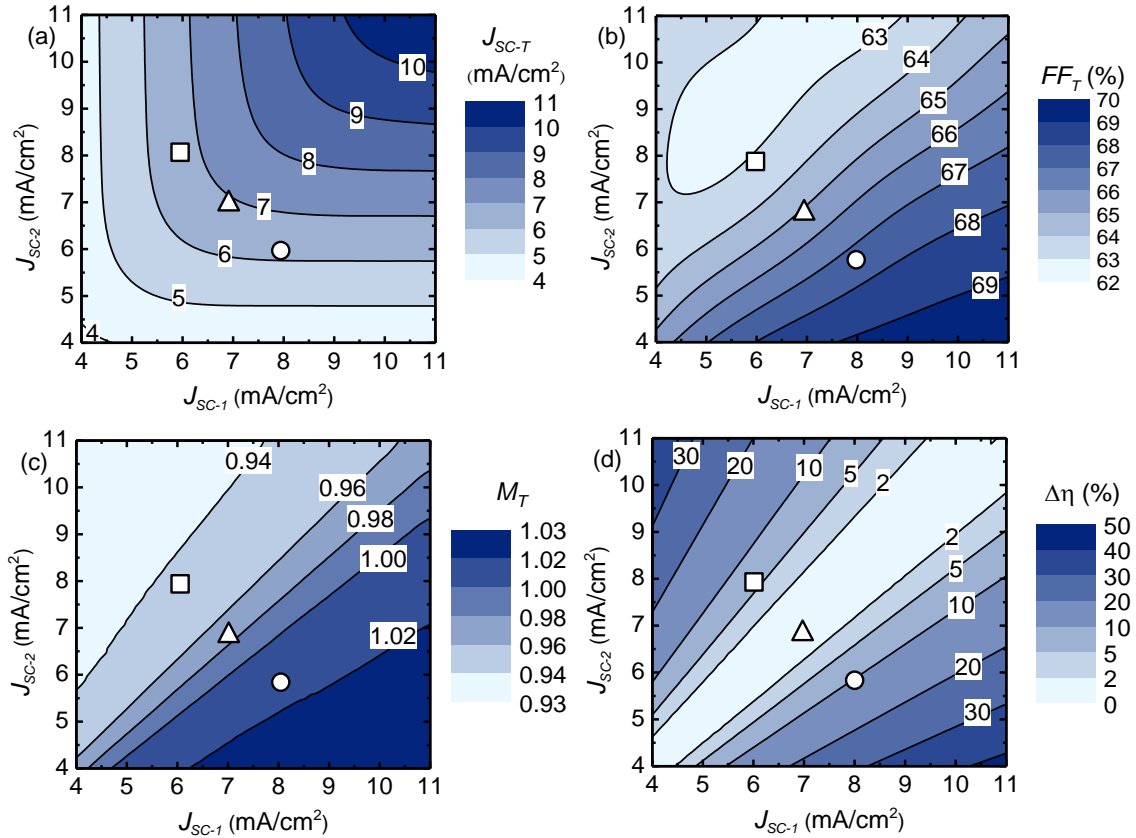
**Figure 7.5** Current-voltage ( $J$ - $V$ ) characteristics of three example Tandem A (solid line), indicated by symbols in Fig. 7.4, each with the constituent sub-cell characteristics shown by dashed lines. The maximum power point (MPPT) is represented by a circle on each line. The vertical dashed line is at  $V_a = 0$ , and the horizontal dotted line marks the current at which the sub-cells are operating when the tandem is at its MPPT.



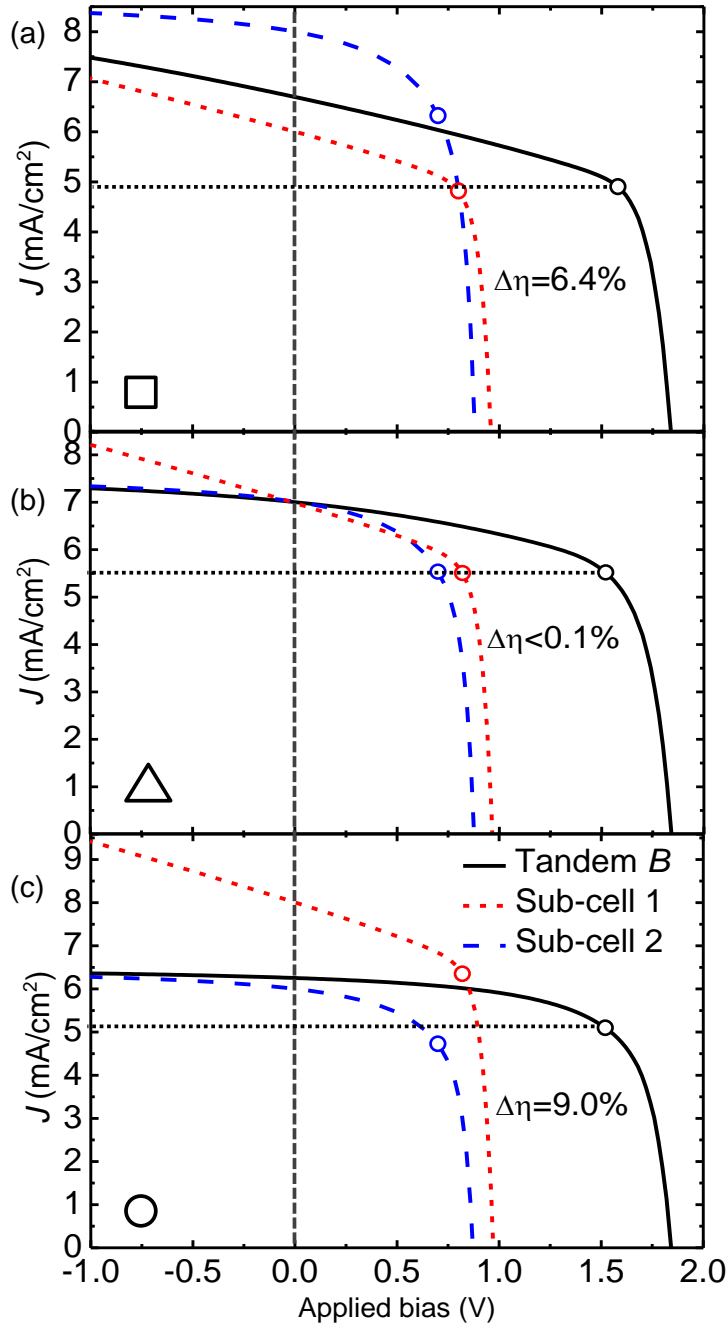
### Sub-cells with dissimilar fill factors

Tandem A is an example of a device that combines Cell a with a high  $FF_1 = 71\%$  as Sub-cell 1, with Cell b as Sub-cell 2 with a low  $FF_2 = 48\%$ . To demonstrate the effect of dissimilar  $FF$ , we simulate the tandem performance while varying  $J_X$  for each sub-cell and obtain contour plots for device performance parameters as functions of both  $J_{SC-1}$  and  $J_{SC-2}$ . Figure 7.4 shows  $J_{SC-T}$ ,  $M_T$ ,  $FF_T$ , and  $\Delta\eta$  calculated for the tandem cells. Now,  $J_{SC-T}$  is limited by  $J_{SC}$  of the individual sub-cells, with  $J_{SC-T}$  increasing along the  $J_{SC-1} = J_{SC-2}$  diagonal in Fig. 7.4(a). In Fig. 7.4(b),  $FF_T$  trends towards that of the sub-cell with the lowest  $J_{SC}$ : i.e. when  $J_{SC-2} \gg J_{SC-1}$ , then  $FF_T \rightarrow FF_1$ , and when  $J_{SC-1} \gg J_{SC-2}$ , then  $FF_T \rightarrow FF_2$ . When the short circuit currents of both sub-cells are equal, then  $FF_T = (FF_1 + FF_2)/2$ . Furthermore,  $M_T$  is a function of both  $J_{SC-T}$  and  $FF_T$ . Since  $M_2 > 1$  and  $M_1 < 1$  for this particular tandem, then  $J_{SC-T}$  increases when  $J_{SC-2} > J_{SC-1}$  and decreases for  $J_{SC-2} < J_{SC-1}$  upon spectral correction. Conversely,  $FF_T$  decreases when  $J_{SC-2} > J_{SC-1}$ , and increases when  $J_{SC-2} < J_{SC-1}$  (Fig. 7.4(b)). In Fig. 7.4(d), we find that  $\Delta\eta$  is minimized when  $J_{SC-2} > J_{SC-1}$ . This can be understood graphically in Fig. 7.5, where  $J$ - $V$  characteristics are shown for three selected conditions, indicated by symbols in Fig. 7.4:  $J_{SC-1} < J_{SC-2}$  (square),  $J_{SC-1} = J_{SC-2}$  (triangle), and  $J_{SC-1} > J_{SC-2}$  (circle). These points correspond to conditions similar to those which have been shown earlier using this particular sub-cell combination. In Fig. 7.5(a),  $J_{SC-1} = 5.3 \text{ mA/cm}^2$  and  $J_{SC-2} = 6.4 \text{ mA/cm}^2$ ; however, each sub-cell characteristic in Fig. 7.5(a) has an MPPT at nearly identical current (shown as circles), leading to  $\Delta\eta < 0.1\%$ . The significant curvature in the slope of the  $J$ - $V$  characteristic for Sub-cell 2 (dashed line), leads to a large difference between  $J_{SC-2}$  and  $J_{M-2}$  compared to Sub-cell 1. Figure 7.5(b) shows the case where  $J_{SC-1}$

$= J_{SC-2} = 6.0 \text{ mA/cm}^2$ , leading to  $\Delta\eta = 2.3\%$  due to the difference in  $J_{M-1}$  and  $J_{M-2}$ . For the case where  $J_{SC-1} = 6.4 \text{ mA/cm}^2$  and  $J_{SC-2} = 5.3 \text{ mA/cm}^2$  (see Fig. 7.5(c)), then  $\Delta\eta = 10\%$ . This significant efficiency penalty can be avoided by adjusting the respective active and spacer layer thicknesses.



**Figure 7.6** Contour plots of simulated device performance characteristics of Tandem *B* using Cell *c* as Sub-cell 1 and Cell *d* as Sub-cell 2. The  $J_{SC}$  of each sub-cell is varied by changing the  $J_X$ . The square, triangle, and circle in the plots denote data points corresponding to example devices used in Fig. 7.7.



**Figure 7.7** The  $J$ - $V$  characteristics of three example Tandem  $B$  (solid line), indicated by symbols in Fig. 7.6, each with the constituent sub-cell characteristics shown by dashed lines. The maximum power point (MPPT) is represented by a circle on each line. The vertical dashed line is at  $V_a = 0$ , and the horizontal dotted line marks the current at which the sub-cells are operating when the tandem is at its MPPT.

### Sub-cells with similar fill factors

Tandem *B*, with Cells *c* and *d* as Sub-cells 1 and 2, respectively, is a case where the sub-cells have comparable *FF*s ( $FF_1 = 66\%$ ,  $FF_2 = 61\%$ ). Figure 7.6 shows  $J_{SC-T}$ ,  $M_T$ ,  $FF_T$ , and  $\Delta\eta$  for the tandem, and Fig. 7.7 shows *J-V* characteristics for selected devices with  $J_{SC-1} < J_{SC-2}$  (square),  $J_{SC-1} = J_{SC-2}$  (triangle), and  $J_{SC-1} > J_{SC-2}$  (circle). These points correspond to conditions similar to those previously discussed with this particular combination of sub-cells. In Fig. 7.6(a), the trend is similar to that of Tandem *A*, where  $J_{SC-T}$  increases along the diagonal corresponding to conditions where the  $J_{SC-1} = J_{SC-2}$ . Interestingly, in Fig. 7.6(b), the trend for  $FF_T$  is reversed compared to that of Fig. 7.4(b), which is due to the shapes of the *J-V* characteristics in Fig. 7.3(b). At zero bias, Cell *c* has a small slope in the reverse *J-V* characteristic in contrast to Cell *d*. Conversely, at the MPPT, Cell *c* has large curvature in the *J-V* characteristic compared to Cell *d*. When combined into Tandem *B*, the slope at zero bias is determined by the sub-cell with the lowest  $J_{SC}$ , while the curvature at the MPPT is determined by that of both sub-cells. Thus, when  $J_{SC-2} = 8.0 \text{ mA/cm}^2$  and  $J_{SC-1} = 6.0 \text{ mA/cm}^2$  in Fig. 7.7(a), the tandem *J-V* characteristic has significant slope at zero bias leading to low *FF*. In Fig. 7.7(c),  $J_{SC-2} = 6.0 \text{ mA/cm}^2$  and  $J_{SC-1} = 8.0 \text{ mA/cm}^2$ , and the slope tends to zero in the tandem *J-V* characteristic at  $V_{OC}$ , leading to a tandem *FF* higher than that of the constituent sub-cells. Now, when  $J_{SC-1} = J_{SC-2} = 7.0 \text{ mA/cm}^2$ , then  $M_T = (M_1 + M_2)/2 = 0.98$  (see Fig. 7.6(c) and Fig. 7.7(b)). In that case,  $FF_T$  varies weakly with both  $J_{SC-1}$  and  $J_{SC-2}$  and, hence,  $M_T$  is solely a function of *M* of the sub-cell with the lowest  $J_{SC}$ . Also,  $\Delta\eta$  is minimized when  $J_{SC-1} = J_{SC-2}$ , as shown in Fig. 7.6(d). This is apparent in Fig. 7.7(b), for  $J_{M-1} \approx J_{M-2}$  and  $J_{SC-1} = J_{SC-2} = 7.0 \text{ mA/cm}^2$ . When  $J_{SC-1} \neq J_{SC-2}$ , as in Fig. 7.7(a) and 7.7(c), then  $\Delta\eta$  is large.

## 7.4 Discussion

We now extend these findings to a tandem cell with  $N$  arbitrary sub-cells to develop general design rules for tandem OPVs. Ideally, to reduce thermalization losses, Sub-cell 1 should absorb the highest energy photons with each subsequent sub-cell absorbing at lower energies.<sup>202,210</sup> In the case of state-of-the-art OPVs, however, the use of fullerenes as an acceptor in nearly all sub-cells leads to absorption of high-energy photons in the small band gap sub-cells even for highly efficient devices. This necessitates a method for the distribution of photons between the sub-cells such that each is optimized to generate the same current at their MPPTs. To minimize  $\Delta\eta$  in this hypothetical optimized cell, this condition is expressed as follows:

$$J_{SC-i}^{opt} = J_{SC}^{total} \left( r_i / \sum_{j=1}^N r_j \right) J_{SC}^{total} = \sum_{i=1}^N \left[ \int \frac{hc}{e\lambda} E_{ref}(\lambda) QE_i(\lambda) d\lambda \right] \quad (7.10)$$

where  $J_{SC-i}^{opt}$  is the optimum  $J_{SC}$  in the  $i$ th sub-cell,  $r_i = J_{SC-i} / J_{M-i}$  (assumed constant),  $h$  is Planck's constant,  $c$  is the speed of light, and  $QE_i(\lambda)$  is the quantum efficiency of the  $i$ th sub-cell at wavelength  $\lambda$ . Note that in the case where  $r_i$  is equal for all sub-cells,  $J_{SC-i}^{opt}$  is also equal in all sub-cells. It is desirable to maximize  $V_{OC-T}$  and  $J_{SC}^{total}$ , which is primarily achieved by selecting sub-cell active materials with the appropriate energy levels and minimally-overlapping optical gaps. Then  $QE_i$  for each sub-cell can be calculated by estimating the absorption and exciton dissociation via the transfer matrix approach,<sup>47</sup> and the thicknesses of the active and spacer layers can be varied to optimize each  $J_{SC-i}$ , ultimately leading to a maximum  $\eta_{P-T}$ .

## 7.5 Conclusions

In this section, we developed a framework to understand tandem OPVs with an arbitrary number of sub-cells. The criteria to minimize the power conversion efficiency penalty,  $\Delta\eta$  (i.e. the loss incurred when one or more sub-cells are not operating at their MPPT when the tandem cell is at its MPPT), is that the current at the maximum power point for each sub-cell must be equal. We also calculate the tandem spectral mismatch factor and fill factor, which are functions of both the  $FF$  and  $J_{SC}$  of all the sub-cells comprising the tandem. Note that while it is desirable to minimize  $\Delta\eta$  for a given combination of materials and sub-cells, this alone does not necessarily lead to the highest tandem power conversion efficiency, which requires the maximization of the product,  $V_{OC-T}J_{SC-T}FF_T$ .

An analytical model is described that accurately represents both bilayer and mixed-layer OPVs used in two archetype tandem cells. This model was used to understand tandem device operation. In the case of tandem cells consisting of sub-cells with dissimilar  $FF$ , the tandem  $FF$  tends towards the sub-cell with lowest  $J_{SC}$ . The tandem spectral mismatch factor is a function of the spectral mismatch,  $J_{SC}$ , and  $FF$  of each sub-cell. Additionally,  $\Delta\eta$  is minimized when the sub-cell with the lowest  $FF$  has the highest  $J_{SC}$ . For the case of tandem cells consisting of sub-cells with similar  $FF$ , the tandem spectral mismatch factor is equal to the average of that of the sub-cells, and  $\Delta\eta$  is minimized when the sub-cells have equal  $J_{SC}$ . We extended these findings to tandem cells with an arbitrary number of sub-cells, where the optimum distribution of the total photocurrent generated in the stack is such that the sub-cell  $J_{SC}$  is proportional to  $J_{SC}/J_M$  (a constant) for each sub-cell. This minimizes  $\Delta\eta$ , leading to a maximum tandem power conversion efficiency for a particular combination of sub-cell architectures and materials combinations.

## 7.6 Future work

Although significant progress has been made over the past ten years in the theoretical modeling of OPVs, there remains significant work to be done. Although the work of Shockley and Queisser<sup>12</sup> detailing the fundamental limits of PV efficiency have recently been adapted for excitonic materials by Giebink et al.,<sup>13</sup> there has still not been a thorough study of the limits of tandem OPV in the manner of Vos.<sup>202</sup> Such an analysis would set an upper limit for tandem OPVs, which is likely to compete with the efficiencies possible with silicon and other inorganic technologies.

# Chapter 8

## **Tandem small molecule organic photovoltaics incorporating solution- and vacuum-processed donor materials**

This chapter details our experimental work with tandem OPVs. We begin with a review of past work in the field, focusing primarily on small molecule-based devices. Next, we report on the design, fabrication, and measurement of three tandem structures consisting of both solution- and vacuum-processed materials. This is followed speculation on the route to further improvements in tandem OPV performance.

### **8.1 Background**

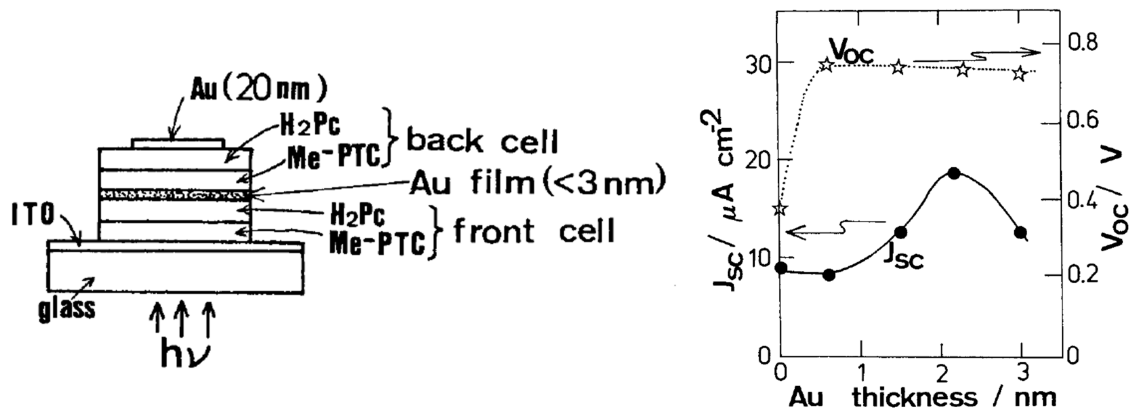
#### **8.1.1 Tandems incorporating phthalocyanines and perylene derivatives**

The first tandem OPV cell was introduced by Hiramoto et al. in 1990.<sup>211</sup> It consisted of two metal-free phthalocyanine/peryene-derivative bilayer heterojunctions in series, as shown



in Fig. 8.1. Although the performance of the tandem device was significantly lower than the single-cell ( $\eta_p \approx 0.5$  and  $0.7\%$ , respectively), the work demonstrated that an ultra-thin metal interlayer between the sub-cells was necessary to achieve a  $V_{OC}$  close to the sum of the sub-cells. Figure 8.1 shows that for no Au layer,  $V_{OC} = 0.40$ , but when  $> 0.5$  nm Au is used, the  $V_{OC}$  increases to  $0.75$  V, which is nearly double that of their single cell.

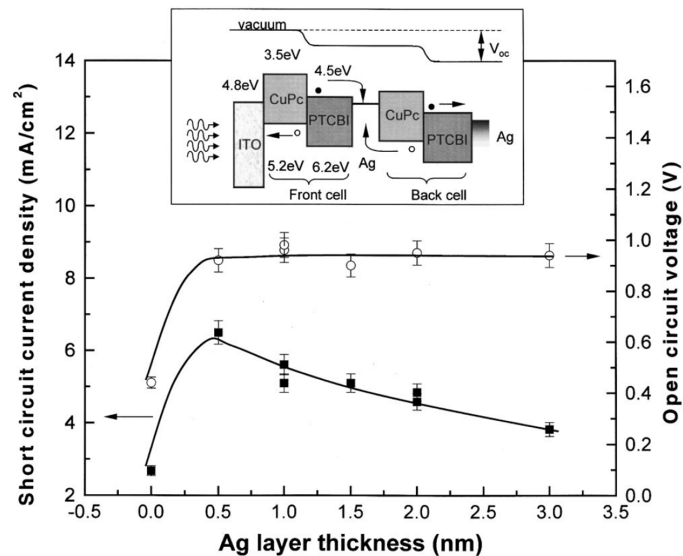
This work was followed in 2002 by Yakimov et al., who incorporated copper phthalocyanine (CuPc)/3,4,9,10 perylenetetracarboxylic bis-benzimidazole (PTCBI) bilayer HJ sub-cells into a tandem architecture.<sup>110</sup> Although similar to the previous work, here the sub-cells were better optimized due to an understanding of the exciton diffusion length in these materials. Figure 8.2 shows the optimization of the Ag interlayer thickness. Yakimov found that only  $0.5$  nm of Ag was required to increase the  $V_{OC}$  to  $0.95$  V, which is double that of a single cell; however, as the Ag thickness is further increased,  $J_{SC}$  drops off significantly due to the absorption and reflection of the Ag layer as it becomes more continuous. Overall, this work demonstrated an increase in  $\eta_p$  from  $1.0\%$  to  $2.5\%$ , which may be the



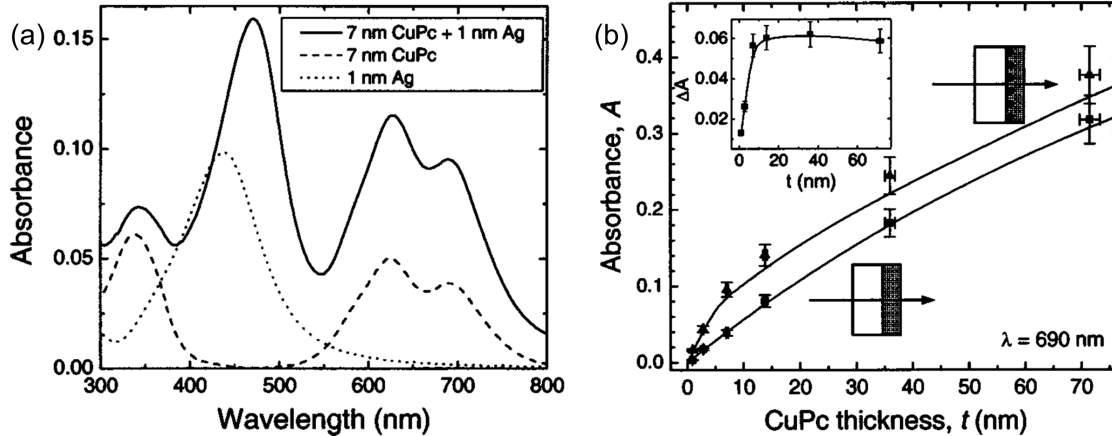
**Figure 8.1** (left) Structure and performance of the first tandem OPV cell. (right) Plot of cell performance vs. Au interlayer thickness. From Ref. 211.

largest improvement seen in a tandem architecture. Additional devices with 3, 4, and 5 sub-cells were also fabricated, although the performance at one sun was lower than for the 2-sub-cell device.

In 2004, Rand et al. examined the optical properties of the Ag interlayer.<sup>207</sup> Electron microscopy images suggested that the Ag was not a continuous layer, but nanoclusters distributed on the surface of the preceding layer. This leads to a surface plasmon effect, enhancing the optical field in the surrounding organic material. Figure 8.3 shows that the absorption in a 1 nm Ag/7 nm CuPc film is significantly greater than the absorption of either layer alone, and that this enhancement extends to 5 nm from the surface of the Ag nanoparticles. Rand's work provides an explanation of how the previous tandem device showed a 150% improvement in  $\eta_p$  by incorporating two sub-cells with the same materials.



**Figure 8.2** Short circuit current density (closed squares, left axis) and open circuit voltage (open circles, right axis) for dual cells having Ag interlayers of different average thicknesses. The measurements were performed under AM 1.5, 100 mW/cm<sup>2</sup>, 1 sun illumination. The inset shows the proposed energy level diagram of the dual-HJ device. From Ref. 110.

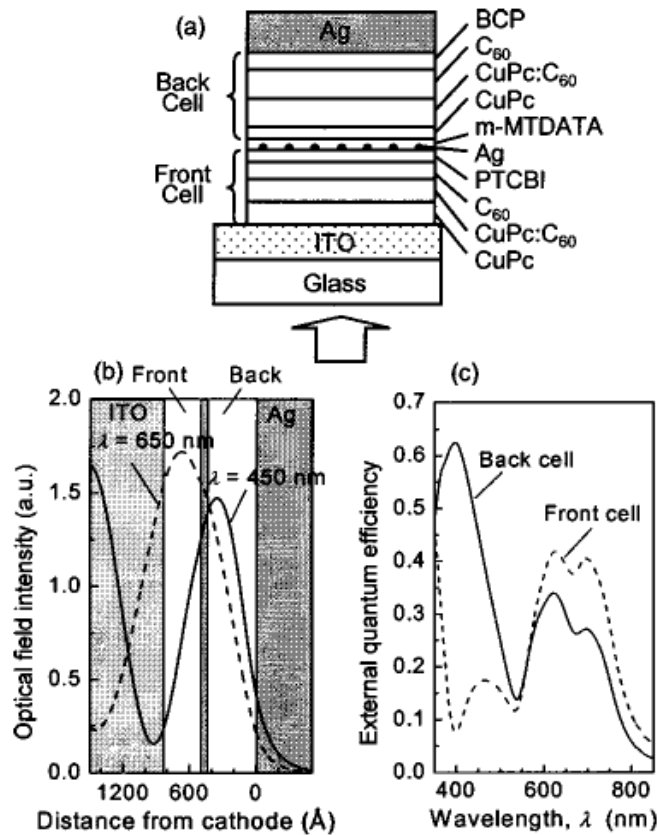


**Figure 8.3** (a) Measured absorbance spectra for 1-nm Ag (dotted curve), 7-nm CuPc (dashed curve), and 7-nm CuPc film on 1-nm Ag (solid curve). All films are deposited on quartz substrates. (b) Measured absorbance  $A$  of varying thicknesses of CuPc on quartz at a wavelength of  $\lambda = 690$  nm with (triangles) and without (squares) a 1-nm Ag cluster layer. Solid curves show fits to the data. Inset: the difference of the absorbance ( $\Delta A$ ) of the CuPc films with and without a Ag layer vs CuPc thickness  $t$ . Solid curve provides a guide to the eye. From Ref. 207

## 8.1.2 Tandems incorporating phthalocyanines and fullerenes

The incorporation of  $C_{60}$  as the acceptor material and BCP as an exciton blocking layer in OPVs led to significant increases in single-cell  $\eta_p$ .<sup>30,96</sup> This was further improved in the CuPc/ $C_{60}$  materials system with the development of the planar-mixed HJ in 2005.<sup>27</sup> This device was subsequently incorporated into a tandem, resulting in a 14% improvement in  $\eta_p$ .<sup>111</sup> As shown in Fig. 8.4, the interlayer consisted of 5 nm PTCBI/0.5 nm Ag/5 nm 4,4',4''-tris(3-methyl-phenyl-phenyl-amino)triphenylamine (*m-M<sub>T</sub>DATA*) p-doped<sup>185</sup> with 5 mol% tetrafluoro-tetracyanoquinodimethane ( $F_4TCNQ$ ). The active layer thicknesses were designed such that the front sub-cell had a thicker CuPc layer and thinner  $C_{60}$  while the back-sub-cell was the opposite, placing the thicker layers in positions to maximize their optical absorption. This design remains one of the commonly used architectures in tandem

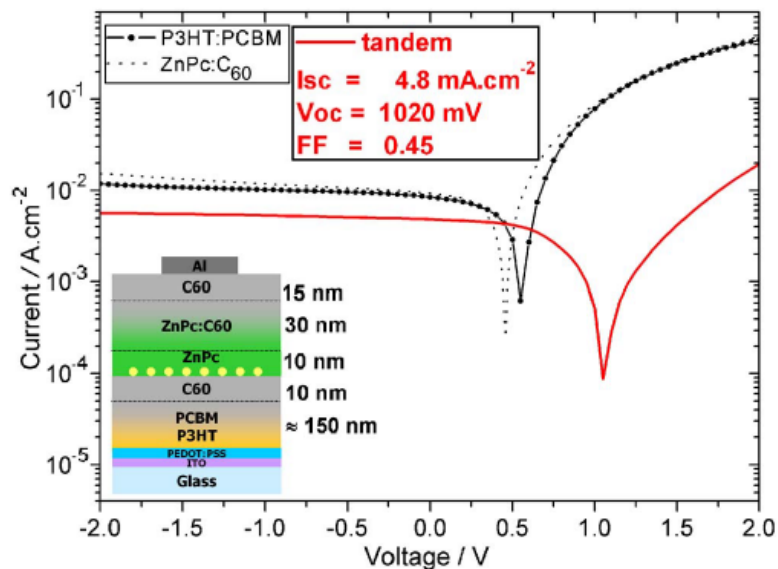
OPV, where the front sub-cell absorbs primarily in the red/infrared, while the back sub-cell absorbs primarily in the blue/green, and all absorption in the active layers occurs within the first optical period.



**Figure 8.4** (a) Structure of an organic tandem PV cell formed by stacking two hybrid PM-HJ cells in series. Each sub-cell (front or back, with respect to the incident light direction as indicated) employs a mixed CuPc:C<sub>60</sub> layer sandwiched between homogeneous CuPc and C<sub>60</sub> layers as the photoactive region, with a PTCBI (front) or BCP (back) layer serving as the EBL. (b) Optical field intensities at  $\lambda = 450$  nm (solid line) and  $\lambda = 650$  nm (dashed line) calculated as functions of the distance from the cathode in an asymmetric organic tandem cell. (c) Calculated external quantum efficiencies for the front (dashed line) and back (solid line) sub-cells of cell B. The asymmetric spectral responses from the two sub-cells result from the placement of the layers within the asymmetric tandem cell structure. From Ref. 111.

The first tandem OPV using more than two different active materials was demonstrated by Dennler et al in 2006,<sup>212</sup> as shown in Fig. 8.5. This work incorporated a solution-processed poly-3-hexylthiophene (P3HT)/[6,6]-phenyl C<sub>61</sub>-butyric acid methyl ester (PCBM) front sub-cell, followed by an evaporated zinc phthalocyanine:C<sub>60</sub> PM-HJ as the back sub-cell. Although the tandem  $V_{OC} = 1.02$  V was equal to the sum of the sub-cell  $V_{OC}$ , the resulting  $\eta_P$  was lower than either single-cell device.

A similar structure shown in Fig. 8.6 was used in 2007 by Janssen et al.<sup>178</sup> which utilized a metal-oxide interlayer. Between their P3HT:PCBM and CuPc:C<sub>60</sub> sub-cells, their interlayer consisted of 0.5 nm LiF/1 nm Al/3 nm WO<sub>3</sub>. The advantage of using a metal oxide in the interlayer is to provide an appropriate work function to the back sub-cell without significant absorption at visible wavelengths. Although the  $J_{SC}$  of their tandem was

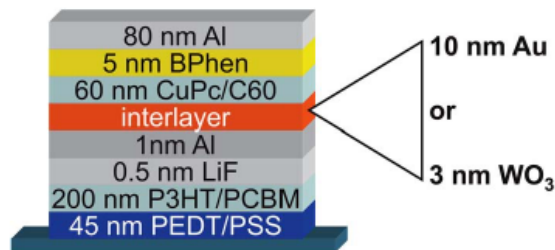


**Figure 8.5** Current vs voltage of (dots) the ZnPc/ZnPc:C<sub>60</sub>/C<sub>60</sub> individual cell, (line plus symbol) the P3HT:PCBM diffused bilayer individual cell, and (full line) the tandem cell. The inset describes the structure of the tandem cell. From Ref. 212.

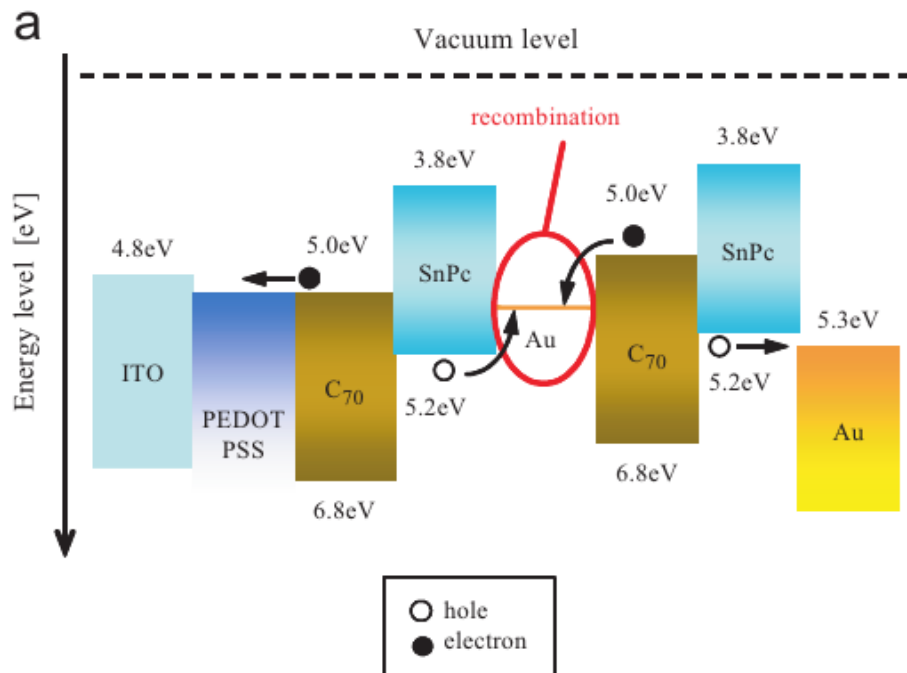
similar to the sub-cells, problems with their interlayer led to a tandem  $V_{OC}$  much less than the sum of the sub-cells, leading to a decrease in  $\eta_p$  compared to the optimized sub-cell. Similar devices using graphene<sup>213</sup> and ZnO<sup>165</sup> as interlayers have also been demonstrated.

The first inverted small molecule tandem OPV was demonstrated in 2007 by Inoue et al.<sup>214</sup> As shown in Fig. 8.7, tin phthalocyanine (SnPc) was used as the donor, C<sub>70</sub> as the acceptor, and 5 nm Au as the interlayer. Though the tandem  $V_{OC}$  and  $\eta_p$  were double the single-cell value, the tandem  $\eta_p$  was only 1.3%.

In 2008, Yu et al. introduced an all-organic tunnel junction as an interlayer.<sup>215</sup> As shown in Fig. 8.8, a heterojunction of tin phthalocyanine dichloride (SnCl<sub>2</sub>Pc)/copper hexadecafluorophthalocyanine (F<sub>16</sub>CuPc) was placed between two ZnPc:C<sub>60</sub> PM-HJs. Here, electrons from the front sub-cell transport from C<sub>60</sub> through the SnCl<sub>2</sub>Pc and F<sub>16</sub>CuPc layers, recombining with holes from the back sub-cell at the F<sub>16</sub>CuPc/ZnPc interface. The resulting tandem cell had a  $V_{OC} = 1.04$  V, which is nearly double that of the single-cell. Overall, they measured a 63% improvement in  $\eta_p$  compared to the optimized single-cell. Other work has since been published using doped organic layers for recombination in the interlayer.<sup>179,216</sup>

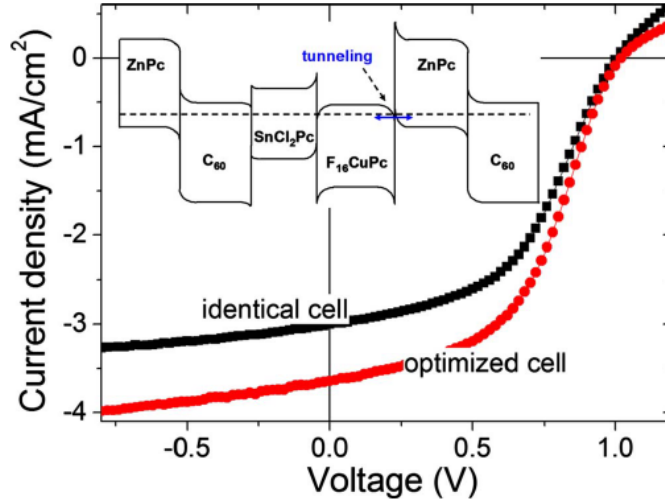


**Figure 8.6** Schematic architectures of the tandem devices with different recombination layers. From Ref. 178.



**Figure 8.7** Energy level diagram of an inverted tandem OPV. From Ref. 214.

In 2010, Cheyns et al. incorporated SubPc and chloroboron subnaphthalocyanine (SubNc) as donor materials in tandem OPVs. As shown in Fig 8.9, when these materials are combined with  $C_{60}$  as an acceptor, photons up to  $\lambda \approx 750$  nm can be harvested. The tandem structure, seen in Fig. 8.10, consisted of SubNc/ $C_{60}$  and SubPc/ $C_{60}$  PHJs, with an interlayer consisting of 5 nm PTCBI/0.1 nm Ag/2 nm  $MoO_3$ . The resulting tandem cell had  $V_{OC} = 1.92$  V, which is nearly identical to the sum of the single-cell values. The tandem device also demonstrated  $\eta_p = 5.2\%$ , a 43% improvement compared to the optimized single-cell device.



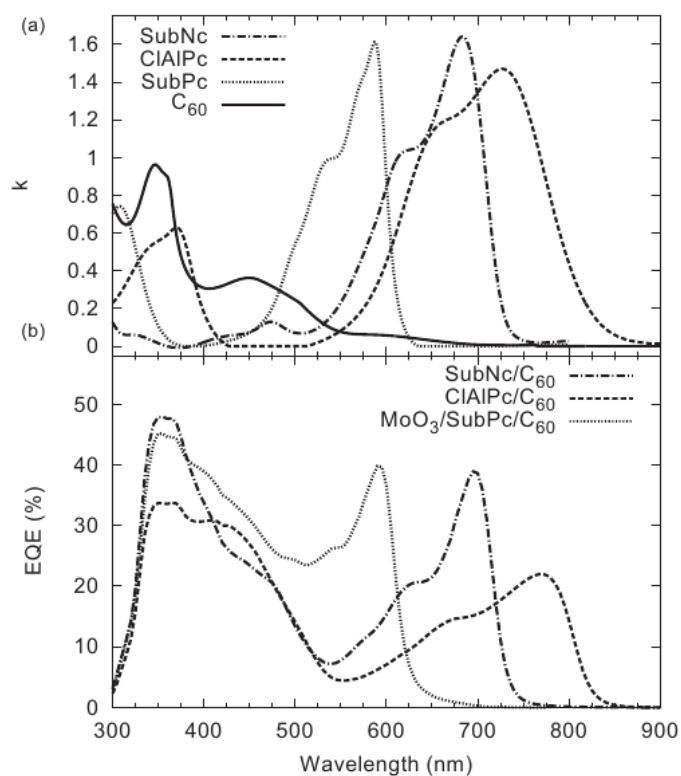
**Figure 8.8** Current density-voltage characteristics of the tandem cells with SnCl<sub>2</sub>Pc/F<sub>16</sub>CuPc layer as connecting units under illumination at 100 mW/cm<sup>2</sup> (AM 1.5G). The film thickness of identical cell was same as the above cell, which was optimized in the optimized cell. The inset exhibits the schematic of the energy level of the tandem cell. From Ref. 215.

### 8.1.3 Tandems incorporating non-phthalocyanine donor materials

Recently, a number of new organic donor materials have been synthesized for use in OPVs. One class is that of merocyanine dyes, which can have very large extinction coefficients in the green.<sup>174,176,218–222</sup> One of these molecules, MD376, was incorporated into a tandem by Steinmann et al. in 2011.<sup>180</sup> Their structure consisted of two MD376:C<sub>60</sub> PMHJ sub-cells separated by an Al/MoO<sub>3</sub> interlayer. Although the tandem  $V_{OC} = 2.07$  V indicates good recombination at the interlayer, the overall tandem  $\eta_p$  was slightly lower than their single cell device (4.7% vs. 5.0%). This is likely due to the fact that the single-cell device has high *EQE* of nearly 70% for  $\lambda$  between 550 and 650 nm, but no absorption for  $\lambda > 700$  nm (Fig. 8.11).

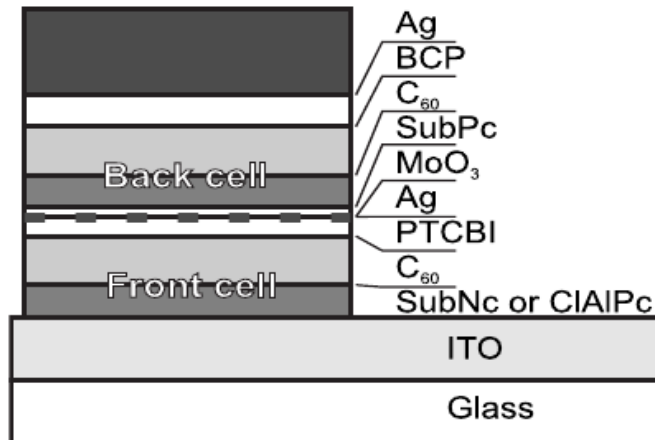
A different approach was taken in 2012 by Zhang et al.<sup>171</sup> Their single-cell device





**Figure 8.9** (a) Extinction coefficient ( $k$ ) of the organic materials used as active layers. (b) Measured EQEs for the reference single cells. From Ref. 217.

consisted of a mixed-HJ incorporating 5% 1,1-bis-(4-bis(4-methyl-phenyl)-amino-phenyl)-cyclohexane (TAPC), which is typically used as an OLED host or transport layer,<sup>223,224</sup> mixed with C<sub>60</sub>. This results in a cell where all of the visible absorption is in C<sub>60</sub>. As seen in Fig. 8.12, their tandem devices consisted of two TAPC:C<sub>60</sub> sub-cells with a 0.3 nm Ag/1.5 nm 1,4,5,8,9,11-hexaazatriphenylene hexacarbonitrile (HAT-CN) interlayer in between. The tandem and 3-fold devices achieved  $\eta_p = 4.1\%$  and  $4.4\%$ , respectively, a 31% and 41% increase compared to a single-cell device (Fig. 8.12). This large improvement is likely due to the fact that C<sub>60</sub> has relatively weak absorption from  $500 < \lambda < 650$  nm. Thus, increasing the total thickness of the active layers via a tandem architecture allows the

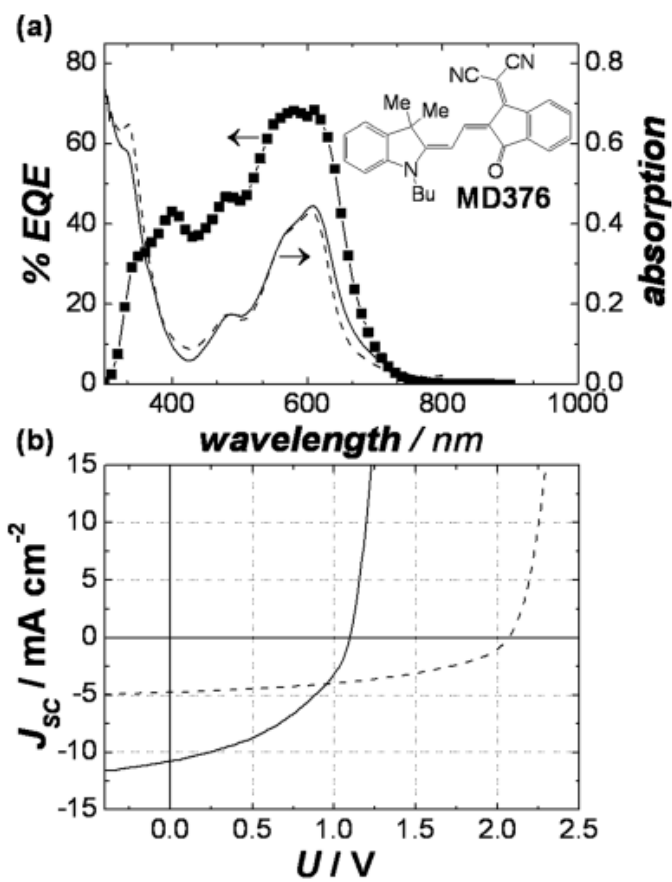


**Figure 8.10** Structure of the tandem configuration utilizing SubPc and SubNc. The front cell consists of a PHJ between SubNc and C<sub>60</sub> or CIAIPc and C<sub>60</sub>, while the back cell consists of a PHJ between SubPc and C<sub>60</sub>. The two cells are connected using a recombination zone of PTCBI, Ag, and MoO<sub>3</sub>. From Ref. 217.

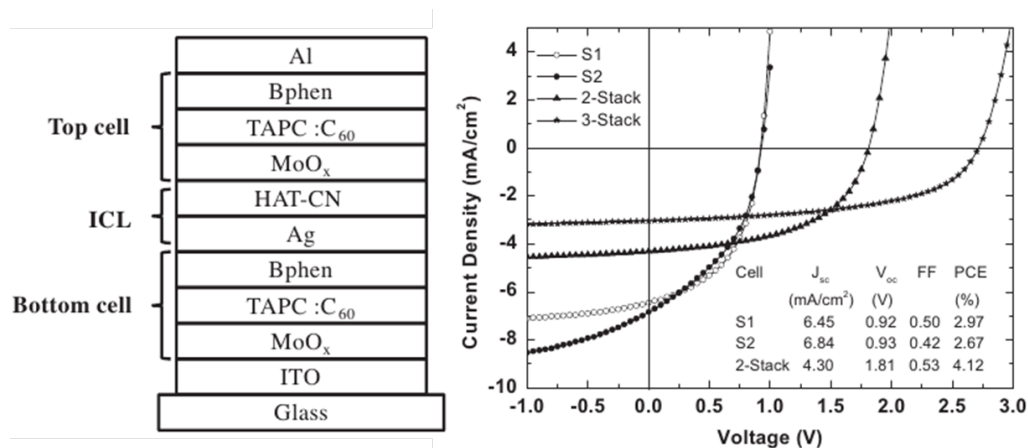
absorption of significantly more visible photons.

### 8.1.4 Tandems incorporating doped, transparent transport layers

While most previously discussed devices place both sub-cells within the first optical period, it is also possible to place one sub-cell in the first optical period and the other sub-cell in the second. This can allow more possibilities for layer thickness variation, as the node of the first optical period is  $\sim 75$  nm from the cathode, which may be greater than the absorption length for many materials. However, to place the front sub-cell at the peak of the second optical period requires a transparent optical spacer thickness of  $\sim 150$  nm. To avoid increases in series resistance in thick organic films, materials are be doped to increase the carrier concentration.<sup>184,185</sup> In their 2010 work, Scheuppel et al. used two ZnPc:C<sub>60</sub> PM-HJs separated by a p-doped N,N'-diphenyl-N,N'-bis(4'-(N,N-bis(naphthyl)-amino)-



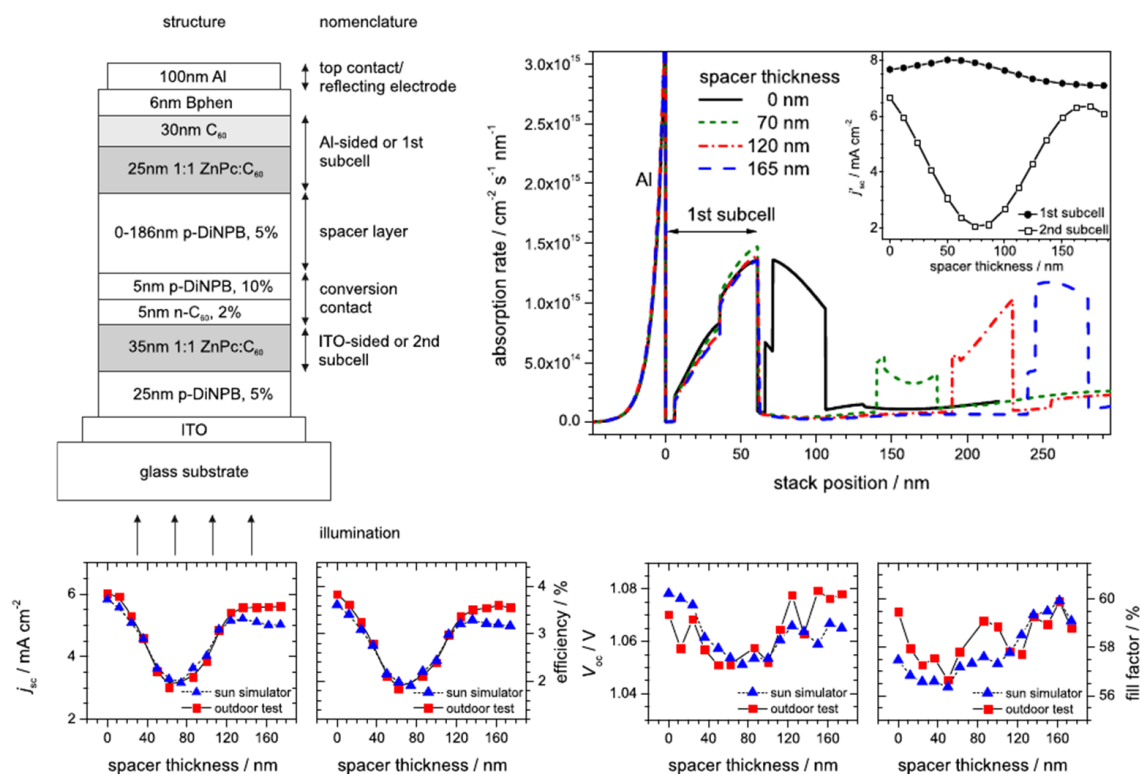
**Figure 8.11** (a) Chemical structure of the merocyanine dye MD376. Absorption (solid line) and *EQE* spectra (symbols) are shown for the MD376 single-cell BJJ solar cell. The dashed line shows the absorption spectrum of the MD376 tandem cell. (b) *J-V* characteristic of best MD376 single cell (solid line) and best tandem cell (dashed line) devices. From Ref. 180.



**Figure 8.12** (left) Schematic layer structure of the 2-stack tandem cell. (right)  $J$ - $V$  characteristics of two single cells, a 2-stack tandem cell, and a 3-stack tandem cell. The inset shows the summary of the cell performance. From Ref. 171.

biphenyl-4-yl)-benzidine (DiNPB) layer in a tandem cell, which is shown in Fig. 8.13.<sup>181</sup> By varying the thickness of the p-DiNPB layer between 0 and 186 nm, they were able to effectively move the front sub-cell from the first period to the second. Modeling of this structure is shown in Fig. 8.13, which matched the experimental data. The optimized tandem devices with the front sub-cell in the first and second period achieved  $\eta_p = 3.8\%$  and  $3.6\%$ , respectively.

Subsequently, the same group incorporated improved active materials into the sub-cells.<sup>225</sup> The front sub-cell consisted of a tetra-fluoro zinc phthalocyanine (F<sub>4</sub>-ZnPc):C<sub>60</sub> PM-HJ, while the back sub-cell consisted of a  $\alpha,\omega$ -bis-(dicyanovinyl)sexithiophene)-Bu(1,2,5,6) (DCV6T):C<sub>60</sub> PM-HJ, which were again separated by a p-DiNPB transport layer. Because F<sub>4</sub>-ZnPc has significantly higher  $V_{OC}$  compared to ZnPc and has complementary absorption with DCV6T, the tandem  $\eta_p = 6.1\%$ , a  $> 40\%$  improvement over the single-cell device (Fig. 8.14). The same materials set was also incorporated into a

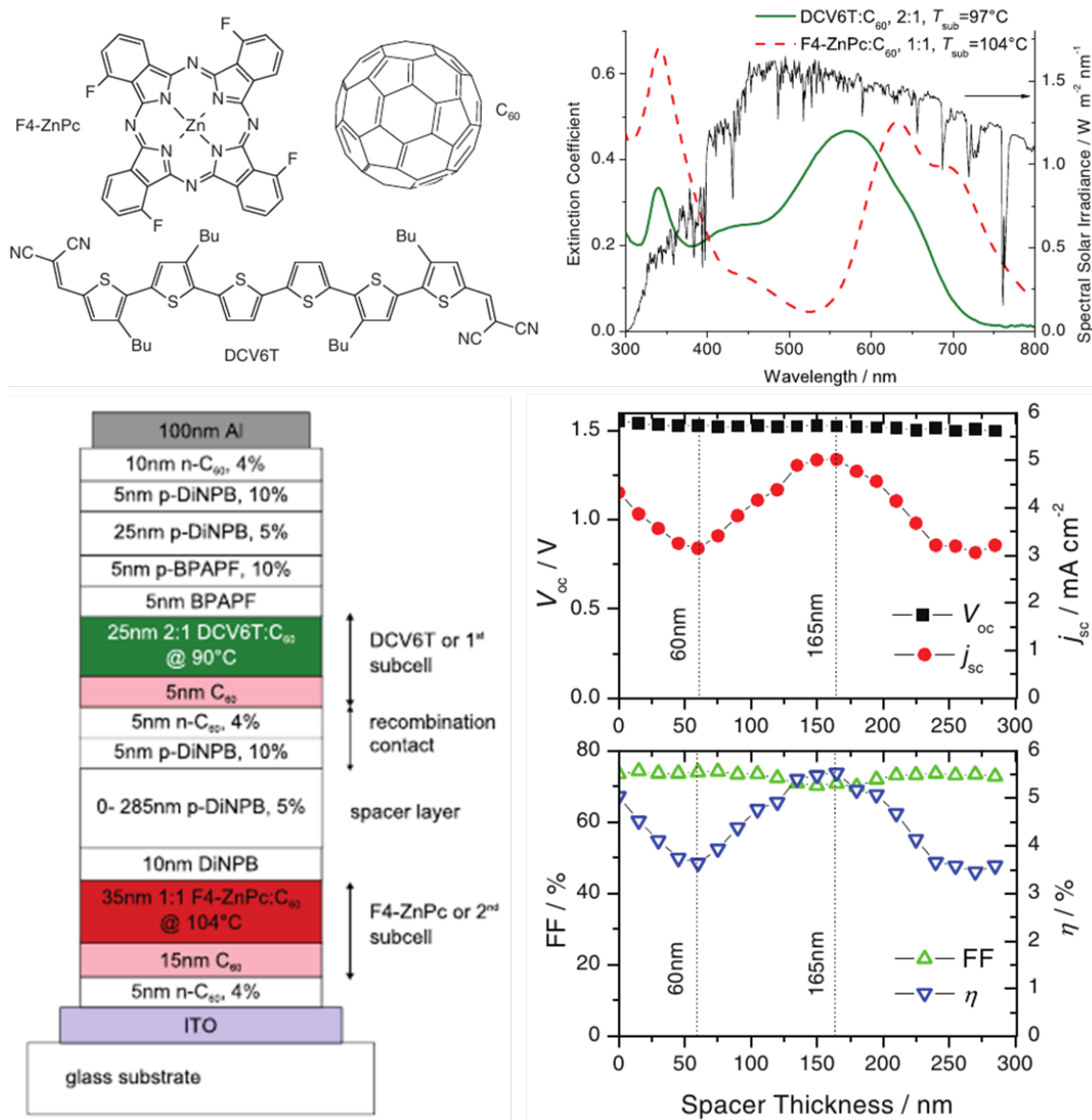


**Figure 8.13** (left) Layer sequence of pin/pii tandem cell including p-doped hole transport layers (p-DiNPB), n-doped electron transport layer (n-C<sub>60</sub>), intrinsic exciton blocking layers (BPhen), and absorbing layers consisting of ZnPc and C<sub>60</sub> (gray). The percentages give the doping ratio by weight. (right) Calculated profile of the number of absorbed photons per unit area, time, and propagation length caused by perpendicular AM1.5g illumination. (bottom) The standard fingerprints  $j_{sc}$ ,  $V_{oc}$ ,  $FF$ ,  $\eta_p$  of the tandem devices as function of the spacer thickness. From Ref. 181.

semitransparent tandem cell which achieved  $\eta_p = 4.9\%$  with a transparency of 24% in the visible.<sup>226</sup>

## 8.2 Modeling tandem current-voltage characteristics

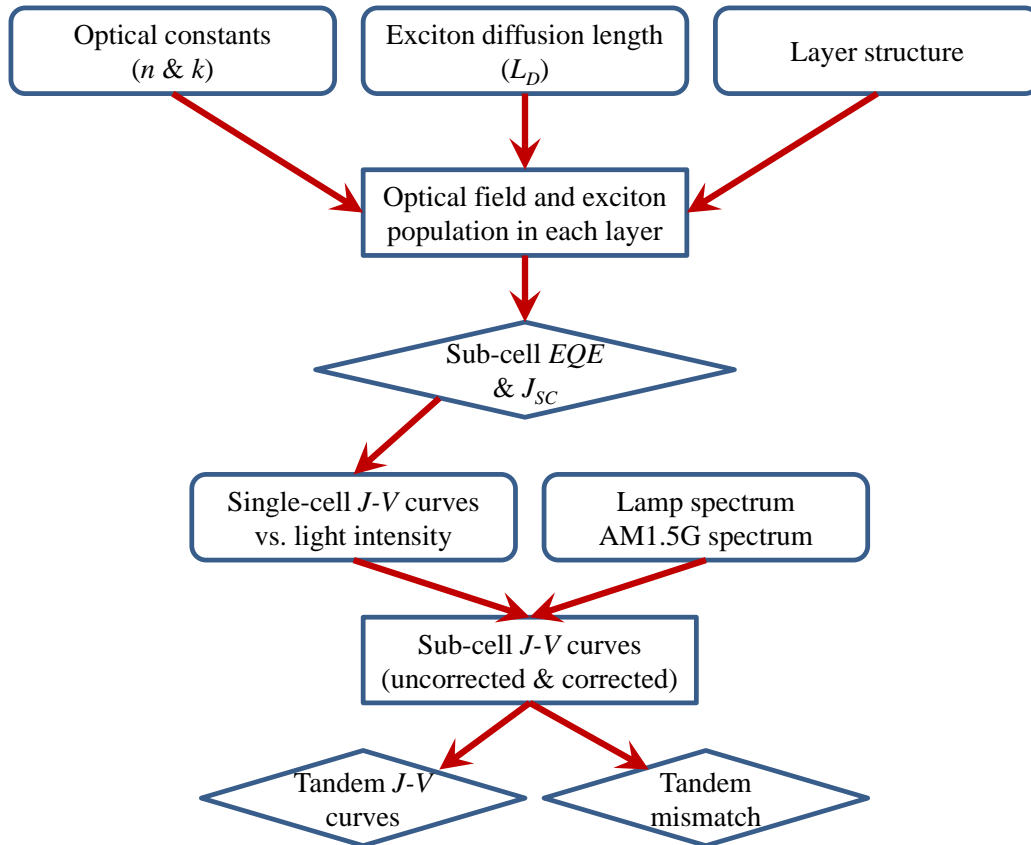
When constructing a tandem cell, the physical requirement that current must be constant throughout the device (i.e. charge conservation) makes it essential to design the layer



**Figure 8.14** (top) Chemical structure of the photovoltaic active molecules tetra-fluoro zinc phthalocyanine (F<sub>4</sub>-ZnPc), α, ω-bis-(dicyanovinyl)sexithiophene-Bu(1,2,5,6) (DCV6T) and C<sub>60</sub> as well as the extinction coefficients in mixed layers. The thin black line shows the spectral solar irradiance of the AM1.5g spectrum. (left) Stack structures of the investigated single and tandem heterojunction devices based on the p-i-n concept. The photovoltaic active regions are highlighted and consist of a pristine layer of C<sub>60</sub> and a mixed heterojunction using either F<sub>4</sub>-ZnPc or DCV6T as electron donor for C<sub>60</sub> with mixing ratios given for volume. The percentages in the doped layers give the doping ratio by weight. (right) Variation of the current-voltage parameters versus spacer thickness in the tandem stack. The vertical dashed lines indicate 60 nm and 165 nm spacer thickness. From Ref. 225.

structure to maximize  $\eta_p$ . This necessitates a model to predict the  $J_{SC}$  of the sub-cells as they operate in the tandem,<sup>111,203–205</sup> along with the sub-cell  $J$ - $V$  characteristics. Here we present a method to fully predict the  $J$ - $V$  characteristics of a tandem device and its constituent sub-cells based on measured parameters.

The process flow diagram is shown in Fig. 8.15. First, the optical constants ( $n$  and  $k$ ) for all materials are measured by spectroscopic variable-angle ellipsometry, and the exciton diffusion length ( $L_D$ ) is measured for each active-layer material.<sup>48</sup> The tandem



**Figure 8.15** Process flow for the modeling of tandem OPVs. Rounded boxes represent experimental measurements, square boxes represent computations, and parallelograms represent output parameters.

layer structure is input into a transfer matrix model that is used to calculate the optical field distribution in each layer, along with exciton generation and population in the active layers. (see Chapter 2.8).<sup>47</sup> From this, the  $J_{SC}$  for each sub-cell is calculated. Next,  $J$ - $V$  characteristics for single-cell devices are measured as a function of light intensity. The sub-cell  $J$ - $V$  characteristics are then interpolated from the single cell characteristics using the modeled sub-cell  $J_{SC}$ .<sup>†</sup> Finally, the tandem  $J$ - $V$  characteristic is calculated by adding the voltages of the sub-cells at each current value, satisfying the criterion that the current must be equal among the series-connected sub-cells.<sup>112</sup> Consequently, the  $J_{SC}$ ,  $FF$ , and  $V_{OC}$  are calculated for a variety of layer structures, and the optimal structure is determined for the device whose layer thicknesses result in a maximum  $\eta_p$  of the tandem OPV. The spectral mismatch factor ( $M$ ) for the tandem cell is calculated by taking the ratio of  $\eta_p$  calculated using the lamp spectrum and  $\eta_p$  using the solar spectra as illumination sources. Note that a change in spectrum can result in a change in charge balance between the sub-cells, requiring the correction of both  $FF$  and  $J_{SC}$  when determining  $M$ , as will be discussed in more detail below. To optimize  $\eta_p$  for the tandem cell, the thicknesses are varied until a maximum is reached.<sup>‡</sup>

---

<sup>†</sup>This assumes that the sub-cells in the tandem behave similarly to a single-cell at a reduced light intensity.

<sup>‡</sup>This assumes that the sub-cell operation is similar to that of the single cell devices. In some cases, increasing or decreasing layer thicknesses past their practical limits can result in degraded performance due to high resistance or other pathologies.



## 8.3 Tandem organic photovoltaics incorporating SubPc and DPSQ as donor materials

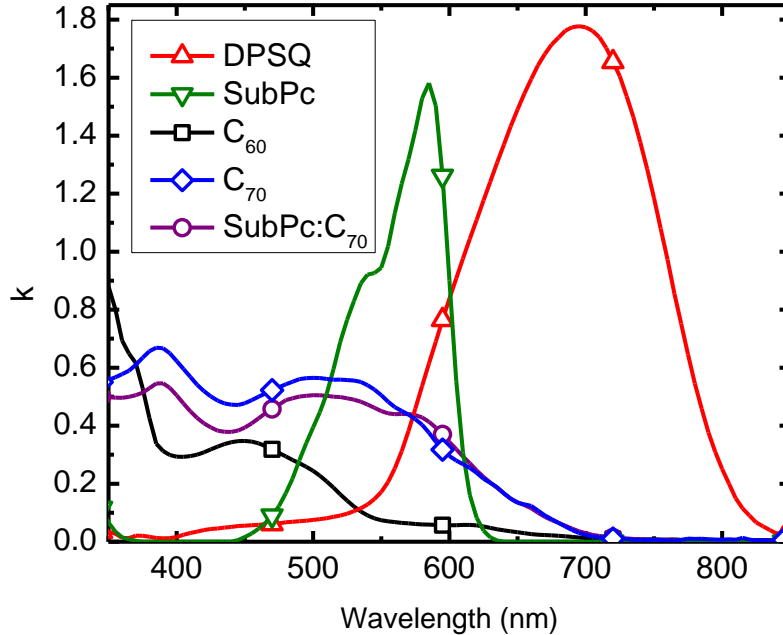
We incorporate a SubPc:C<sub>70</sub> graded HJ<sup>227</sup> for the blue and green absorbing sub-cell, and a solution-deposited and solvent-vapor-annealed (SVA) 2,4-bis[4-(N,N-diphenylamino)-2,6-dihydroxyphenyl] squaraine<sup>193</sup> (DPSQ)/C<sub>70</sub> bilayer HJ for absorption into the near infrared (NIR). Here, SVA produces a nanocrystalline morphology that results in an increased photocurrent.<sup>190,194</sup> By stacking these two sub-cells, light is harvested between wavelengths of  $\lambda = 350$  nm and 800 nm, resulting in  $\eta_p = 6.6 \pm 0.1\%$ . The tandem  $V_{OC}$  is equal to the sum of the  $V_{OC}$ s of the constituent sub-cells, indicating that the transparent, compound Ag/MoO<sub>3</sub> charge recombination layer interposed between the cells is nearly lossless.

### 8.3.1 Experiment

Devices were grown on 100 nm thick layers of indium tin oxide (ITO) with a sheet resistance of 15  $\Omega/\square$  pre-coated onto glass substrates. Prior to deposition, the ITO surface was cleaned in a surfactant and a series of solvents,<sup>28</sup> and then exposed to ultraviolet-ozone for 10 min prior to loading into a high vacuum chamber (base pressure  $< 10^{-7}$  Torr) where MoO<sub>3</sub><sup>195</sup> was deposited by vacuum thermal evaporation (VTE) at 1 nm/s. Substrates were transferred into a high-purity N<sub>2</sub>-filled glovebox, where 13 nm thick DPSQ films were spin-coated at 3000 rpm from 20 nm alumina-filtered, 1.6 mg/ml solutions in chloroform. Substrates were returned to the high vacuum chamber without exposure to air for deposition of train-sublimation-purified<sup>152</sup> C<sub>70</sub> and a 3,4,9,10 perylenetetracarboxylic bisbenzimidazole (PTCBI) exciton blocking and electron transporting layer<sup>228</sup> at a rate of 0.1 nm/s.

This was followed by transfer back into the glovebox for SVA, consisting of exposure to a saturated dichloromethane vapor for 10 min to create the desired nanocrystalline film morphology.<sup>190,194</sup> For more details on *f*SQs and SVA, see Section 6.1.2. Next, the transparent, compound charge recombination layer consisting of a dense Ag nanoparticle layer (average thickness of 0.1 nm)<sup>110,207</sup> and a 5 nm thick film of MoO<sub>3</sub> was deposited by VTE. For the back sub-cell (i.e. that closest to the cathode), a mixed film of SubPc and C<sub>70</sub> was co-evaporated, where the rate of SubPc deposition was 0.012 nm/s and that of C<sub>70</sub> was varied from 0.02 to 0.08 nm/s, thereby forming a graded heterojunction.<sup>227</sup> After deposition of the bathocuproine (BCP) exciton blocking layer<sup>30</sup> at 0.1 nm/s, a 100 nm-thick Ag cathode was deposited at 0.1 nm/s through a shadow mask with an array of 1 mm diameter openings. Layer thicknesses and optical constants were measured with quartz crystal monitors and calibrated by variable-angle spectroscopic ellipsometry, the latter shown in Fig. reffig:tandem1.

Current density-vs.-voltage (*J-V*) characteristics were measured in an ultra-pure N<sub>2</sub> ambient in the dark and under simulated AM1.5G solar illumination from a filtered 300 W Xe lamp whose intensity was varied using neutral density filters. The incident light intensity was measured using an NREL-traceable Si detector.<sup>37</sup> Short-circuit currents ( $J_{SC}$ ) of single-cell reference devices deposited concurrently with the tandem were corrected for spectral mismatch.<sup>38</sup> Spectrally resolved external quantum efficiencies (*EQE*) were measured using monochromated light from a 150 W Xe source using output optics that focused the beam to under-fill the device area. Integration of the *EQE* convoluted with the solar spectrum resulted in values within  $\pm 10\%$  of the corrected  $J_{SC}$  for the sub-cells as well as the tandem device. Input intensity was calibrated with a NIST-traceable Si detector.



**Figure 8.16** Extinction coefficients ( $k$ ) for the active materials used in the organic photovoltaic cells, as measured via spectroscopic ellipsometry.

Errors quoted correspond to the deviation from the average value of three or more devices on the same substrate.

### 8.3.2 Single-cell results

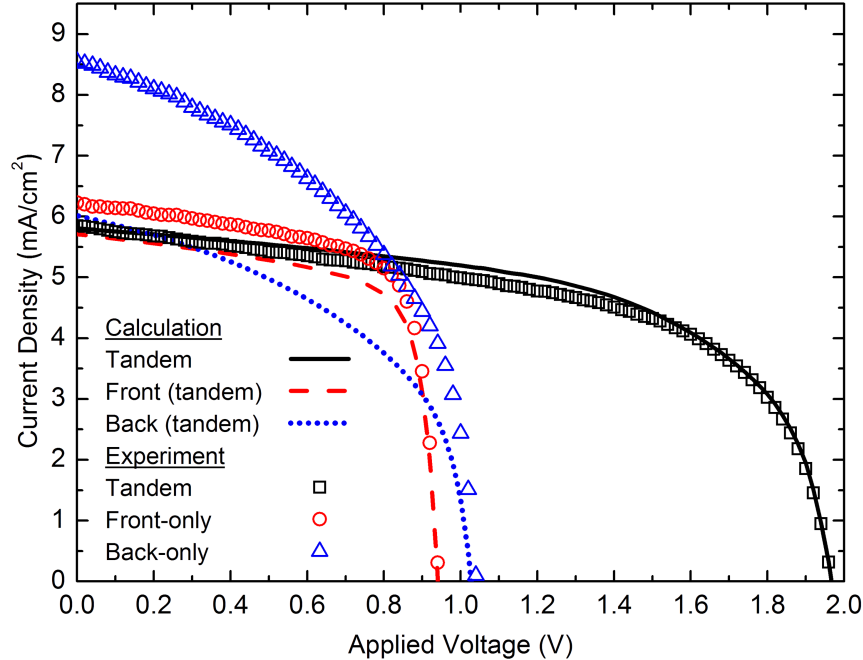
For the front-only device (i.e. the structure that ultimately is positioned next to the anode), the optimized bilayer double HJ has the following structure: glass substrate/100 nm ITO/20 nm MoO<sub>3</sub>/13 nm DPSQ/10 nm C<sub>70</sub>/5 nm PTCBI/0.1 nm Ag/30 nm MoO<sub>3</sub>/100 nm Ag. The 20 nm thick MoO<sub>3</sub> determines the work function of the anode.<sup>82,195</sup> The 30 nm thick MoO<sub>3</sub> layer is used as an electron transport layer and spacer to create a similar optical field to that in the tandem device. The device has a front-cell open circuit voltage of  $V_{OCF}$

$= 0.94 \pm 0.01$  V,  $FF = 71 \pm 1\%$ ,  $J_{SC} = 6.1 \pm 0.1$  mA/cm $^2$ ,  $\eta_p = 4.1 \pm 0.1\%$  and  $M = 0.94 \pm 0.01$ , as shown in Table 8.1 and Fig. 8.17 (circles). From the *EQE* spectrum, we calculate  $L_D = 5.9 \pm 0.2$  and  $6.9 \pm 0.3$  nm for DPSQ and C $_{70}$ , respectively. The SVA process significantly increases the exciton diffusion length of DPSQ due to the formation of a nanocrystalline morphology. Indeed, as-cast amorphous films of this material have a short diffusion length of only  $L_D = 3.4 \pm 0.7$  nm.<sup>193</sup> After SVA, we observe an approximate doubling of  $L_D$  accompanied by a 50% increase in *EQE* in the NIR. We also found that the exciton diffusion length in C $_{70}$  is shorter than for C $_{60}$ , the latter of which is between 20 nm and 40 nm,<sup>23,163</sup> presumably due to the lower symmetry and hence less dense packing of C $_{70}$ . Note that the value of  $L_D$  inferred from analysis of the *EQE* is similar to that obtained by spectrally resolved photoluminescence quenching,<sup>229</sup> which yields  $L_D = 8.0 \pm 0.8$  nm. Although the short diffusion length limits the optimized single-cell efficiency compared to previously reported DPSQ/C $_{60}$  OPVs,<sup>193</sup> utilizing C $_{70}$  significantly increases the green absorption in the front sub-cell compared to that of C $_{60}$  when using a 10 nm thick layer, leading to an overall 30% increase in  $J_{SC}$ .

We also fabricated an optimized back-only cell with the structure: glass sub-

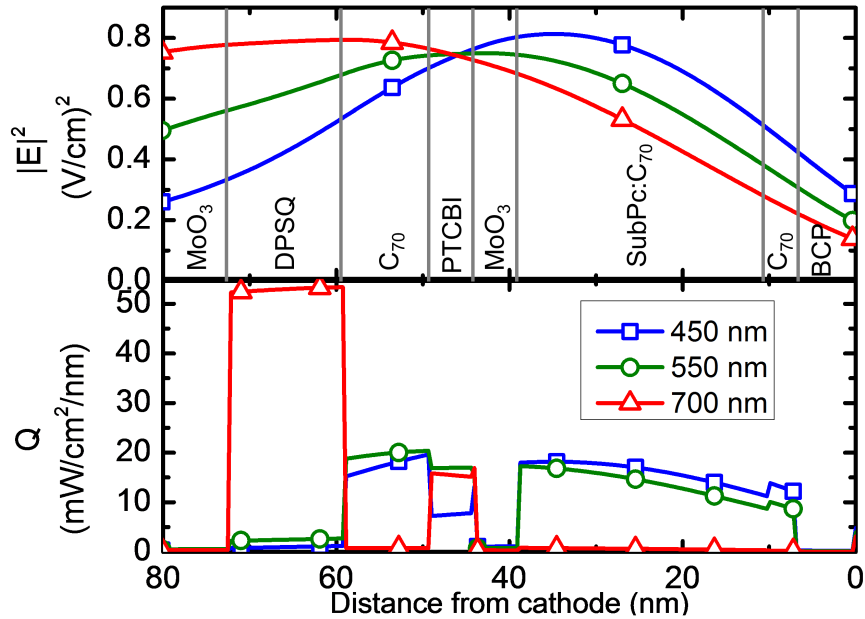
**Table 8.1** Organic photovoltaic performance under simulated 1 sun AM1.5G illumination, corrected for spectral mismatch.

Device	Data source	$V_{oc}$ (V)	$FF$ (%)	$J_{sc}$ (mA/cm $^2$ )	$\eta_p$ (%)	$M$
Back-only	Experiment	$1.04 \pm 0.01$	$48 \pm 1$	$8.5 \pm 0.1$	$4.3 \pm 0.1$	$1.04 \pm 0.01$
Back sub-cell	Calculation	1.03	49	6.0	3.0	1.03
Front-only	Experiment	$0.94 \pm 0.01$	$71 \pm 1$	$6.1 \pm 0.1$	$4.1 \pm 0.1$	$0.94 \pm 0.01$
Front sub-cell	Calculation	0.94	71	5.7	3.8	0.90
Tandem	Experiment	$1.97 \pm 0.01$	$54 \pm 1$	$6.2 \pm 0.1$	$6.6 \pm 0.3$	$0.98 \pm 0.01$
Tandem	Calculation	1.97	58	5.8	6.6	0.98



**Figure 8.17** Experimental current density vs. voltage characteristics in the 4th quadrant under 1 sun, simulated AM1.5G illumination for front-only (circle), back-only (triangle), and tandem (square) organic photovoltaic cells, along with calculated characteristics for the front sub-cell (dashed), back sub-cell (dotted), and tandem (solid) cell under similar illumination conditions.

strate/100 nm ITO/5 nm MoO<sub>3</sub>/29 nm SubPc:C<sub>70</sub>/3 nm C<sub>70</sub>/7 nm BCP/100 nm Ag. The active layer consists of a graded heterojunction,<sup>227</sup> where the SubPc volume fraction varies from 38% to 13% throughout the layer. Figure 8.17 (triangles) shows the  $J$ - $V$  characteristics for the back-only cell, with open circuit voltage  $V_{OCB} = 1.04 \pm 0.01$  V,  $FF = 48 \pm 1\%$ ,  $J_{SC} = 8.5 \pm 0.1$  mA/cm<sup>2</sup>,  $\eta_p = 4.3 \pm 0.1\%$ , and  $M = 1.04 \pm 0.01$ . The use of C<sub>70</sub> in place of C<sub>60</sub> increases  $J_{SC}$  by 40% due to the additional absorption in the green.<sup>230</sup>



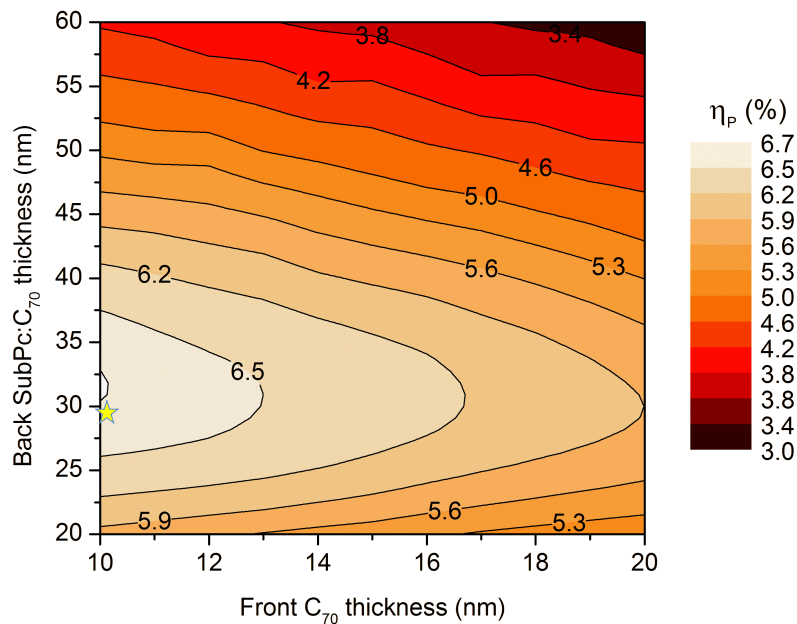
**Figure 8.18** Calculated optical-electric field strength ( $|E|_2$ ) and absorbed spectral power ( $Q_j$ ) for a modeled tandem OPV cell.

### 8.3.3 Tandem results

Based on the single-cell device characteristics, the optimal tandem layer structure was found using the transfer-matrix model via a genetic algorithm for rapid calculational convergence. In these calculations, the blocking and transport layers (i.e. MoO<sub>3</sub>, PTCBI, BCP) and the front-cell C<sub>70</sub> were experimentally determined to have minimum practical thicknesses required to maintain a high  $FF$  and  $V_{OC}$ . Further, the DPSQ and back-cell C<sub>70</sub> layers are found to have optimal thicknesses of 13 and 3 nm, respectively. The optical-electric field strength ( $|E|_2$ ) and absorbed spectral power ( $Q_j$ ) for this device are shown in Fig. 8.18, where it can be seen that the layer order is designed to place each material in its absorption maximum. A contour plot of the dependence of  $\eta_p$  on the thicknesses of the remaining active layers (front C<sub>70</sub> and SubPc:C<sub>70</sub>) is shown in Fig 8.19, with peak tandem cell effi-

ciencies for 10 nm thick front and 30 nm thick back SubPc:C<sub>70</sub> (see Fig. 8.17) layers. The *J-V* characteristics of the discrete devices comprising the tandem based on the measured results, are then calculated when placed as sub-cells in the stack (see dotted and dashed lines in Fig. 8.17). Finally, the *J-V* characteristic of the full tandem structure are calculated, and is shown by the solid line in Fig. 8.17.

We fabricated the following tandem device based on the optimized thicknesses: glass substrate/100 nm ITO/20 nm MoO<sub>3</sub>/13 nm DPSQ/10 nm C<sub>70</sub>/5 nm PTCBI/0.1 nm Ag/5 nm MoO<sub>3</sub>/29 nm SubPc:C<sub>70</sub>/3 nm C<sub>70</sub>/7 nm BCP/100 nm Ag. The equilibrium energy level diagram of the device illustrating the layer structure is shown in of Fig. 8.20.<sup>74,82,193,228,230</sup>



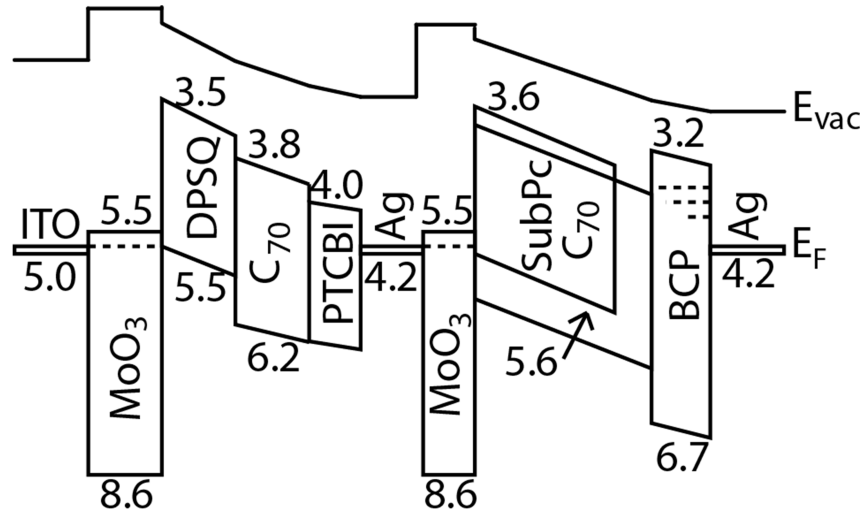
**Figure 8.19** Calculated contour plot of the power conversion efficiency ( $\eta_p$ ) of a tandem device as a function of the back-cell SubPc:C<sub>70</sub> thickness (left axis) and front-cell C<sub>70</sub> thickness (bottom axis). The star represents coordinates of the fabricated device, in close agreement with the measured device performance.

In the front sub-cell, excitons are dissociated into free carriers at the DPSQ/C<sub>70</sub> interface. Holes are transported to the MoO<sub>3</sub>/DPSQ interface, where they recombine with electrons injected from the ITO anode, while electrons are transported through the PTCBI and MoO<sub>3</sub> layers. In the back sub-cell, excitons are dissociated throughout the mixed layer. Electrons are transported to the C<sub>70</sub>/BCP interface, where transport to the Ag cathode occurs via defect states introduced into the BCP during cathode deposition<sup>82</sup> (shown by the array of dashes in BCP in the inset), while holes are transported to the MoO<sub>3</sub>/SubPc interface, where they recombine with electrons generated in the front sub-cell. Here, Ag primarily serves to pin the Fermi levels of PTCBI and MoO<sub>3</sub>, thereby resulting in their alignment. This facilitates electron conduction from the front cell to the MoO<sub>3</sub>/SubPc interface where they recombine with holes. Omitting the Ag nanoparticles results in a 25% reduction in  $V_{OC}$ , attributable to Fermi level splitting at the PTCBI/MoO<sub>3</sub> interface. Figure 8.17 shows the measured  $J$ - $V$  characteristics (squares), with  $V_{OC} = 1.97 \pm 0.01$  V,  $FF = 54 \pm 1\%$ ,  $J_{SC} = 6.2 \pm 0.1$  mA/cm<sup>2</sup>,  $\eta_p = 6.6 \pm 0.1\%$ , and  $M = 0.98$ , as summarized in Table 8.1. The experimental and calculated tandem characteristics agree under forward bias, from which we can infer the accuracy of our models.

### 8.3.4 Discussion

Now  $V_{OC} = V_{OCF} + V_{OCB} = 1.97 \pm 0.01$  V, which indicates that the internal charge recombination process is nearly lossless. However, there is a discrepancy between the slopes of the experimental and calculated currents of the individual sub-cells in Fig. 8.17 near zero bias, which is likely due to contributions from photoconductivity arising from exciton dissociation within the layer bulks,<sup>198,199</sup> which is not considered in the model.





**Figure 8.20** Equilibrium energy level diagram of the tandem device. Here,  $E_{vac}$  is the vacuum and  $E_F$  the Fermi energy levels. The array of dashes in the BCP layer indicates defect states induced during cathode deposition that transport electrons from the cathode to the  $C_{70}$  acceptor.

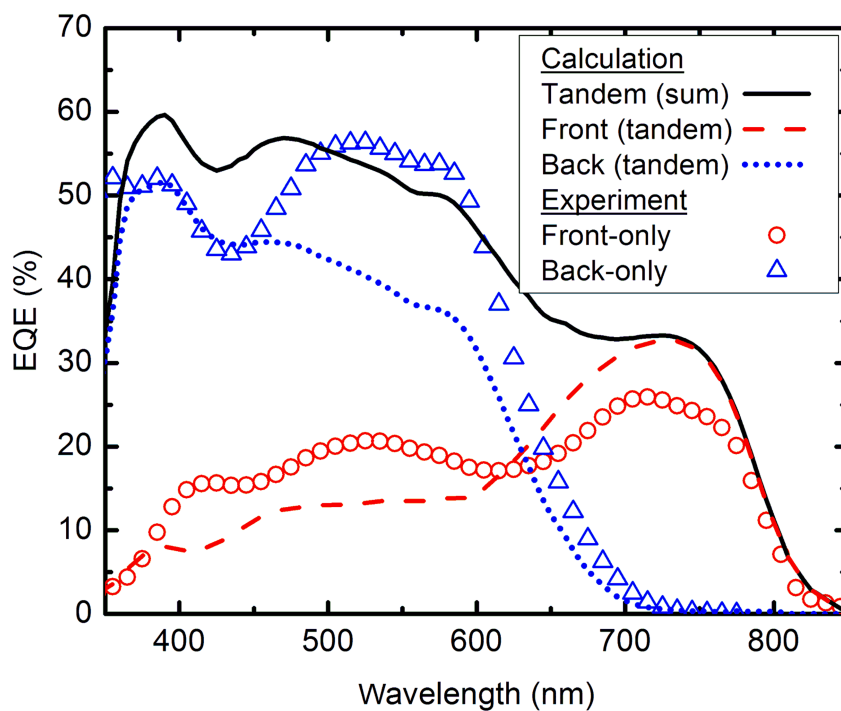
The spectral mismatch factor,  $M$ , calculated for the front and back sub-cells are 0.90 and 1.03, respectively, resulting in a net increase in  $J_{SC}$  for the tandem device. The change in current balance, however, also affects  $FF$ , leading to  $M = 0.98$  for the tandem device. The calculation of  $M$  for tandem OPVs will be discussed later in this chapter.

The experimental and calculated  $EQE$  spectra are shown in Fig 8.21. The DPSQ/ $C_{70}$  device is photosensitive into the NIR, with a cut-off at approximately  $\lambda = 800$  nm, while the SubPc: $C_{70}$  sub-cell has  $EQE > 50\%$  for  $\lambda < 600$  nm. The  $EQE$  in the blue-green spectral region is decreased in the tandem compared with that of the constituent sub-cells since both the DPSQ/ $C_{70}$  and SubPc: $C_{70}$  sub-cells absorb in the green. Nevertheless, the sum of the  $EQE$  of the modeled sub-cells exceeds 50% at  $\lambda < 600$  nm, and is at least 35% up to  $\lambda = 750$  nm, indicating that efficient photon harvesting is occurring across the visible and into the NIR. Interestingly, the active layer thicknesses are the same for both optimized discrete

devices, as well as for the sub-cells in the tandem, which to our knowledge is unique for a tandem OPV.

### 8.3.5 Conclusions

In summary, we have demonstrated a tandem OPV consisting of vapor-deposited SubPc:C<sub>70</sub> graded heterojunction and solution-processed SVA-DPSQ/C<sub>70</sub> bilayer heterojunction sub-cells that efficiently harvests photons up to wavelengths of  $\lambda = 800$  nm. The incorporation of C<sub>70</sub> in both sub-cells in the place of the archetypal C<sub>60</sub> leads to higher absorption across the green and yellow spectral regions, increasing  $J_{SC}$  by > 30%. The resulting tandem



**Figure 8.21** Experimental external quantum efficiency ( $EQE$ ) spectra for front-only (circle) and back-only (triangle) organic photovoltaic cells, along with calculated spectra for front sub-cell (dashed), back sub-cell (dotted), and the sum of the two sub-cells (solid).

device demonstrated  $\eta_p = 6.6 \pm 0.1\%$ , with  $V_{OC} = 1.97 \pm 0.1$ , indicating a nearly lossless Ag nanoparticle/MoO<sub>3</sub> charge recombination layer interposed between the sub-cells.

## 8.4 Tandem organic photovoltaics incorporating DBP and blended squaraines as donor materials

Here, we demonstrate a high efficiency small molecular weight tandem cell consisting of one partially solution-processed, and one entirely vapor-deposited sub-cell. Specifically, in one sub-cell, we employ a blend of the solution processed near infrared absorbing diphenyl squaraine, DPSQ blended with its green absorbing asymmetric analogy, [2-[4-(N,N-diphenylamino)-2,6-dihydroxyphenyl]-4-[4-diphenyliminio] squaraine] (DPASQ), combined with the fullerene acceptor, C<sub>70</sub>. This is combined with a broadly visible absorbing sub-cell based on a mixture of tetraphenyldibenzoperiflanthene (DBP):C<sub>70</sub>.<sup>209,231–237</sup> The resulting tandem cell efficiently harvest photons of  $\lambda < 800$  nm, resulting in  $\eta_p = 7.8 \pm 0.4\%$ .

### 8.4.1 Experiment

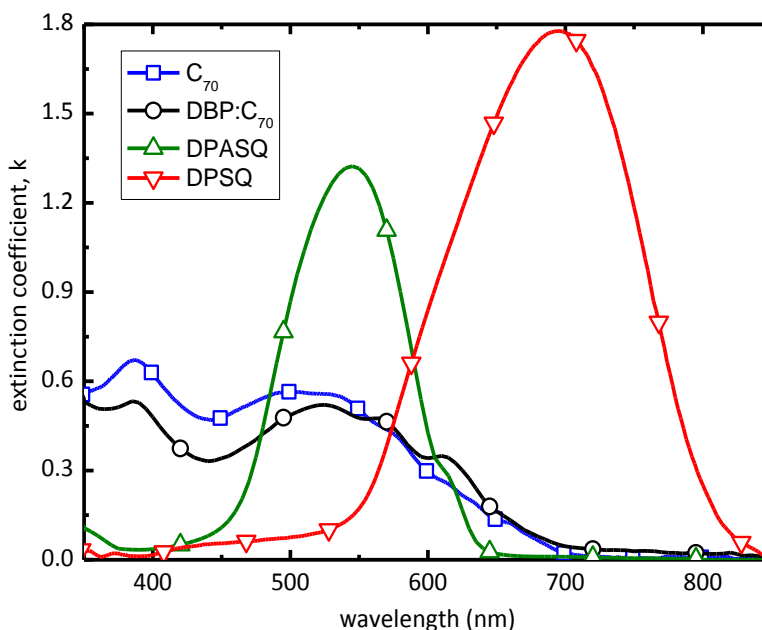
Devices were grown on 100 nm thick layers of indium tin oxide (ITO) with a sheet resistance of 15  $\Omega/\square$  pre-coated onto glass substrates. Prior to deposition, the ITO surface was cleaned in a surfactant and a series of solvents,<sup>28</sup> and then exposed to ultraviolet-ozone for 10 min prior to loading into a high vacuum chamber (base pressure < N<sub>2</sub> Torr) where MoO<sub>3</sub><sup>82</sup> was deposited by vacuum thermal evaporation (VTE) at 0.1 nm/s. Substrates were transferred into a high-purity N<sub>2</sub>-filled glovebox, where 16 nm thick bSQ films were

spin-coated at 3000 rpm from 20 nm alumina-filtered, 1.6 mg/ml solutions in chloroform. Substrates were returned to the high vacuum chamber without exposure to air for deposition of train-sublimation-purified<sup>152</sup> C<sub>70</sub> and a 3,4,9,10 perylenetetracarboxylic bisbenzimidazole (PTCBI) exciton blocking and electron transporting layer<sup>228</sup> at a rate of 0.1 nm/s. This was followed by transfer back into the glovebox for SVA, consisting of exposure to a saturated dichloromethane vapor for 7.5 min to create the desired nanocrystalline film morphology.<sup>194</sup> Next, the transparent, compound charge recombination layer consisting of a dense Ag nanoparticle layer (average thickness of 0.1 nm)<sup>110,207</sup> and a 5 nm thick film of MoO<sub>3</sub> was deposited by VTE. For the back sub-cell (i.e. that closest to the cathode), a mixed film of DBP and C<sub>70</sub> was co-evaporated, where the rate of DBP and C<sub>70</sub> deposition were 0.02 and 0.16 nm/s, respectively. After deposition of the 4,7-diphenyl-1,10-phenanthroline (BPhen) exciton blocking layer at 0.1 nm/s, a 100 nm-thick Ag cathode was deposited at 0.1 nm/s through a shadow mask with an array of 1 mm diameter openings. Layer thicknesses and optical constants were measured with quartz crystal monitors and calibrated by variable-angle spectroscopic ellipsometry, the latter of which are shown in Fig. reffig:tandem11. Current density-vs.-voltage (J-V) characteristics were measured in an ultra-pure N<sub>2</sub> ambient in the dark and under simulated AM1.5G solar illumination from a filtered 300 W Xe lamp whose intensity was varied using neutral density filters. The incident light intensity was measured using an NREL-traceable Si detector.<sup>37</sup> The  $J_{SC}$  of single-cell reference devices deposited concurrently with the tandem were corrected for spectral mismatch.<sup>38</sup> Spectrally resolved  $EQE$  were measured using monochromated light from a 150 W Xe source using output optics that focused the beam to under-fill the device area. Input intensity was calibrated with a NIST-traceable Si detector. Errors quoted

correspond to the deviation from the average value of three or more devices on the same substrate. Integrating the convolution of the  $EQE$  of the single-cell devices with the solar spectrum leads to an agreement of  $< \pm 5\%$  compared to the measured  $J_{SC}$  under simulated 1-sun illumination.

## 8.4.2 Single-cell results

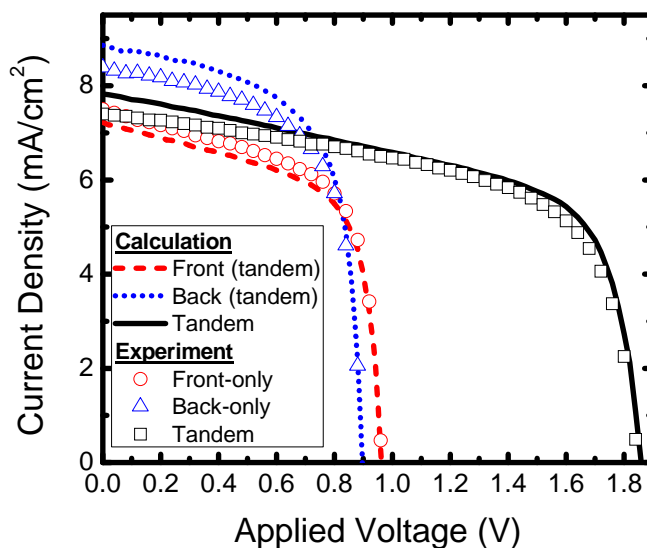
For the front-only device (i.e. the structure that ultimately is positioned next to the anode), the optimized bilayer double HJ has the following structure: glass substrate/100 nm ITO/15 nm MoO<sub>3</sub>/16 nm bSQ/10 nm C<sub>70</sub>/5 nm PTCBI/0.1 nm Ag/30 nm MoO<sub>3</sub>/100 nm Ag. The 15 nm thick MoO<sub>3</sub> determines the work function of the anode and improves charge extrac-



**Figure 8.22** Extinction coefficients ( $k$ ) for the active materials used in the organic photovoltaic cells, as measured via spectroscopic ellipsometry.

tion,<sup>82</sup> while the 30 nm thick MoO<sub>3</sub> layer is used as an electron transport layer and spacer to create a similar optical field to that in the tandem device. The device has a front-cell open circuit voltage of  $V_{OCF} = 0.96 \pm 0.01$  V,  $FF = 63 \pm 1\%$ ,  $J_{SC} = 7.2 \pm 0.1$  mA/cm<sup>2</sup>,  $\eta_p = 4.4 \pm 0.1\%$  and  $M = 0.95 \pm 0.01$ , as shown in Table 8.2 and Fig. 8.23 (circles). From the *EQE* spectrum, we calculate  $L_D = 9.0 \pm 0.2$  and  $9.9 \pm 0.3$  nm for DPSQ and C<sub>70</sub>, respectively. The SVA process significantly increases the exciton diffusion length of bSQ due to the formation of a nanocrystalline morphology.

We also fabricated an optimized back-only cell with the structure: glass substrate/100 nm ITO/5 nm MoO<sub>3</sub>/25 nm DBP:C<sub>70</sub> (1:10 volume ratio)/7 nm C<sub>70</sub>/7 nm BPhen/100 nm Ag. Figure 8.17 (triangles) shows the *J-V* characteristics for the back-only cell, with open



**Figure 8.23** Experimental current density vs. voltage characteristics in the 4th quadrant under 1 sun, simulated AM1.5G illumination for front-only (circle), back-only (triangle), and tandem (square) organic photovoltaic cells, along with calculated characteristics for the front sub-cell (dashed), back sub-cell (dotted), and tandem (solid) cell under similar illumination conditions.

circuit voltage  $V_{OCB} = 0.90 \pm 0.01$  V,  $FF = 64 \pm 1\%$ ,  $J_{SC} = 8.4 \pm 0.1$  mA/cm<sup>2</sup>,  $\eta_p = 4.8 \pm 0.3\%$ , and  $M = 1.01 \pm 0.01$ .

### 8.4.3 Tandem results

We then fabricated an optimized tandem with the following structure: glass substrate/100 nm ITO/15 nm MoO<sub>3</sub>/16 nm blended SQ/10 nm C<sub>70</sub>/5 nm PTCBI/0.1 nm Ag/5 nm MoO<sub>3</sub>/25 nm DBP:C<sub>70</sub>/7 nm C<sub>70</sub>/7 nm BPhen/100 nm Ag, Figure 8.23 shows the measured  $J$ - $V$  characteristics for the optimized device (squares), with  $V_{OC} = 1.85 \pm 0.01$  V,  $FF = 61 \pm 1\%$ ,  $J_{SC} = 7.4 \pm 0.1$  mA/cm<sup>2</sup>,  $\eta_p = 8.3 \pm 0.3\%$ , and  $M = 0.94$ , as summarized in Table 8.2. There is a discrepancy between the slopes of the experimental and calculated currents of the tandem device in Fig. 8.23 near zero bias, which is likely due to contributions from photoconductivity arising from exciton dissociation within the layer bulks,<sup>198</sup> which is not considered in the model; nonetheless, there is good agreement near the maximum power point.

The experimental and calculated EQE spectra are shown in Fig 8.24. The bSQ/C<sub>70</sub> device is photosensitive into the NIR, with a cut-off at approximately  $\lambda = 800$  nm, while

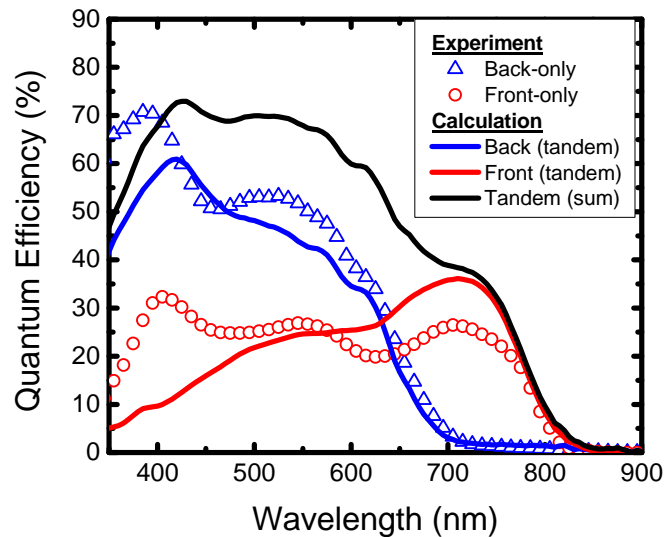
**Table 8.2** Organic photovoltaic performance under simulated 1 sun AM1.5G illumination, corrected for spectral mismatch.

Device	Datasource	$V_{oc}$ (V)	$FF$ (%)	$J_{sc}$ (mA/cm <sup>2</sup> )	$\eta_p$ (%)	$M$
Back-only	Experiment	$0.90 \pm 0.01$	$64 \pm 1$	$8.4 \pm 0.1$	$4.8.0 \pm 0.3$	$1.01 \pm 0.01$
Back sub-cell	Calculation	0.90	64	8.8	5.1	1.02
Front-only	Experiment	$0.96 \pm 0.01$	$63 \pm 1$	$7.5 \pm 0.1$	$4.6 \pm 0.2$	$0.96 \pm 0.01$
Front sub-cell	Calculation	0.96	63	7.2	4.4	0.95
Tandem	Experiment	$1.85 \pm 0.01$	$61 \pm 1$	$7.4 \pm 0.1$	$8.3 \pm 0.3$	$0.94 \pm 0.01$
Tandem	Calculation	1.86	60	7.8	8.6	0.94

the DBP:C<sub>70</sub> sub-cell has EQE > 50% for  $\lambda < 600$  nm. Overall, the tandem device harvests  $\sim 70\%$  of the photons  $\lambda < 600$  nm, and  $> 40\%$  for  $\lambda < 750$  nm.

#### 8.4.4 Discussion

The optimization of the tandem shown in Fig. ?? occurs primarily by maximizing the  $J_{SC}$ . As the back sub-cell active layer is increased in thickness, the absorption (and, therefore,  $J_{SC}$ ) of the back sub-cell is increased. Simultaneously, the distance between the front sub-cell active layers and the reflective cathode is also increased, changing the layer positions in the optical field and decreasing the absorption in the front sub-cell. Thus, by varying this thickness, the photocurrent generated in each sub-cell is balanced. From Fig. ??,  $FF$  and



**Figure 8.24** Experimental external quantum efficiency ( $EQE$ ) spectra for front-only (circle) and back-only (triangle) organic photovoltaic cells, along with calculated spectra for front sub-cell (dashed), back sub-cell (dotted), and the sum of the two sub-cells (solid).



$V_{OC}$  are nearly constant with respect to  $C_{70}$  thickness, and the  $J_{SC}$  (and therefore  $\eta_p$ ) is maximized for a thickness of 4 nm.

In a tandem device, there can be losses due to inefficient electron-hole recombination between the two sub-cells, leading to a decrease in the  $V_{OC}$  of the tandem when compared to the sum of the sub-cells. In the case of our tandem cell, we find  $V_{OCF} + V_{OCB} = 1.86 \text{ V} \pm 0.02$ , nearly identical to that of  $V_{OC} = 1.85 \pm 0.01 \text{ V}$  for the tandem, indicating that recombination is highly efficient.

### 8.4.5 Conclusions

In conclusion, we incorporate a solution-processed, solvent-vapor-annealed blended squaraine/ $C_{70}$  bilayer heterojunction, with a vapor-deposited DBP: $C_{70}$  planar-mixed heterojunction. When used in a tandem cell, we obtain efficient photon harvesting at  $\lambda < 800 \text{ nm}$  while providing an open-circuit voltage ( $V_{OC}$ ) of 1.85 V and  $\eta_p = 8.3 \pm 0.4\%$ . By analyzing the losses present in the device, we have identified the two primary routes to further increase  $\eta_p$  are to increase the  $V_{OC}$  in the DBP-based sub-cell and decrease the optical gap of the  $fSQ$ -based sub-cell for increased spectral coverage.

## 8.5 Future work

Moving forward with tandem OPVs, the key to further improvements in performance is to decrease the losses present in the devices.

Relating to the specific structures mentioned in this work, we have learned recently that excitons are quenched at  $\text{MoO}_3$ /squaraine interfaces. This leads to a significant loss

of photons at  $\lambda > 700$  nm, limiting the  $EQE$  to  $\approx 40\%$  (as seen in Fig. 8.24). My colleagues are currently working on developing new materials to replace  $\text{MoO}_3$  that do not quench excitons, yet still have similar work function, charge extraction, transparency, and chemical robustness. Additionally, we have also found that a similar problem occurs at the fullerene/PTCBI interface, where excitons are quenched. In Chapter 10.3, I discuss preliminary work addressing this problem.

Next, the relationship between the optical gap and  $V_{OC}$  are essential parameters to maximize tandem performance. The tandem devices have a higher  $\eta_p$  than single-cell devices due to a reduction of thermalization losses: by matching the optical gap ( $E_{op}$ ) of each sub-cell to the photon energy, the losses from the thermalization of carriers can be reduced. The blended SQ/ $C_{70}$  device has an energy loss  $E_{loss} = E_{op} - eV_{OC} \approx 0.59$  eV, which is among the lowest measured for OPVs; conversely, the DBP: $C_{70}$  device has  $E_{loss} \approx 0.95$  eV, which is substantially higher than that for devices with a similar absorption range (e.g. SubPc: $C_{70}$   $E_{loss} \approx 0.85$  eV). As shown in Fig. 8.24, both sub-cells absorb between  $450 \text{ nm} < \lambda < 650 \text{ nm}$  due to the inclusion of  $C_{70}$ . Since neither sub-cell absorbs at  $\lambda > 800$  nm, the device is transparent to  $> 60\%$  of all photons in the solar spectrum. Decreasing  $E_{op}$  in the squaraine material could lead to a significant increase in the number of photons absorbed.

Lastly, the squaraine-based sub-cell is limiting in many regards. The total thickness of a squaraine/ $C_{70}$  sub-cell is limited to  $\approx 25$  nm, and the solvent processing and solvent vapor annealing complicates the use of these materials in a tandem structure. Previous efforts to incorporate DPSQ and other high-efficiency squaraines into a solution-processed bulk-heterojunction structure have yielded disappointing results, with  $FF < 40\%$ . A logical

next step would be to replace this sub-cell a vacuum-processed red/infrared absorbing material such as the recently reported donor-acceptor-acceptor type molecule, DTDCTB.<sup>170</sup> By using a vacuum-evaporated bulk heterojunction-compatible molecule, a wider range of thickness is possible, easing the constraints we have seen from the use of squaraines in this work, along with increasing the maximum photocurrent. However, it is unclear if these improvements would offset the loss in  $V_{OC}$  and  $FF$  which would occur from using this material.

# Chapter 9

## Tandem organic photovoltaics incorporating two solution-processed small molecule donor layers

### 9.1 Background

To expand materials options, we also explored the fabrication of tandem OPVs with multiple solution-processed layers. When both sub-cells consist of solution-processed polymers, the interconnecting layers must provide a barrier to protect the underlying cell from being redissolved when the second cell is deposited. For example, poly(ethylene dioxythiophene)/poly(styrene sulfonic acid) (PEDOT:PSS) has been used due to its insolubility in chlorinated solvents typically used for the deposition of active-layer materials.<sup>212</sup> Multiple layers such as TiO<sub>2</sub>/PEDOT:PSS,<sup>238</sup> ZnO/self-assembled monolayers,<sup>239</sup> and TiO<sub>2</sub>/Al/MoO<sub>3</sub><sup>240</sup> have also been used to prevent re-dissolving of the active layers. Protection layers must be relatively thick (> 30 nm) to limit the penetration of solvents through pin-holes or other physical defects. Thick layers have the disadvantage that they

may prevent optimization of the optical field distribution within the cell to maximize the photocurrent. <sup>181,241</sup>

Tetrahydrofuran (THF) is an alternative to the ubiquitously used chlorinated solvents, often used in polymer synthesis <sup>242</sup> and as a solvent for some solution-processed OPVs. <sup>243,244</sup> The boiling point and viscosity of THF is similar to that of chloroform (CF), with values of 66 and 61 °C, and 0.48 and 0.54 cP, respectively. Small molecule materials such as functionalized squaraines (*f*SQs), <sup>76,189,191–193</sup> have a lower solubility in THF than in CF (~ 2 mg/ml vs. >8 mg/ml), although even this low solubility is sufficient for deposition via spin-coating under similar conditions. However, the solubility for C<sub>60</sub> is drastically lower in THF (<0.01 mg/ml) <sup>245,246</sup> than in CF (~ 0.16 mg/ml). <sup>247</sup> This solubility “contrast” presents an opportunity for the fabrication of tandem OPVs with two solution-processed small molecule layers.

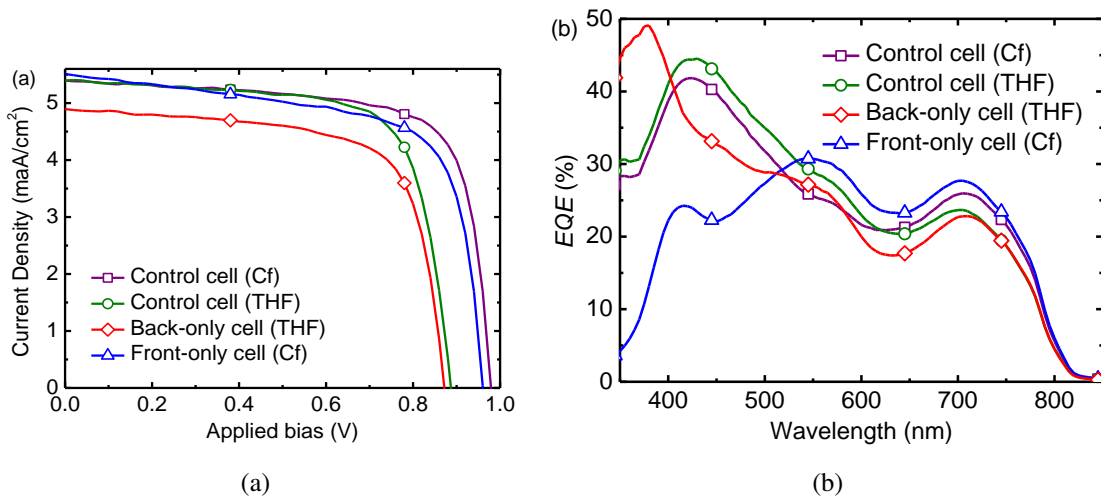
Here we incorporate two solution- and vapor-processed blended-*f*SQ sub-cells into a tandem OPV. The first sub-cell consists of a blend that is cast from a CF solution, followed by evaporation of the fullerene acceptor and transport materials. The second sub-cell, also based on *f*SQs, is then cast from a THF solution, that minimizes dissolution of the relatively insoluble, underlying C<sub>60</sub> layer which acts to protect the blended *f*SQ donor layer. Furthermore, solvent vapor annealing (SVA) is found to decrease the amount of damage caused by spin-coating of the second *f*SQ layer due to the increased crystallinity in the film that reduces the rate of solvent penetration. The resulting tandem cell has a power conversion efficiency of  $\eta_p = 6.2 \pm 0.3\%$  and an open circuit voltage of  $V_{OC} = 1.78 \pm 0.01$ , or nearly equal to the sum of the constituent sub-cells.

## 9.2 Experiment

Devices were grown on glass substrates pre-coated with 130 nm-thick layer of indium tin oxide (ITO) with a sheet resistance of  $15 \Omega/\square$ . Prior to deposition, the ITO surface was cleaned in a surfactant and a series of solvents, and then exposed to ultraviolet-ozone for 10 min prior to loading into a high vacuum chamber (base pressure  $<10^{-7}$  Torr) where  $\text{MoO}_3$ <sup>248</sup> was deposited by vacuum thermal evaporation (VTE) at  $\sim 0.1$  nm/s. Substrates were subsequently transferred into a high-purity  $\text{N}_2$ -filled glovebox, where 15 nm-thick blended squaraine films were spin-coated at 3000 rpm from 1.9 mg/ml solutions of 4:6 volume ratio of [2-[4-(N,N-diphenylamino)-2,6-dihydroxyphenyl]-4-[4-diphenyliminio] squaraine] (DPASQ), and 2,4-bis[4-(N,N-diphenylamino)-2,6-dihydroxyphenyl] squaraine (DPSQ) dissolved in CF or THF (used for processing the “front” sub-cell adjacent to the anode, or “back” sub-cell adjacent to the cathode, respectively) and filtered through anodic alumina membranes with a 20 nm pore size. Substrates were returned to the high vacuum chamber in an ultrahigh purity  $\text{N}_2$  environment for deposition of train-sublimation-purified  $\text{C}_{70}$  and a 3,4,9,10 perylenetetracarboxylic bisbenzimidazole (PTCBI) electron transporting layer<sup>228</sup> at a rate of 0.1 nm/s. Some samples were transferred back into the glovebox for SVA consisting of exposure to a saturated dichloromethane vapor for 7.5 min to create the desired nanocrystalline film morphology.<sup>194</sup> For more details on *f*SQs and SVA, see Section 6.1.2. Next, the transparent charge-recombination layer consisting of a Ag nanoparticle layer (average thickness of 0.1 nm)<sup>110,207</sup> and  $\text{MoO}_3$  was deposited by VTE. For the back sub-cell, an identical blend of squaraines dissolved in THF was spin-cast under similar conditions, followed by evaporation of  $\text{C}_{60}$  and PTCBI and SVA. The device was completed by evaporating the 100 nm-thick Ag cathode at 0.1 nm/s through a shadow mask with an

array of 1 mm diameter openings. Layer thicknesses were measured using quartz crystal monitors during deposition, and ex situ by variable-angle spectroscopic ellipsometry.

Current density-vs.-voltage ( $J$ - $V$ ) characteristics were measured in an ultra-pure  $N_2$  ambient in the dark and under simulated AM1.5G solar illumination from a filtered 300 W Xe lamp whose intensity was varied using neutral density filters. The incident light intensity of  $70 \text{ mW/cm}^2$  was measured using an NREL-traceable Si detector. The efficiency is found to be nearly constant from  $20 \text{ mW/cm}^2$  up to approximately 1 sun intensity. Short-circuit current densities ( $J_{SC}$ ) of discrete OPVs were corrected for spectral mismatch.<sup>38</sup> Spectrally resolved external quantum efficiencies ( $EQE$ ) were measured using monochromated light from a 150 W Xe arc-lamp using optics that under-filled the device area; optical power was calibrated with a NIST-traceable Si detector. Integration of the  $EQE$  convoluted with the solar spectrum resulted in values within  $\pm 10 \%$  of the corrected  $J_{SC}$  for the single-cell devices. Errors quoted correspond to the deviation from the average value of three or more devices on the same substrate. The tandem sub-cell  $J$ - $V$  characteristics and  $EQE$  were obtained using a model that considers the optical field distribution within the layers, exciton diffusion, and light-intensity-dependent  $J$ - $V$  characteristics taken from single-cell devices, as previously.<sup>47,241</sup> The spectral mismatch factor ( $M$ ) for the tandem cell was calculated by dividing the power conversion efficiency calculated using the lamp spectrum and that calculated using the standard solar spectrum.



**Figure 9.1** (a) Current density vs. voltage ( $J$ - $V$ ) characteristics in the 4th quadrant under  $70 \text{ mW/cm}^2$ , simulated AM1.5G illumination for a blended functionalized squaraine/ $\text{C}_{60}$  organic solar cell using a chloroform (CF) solvent (square), and a similar cell cell using tetrahydrofuran (THF) solvent (circle), a cell using THF (diamond) for positioning near the cathode of the tandem (back-only cell), and a cell for positioning near the transparent anode in the tandem (front-only cell) using CF (triangle), (b) along with external quantum efficiencies ( $EQE$ s) for the same cells.

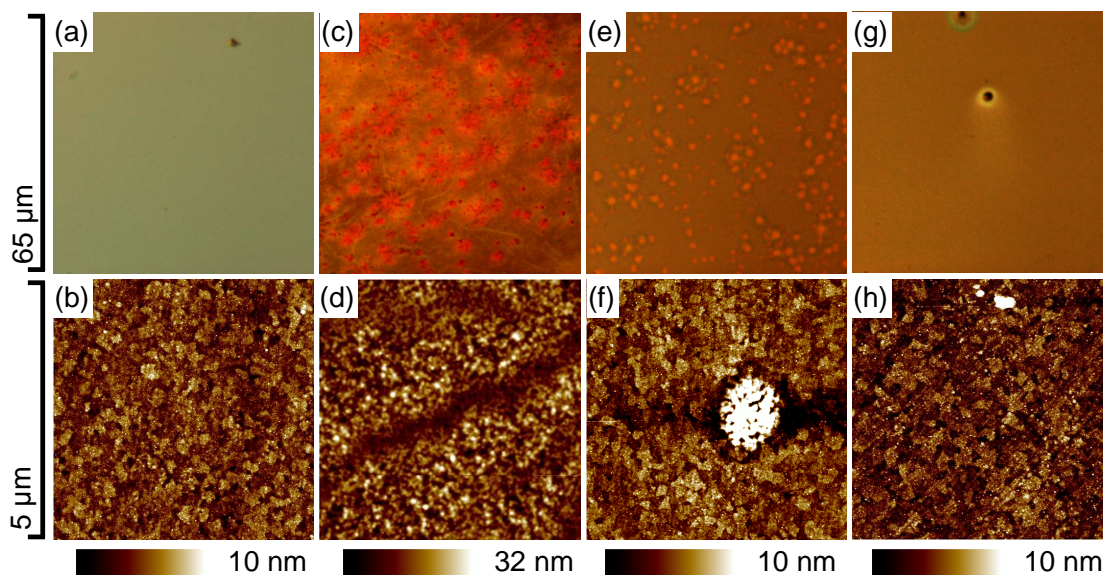
### 9.3 Results and Discussion

To compare devices with blended  $f$ SQs dissolved in either CF or THF, single-junction cells were fabricated with the following structure: glass/ITO/25 nm  $\text{MoO}_3$ /15 nm blended  $f$ SQ/40 nm  $\text{C}_{60}$ /8 nm PTCBI/100 nm Ag, where the blend was dissolved in either chloroform or THF, and then solvent vapor annealed after deposition of the PTCBI buffer layer. The  $J$ - $V$  characteristics under illumination, and the  $EQE$  spectra are shown in Figure 9.1, with device performance parameters summarized in Table 9.1. The CF-solubilized cell had  $V_{OC} = 0.96 \pm 0.01$ ,  $FF = 73 \pm 1\%$ , responsivity ( $R$ ) =  $7.7 \pm 0.3 \times 10^{-2} \text{ A/W}$ , and  $\eta_p = 5.5 \pm 0.2\%$ , which is within experimental error of previously reported results for analogous devices. The THF-based cell had  $V_{OC} = 0.89 \pm 0.02 \text{ V}$ ,  $FF = 71 \pm 1\%$ ,  $R$



$= 7.7 \pm 0.3 \times 10^{-2} \text{ A/W}$ , and  $\eta_p = 4.9 \pm 0.2\%$ . The decrease in  $V_{OC}$  compared to the CF-based cell is likely due to a difference in the phase segregation between the two *f*SQ molecules.<sup>194</sup>

To simulate the damage to the underlying layers caused by the spin-coating of a second solution-based material onto its surface, we investigated the effects of spinning THF on the top of the following structure: glass/ITO/25 nm  $\text{MoO}_3$ /15 nm blended *f*SQ (spun on using CF)/10 nm  $\text{C}_{70}$ /5 nm PTCBI/0.1 nm Ag/*x*  $\text{MoO}_3$ , where  $x = 5$  or 20 nm. Figures 9.2a and b correspond to the case of a solvent vapor annealed sample with  $x = 5$  nm. The layer was not exposed to THF, resulting in a film that appears featureless under microscopic examination. The surface morphology of the film is similar to that of the ITO, with a root-mean-square



**Figure 9.2** Optical (top row) and atomic force (bottom row) micrographs for samples having undergone different processing procedures: (a, b) solvent-vapor annealed (SVA), no THF exposure; (c, d) as-cast, 5 nm  $\text{MoO}_3$  layer, THF exposure; (e, f) SVA, 5 nm  $\text{MoO}_3$  layer, THF exposure; (g, h) SVA, 20 nm  $\text{MoO}_3$  layer, THF exposure. The vertical scales for the bottom row of micrographs are indicated below each image.

(RMS) roughness of 1.5 nm. Figures 9.2c and d show as-cast films with  $x = 5$  nm where THF was spun on the top of the same structure. The films significantly roughen to a RMS = 4.9 nm due to re-dissolution of the underlying *f*SQ layers. In Figures 9.2e and f, the layers for an  $x = 5$  nm sample were solvent vapor annealed after the PTCBI layer is deposited, followed by spinning of THF onto the surface. The film contains 1  $\mu$ m-diameter by 10 nm-high protrusions covering 10% of its surface, suggesting that solvent has penetrated into the underlying layers resulting in swelling. In this case, the damage is confined to a small area, with RMS = 1.5 nm outside of the damaged areas, similar to the un-exposed case. As the MoO<sub>3</sub> thickness is increased, the density of these protrusions decreases. Figures 9.2g and h show that they are nearly eliminated for  $x = 20$  nm.

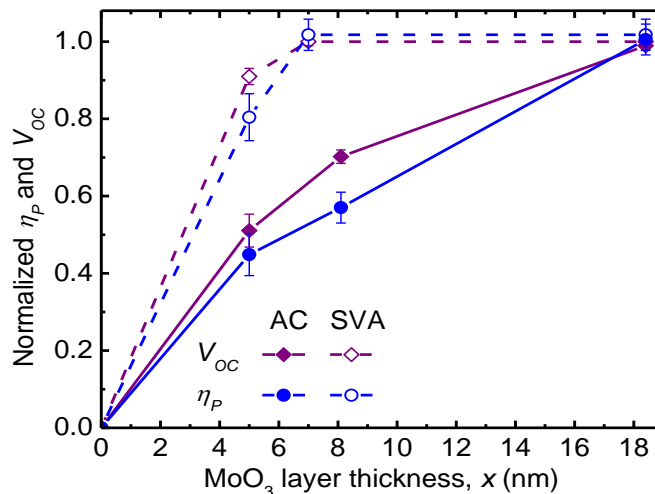
Re-dissolution caused by the deposition of the second solution-processed layer is minimized in two ways. First, Figure 9.2 shows that solvent vapor annealing decreases the radius of the defects caused by the exposure to the second THF solution. The roughness of the sample in Figure 9.2f is the same as that of the unexposed film in Figure 9.2b, indicating that solvent is penetrating only through pinholes. The SVA increases the density of the the

**Table 9.1** Organic photovoltaic performance under 70 mW/cm<sup>2</sup> simulated AM1.5G illumination, corrected for spectral mismatch. Experimental errors: <sup>a</sup>  $\pm 0.01$ , <sup>b</sup>  $\pm 1$ , <sup>c</sup>  $\pm 0.3$ .

Device	Data source	Solvent	$V_{oc}$ (V) <sup>a</sup>	$FF$ (%) <sup>b</sup>	$R$ ( $10^{-2}$ A/W <sup>c</sup> )	$\eta_p$ (%)	$M^a$
Control	Experiment	CF	0.96	73	7.7	$5.5 \pm 0.2$	0.98
Control	Experiment	THF	0.89	71	7.7	$4.9 \pm 0.2$	0.98
Back-only	Experiment	THF	0.88	69	7.0	$4.2 \pm 0.2$	1.00
Front-only	Experiment	CF	0.96	67	7.8	$5.0 \pm 0.2$	0.96
Back sub-cell	Calculation	THF	0.86	70	5.0	3.0	0.98
Front sub-cell	Calculation	CF	0.94	69	5.2	3.4	0.92
Tandem	Calculation	Both	1.80	70	5.1	6.4	0.95
Tandem	Experiment	Both	1.78	67	4.9	$6.2 \pm 0.3$	0.95

donor and acceptor layers as they reorganize and crystallize, filling in some of the voids in the as-cast film. This limits the area of exposure to solvent penetration that otherwise results in significant local roughening (see Figure 9.2c). Additionally, the damage from applying the second solution-processed layer can be decreased by increasing the MoO<sub>3</sub> protection layer thickness. Figure 9.3 shows that, for the case of as-cast films exposed to THF, ~20 nm of MoO<sub>3</sub> is necessary to achieve the same performance as cells unexposed to the solution. By combining both approaches – a SVA-processed device with a MoO<sub>3</sub> protection layer of 7 nm – the same power conversion efficiency is achieved as an analogous device that has not been exposed to THF. As shown previously, the ability to use a thin MoO<sub>3</sub> layer also leads to a maximum tandem  $J_{SC}$ .

We fabricated a series of devices to simulate the behavior of the front sub-cell (i.e.



**Figure 9.3** Power conversion efficiencies ( $\eta_P$ , circles) and open-circuit voltages ( $V_{OC}$ , diamonds) for “front-only” single cells exposed to THF as a function of the MoO<sub>3</sub> layer thickness, normalized to values for cells not exposed to THF. As-cast cells are indicated with closed symbols, while solvent-vapor-annealed (SVA) cells are indicated with open symbols. Cells having undergone SVA appear to be damaged less by exposure to THF than unannealed samples. Inset: Schematic of the cell layer structure indicating the points during processing SVA and application of THF occur.

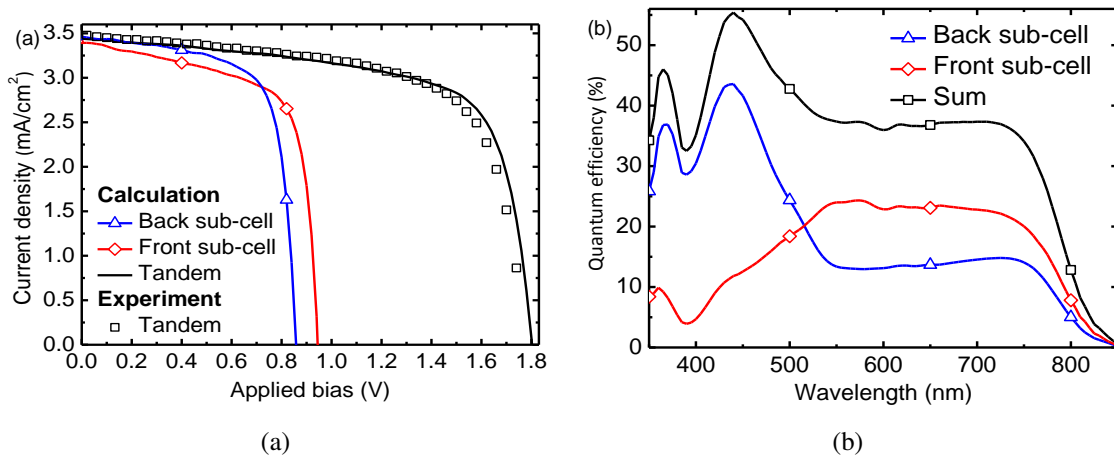
that positioned closest to the ITO anode in the tandem) using the following structure: glass/ITO/25 nm MoO<sub>3</sub>/15 nm blended *f*SQ (CF)/10 nm C<sub>70</sub>/5 nm PTCBI/0.1 nm Ag/*x* nm MoO<sub>3</sub>/30 - *x* nm MoO<sub>3</sub>/100 nm Ag. These cells were fabricated by vacuum depositing the MoO<sub>3</sub> layer on ITO, spinning on the blended *f*SQ, and the vacuum depositing the C<sub>70</sub>, and PTCBI layers. At this point, some films were solvent vapor annealed. The second MoO<sub>3</sub> layer was then deposited (with *x* = 0 to 18 nm) and exposed to spin cast THF, thereby simulating the effects of the deposition of a second blended *f*SQ layer. The devices were completed by depositing the final layer of MoO<sub>3</sub> and Ag, keeping the total amount of MoO<sub>3</sub> constant for all samples.

Figure 9.3 shows  $V_{OC}$  (diamonds) and  $\eta_p$  (circles) for as-cast (AC, filled points) and SVA (open points) cells as functions of *x*, where values for both parameters are normalized to their values for similar cells unexposed to THF. For both AC and SVA cells, *x* = 0 (i.e. no MoO<sub>3</sub> protection layer) leads to device shorts. As *x* increases,  $V_{OC}$  and  $\eta_p$  increase monotonically. The AC cell performance is similar to that of the unexposed cell at *x* = 18 nm, while the SVA cell requires only *x* = 7 nm. This is consistent with the images in Figure 9.2, where there is substantially more damage to the AC films compared to the SVA films at *x* = 5 nm.

We also fabricated a tandem cell using the optimized MoO<sub>3</sub> protection layer thicknesses. The discrete cell with a design optimized for the position nearest to the anode (i.e. a front-only cell) had the same structure as above with *x* = 7 nm, while the cathode-optimized (back-only) cell has the structure: glass/ITO/25 nm MoO<sub>3</sub>/15 nm blended *f*SQ (dissolved in THF)/28 nm C<sub>60</sub>/5 nm PTCBI/100 nm Ag, layer. The front-only and back-only *J-V* and *EQE* data are shown in Figure 9.1 and summarized in Table 9.1. The tandem cell structure

using these sub-cells is: glass/ITO/25 nm MoO<sub>3</sub>/15 nm blended *f*SQ (CF)/10 nm C<sub>70</sub>/5 nm PTCBI/0.1 nm Ag/7 nm MoO<sub>3</sub>/15 nm blended *f*SQ (THF)/28 nm C<sub>60</sub>/5 nm PTCBI/100 nm Ag, with the layers solvent annealed after deposition of each PTCBI layer. The optimized tandem cell had  $V_{OC} = 1.78 \pm 0.01$  V,  $FF = 67 \pm 1\%$ ,  $R = 4.9 \pm 0.02 \times 10^{-2}$  A/W, and  $\eta_p = 6.2 \pm 0.3\%$ , (with  $M = 0.95 \pm 0.01$ ).

The measured and simulated  $J$ - $V$  characteristics and the  $EQE$  spectra are shown in Figure 9.4. The experimental and calculated  $J$ - $V$  characteristics are in agreement, indicating the absence of significant damage to the front sub-cell due to either the deposition of the second blended *f*SQ layer, or from subsequent SVA. The quantum efficiencies of each sub-cell shown in Figure 9.4(b) show less curvature at  $\lambda = 650$  nm than for the single-cell in Figure 9.1(b). This is due to the fact that >90% of the photons are absorbed between 550 nm



**Figure 9.4** (a) Current density vs. voltage ( $J$ - $V$ ) characteristics in the 4th quadrant under  $70 \text{ mW/cm}^2$ , simulated AM1.5G illumination for the optimized tandem cell (squares), along with the calculated  $J$ - $V$  characteristics for the tandem (line), back sub-cell (triangle), and front sub-cell (diamond). (b) Quantum efficiency calculations for the back sub-cell (triangle) and front-sub-cell (diamond). The sum of these two curves (square) represents the total photon harvesting efficiency for the tandem cell.

$< \lambda < 720$  nm in the blended *f*SQ layers with a total thickness of 30 nm. Consequently, there is an increase in photon harvesting at  $\lambda = 700$  from 26% for the optimized discrete cell, to 38% for the tandem. While the total quantum efficiency of the tandem cell is limited due to significant spectral overlap between the active materials in the front and back sub-cells, there is nevertheless a >25% increase compared to the optimized discrete cell. The *FF* of the tandem is similar to that of the discrete devices, and the tandem  $V_{OC} = 1.78 \pm 0.01$  V is nearly equal to the sum of the respective discrete cells of  $V_{OC} = 1.84 \pm 0.02$  V, indicating that there is efficient charge transport and recombination in the interlayer between the sub-cells in the tandem device. Overall,  $\eta_p$  for the tandem cell is 12% higher than that of the optimized discrete cells.

## 9.4 Conclusions

In summary, we have demonstrated a small molecule tandem OPV consisting of two solution- and vapor-processed, blended functionalized-squaraine/fullerene sub-cells. Here, the relatively low solubility of fullerenes in THF leads to prevention of penetration of this solvent into the underlying blended *f*SQ donor layer, thereby minimizing layer dissolution and damage. Damage was further reduced by solvent vapor annealing of the front sub-cell, where the increased crystallinity of the blended-*f*SQ layer also reduced the ability of this solvent from penetrating and ultimately damaging the pre-deposited layers. The resulting tandem cell has a power conversion efficiency of  $\eta_p = 6.2 \pm 0.3\%$  and an open circuit voltage of  $V_{OC} = 1.78 \pm 0.01$ , or nearly the sum of the constituent sub-cells.

# Chapter 10

## Additional work on buffer layers

This chapter covers three topics in buffer layers in OPVs.

### 10.1 Organic electronics with symmetric electrodes

#### 10.1.1 Background

Molybdenum trioxide ( $\text{MoO}_3$ ) was introduced as an anode buffer layer in organic photovoltaics (OPVs) by Shrotriya et al.<sup>248</sup> It has a number of advantages that have made it one of the most commonly used anode buffer layers in the literature: easy deposition from vacuum or solution; high transparency in the visible; and favorable energy level alignment with organic hole transport materials. Although  $\text{MoO}_3$  functions similarly to an organic hole transport layer, it was determined that it is an n-type semiconductor which transports holes as a minority carrier.<sup>82</sup> Typically in photovoltaic devices, one of the limiting factors for the open-circuit voltage ( $V_{OC}$ ) is the work function ( $\Phi$ ) difference between the anode and cathode.<sup>24</sup> For example, many devices use ITO ( $\Phi_{ITO} = 5.3$  eV) and Ag ( $\Phi_{Ag} = 4.2$  eV),

that allows for  $V_{OC}$  as high as 1.1 V. However, Tao et al. found that when  $\text{MoO}_3$  is used as an anode buffer layer, the choice of electrode  $\Phi$  does not affect  $V_{OC}$ .<sup>83</sup> In fact, a device with an  $\text{Ag}/\text{MoO}_3$  anode functioned nearly identically to one with Au ( $\Phi_{Au} = 5.2$  eV), even though Ag was used as the cathode.

In this work, we demonstrate OPVs with symmetric electrodes consisting of  $\text{Ag}/\text{MoO}_3$  or  $\text{ITO}/\text{MoO}_3$ . The active layers of these devices function comparably to a device with archetypal  $\text{ITO}/\text{MoO}_3$  anode and Ag cathode. More generally, this suggests a new design criteria of organic electronic devices with an arbitrary choice of electrodes (metals, conductive polymers, nanowire sheets, graphene, nanotubes, etc) in combination with a transition metal oxide contact layer ( $\text{MoO}_3$ ,  $\text{V}_2\text{O}_5$ ,  $\text{WO}_3$ , etc.), allowing a new device architectures to be fabricated. It also suggests routes to fabricate inverted and/or semi-transparent organic electronic devices that could be used as solar power generating films on glass or automobile windscreens and sun-roofs, or paints, as just a few examples.

### 10.1.2 Experiment

Devices were grown on either 130 nm thick layers of ITO pre-coated onto glass substrates or 20 nm thick layers of Ag on glass. Prior to deposition, the ITO or glass surface was cleaned in a surfactant and a series of solvents and then exposed to ultraviolet-ozone for 10 min before loading into a high vacuum chamber (base pressure  $< 10^{-7}$  Torr) where  $\text{MoO}_3$  was thermally evaporated at 0.1 nm/s. Substrates were then transferred to a  $\text{N}_2$  glovebox where 2,4-bis[4-(N,N-diphenylamino)-2,6-dihydroxyphenyl] squaraine (DPSQ) films were spin-coated from filtered 1.6 mg/ml solutions in chloroform. Substrates were again transferred into the high vacuum chamber for deposition of purified organics at

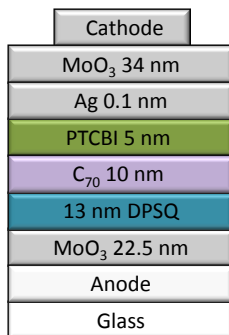


0.1 nm/s, followed by transfer back into the glovebox and exposure to saturated chloroform vapors to for 10 min to create a favorable film morphology.<sup>194</sup> After a transfer back to the vacuum chamber, a 0.1 nm Ag silver nanocluster layer<sup>110</sup> and a MoO<sub>3</sub> transport layer. The cathode material (Ag or ITO) was deposited through a shadow mask with an array of 1 mm diameter openings. Sputtered ITO (sITO) was deposited at 0.01 nm/s with 20 W DC power. Current density versus voltage (*J-V*) characteristics were measured in an ultra-pure N<sub>2</sub> ambient, in the dark and under simulated AM1.5G solar illumination from a filtered 300 W Xe lamp. Lamp intensity was varied using neutral density filters. Optical intensities were referenced using an NREL-calibrated Si detector, and photocurrent measurements were corrected for spectral mismatch.<sup>38</sup>

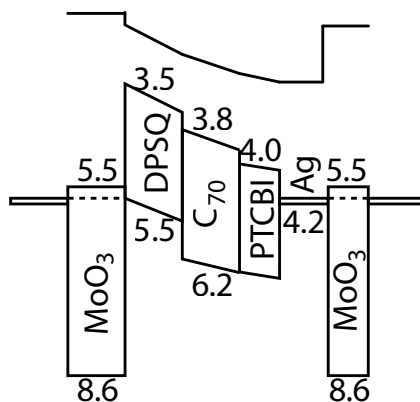
### 10.1.3 Results and Discussion

We fabricated OPVs with the following structure: glass/anode/22.5 nm MoO<sub>3</sub>/13 nm DPSQ/10 nm C<sub>70</sub>/5 nm PTCBI/0.1 nm Ag/34 nm MoO<sub>3</sub>/cathode, where the anode was either ITO (pre-coated) or 20 nm Ag, and the cathode consisted of 100 nm Ag, 20 nm Ag, or 40 nm sITO. A schematic is shown in Fig. 10.1. Although MoO<sub>3</sub> typically has an electronegative lowest unoccupied molecular orbital (LUMO), the Ag nanocluster layer deposited on top of PTCBI has the effect of aligning the Fermi level of PTCBI and MoO<sub>3</sub>, as shown in Fig. 10.2. The result is efficient electron transport from PTCBI to MoO<sub>3</sub> to the cathode.

Device characteristics under 1 sun AM1.5G simulated illumination and in the dark are shown in Fig. 10.3, and performance is summarized in Table 10.1. The difference in  $J_{SC}$  can be attributed to the difference in reflectivity of the electrodes used. For an ITO anode,

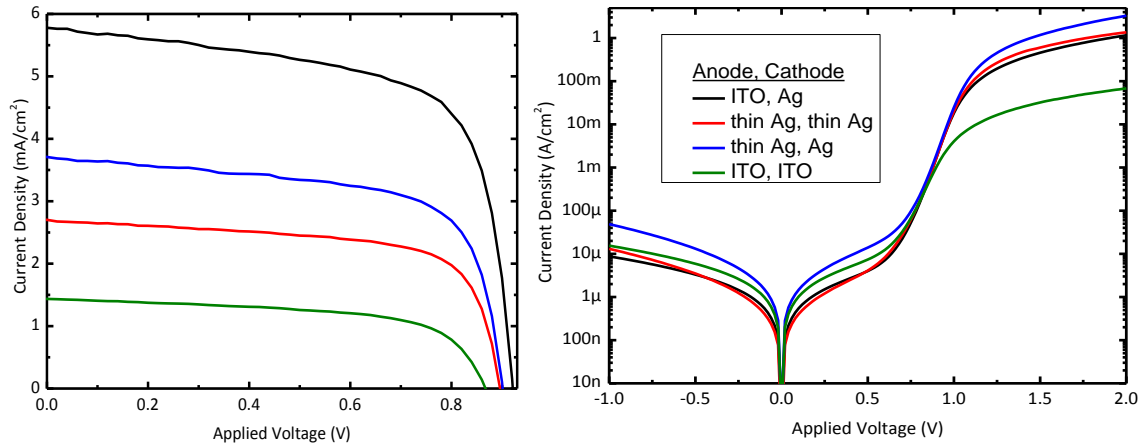


**Figure 10.1** Schematic diagram of the device (not to scale), where the anode is 100 nm ITO or 20 nm Ag and the cathode is 100 nm Ag, 20 nm Ag, or 40 nm sITO.



**Figure 10.2** Energy level diagram for the symmetric-contact device.

reflectivity is low, leading to more light absorbed at the active layer. Using 20 nm Ag as the anode is more reflective, decreasing responsivity. For the cathode, using 100 nm Ag reflects light back through the active layers, further increasing responsivity, while 20 nm Ag and sITO are increasingly transparent, leading to lower responsivity. However, this transparency can be advantageous when designing a semitransparent OPV.<sup>226,249–256</sup> These differences in responsivity can also be seen in the *EQE* data, shown in Fig. 10.4. For the device with 20 nm Ag as the anode and 100 nm Ag as the cathode, the peak at  $\lambda = 500$  nm



**Figure 10.3** a) Linear plot of the  $J$ - $V$  characteristic of devices with various electrodes under one-sun simulated illumination and b) semilog plot of the same devices in the dark.

can be attributed to microcavity effects, which can be tuned to enhance certain wavelengths.

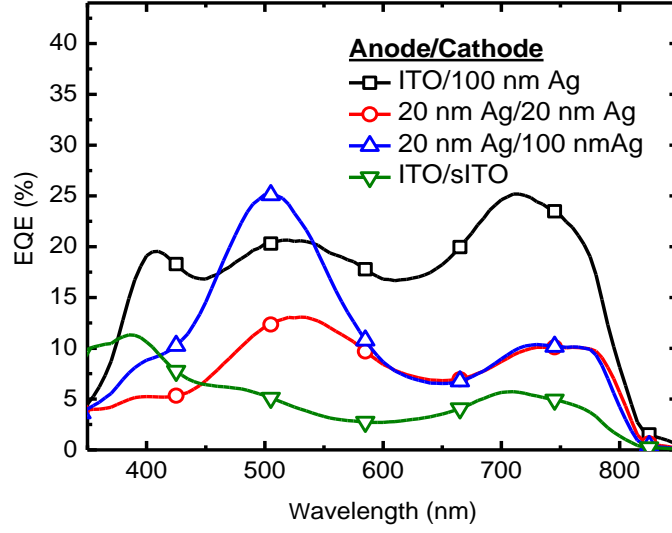
The difference in  $V_{OC}$  between these four devices can be correlated to the difference in  $J_{SC}$ . There is a known relationship between  $V_{OC}$  and  $J_{SC}$ :

$$qV_{OC} = \Delta E_{HL} + k_b T \ln(J_{SC}/J_s) \quad (10.1)$$

where  $q$  is the electron charge,  $\Delta E_{HL}$  is the energy difference between the donor highest occupied molecular orbital (HOMO) and the acceptor LUMO,  $k_b$  is Boltzmann's constant,  $T$  is the temperature and  $J_s$  is the saturation dark current. It can be seen from Eq. (10.1) that

**Table 10.1** Device performance at one sun illumination.

Anode	Cathode	$J_{SC}$ (mA/cm <sup>2</sup> )	$V_{OC}$ (V)	$FF$ (%)	$\eta_P$ (%)	$R_S$ ( $\Omega$ cm <sup>2</sup> )
ITO	100 nm Ag	6.0	0.92	67	3.7	0.87
20 nm Ag	20 nm Ag	2.8	0.89	65	1.6	0.64
20 nm Ag	100 nm Ag	3.7	0.90	67	2.2	0.29
ITO	sITO	1.4	0.86	52	0.8	14.1



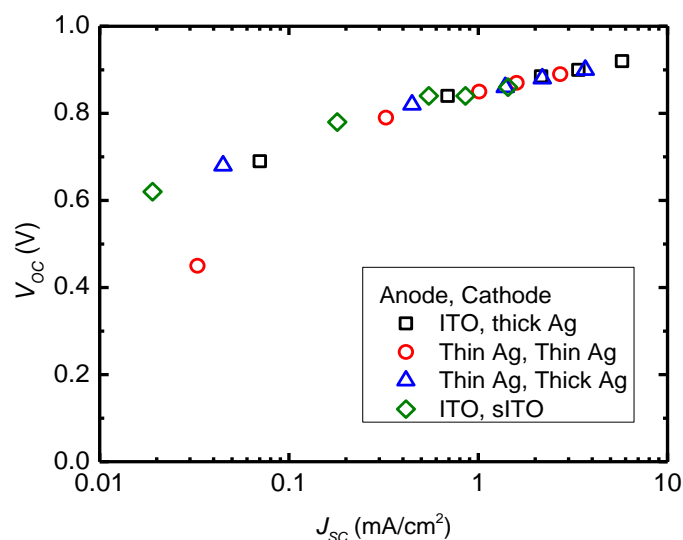
**Figure 10.4** External quantum efficiencies for devices with various electrodes.

there is a logarithmic dependence of  $V_{OC}$  on  $J_{SC}$ . By plotting  $V_{OC}$  as a function of  $J_{SC}$  in Figure 10.5, we can see that the data for all four devices are collinear. This indicates that all four devices are operating similarly, and the differences in  $V_{OC}$  are only due to differences in the amount of light absorbed by the active layers.

By fitting the dark  $J$ - $V$  data to the ideal diode equation, we can also extract the series resistance ( $R_S$ ) for each device:

$$J = J_s \left[ \exp\left(\frac{q(V - JR_S)}{nk_bT}\right) - 1 \right] \quad (10.2)$$

where  $n$  is the ideality factor. As shown in Table 10.1, devices with ITO and Ag have very low  $R_S$ ,  $< 1 \Omega\text{cm}^2$ . For the device with sITO, it is much higher, with  $R_S = 14.1 \Omega\text{cm}^2$ . This is due to the fact that sITO is of lower quality than ITO (sheet resistance  $200 \Omega/\square$  vs.  $15 \Omega/\square$ ), leading to increased  $R_S$  and decreased  $FF$  for this device.



**Figure 10.5** Open-circuit voltage vs. short-circuit current for devices with various electrodes.

### 10.1.4 Conclusions

In this work, we demonstrated OPVs with symmetric contacts. By using either Ag/MoO<sub>3</sub> or ITO/MoO<sub>3</sub> as both anode and cathode, we achieved similar device operation to that of our archetypical device with ITO/MoO<sub>3</sub> as the anode and Ag as the cathode. This presents a route to create semitransparent devices, in addition to the possibility of ITO-free devices.

## 10.2 Doping of metal oxide charge transport layers with organic molecules

Metal oxides are commonly used in organic and molecular electronics as charge transport layers due to their unique physical properties. They provide favorable energy level alignment with a wide range of materials which improves carrier injection and extraction, and

their optical transparency allows their use of optical spacers.<sup>82,83,105,171,228,248,252,257–260</sup> They are compatible with a wide range of deposition processes (vacuum evaporation, spin-coating from solution, and others), and their chemical robustness allows the solvent-based deposition of subsequent layers. Materials of this class include MoO<sub>3</sub>, CrO<sub>3</sub>, V<sub>2</sub>O<sub>5</sub>, WO<sub>3</sub>, NiO, Cr<sub>3</sub>O<sub>4</sub>, Cr<sub>2</sub>O<sub>3</sub>, CuO, TiO<sub>2</sub>, Ta<sub>2</sub>O<sub>5</sub>, Cu<sub>2</sub>O, and many others. A limitation, however, is that many of these materials must be very thin (< 20 nm) due to their high resistivity. This reduces their usefulness as optical spacers, where layers of 100 nm or more may be necessary. If layers >20 nm are used in devices, the low conductivity leads to increased series resistance ( $R_S$ ) and decreased device performance.

Here, we present doping as a method to increase the conductivity of metal oxide thin films with organic molecules. As examples to this concept, we utilize MoO<sub>3</sub> as the metal oxide and 2,3,5,6-tetrafluoro-7,7,8,8-tetracyanoquinodimethane (F<sub>4</sub>TCNQ),<sup>261–263</sup> acridine orange base (AOB),<sup>90,179,181</sup> and boron subphthalocyanine chloride (SubPc)<sup>74,75</sup> as the dopants. We show that doping with these materials results in decreased resistivity, similar to doping with Ag, which then leads to decreased  $R_S$  in OPVs.

### 10.2.1 Experimental Method

Substrates consisting of indium tin oxide-coated glass (ITO) (130 nm, <15Ω/□, Prazisions Glas & Optik GmbH) quartz (qtz), or silicon were cleaned sequentially in Tergitol, deionized water, acetone, trichloroethylene, acetone, and isopropanol. C<sub>60</sub> (MER, 99.9% sublimed) and AOB (Aldrich, 75%) were purified once and SubPc (Aldrich, 85%) was purified three times by thermal gradient sublimation at <1x10<sup>-7</sup> Torr.<sup>152</sup> Other materials were used as received. ITO substrates were subjected to a UV-ozone treatment for 10 min

and transferred into a nitrogen glovebox with  $<0.1$  ppm  $O_2$  and  $H_2O$ . Substrates were loaded into a high-vacuum chamber with base pressure  $< 1.0 \times 10^{-6}$  Torr, where materials were evaporated at 0.10 nm/s. Squaraine films were deposited from solution via spin coating in a purified  $N_2$  environment. All rates were measured by quartz crystal monitor and calibrated by spectroscopic ellipsometry.

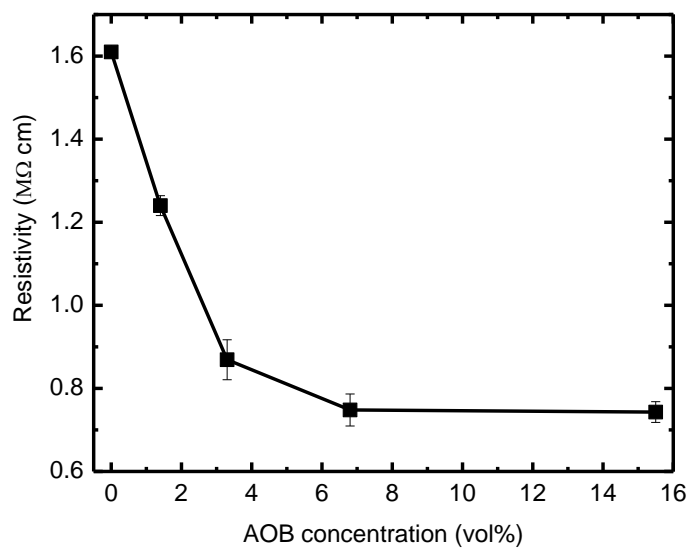
Device performance was measured in a nitrogen glovebox with  $<1.0$  ppm  $O_2$  and  $<0.1$  ppm  $H_2O$  by an Agilent semiconductor parameter analyzer under illumination by a 150 W Xe lamp with AM1.5G filters (Oriel). Lamp intensity was varied by using neutral density filters and measured using an NREL-calibrated Si photodiode. Incident light intensity was corrected for spectral mismatch.<sup>38,195</sup>

## 10.2.2 Results

First, we fabricated single-layer "sandwich-type" devices of the structure glass/ITO/MoO<sub>3</sub>/Au. By measuring the  $J$ - $V$  characteristics of these devices, we extracted the resistivity  $\rho = RA/t$ , where  $R$  is the resistance,  $A$  is the device area, and  $t$  is the layer thickness, by using the Mott-Gurney relation:

$$I = \frac{V}{R} + \frac{9A\epsilon\mu V^2}{8t^3} \quad (10.3)$$

We first measured this for 90 nm MoO<sub>3</sub> layers doped with various concentrations of AOB. For the neat film,  $\rho = 1.6$  M $\Omega$ cm and decreased below 800 k $\Omega$ cm with 7 vol% doping (Figure 10.6). Next, we measured the absorption coefficient ( $\alpha$ ) of the doped films. As seen in Figure 10.7, increased doping led to increased  $\alpha$  at longer wavelengths. Additionally,

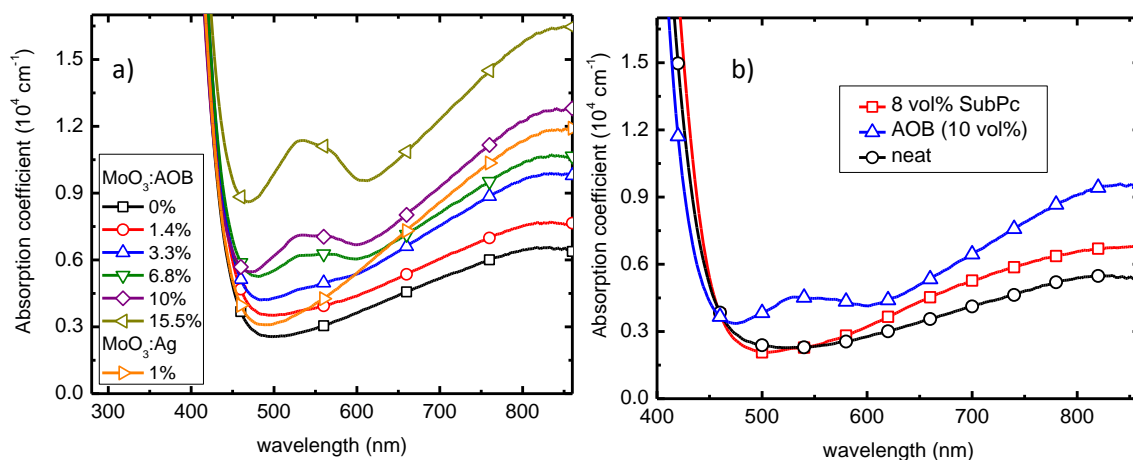


**Figure 10.6** Resistivity of MoO<sub>3</sub> films doped with AOB, measured from ITO/MoO<sub>3</sub>:AOB/Au sandwich-type devices.

we see the emergence of a new absorption peak appear near  $\lambda = 530$  nm for higher doping concentrations of AOB. This absorption does not correspond to that of neat AOB, but may indicate energy transfer from dopant to host. This peak does not appear when doping with SubPc, indicating that energy transfer is not occurring in that case.

Doped MoO<sub>3</sub> films were then incorporated into OPVs. The first device structure consisted of glass/ITO/40 nm MoO<sub>3</sub>:dopant/9 nm MoO<sub>3</sub>/13 nm SubPc/40 nm C<sub>60</sub>/8 nm bathocuproine (BCP)/100 nm Ag. A control device with no MoO<sub>3</sub> was also included for comparison. The dark and illuminated *J-V* curves for these devices are shown in Figure 10.8. We can extract  $R_S$  from the dark *J-V* curves at forward bias by using a simplified version of the ideal diode equation in Eq. (6.1). Table 10.2 shows that while  $R_S = 112 \pm 1 \Omega\text{cm}^2$  for the undoped case, it is reduced to  $4.3 \pm 0.1 \Omega\text{cm}^2$  when doped with 1 vol% Ag and  $6.5 \pm 0.1 \Omega\text{cm}^2$  when doped with 10 vol% AOB, which is near the value of  $4.4 \pm 0.3$

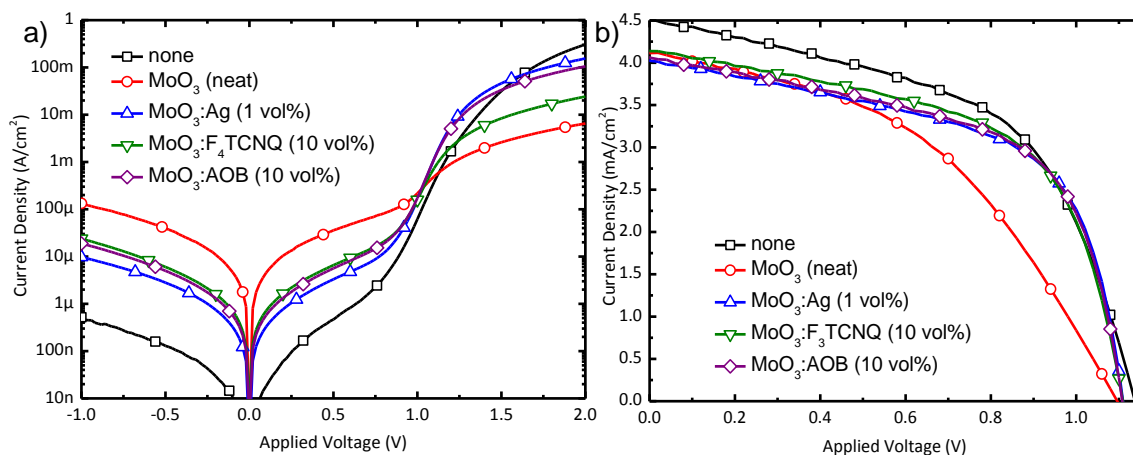




**Figure 10.7** Absorption coefficient of doped MoO<sub>3</sub> films deposited on quartz.

$\Omega\text{cm}^2$  obtained without a MoO<sub>3</sub> layer.  $R_S$  also decreases when F<sub>4</sub>TCNQ is used, though to a lesser degree. This is unexpected, as F<sub>4</sub>TCNQ is typically used as a p-type dopant for organic materials and MoO<sub>3</sub> is an n-type material. It is possible that, because the ionization potential of MoO<sub>3</sub> is larger, F<sub>4</sub>TCNQ in this case is acting as a weak n-type dopant.

Similar devices were fabricated with 90 nm MoO<sub>3</sub> layers and varying concentrations of



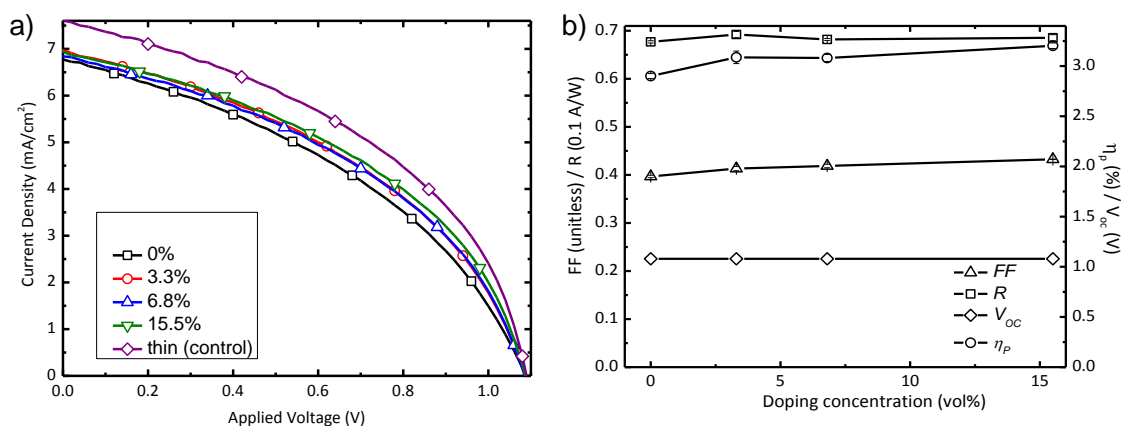
**Figure 10.8** Dark (a) and one-sun illuminated (b) plots of the  $J$ - $V$  characteristics of OPVs incorporating MoO<sub>3</sub> layers doped with Ag, F<sub>4</sub>TCNQ, and AOB.

**Table 10.2** Comparison of the series resistance for OPVs with different buffer layers.

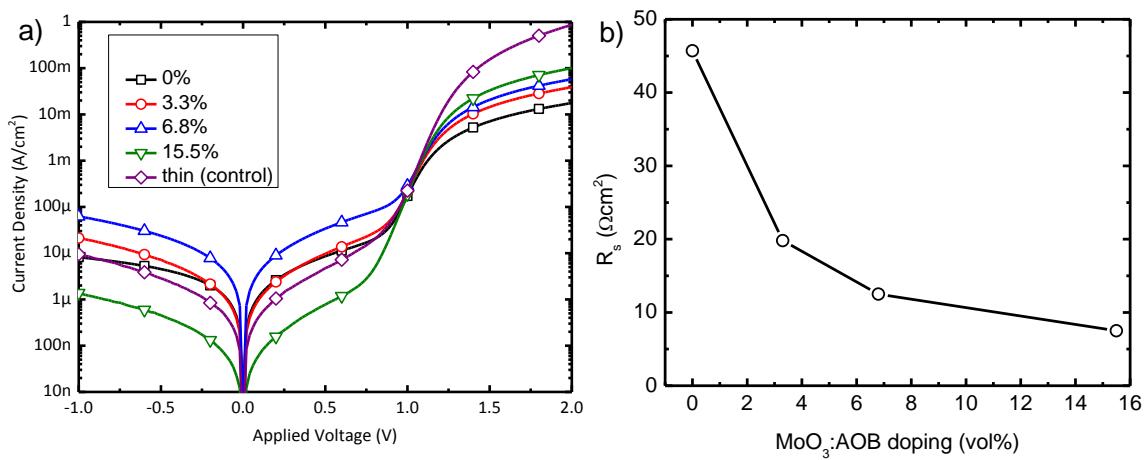
Buffer	Dopant	Ratio(vol%)	$R_S(\Omega\text{cm}^2)$
None	n/a	n/a	$4.4\pm 0.3$
MoO <sub>3</sub>	None	0	$112\pm 1$
MoO <sub>3</sub>	Ag	1	$4.3\pm 0.1$
MoO <sub>3</sub>	F <sub>4</sub> TCNQ	10	$29.8\pm 0.4$
MoO <sub>3</sub>	AOB	10	$6.5\ 0.1$
MoO <sub>3</sub>	SubPc	4	$70.7\pm 0.3$

AOB as the dopant. Device performance is shown in Figure 10.9. As shown in Figure 10.10,  $R_S$  decreased from  $46\ \Omega\text{cm}^2$  for the neat case to  $8\ \Omega\text{cm}^2$  for 15.6 vol% AOB.

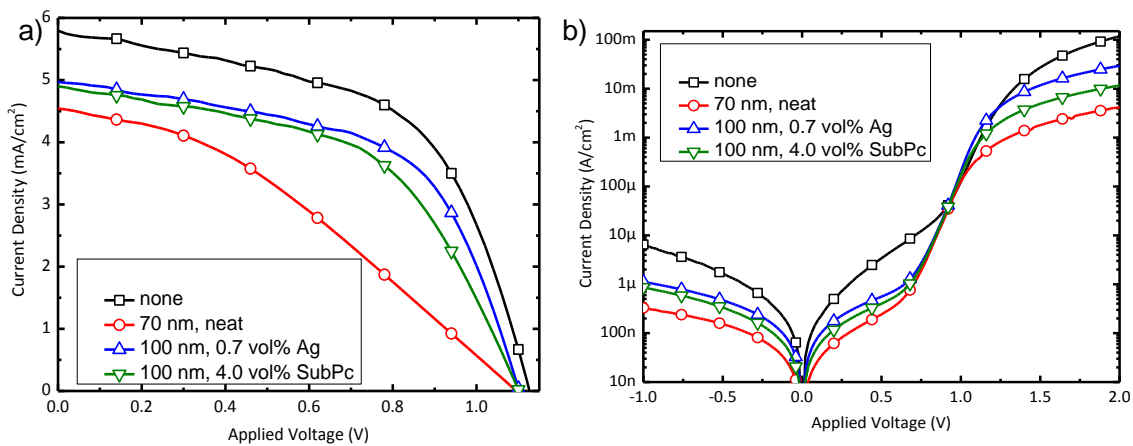
Similar devices were also fabricated using SubPc as a dopant. In this case, a thick MoO<sub>3</sub> layer was doped with 0.7 vol% Ag, 4.0 vol% SubPc, or undoped. Device performance is shown in Figure 10.11. Performance is improved with SubPc doping as compared to the undoped case, though less so than with Ag. It is likely that optimizing the doping ratio would further improve performance.



**Figure 10.9** One-sun illuminated  $J$ - $V$  characteristics (a) and performance parameters (b) of OPV devices as a function of AOB doping concentration.



**Figure 10.10** Dark  $J$ - $V$  characteristics (a) and series resistance (b) of OPV devices as a function of AOB doping concentration.



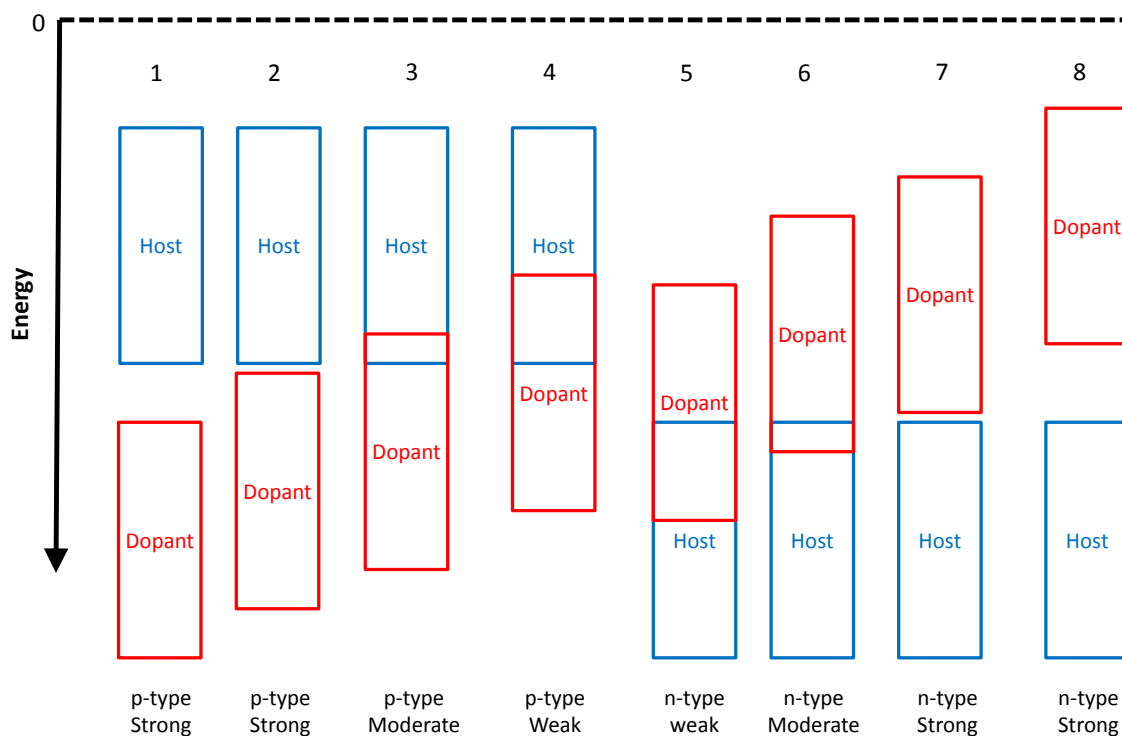
**Figure 10.11** One-sun illuminated  $J$ - $V$  characteristics (a) and performance parameters (b) of OPV devices comparing different buffer layers.

### 10.2.3 Discussion

Generally, the doping of metal oxide films seems to behave similarly to the doping of small molecule organic films. When the highest occupied molecular orbital (HOMO) of the dopant is smaller than the lowest unoccupied molecular orbital (LUMO) of the host, n-type doping occurs, as shown in Fig. 10.12. Conversely, when the LUMO of the dopant is larger than the HOMO of the host, p-type doping occurs. Because the LUMO of MoO<sub>3</sub> is very large (~6 eV), a wide range of organic materials may be used for n-type doping: AOB (~3 eV), pentacene (5.0 eV), tetracene (5.2 eV), CuPc (5.2 eV), NPD (5.3 eV), DIP (5.5 eV), SubPc (5.6 eV), Alq<sub>3</sub> (5.8 eV), or many others. This would also apply to other metal oxides with similar energy levels (CrO<sub>3</sub>, V<sub>2</sub>O<sub>5</sub>, WO<sub>3</sub>, etc); however, this group of materials is very difficult to p-type dope because of their very large HOMO (~9 eV). This is corroborated by our experimental data, where doping with the organic with a large LUMO (F<sub>4</sub>TCNQ, 5.2 eV) leads to weak n-type doping. In the case of metal oxides with smaller HOMO levels such as CuO at 5.2 eV, p-type doping with F<sub>4</sub>TCNQ is likely possible. Because the HOMO of AOB is very small (~3 eV), it is likely to act as an n-type dopant for a wide range of metal oxides, including MoO<sub>3</sub>, CrO<sub>3</sub>, V<sub>2</sub>O<sub>5</sub>, WO<sub>3</sub>, NiO, Cr<sub>3</sub>O<sub>4</sub>, Cr<sub>2</sub>O<sub>3</sub>, CuO, TiO<sub>2</sub>, Ta<sub>2</sub>O<sub>5</sub>, Cu<sub>2</sub>O, and many others.

The use of doped metal oxide films is likely to be beneficial in other devices. For example, Timmreck et al.<sup>179</sup> recently demonstrated the use of doped organic transport layers for the recombination zone in tandem OPVs. Rather than organic transport layers, metal oxides doped with organic molecules could be used for either the hole-transport layer, the electron transport layer, or both.

Another application is in stacked organic light emitting diodes (SOLEDs), where mul-



**Figure 10.12** Schematic of energy levels necessary for n- and p-type doping.

multiple active layers are combined monolithically. In this case, a charge generation layer (CGL) consisting of doped organic/MoO<sub>3</sub> has been used by Kanno et al.<sup>264</sup> When voltage is applied to the device, the CGL generates an electron on the organic side and a hole on the MoO<sub>3</sub> side, which then contribute to light emission. As this process is dependent on the availability of free charges,<sup>265</sup> it is likely that doping the MoO<sub>3</sub> layer with an organic molecule, thereby increasing the free charge density, would lead to improved performance.

It may also be possible to dope oxide films that are deposited from solution. Although all data shown here utilizes MoO<sub>3</sub> deposited by vacuum thermal evaporation, it is also possible to deposit MoO<sub>3</sub> from solution via spincoating, spray coating, doctor-blading, or

other techniques. Doping of oxide films deposited from solution with organic molecules is also possible, if a solvent is chosen in which both materials are soluble.

#### **10.2.4 Conclusions**

In this work, we demonstrated reduced resistivity in metal oxide thin films by doping with organic molecules. As examples, we presented MoO<sub>3</sub> doped with Ag, F<sub>4</sub>TCNQ, AOB, or SubPc. In all cases, the resistivity decreased, leading to decreased series resistance when incorporated into OPV devices. We have shown that doping with organic molecules is a viable method for improving the charge transport properties of metal oxide thin films.

### **10.3 Mixed buffer layers**

#### **10.3.1 Background**

In Chapter 6 we employed PTCBI as a cathode buffer layer,<sup>228</sup> leading to a significant increase in fill factor ( $FF$ ) in squaraine-based OPVs. Our recent experimental data indicates that the C<sub>60</sub>/PTCBI interface quenches excitons, leading to a reduction in  $J_{SC}$  for bilayer devices. In this appendix, we investigate using a mixture of C<sub>60</sub> and bathocuproine as a cathode buffer layer, leading to improved performance in bilayer OPVs.

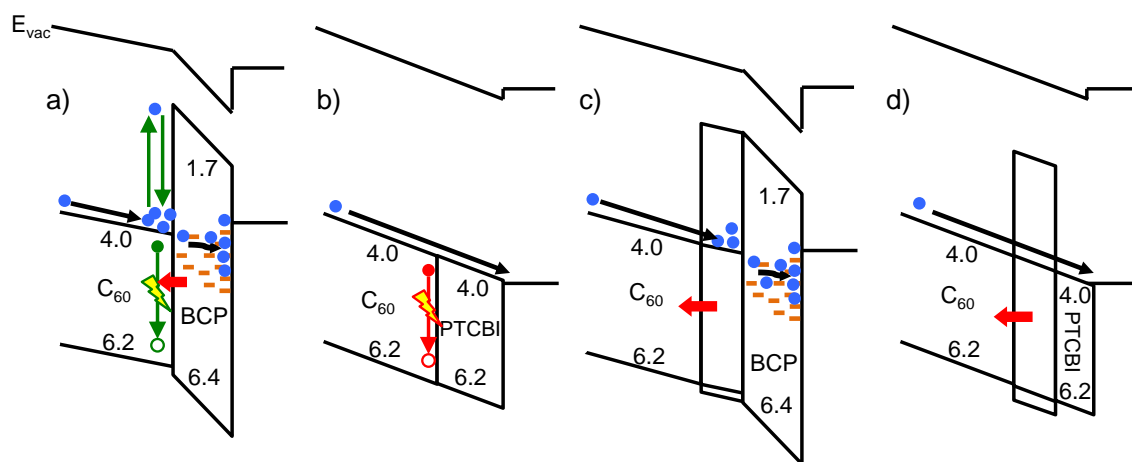
#### **10.3.2 Theory**

Our proposed energy level diagram for different buffer layers is shown in Fig. 10.13. Electrons are represented by blue circles, excitons by a filled circle connected to an open circle,

exciton quenching is represented by a lightning bolt, exciton blocking is represented by a red horizontal arrow, electron conduction is represented by black arrows, exciton-polaron annihilation is represented by green arrows, and exciton quenching is represented by red vertical arrows. For the case of BCP, conduction through the defect states (orange rectangles) is slow, leading to a build-up of electrons at the  $C_{60}$ /BCP interface.<sup>200</sup> Although excitons are blocked at this interface, the build-up of electrons increases the probability of exciton-polaron annihilation, where the exciton energy transfers to the electron, which then relaxes back to the  $C_{60}$  LUMO. For PTCBI, electron conduction occurs through the LUMO of both  $C_{60}$  and PTCBI without significant barriers;<sup>228</sup> however, there is significant exciton quenching at the  $C_{60}$ /PTCBI interface, we will demonstrate subsequently. For the case of a  $C_{60}$ :BCP buffer layer followed by neat BCP, some excitons are blocked at the  $C_{60}$ / $C_{60}$ :BCP interface, but there is still a build-up of charges. For the fourth case, exciton blocking is provided by the  $C_{60}$ :BCP layer, and electron conduction occurs through the LUMO of  $C_{60}$ , the LUMO of  $C_{60}$  in the  $C_{60}$ :BCP layer, and then PTCBI.

### 10.3.3 Experiment

Devices were fabricated similarly to the DPSQ/ $C_{60}$  single-cells discussed in Chapter 8.3.1. Mixed layers of  $C_{60}$ :BCP were coevaporated at a total rate of 0.1 nm/s. Biased *EQE* measurements were performed by utilizing a current amplifier in series with the lock-in amplifier. Samples for photoluminescence (PL) experiments consisted of glass/60 nm  $C_{70}$ /8 nm test layer, where the test layer consisted of BPhen as a blocker,<sup>173</sup> N,N'-bis(1-naphthyl)-N,N'-diphenyl-1,1'-biphenyl-4,4'-diamine (NPD) as a quencher,<sup>122,266</sup> and PTCBI, and were illuminated at  $\lambda = 300$  nm. Modeled *EQE* spectra were calculated as described in



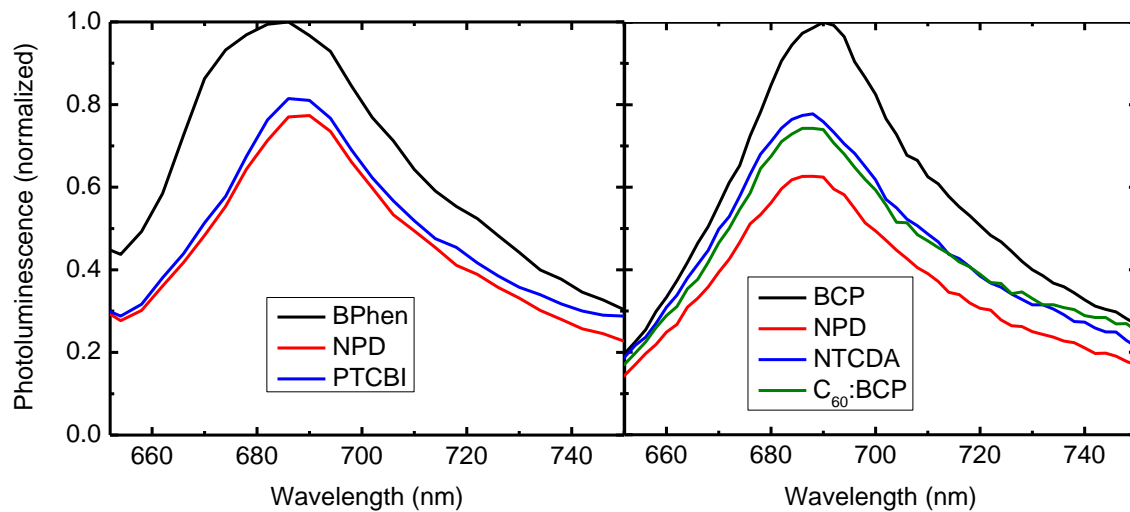
**Figure 10.13** Proposed equilibrium energy level diagram for various buffer layers. Electrons are represented by blue circles, excitons by a filled circle connected to an open circle, quenching is represented by a lightning bolt, blocking is represented by a red horizontal arrow, black arrows represent electron conduction, green arrows represent exciton-polaron annihilation, and red arrows represent exciton quenching. Note: figure is not to scale.

Chapter 2.8.<sup>47</sup> Optical constants were measured by variable-angle scanning ellipsometry.

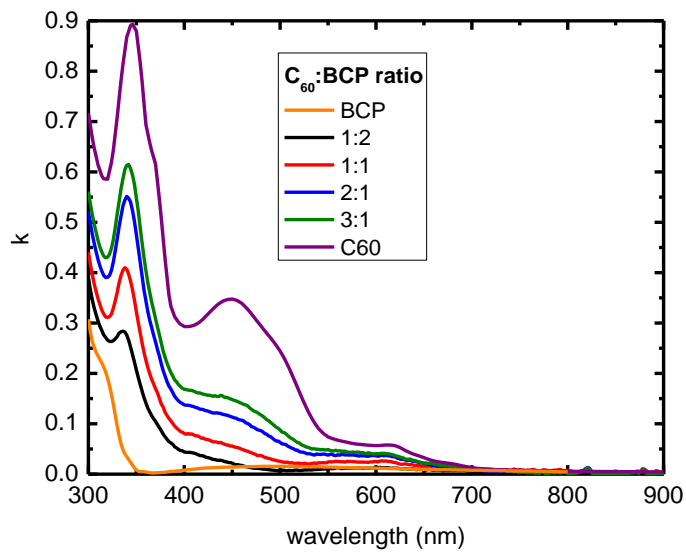
### 10.3.4 Results

Photoluminescence spectra were measured for samples of  $C_{70}$  with BPhen, NPD, NTCDA,  $C_{60}$ :BCP, and PTCBI as test layers, shown in Fig. 10.14. The samples with NPD and PTCBI have similar magnitudes, while the sample with BPhen is significantly larger. For NTCDA and  $C_{60}$ :BCP films, the PL intensity is between that of the blocking (BCP) and quenching (NPD) layers, indicating that the interfaces are partially blocking. The extinction coefficients ( $k$ ) for neat  $C_{60}$ , neat BCP, and mixtures thereof, are shown in Fig. 10.15. As BCP is mixed with  $C_{60}$ , the absorption peak at  $\lambda = 340$  nm decreases linearly, while the peak at  $\lambda = 460$  nm decreases significantly more, with  $k$  decreasing  $> 80\%$  at a 1:1 mixing ratio.





**Figure 10.14** Normalized photoluminescence spectra for  $C_{70}$  films capped with various test layers. Data courtesy of Kevin J. Bergemann and Anurag Panda.



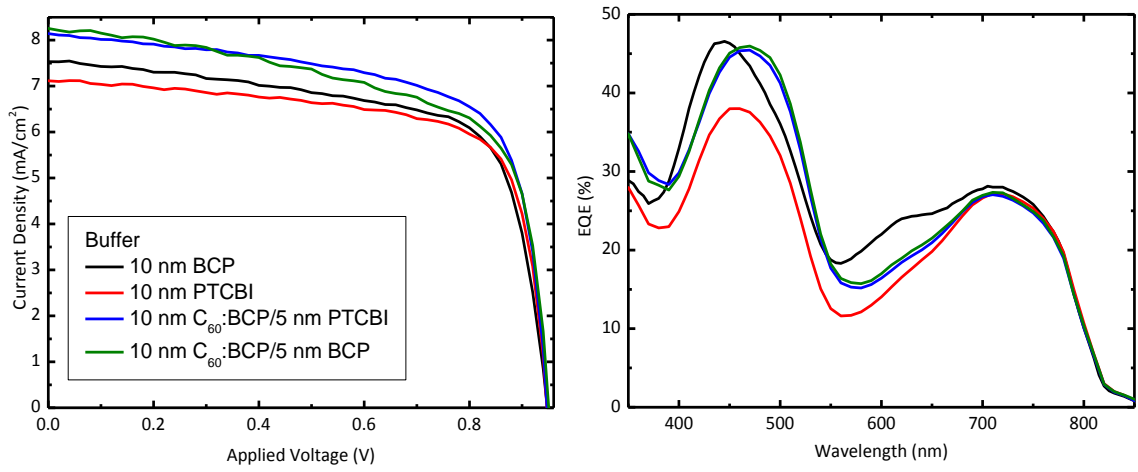
**Figure 10.15** Extinction coefficients for thin films of  $C_{60}$ , BCP, and mixtures thereof.

Devices were fabricated with the following structure: glass/100 nm ITO/15 nm MoO<sub>3</sub>/13 nm DPSQ/40 nm C<sub>60</sub>/buffer/100 nm Al, where the buffer layers consisted of 10 nm BCP, 10 nm PTCBI, 10 nm C<sub>60</sub>:BCP (1:1 vol. ratio)/5 nm BCP, and 10 nm C<sub>60</sub>:PTCBI (1:1 vol. ratio)/5 nm BCP. Data for *J-V* characteristics and *EQE* spectra are shown in Fig. 10.16, and device performance is summarized in Table 10.3. Figure 10.17 shows the *EQE* spectra when the devices were biased to +0.5 or -1.0 V, normalized to the zero-bias spectra. For all devices, the change in the DPSQ response ( $\lambda > 600$  nm) upon biasing is similar, while there is a significant difference in the C<sub>60</sub> response ( $\lambda < 600$  nm). The two devices with PTCBI have a change in *EQE* of approximately -15% +15% at +0.5 and -1.0 V, respectively, while the device with BCP has changes of -30% and +20%, respectively.

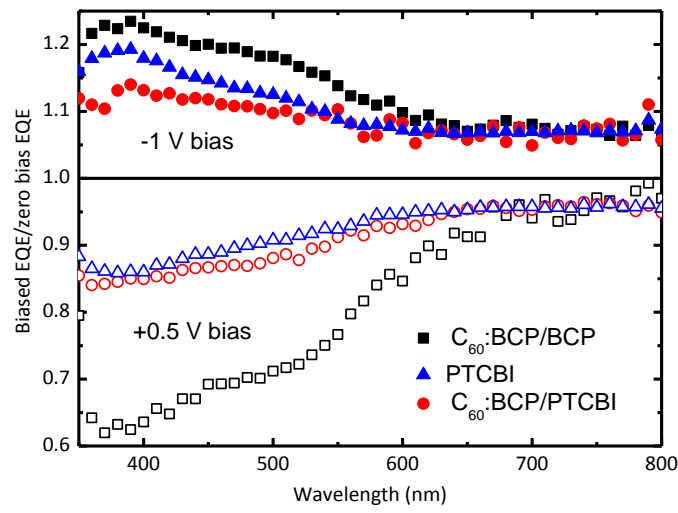
Devices were also fabricated where the volume fraction of BCP in C<sub>60</sub> was varied from 0 to 70% for a device with the following structure: glass/100 nm ITO/15 nm MoO<sub>3</sub>/13 nm DPSQ/35 nm C<sub>60</sub>/15 nm C<sub>60</sub>:BCP/100 nm Ag. Device *J-V* characteristics and *EQE* spectra are shown in Fig. 10.16, where the *J*<sub>SC</sub> increases with the volume fraction from 7.7 mA/cm<sup>2</sup> at 0 vol% to a peak of 8.1 mA/cm<sup>2</sup> at 50 vol%, decreasing at higher volume fractions. The *EQE* spectra show a similar trend, with nearly all of the increases occurring in the C<sub>60</sub>

**Table 10.3** Organic photovoltaic performance for devices with various buffer layers under simulated 1 sun AM1.5G illumination, corrected for spectral mismatch. Films of C<sub>60</sub>:BCP have  $\approx$  1:1 volume ratio.

Buffer	$V_{OC}$ (V)	$FF$ (%)	$J_{SC}$ (mA/cm <sup>2</sup> )	$\eta_p$ (%)	$M$
10 nm PTCBI	0.95	71	7.1	4.8 ± 0.1	0.96
10 nm BCP	0.95	65	7.5	4.8 ± 0.1	0.96
10 nm C <sub>60</sub> :BCP/5 nm BCP	0.95	64	8.3	5.0 ± 0.1	0.97
10 nm C <sub>60</sub> :BCP/5 nm PTCBI	0.95	68	8.1	5.3 ± 0.1	0.97



**Figure 10.16** (left) *J-V* characteristics at 1-sun simulated illumination and (right) *EQE* spectra for DPSQ/C<sub>60</sub> devices with various buffer layers.



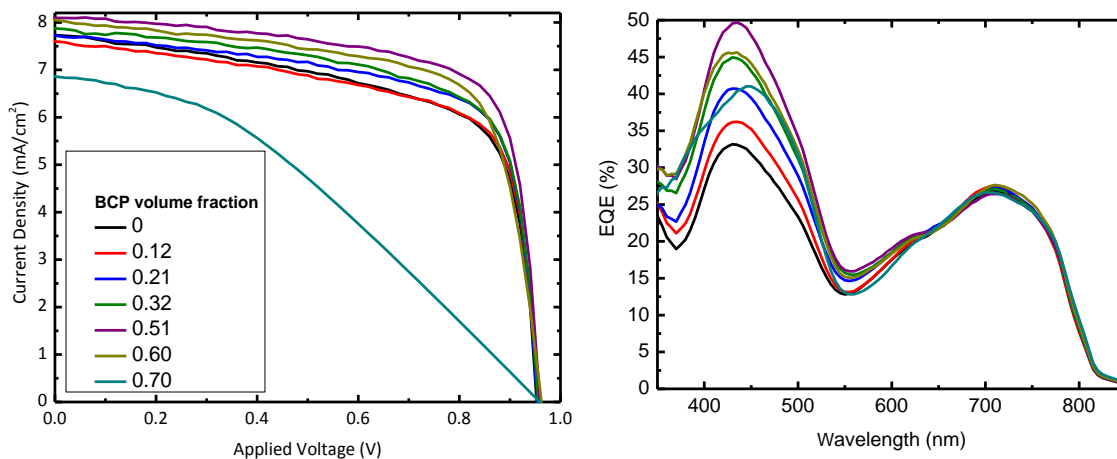
**Figure 10.17** Voltage-biased, normalized external quantum efficiency spectra for devices with various buffer layers. Filled symbols are biased at -1.0 V, while open symbols are biased at +0.5 V.

response at  $\lambda < 600$  nm.

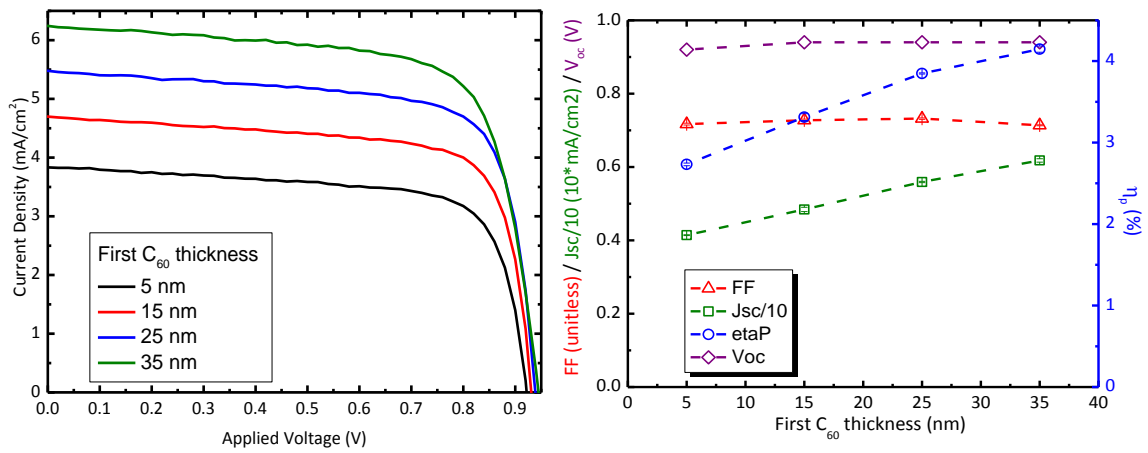
Finally, devices were fabricated with a layer of  $C_{60}$ :BCP inserted into the  $C_{60}$  active layer in the following structure: glass/100 nm ITO/15 nm  $MoO_3$ /13 nm DPSQ/ $x$  nm  $C_{60}$ /10 nm  $C_{60}$ :BCP/40 -  $x$  nm  $C_{60}$ /100 nm Ag. Figure 10.19 shows the  $J$ - $V$  characteristics and performance parameters as a function of  $x$ , where  $J_{SC}$  and  $\eta_p$  increase linearly with  $x$ , while Fig. 10.20 shows the  $EQE$  spectra for the same devices (symbols). Here, the  $L_D$  for the active layers have been fit to the experimental  $EQE$  spectra, and the resulting modeled  $EQE$  spectra are shown as solid lines. Nearly all of the change in  $EQE$  occurs in the  $C_{60}$  response at  $\lambda < 600$  nm.

### 10.3.5 Discussion

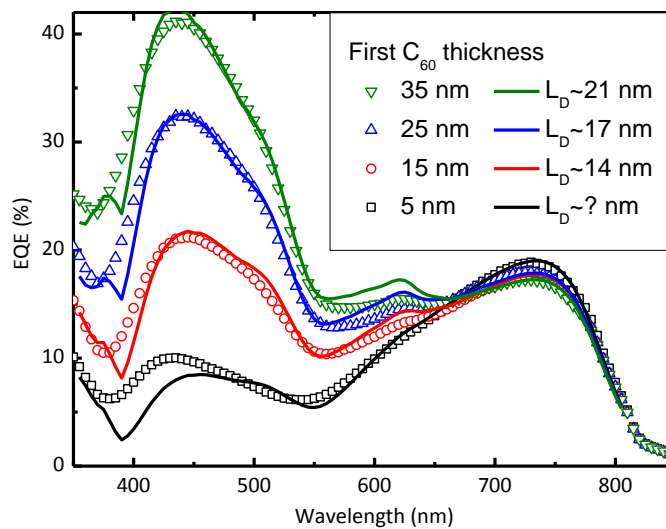
The PL data in Fig. 10.14 indicates that the  $C_{70}$ /PTCBI interfaces quenches excitons, similarly to NPD. From this, we infer that  $C_{60}$ /PTCBI interfaces are also quenching, as  $C_{60}$  and



**Figure 10.18** (left)  $J$ - $V$  characteristics at 1-sun simulated illumination and (right)  $EQE$  spectra for DPSQ/ $C_{60}$  devices with various  $C_{60}$ :BCP mixing ratios in the buffer layer.



**Figure 10.19** (left) *J-V* characteristics at 1-sun simulated illumination and (right) performance parameters devices with various C<sub>60</sub>:BCP mixing ratios positions.



**Figure 10.20** Experimental (symbols) and modeled (lines) *EQE* spectra for devices varying the C<sub>60</sub>:BCP buffer layer position.

C<sub>70</sub> are known to have nearly identical energy levels.

Comparing different buffer layers shown in Fig. 10.16, we see two differences: the magnitude of  $J_{SC}$  and the slope of the  $J_{SC}$  at  $V = 0$ . Devices with BCP as the final organic layer have larger slope, while those with PTCBI have smaller slope. Additionally, we see that the insertion of a C<sub>60</sub>:BCP layer increases the value of  $J_{SC}$ . By combining both the C<sub>60</sub>:BCP and PTCBI layers, we arrive at the highest-performing device, increasing  $\eta_p$  from  $4.8 \pm 0.1\%$  to  $5.3 \pm 0.1\%$ , as shown in Table 10.3.

To further understand the origin of this improvement, in Fig. 10.17 we analyze the voltage-biased  $EQE$  where the bias dependence is primarily from the C<sub>60</sub> contribution at  $\lambda < 550$  nm. The magnitude of this change is much larger when BCP is used rather than PTCBI. This lends credence to the notion that there is charge build-up at the C<sub>60</sub>/BCP interface, which gives rise to exciton-polaron annihilation. Applying reverse bias sweeps the charges out more effectively, leading to less quenching; however, this may instead be due to the electric-field dependence of charge transfer (CT) excitons in C<sub>60</sub> or some other mechanism.

For a device that incorporates C<sub>60</sub>:BCP, increasing the BCP concentration in the buffer leads to increased  $J_{SC}$ , as shown in Fig. 10.18. Increases in concentration lead to a monotonic increase in  $J_{SC}$  and C<sub>60</sub>  $EQE$  up to 50 vol%. Higher concentrations lead to decreased performance due to increased series resistance, as BCP has inappropriate energy levels for electron extraction (see Fig. 10.13).

One reason that C<sub>60</sub>:BCP works well as a buffer layer is that it is nearly transparent in the visible spectrum. Although C<sub>60</sub> has a significant absorption peak at  $\lambda = 450$  nm, Fig. 10.15 shows that the peak decreases faster than the volume fraction of C<sub>60</sub> decreases.

At a mixing ratio of 1:1, this peak has decreased  $> 80\%$ . This is due to the fact that this peak originates from a CT exciton which spans a molecule and its nearest neighbors. As BCP is mixed in, each  $C_{60}$  has less nearest neighbors, destabilizing the CT exciton. On the other hand, the absorption peak at  $\lambda = 340$  nm is due to a mono-molecular Frenkel exciton, causing this peak to decrease proportionally to the concentration of BCP.

The data in Fig. 10.16 suggest that the  $C_{60}$ :BCP buffer layer does not completely quench or block excitons. To further understand this behavior, we fabricated a device which places a 10 nm  $C_{60}$ :BCP layer into the middle of the  $C_{60}$  active layer. The  $J$ - $V$  characteristics and performance parameters for these devices is shown in Fig. 10.19 as a function of the thickness of the first  $C_{60}$  neat layer. The total layer thickness in the devices was kept constant. It can be seen that  $J_{SC}$  and  $\eta_p$  increase monotonically with thickness, while other parameters stay nearly constant. More insight can be gleaned by analyzing the  $EQE$  spectra for these devices, shown in Fig. 10.20. The open symbols represent the experimental data, while the lines are calculated to a transfer matrix/exciton dynamics model with the exciton diffusion lengths ( $L_D$ ) as the fitting parameters. The decrease in  $L_D$  with layer thickness indicates that the model is not accurately characterizing  $L_D$ . This is likely due to the assumption that the  $C_{60}/C_{60}$ :BCP interface is perfectly blocking, whereas it is likely partially blocking; nevertheless, this does show that this interface is not completely quenching excitons, as  $L_D$ s are on the order of the layer thickness.

### 10.3.6 Conclusions

While this project is still in progress, the data thus far indicate that an electron-conducting buffer layer consisting of a mixture of  $C_{60}$  and BCP is beneficial to device performance.

By combining C<sub>60</sub>:BCP and PTCBI in a buffer layer, we have increased both the  $J_{SC}$  and  $FF$  of the device, leading to an improvement in power conversion efficiency of > 10%.



# Chapter 11

## Conclusions

In this work, we have demonstrated progress in the field of organic photovoltaics. In Chapter 3, we presented a simple organic vapor phase deposition system scaled to a substrate size of 200 mm. The design used a large gas transport tube for all materials, eliminating the problems with pressure drops and cold spots experienced in previous designs. Using this system, we demonstrated a uniformity of  $\pm 1.6\%$  over a 200 mm wafer and a material utilization exceeding 40%. Our simulations showed the potential adaptability of this approach to large scale deposition of organic films, with the possibility of low-cost deposition of OPVs.

In Chapter 4, we demonstrated a fully-inverted OPV device based on a simple SubPc/C<sub>60</sub> bilayer structure with a power conversion efficiency of 2.5%. We did this by eliminating the cathode buffer layer entirely and varying the cathode metal and anode buffer layer work function to maximize the open-circuit voltage. By doing so, we were able to achieve similar performance to that of a conventional device. This was followed in Chapter 5, where we demonstrated improved OPV performance resulting from a change in crystalline orientation achieved via structural templating of subsequently deposited layers of DIP and CuPc. Using

PTCDA as a crystalline template, the DIP and CuPc molecular stacking were modified from a standing-up to a flat-lying orientation relative to the substrate plane. For CuPc, this led to improvement in orbital overlap between adjacent molecules, and hence changes in frontier energy levels and absorption coefficient that combine to substantially increase the power conversion efficiency. In addition, DIP propagated the structural templating, changed CuPc film morphology, and served as an exciton blocking layer between PTCDA and CuPc. The OPV efficiency increased from  $1.42 \pm 0.04\%$  to  $2.19 \pm 0.05\%$  for a planar heterojunction, and from  $1.89 \pm 0.05\%$  to  $2.49 \pm 0.03\%$  for a planar-mixed heterojunction by the improved stacking arrangements of CuPc in a CuPc/C<sub>60</sub> OPV cell. Our results showed the impact of controlling the crystalline morphology and orientation on organic optoelectronic properties.

Next, in Chapter 6 we demonstrated the use of electron conducting buffer layers in OPVs. Here, electrons are transported via the LUMO states directly from that of the acceptor to the cathode. By using PTCBI as a buffer layer, we found  $FF = 0.70 \pm 0.01$ , compared to  $FF = 0.60 \pm 0.01$  for conventional BCP-based devices. Adding an NTCDA electron-conducting EBL in combination with PTCBI allowed for optimized optical spacing and efficient exciton blocking, leading to an increase in  $\eta_p$  that is  $>25\%$  for an analogous fSQ/C<sub>60</sub>/BCP OPV.

In Chapters 8 and 9, we demonstrated three high-efficiency tandem OPV devices. First, we incorporated a vapor-deposited SubPc:C<sub>70</sub> graded heterojunction and solution-processed SVA-DPSQ/C<sub>70</sub> bilayer heterojunction sub-cells that efficiently harvests photons up to wavelengths of  $\lambda = 800$  nm. The incorporation of C<sub>70</sub> in both sub-cells in the place of the archetypal C<sub>60</sub> leads to higher absorption across the green and yellow spectral regions, increasing  $J_{SC}$  by  $> 30\%$ . The resulting tandem device demonstrated  $\eta_p = 6.6 \pm 0.1\%$ ,

with  $V_{OC} = 1.97 \pm 0.1$ , indicating a nearly lossless Ag nanoparticle/MoO<sub>3</sub> charge recombination layer interposed between the sub-cells. A similar device consisting of a solution-processed solvent-vapor-annealed blended squaraine/C<sub>70</sub> bilayer heterojunction, with a vapor-processed DBP:C<sub>70</sub> planar-mixed heterojunction obtained efficient photon harvesting at  $\lambda < 800$  nm while providing an open-circuit voltage ( $V_{OC}$ ) of 1.85 V and  $\eta_p = 8.3 \pm 0.4\%$ . We also demonstrated a small molecule tandem OPV consisting of two solution- and vapor-processed, blended functionalized-squaraine/fullerene sub-cells. Here, the relatively low solubility of fullerenes in THF lead to prevention of penetration of this solvent into the underlying blended *f*SQ donor layer, thereby minimizing layer dissolution and damage. Damage was further reduced by solvent vapor annealing of the front sub-cell, where the increased crystallinity of the blended-*f*SQ layer also reduced the ability of this solvent from penetrating and ultimately damaging the pre-deposited layers. The resulting tandem cell had a power conversion efficiency of  $\eta_p = 6.2 \pm 0.3\%$  and an open circuit voltage of  $V_{OC} = 1.78 \pm 0.01$ , or nearly the sum of the constituent sub-cells.

Lastly, we developed a framework to understand tandem OPVs with an arbitrary number of sub-cells. The criteria to minimize the power conversion efficiency penalty,  $\Delta\eta$  (i.e. the loss incurred when one or more sub-cells are not operating at their MPPT when the tandem cell is at its MPPT), was found to be that such the current at the maximum power point for each sub-cell must be equal. We also calculated the tandem spectral mismatch factor and fill factor, which are functions of both the  $FF$  and  $J_{SC}$  of all the sub-cells comprising the tandem. We developed an analytical model that accurately represents both bilayer and mixed-layer OPVs used in two archetype tandem cells. This model was used to understand tandem device operation. In the case of tandem cells consisting of sub-cells with dissimilar

$FF$ , the tandem  $FF$  tends towards the sub-cell with lowest  $J_{SC}$ . The tandem spectral mismatch factor is a function of the spectral mismatch,  $J_{SC}$ , and  $FF$  of each sub-cell. Additionally,  $\Delta\eta$  is minimized when the sub-cell with the lowest  $FF$  has the highest  $J_{SC}$ . For the case of tandem cells consisting of sub-cells with similar  $FF$ , the tandem spectral mismatch factor is equal to the average of that of the sub-cells, and  $\Delta\eta$  is minimized when the sub-cells have equal  $J_{SC}$ . We extended these findings to tandem cells with an arbitrary number of sub-cells, where the optimum distribution of the total photocurrent generated in the stack is such that the sub-cell  $J_{SC}$  is proportional to  $J_{SC}/J_M$  (a constant) for each sub-cell. This minimizes  $\Delta\eta$ , leading to a maximum tandem power conversion efficiency for a particular combination of sub-cell architectures and materials combinations.

Looking forward, many challenges and opportunities in OPVs remain. As seen in Fig. 1.5, the progress in power conversion efficiencies of OPVs has been rapid over the past 5 years, recently reaching 12.0%. As performance approaches that of established technologies such as CdTe and CIGS, OPVs must begin to address other practical issues. First and foremost, OPV lifetime must be determined. What is the inherent stability of OPV materials? What form of encapsulation will be necessary to minimize water and oxygen exposure? Will UV filters be necessary to decrease damage caused by high energy photons? What properties will create the organic active materials with the longest lifetime? These are the questions that are now being addressed by the world-wide research community.

After efficiency and lifetime have been addressed, the last question is cost. Simply having a lower cost for the thin-film active layer materials will not be sufficient, as the active materials in CdTe and CIGS thin film cells is already a small fraction of the total module and balance of systems cost. Low temperature deposition onto low-cost substrates

such as plastic or metal foils may decrease the cost slightly, especially if a lower-cost alternative to ITO as an anode can be used. It may be possible for OPVs to find niche applications such as highly portable PV, where low weight is more important than long lifetime. Nevertheless, it is a competitive market, and it is unclear at this point what role OPV will play in the future. As a wise man once said, "Never underestimate silicon."

# Appendix

# Appendix A

## List of publications, conference presentations, and patents

### A.1 Publications

1. B. E. Lassiter et al., "Tandem organic photovoltaics incorporating two solution-processed small molecule donor layers," submitted **xxx**, xxxxxx (2013).
2. A. Bartynski et al., "A Fullerene-Based Organic Exciton Blocking Layer with High Electron Conductivity," submitted **xxx**, xxxxxx (2013).
3. B. E. Lassiter et al., "Understanding tandem organic photovoltaic cell performance," accepted J. Appl. Phys. **xxx**, xxxxxx (2013).
4. J. D. Zimmerman et al., "Morphology control and epitaxy in blended squaraine films," submitted **xxx**, xxxxxx (2013).
5. X. Xiao et al., "A hybrid planar-mixed tetraphenyldibenzoperiflanthene/C<sub>70</sub> photovoltaic cell," Appl. Phys. Lett. **102**, 073302 (2013).
6. B. E. Lassiter et al., "Tandem organic photovoltaics using both solution and vacuum deposited small molecules," Appl. Phys. Lett. **101**, 063303 (2012).
7. C. K. Renshaw, J. D. Zimmerman, B. E. Lassiter, et al., "Photoconductivity in Or-

ganic Photovoltaics," Phys. Rev. B **86**, 085324 (2012).

8. K. S. Yook et al., "Vertical orientation of copper phthalocyanine in organic solar cells using a small molecular weight organic templating layer," Appl. Phys. Lett. **99**, 043308 (2011).
9. B. E. Lassiter et al., "Organic photovoltaics incorporating electron conducting exciton blocking layers," Appl. Phys. Lett. **98**, 243307 (2011).
10. B. E. Lassiter et al., "Structural templating of multiple polycrystalline layers in organic photovoltaic cells," Optics Express **18**, A444 (2010).
11. X. R. Tong, B. E. Lassiter, and S. R. Forrest, "Inverted organic photovoltaic cells with high open-circuit voltage" Organic Electronics **11**, 705 (2010).
12. N. C. Giebink, B. E. Lassiter, G. P. Wiederrecht, M. R. Wasielewski, and S. R. Forrest "Ideal diode equation for organic heterojunctions. II. The role of polaron pair recombination" Phys. Rev. B **82**, 155306 (2010).
13. R. R. Lunt, B. E. Lassiter, J. B. Benziger, and S. R. Forrest, "Organic vapor phase deposition for the growth of large area organic electronic devices" Appl. Phys. Lett. **95**, 233305 (2009).
14. N. Li, B. E. Lassiter, G. Wei, and S. R. Forrest, "Open circuit voltage enhancement due to reduced dark current in small molecule photovoltaic cells" Appl. Phys. Lett. **94**, 023307 (2009).

## A.2 Conferences

1. "Tandem organic photovoltaics using both solution and vacuum deposited small molecules," MRS Fall 2012 Meeting, Boston (2012).
2. "Electron Conducting Buffer Layers in Organic Photovoltaics," 37th IEEE PVSC, Seattle, WA (2011).
3. "Structural templating of organic photovoltaic cells to achieve increased power con-



version efficiency," International Conference on Electroluminescence (2010).

4. "Scaling of Organic Vapor Phase Deposition for Large-Area Organic Optoelectronics" B. E. Lassiter, R. R. Lunt, S. R. Forrest. MRS Fall Meeting, Boston, MA (2009).
5. "Improved Open-circuit Voltage of Inverted Small Molecule Organic Photovoltaic Cells" X. R. Tong, B. E. Lassiter, S. R. Forrest. MRS Fall Meeting, Boston, MA (2009).
6. "Understanding Organic Solar Cells Near Open Circuit: Direct Evidence for the Roles of Geminate and Bimolecular Recombination" N. C. Giebink, B. E. Lassiter and S. R. Forrest. MRS Fall Meeting, Boston, MA (2009).
7. "Broad spectral absorbance and high open circuit voltage organic tandem solar cells based on Subphthalocyanines" B. E. Lassiter, G. Wei, and S. R. Forrest. MRS Fall Meeting, Boston, MA (2008).

### **A.3 Patents**

1. "Mixed-layer buffer layers for OPV devices." US Provisional pending (filed 2013)
2. "Hybrid Planar-Graded Heterojunction for Organic Photovoltaics." US Provisional pending (filed 2012)
3. "Tandem organic photovoltaics incorporating blended squaraines." US Provisional pending (filed 2012)
4. "Tandem photovoltaic incorporating small molecular weight organic materials." (disclosed 2012)
5. "Organic electronics with symmetric electrodes." US Provisional pending (filed 2012)
6. "Multijunction organic photovoltaics incorporating solution and vacuum deposited active layers." US Provisional pending (filed 2012)
7. "Semi-orthogonal solvents for organic electronics." (disclosed 2012)

8. "Metal Oxide Charge Transport Material Doped with Organic Molecules." (disclosed 2011)
9. "Organic Photovoltaic Cell Incorporating Electron Conducting Exciton Blocking Layers." Application pending (filed 2011)
10. "Materials for Controlling the Epitaxial Growth of Photoactive Layers in Photovoltaic Devices." Application pending (filed 2011)
11. "Organic Tandem Solar Cells." Application pending (filed 2009)
12. "Structural Templating for Organic Electronic Devices Having an Organic Film with Long Range Order." Application pending (filed 2009)

## **A.4 Awards**

1. **Best Student Presentation Award (Area 6):** IEEE PV Specialist Conference (2011)
2. **Second Place:** Optical Microscopy, UM Imaging Microstructure Contest (2011)
3. **Second Place:** Optical Microscopy, UM Imaging Microstructure Contest (2010)
4. **Honorable Mention:** National Science Foundation Graduate Research Fellowship (2008)

# Bibliography

- [1] B. Metz, O. R. Davidson, P. R. Bosch, R. Dave, and L. A. Meyer, Climate change 2007: Mitigation. contribution of working group iii to the fourth assessment report of the intergovernmental panel on climate change, Technical report, 2007.
- [2] B. Prindle, M. Eldridge, M. Eckhardt, and A. Frederick, The twin pillars of sustainable energy: Synergies between energy efficiency and renewable energy technology and policy, Technical report, 2007.
- [3] N. S. Lewis, MRS Bulletin **32**, 808 (2007).
- [4] O. Edenhofer, *IPCC Special Report on Renewable Energy Sources and Climate Change Mitigation*, Cambridge University Press, 2011.
- [5] Worldwide electricity production from renewable energy sources, Technical report, Observ'ER, 2012.
- [6] AGEE-Stat, Zeitreihen zur entwicklung der erneuerbaren energien in deutschland, Technical report, 2012.
- [7] J. Kalowekamo and E. Baker, Solar Energy **83**, 1224 (2009).
- [8] C. Powell, Y. Lawryshyn, and T. Bender, Solar Energy Materials and Solar Cells **107**, 236 (2012).
- [9] E. Yablonovitch, T. Gmitter, J. P. Harbison, and R. Bhat, Applied Physics Letters **51**, 2222 (1987).
- [10] M. G. Mauk, *Low-Cost III-V Compound Semiconductor Solar Cells: Progress and Prospects*, Igi Global, Hersey, 2013, WOS:000312829600010.
- [11] M. A. Green, K. Emery, Y. Hishikawa, W. Warta, and E. D. Dunlop, Progress in Photovoltaics: Research and Applications **21**, 1 (2013).

- [12] W. Shockley and H. J. Queisser, *Journal of Applied Physics* **32**, 510 (1961).
- [13] N. C. Giebink, G. P. Wiederrecht, M. R. Wasielewski, and S. R. Forrest, *Physical Review B* **83**, 195326 (2011).
- [14] I. I. Inc., About amoled displays, <http://www.ignisinnovation.com/technology/about-amoled-displays>, 2012.
- [15] F. Gutmann and L. E. Lyons, *Organic solar cells: A review*, Wiley, 1967.
- [16] H. Kallmann and M. Silver, *Symposium on Electrical Conductivity in Organic-Solids*, Wiley-Interscience, New York, 1961.
- [17] C. G.A., *Solar Cells* **8**, 47 (1983).
- [18] C. W. Tang, *Applied Physics Letters* **48**, 183 (1986).
- [19] Z. He et al., **6**, 591 (2012).
- [20] J. You et al., **4**, 1446 (2013).
- [21] M. Pope and C. E. Swenberg, *Electronic Processes in Organic Crystals*, Clarendon Press, Oxford University Press, 1999.
- [22] J. Takeya et al., *Applied Physics Letters* **90**, 102120 (2007).
- [23] P. Peumans, A. Yakimov, and S. R. Forrest, *Journal of Applied Physics* **93**, 3693 (2003).
- [24] N. C. Giebink, G. P. Wiederrecht, M. R. Wasielewski, and S. R. Forrest, *Phys. Rev. B* **82**, 155305 (2010).
- [25] N. S. Sariciftci et al., *Applied Physics Letters* **62**, 585 (1993).
- [26] S. Uchida, J. Xue, B. P. Rand, and S. R. Forrest, *Applied Physics Letters* **84**, 4218 (2004).
- [27] J. Xue, B. P. Rand, S. Uchida, and S. R. Forrest, *Advanced Materials* **17**, 66 (2005).
- [28] F. Yang, K. Sun, and S. Forrest, *Advanced Materials* **19**, 4166 (2007).
- [29] L. Stolz Roman et al., *Advanced Materials* **12**, 189 (2000).
- [30] P. Peumans, V. Bulovic, and S. R. Forrest, *Applied Physics Letters* **76**, 2650 (2000).

- [31] K. Tvingstedt, V. Andersson, F. Zhang, and O. Inganäs, *Applied Physics Letters* **91**, 123514 (2007).
- [32] M. Agrawal and P. Peumans, *Optics Express* **16**, 5385 (2008).
- [33] M. Niggemann, M. Riede, A. Gombert, and K. Leo, *physica status solidi (a)* **205**, 2862 (2008).
- [34] S.-I. Na et al., *Advanced Functional Materials* **18**, 3956 (2008).
- [35] K. S. Nalwa and S. Chaudhary, *Optics Express* **18**, 5168 (2010).
- [36] M. Niggemann, M. Glatthaar, A. Gombert, A. Hinsch, and V. Wittwer, *Thin Solid Films* **451**, 619 (2004).
- [37] A. society for testing and materials, Standards Nos. E1021, E948, and E973 .
- [38] C. H. Seaman, *Solar Energy* **29**, 291 (1982).
- [39] W. H. Bragg and W. L. Bragg, *Proceedings of the Royal Society of London. Series A* **88**, 428 (1913).
- [40] W. L. Bragg, *Proceedings of the Royal Society of London. Series A* **89**, 248 (1913).
- [41] A. Einstein, *ANNALEN DER PHYSIK* **17**, 132 (1905).
- [42] D. W. Turner and M. I. A. Jobory, *The Journal of Chemical Physics* **37**, 3007 (1962).
- [43] Y. Gao, *Materials Science and Engineering: R: Reports* **68**, 39 (2010).
- [44] G. Binnig, C. F. Quate, and C. Gerber, *Physical Review Letters* **56**, 930 (1986).
- [45] Y. Martin, C. C. Williams, and H. K. Wickramasinghe, *Journal of Applied Physics* **61**, 4723 (1987).
- [46] Q. Zhong, D. Inniss, K. Kjoller, and V. Elings, *Surface Science Letters* **290**, L688 (1993).
- [47] L. A. A. Pettersson, L. S. Roman, and O. Inganäs, *Journal of Applied Physics* **86**, 487 (1999).
- [48] R. R. Lunt, N. C. Giebink, A. A. Belak, J. B. Benziger, and S. R. Forrest, *Journal of Applied Physics* **105**, 053711 (2009).

- [49] P. E. Burrows et al., *Journal of Crystal Growth* **156**, 91 (1995).
- [50] M. A. Baldo et al., *Applied Physics Letters* **71**, 3033 (1997).
- [51] T. X. Zhou, T. Ngo, J. J. Brown, M. Shtein, and S. R. Forrest, *Applied Physics Letters* **86**, 021107 (2005).
- [52] M. Bosing et al., **1154** (2009).
- [53] F. Lindla et al., **1154** (2009).
- [54] M. Shtein, J. Mapel, J. B. Benziger, and S. R. Forrest, *Applied Physics Letters* **81**, 268 (2002).
- [55] C. Rolin et al., *Applied Physics Letters* **89**, 203502 (2006).
- [56] C. Rolin et al., *Applied Physics Letters* **93**, 033305 (2008).
- [57] F. Yang, M. Shtein, and S. R. Forrest, *Nat Mater* **4**, 37 (2005).
- [58] F. Yang and S. R. Forrest, *Advanced Materials* **18**, 2018 (2006).
- [59] F. Yang, M. Shtein, and S. R. Forrest, *Journal of Applied Physics* **98**, 014906 (2005).
- [60] W. Y. Tong et al., *The Journal of Physical Chemistry B* **110**, 17406 (2006).
- [61] M. Rusu et al., *Thin Solid Films* **516**, 7160 (2008).
- [62] F. Yang, R. R. Lunt, and S. R. Forrest, *Applied Physics Letters* **92**, 053310 (2008).
- [63] R. R. Lunt, J. B. Benziger, and S. R. Forrest, *Applied Physics Letters* **90**, 181932 (2007).
- [64] R. R. Lunt, J. B. Benziger, and S. R. Forrest, *Advanced Materials* **22**, 1233 (2010).
- [65] R. R. Lunt, J. Benziger, and S. Forrest, *Advanced Materials* **19**, 4229 (2007).
- [66] D. Hsieh, Auo announces gen 11: What size will the substrate be?, [://www.displaysearchblog.com/2008/09/auo-announces-gen11-what-will-be-the-substrate-size/](http://www.displaysearchblog.com/2008/09/auo-announces-gen11-what-will-be-the-substrate-size/), 2008.
- [67] M. Schwambera et al., page 370 (2004), 8th Asian Symposium on Information Display, Nanjing, PEOPLES R CHINA, FEB 15-17, 2004.

- [68] B. Marheineke, page 1676 (2006), 6th International Meeting on Information Displays/5th International Display Manufacturing Conference (IMID/IDMC 2006), Daegu, SOUTH KOREA, AUG 22-25, 2006.
- [69] W. G. Strang and G. J. Fix, *An Analysis of the Finite Element Method*, Wellesley Cambridge Press, 1973.
- [70] M. Shtein, *Organic Vapor Phase Deposition and Vapor Jet Printing for Electronic and Optoelectronic Device Applications*, PhD thesis, Princeton University, 2004.
- [71] R. Bird, W. Steward, and E. Lightfoot, *Transport Phenomena*, Wiley, 2002.
- [72] R. R. Lunt, B. E. Lassiter, J. B. Benziger, and S. R. Forrest, *Applied Physics Letters* **95**, 233305 (2009).
- [73] R. F. Bailey-Salzman, B. P. Rand, and S. R. Forrest, *Applied Physics Letters* **91**, 013508 (2007).
- [74] K. L. Mutolo, E. I. Mayo, B. P. Rand, S. R. Forrest, and M. E. Thompson, *J. Am. Chem. Soc.* **128**, 8108 (2006).
- [75] H. H. Gommans et al., *Advanced Functional Materials* **17**, 2653 (2007).
- [76] S. Wang et al., *Applied Physics Letters* **94**, 233304 (2009).
- [77] T. Nyberg, *Synthetic Metals* **140**, 281 (2004).
- [78] B. O'Connor, K. H. An, K. P. Pipe, Y. Zhao, and M. Shtein, *Applied Physics Letters* **89**, 233502 (2006).
- [79] Q. L. Song et al., *Applied Physics Letters* **89**, 251118 (2006).
- [80] Z. Hong, Z. Huang, and X. Zeng, *Chemical Physics Letters* **425**, 62 (2006).
- [81] M. Glatthaar et al., *Thin Solid Films* **491**, 298 (2005).
- [82] M. T. Greiner et al., *Nature Materials* **11**, 76 (2011).
- [83] C. Tao et al., *Applied Physics Letters* **93**, 193307 (2008).
- [84] B. O'Connor, K. P. Pipe, and M. Shtein, *Applied Physics Letters* **92**, 193306 (2008).
- [85] X. Tong, R. F. Bailey-Salzman, G. Wei, and S. R. Forrest, *Applied Physics Letters* **93**, 173304 (2008).

- [86] T. Oyamada, Y. Sugawara, Y. Terao, H. Sasabe, and C. Adachi, *Energy* **4**, 4 (2007).
- [87] J. Meiss, N. Allinger, M. K. Riede, and K. Leo, *Applied Physics Letters* **93**, 103311 (2008).
- [88] J. Meiss, M. K. Riede, and K. Leo, *Applied Physics Letters* **94**, 013303 (2009).
- [89] J. Meiss, M. K. Riede, and K. Leo, *Journal of Applied Physics* **105**, 063108 (2009).
- [90] C. Falkenberg et al., *Journal of Applied Physics* **104**, 034506 (2008).
- [91] J. Huang, J. Yu, H. Lin, and Y. Jiang, *Journal of Applied Physics* **105**, 073105 (2009).
- [92] B. P. Rand et al., *Advanced Materials* **17**, 2714 (2005).
- [93] M. Vogel, S. Doka, C. Breyer, M. C. Lux-Steiner, and K. Fostiropoulos, *Applied Physics Letters* **89**, 163501 (2006).
- [94] H. Gommans et al., *Advanced Functional Materials* **18**, 3686 (2008).
- [95] P. Peumans, V. Bulovic, and S. R. Forrest, *Applied Physics Letters* **76**, 2650 (2000).
- [96] P. Peumans and S. R. Forrest, *Applied Physics Letters* **79**, 126 (2001).
- [97] Z. Hong, Z. Huang, and X. Zeng, *Thin Solid Films* **515**, 3019 (2007).
- [98] Q. L. Song, C. M. Li, M. L. Wang, X. Y. Sun, and X. Y. Hou, *Applied Physics Letters* **90**, 071109 (2007).
- [99] A. F. Hebard et al., *Physical Review B* **50**, 17740 (1994).
- [100] J. P. Liu, S. S. Wang, Z. Q. Bian, M. N. Shan, and C. H. Huang, *Chemical Physics Letters* **470**, 103 (2009).
- [101] N. C. Giebink, B. E. Lassiter, G. P. Wiederrecht, M. R. Wasielewski, and S. R. Forrest, *Physical Review B* **82**, 155306 (2010).
- [102] B. P. Rand, J. Genoe, P. Heremans, and J. Poortmans, *Progress in Photovoltaics: Research and Applications* **15**, 659 (2007).
- [103] R. F. Salzman et al., *Organic Electronics* **6**, 242 (2005).
- [104] D. Cheyngs et al., *Physical Review B* **77**, 165332 (2008).



- [105] Y. Kinoshita, R. Takenaka, and H. Murata, *Applied Physics Letters* **92**, 243309 (2008).
- [106] J. Xue and S. R. Forrest, *Journal of Applied Physics* **95**, 1869 (2004).
- [107] M. A. Baldo and S. R. Forrest, *Physical Review B* **64**, 085201 (2001).
- [108] T. W. Ng et al., *Journal of Applied Physics* **106**, 114501 (2009).
- [109] T. Ameri, G. Dennler, C. Lungenschmied, and C. J. Brabec, *Energy Environ. Sci.* **2**, 347 (2009).
- [110] A. Yakimov and S. R. Forrest, *Applied Physics Letters* **80**, 1667 (2002).
- [111] J. Xue, S. Uchida, B. P. Rand, and S. R. Forrest, *Applied Physics Letters* **85**, 5757 (2004).
- [112] A. Hadipour, B. de Boer, and P. Blom, *Organic Electronics* **9**, 617 (2008).
- [113] A. Hadipour et al., *Advanced Functional Materials* **16**, 1897 (2006).
- [114] S. Tanaka et al., *Applied Physics Letters* **94**, 113506 (2009).
- [115] X. Guo et al., *Organic Electronics* **10**, 1174 (2009).
- [116] H. Z. Yu and J. B. Peng, *Organic Electronics* **9**, 1022 (2008).
- [117] J. A. Hauch, P. Schilinsky, S. A. Choulis, S. Rajooelson, and C. J. Brabec, *Applied Physics Letters* **93**, 103306 (2008).
- [118] S. Cros et al., *Proceedings of SPIE* **7048**, 70480U (2008).
- [119] S. Schuller, P. Schilinsky, J. Hauch, and C. Brabec, *Applied Physics A: Materials Science & Processing* **79**, 37 (2004).
- [120] J. A. Hauch et al., *Solar Energy Materials and Solar Cells* **92**, 727 (2008).
- [121] S. R. Forrest, *Nature* **428**, 911 (2004).
- [122] B. P. Rand, D. P. Burk, and S. R. Forrest, *Physical Review B* **75**, 115327 (2007).
- [123] N. Li and S. R. Forrest, *Applied Physics Letters* **95**, 123309 (2009).
- [124] G. Wei, S. Wang, K. Renshaw, M. E. Thompson, and S. R. Forrest, *ACS Nano* **4**, 1927 (2010).

- [125] K. V. Chauhan, P. Sullivan, J. L. Yang, and T. S. Jones, *J. Phys. Chem. C* **114**, 3304 (2010).
- [126] S. Heutz, R. Cloots, and T. S. Jones, *Applied Physics Letters* **77**, 3938 (2000).
- [127] T. Sakurai, R. Fukasawa, K. Saito, and K. Akimoto, *Organic Electronics* **8**, 702 (2007).
- [128] T. Sakurai, S. Kawai, R. Fukasawa, J. Shibata, and K. Akimoto, *Japanese Journal of Applied Physics* **44**, 1982 (2005).
- [129] S. R. Forrest, L. Y. Leu, F. F. So, and W. Y. Yoon, *Journal of Applied Physics* **66**, 5908 (1989).
- [130] P. E. Burrows, Y. Zhang, E. I. Haskal, and S. R. Forrest, *Applied Physics Letters* **61**, 2417 (1992).
- [131] J. Danziger, J. P. Dodelet, P. Lee, K. W. Nebesny, and N. R. Armstrong, *Chem. Mater.* **3**, 821 (1991).
- [132] S. R. Forrest, P. E. Burrows, E. I. Haskal, and F. F. So, *Physical Review B* **49**, 11309 (1994).
- [133] Y. Hirose et al., *Physical Review B* **54**, 13748 (1996).
- [134] T. Ogawa, K. Kuwamoto, S. Isoda, T. Kobayashi, and N. Karl, *Acta Crystallographica Section B* **55**, 123 (1999).
- [135] S. Heutz and T. S. Jones, *Journal of Applied Physics* **92**, 3039 (2002).
- [136] O. Gordan, T. Sakurai, M. Friedrich, K. Akimoto, and D. Zahn, *Organic Electronics* **7**, 521 (2006).
- [137] T. Sakurai, R. Fukasawa, and K. Akimoto, *Japanese Journal of Applied Physics* **45**, 255 (2006).
- [138] P. Sullivan, T. S. Jones, A. J. Ferguson, and S. Heutz, *Applied Physics Letters* **91**, 233114 (2007).
- [139] K. V. Chauhan, P. Sullivan, J. L. Yang, and T. S. Jones, *The Journal of Physical Chemistry C* **114**, 3304 (2010).
- [140] H. Ying Mao et al., *Applied Physics Letters* **99**, 093301 (2011).

- [141] B. Verreert, R. Müller, B. P. Rand, K. Vasseur, and P. Heremans, *Organic Electronics* **12**, 2131 (2011).
- [142] A. Hinderhofer et al., *The Journal of Physical Chemistry C* **115**, 16155 (2011).
- [143] H. Huang, J.-T. Sun, Y. P. Feng, W. Chen, and A. T. S. Wee, *Physical Chemistry Chemical Physics* **13**, 20933 (2011).
- [144] J. Yang, S. Schumann, and T. Jones, *Thin Solid Films* **519**, 3709 (2011).
- [145] W. Chen et al., *The Journal of Physical Chemistry C* **113**, 12832 (2009).
- [146] J. L. Yang, S. Schumann, and T. S. Jones, *J. Mater. Chem.* **21**, 5812.
- [147] W. Chen, D.-C. Qi, H. Huang, X. Gao, and A. T. S. Wee, *Advanced Functional Materials* **21**, 410 (2011).
- [148] B. P. Rand et al., *Advanced Functional Materials* **22**, 2987 (2012).
- [149] W. Zhao et al., *Organic Electronics* **13**, 129 (2012).
- [150] T. Sakurai et al., *Organic Electronics* **12**, 966 (2011).
- [151] C. H. Cheng et al., *Applied Physics Letters* **97**, 083305 (2010).
- [152] S. R. Forrest, *Chem. Rev.* **97**, 1793 (1997).
- [153] A. Dürr, B. Nickel, V. Sharma, U. Täffner, and H. Dosch, *Thin Solid Films* **503**, 127 (2006).
- [154] W. Chen et al., *Chem. Mater.* **20**, 7017 (2008).
- [155] J. Xue, S. Uchida, B. P. Rand, and S. R. Forrest, *Applied Physics Letters* **84**, 3013 (2004).
- [156] M. D. Perez, C. Borek, S. R. Forrest, and M. E. Thompson, *J. Am. Chem. Soc.* **131**, 9281 (2009).
- [157] Y. Áđahin, S. Alem, R. de Bettignies, and J.-M. Nunzi, *Thin Solid Films* **476**, 340 (2005).
- [158] Y. Kanai, T. Matsushima, and H. Murata, *Thin Solid Films* **518**, 537 (2009).
- [159] V. Bhosle et al., *Journal of Applied Physics* **102**, 023501 (2007).

- [160] C. W. Schlenker et al., *Chem. Mater.* **23**, 4132 (2011).
- [161] M. Y. Chan et al., *Journal of Applied Physics* **100**, 094506 (2006).
- [162] N. Wang, J. Yu, Y. Zang, J. Huang, and Y. Jiang, *Solar Energy Materials and Solar Cells* **94**, 263 (2010).
- [163] D. Qin, P. Gu, R. S. Dhar, S. G. Razavipour, and D. Ban, *physica status solidi (a)* **208**, 1967 (2011).
- [164] G. Chen et al., *Advanced Materials*, *Advanced Materials* (2012).
- [165] D. Lee et al., *Solar Energy Materials and Solar Cells* **95**, 365 (2011).
- [166] B. Joon Lee, H. Jung Kim, W.-i. Jeong, and J.-J. Kim, *Solar Energy Materials and Solar Cells* **94**, 542 (2010).
- [167] F.-C. Chen and C.-H. Lin, *Journal of Physics D: Applied Physics* **43**, 025104 (2010).
- [168] M. F. Lo et al., *Applied Physics Letters* **97**, 143304 (2010).
- [169] I. Yoo et al., *Synthetic Metals* **153**, 97 (2005).
- [170] L.-Y. Lin et al., *J. Am. Chem. Soc.* **133**, 15822 (2011).
- [171] M. Zhang, H. Wang, and C. Tang, *Organic Electronics* **13**, 249 (2012).
- [172] I. Bruder et al., *Solar Energy Materials and Solar Cells* **93**, 1896 (2009).
- [173] K. Schulze et al., *Advanced Materials* **18**, 2872 (2006).
- [174] N. M. Kronenberg et al., *Advanced Materials* **22**, 4193 (2010).
- [175] J. Li et al., *Journal of Materials Chemistry* **22**, 6285 (2012).
- [176] A. Ojala et al., *Advanced Functional Materials* **22**, 86 (2012).
- [177] G. Schwartz et al., *Proceedings of SPIE* **7416**, 74160K (2009).
- [178] A. G. F. Janssen, T. Riedl, S. Hamwi, H. H. Johannes, and W. Kowalsky, *Applied Physics Letters* **91**, 073519 (2007).
- [179] R. Timmreck, S. Olthof, K. Leo, and M. K. Riede, *Journal of Applied Physics* **108**, 033108 (2010).

- [180] V. Steinmann et al., *Applied Physics Letters* **99**, 193306 (2011).
- [181] R. Schueppel et al., *Journal of Applied Physics* **107**, 044503 (2010).
- [182] K. Suemori, T. Miyata, M. Yokoyama, and M. Hiramoto, *Applied Physics Letters* **85**, 6269 (2004).
- [183] M. Y. Chan, S. L. Lai, K. M. Lau, C. S. Lee, and S. T. Lee, *Applied Physics Letters* **89**, 163515 (2006).
- [184] D. Gebeyehu et al., *Thin Solid Films* **451**, 29 (2004).
- [185] B. Maennig et al., *Applied Physics A: Materials Science & Processing* **79**, 1 (2004).
- [186] C. K. Renshaw, C. W. Schlenker, M. E. Thompson, and S. R. Forrest, *Physical Review B* **84**, 045315 (2011).
- [187] A. Kahn, N. Koch, and W. Gao, *Journal of Polymer Science Part B: Polymer Physics* **41**, 2529 (2003).
- [188] S. Sreejith, P. Carol, P. Chithra, and A. Ajayaghosh, *J. Mater. Chem.* **18**, 264.
- [189] G. Wei et al., *Nano Lett.* **10**, 3555 (2010).
- [190] G. Wei, S. Wang, K. Sun, M. E. Thompson, and S. R. Forrest, *Advanced Energy Materials* **1**, 184 (2011).
- [191] S. Wang et al., *Chem. Mater.* **23**, 4789 (2011).
- [192] G. Wei et al., *Nano Lett.* **11**, 4261 (2011).
- [193] G. Wei et al., *ACS Nano* **6**, 972 (2011).
- [194] J. D. Zimmerman et al., *Nano Lett.* **12**, 4366 (2012).
- [195] V. Shrotriya et al., *Advanced Functional Materials* **16**, 2016 (2006).
- [196] I. Hill, J. Schwartz, and A. Kahn, *Organic Electronics* **1**, 5 (2000).
- [197] N. J. Watkins, G. P. Kushto, and A. J. Mäkinen, *Journal of Applied Physics* **104**, 013712 (2008).
- [198] C. K. Renshaw, J. D. Zimmerman, B. E. Lassiter, and S. R. Forrest, **86**, 085324 (2012).

- [199] W. I. Jeong et al., **22**, 3089 (2012).
- [200] B. Verreet et al., **102**, 043301 (2013).
- [201] G. Conibeer, *Materials Today* **10**, 42 (2007).
- [202] A. D. Vos, *Journal of Physics D: Applied Physics* **13**, 839 (1980).
- [203] G. Dennler et al., *Advanced Materials* **20**, 579 (2008).
- [204] G. Dennler et al., *Journal of Applied Physics* **102**, 123109 (2007).
- [205] J. Gilot, M. M. Wienk, and R. A. J. Janssen, *Advanced Materials* **22**, E67â€”E71 (2010).
- [206] A. Braun et al., *Applied Physics Letters* **98**, 223506 (2011).
- [207] B. P. Rand, P. Peumans, and S. R. Forrest, *Journal of Applied Physics* **96**, 7519 (2004).
- [208] F. Yang and S. R. Forrest, *ACS Nano* **2**, 1022 (2008).
- [209] X. Xiao, J. D. Zimmerman, B. E. Lassiter, K. J. Bergemann, and S. R. Forrest, *Applied Physics Letters* **102**, 073302 (2013).
- [210] A. S. Brown and M. A. Green, *Progress in Photovoltaics: Research and Applications* **10**, 299 (2002).
- [211] M. Hiramoto, M. Suezaki, and M. Yokoyama, *Chemistry Letters* **19**, 327 (1990).
- [212] G. Dennler et al., *Applied Physics Letters* **89**, 073502 (2006).
- [213] S. W. Tong, Y. Wang, Y. Zheng, M. Ng, and K. P. Loh, *Advanced Functional Materials* **21**, 4430 (2011).
- [214] J. Inoue, K. Yamagishi, and M. Yamashita, *Journal of Crystal Growth* **298**, 782 (2007).
- [215] B. Yu, F. Zhu, H. Wang, G. Li, and D. Yan, *Journal of Applied Physics* **104**, 114503 (2008).
- [216] S. Olthof, R. Timmreck, M. Riede, and K. Leo, *Applied Physics Letters* **100**, 113302 (2012).

- [217] D. Cheyns, B. P. Rand, and P. Heremans, *Applied Physics Letters* **97**, 033301 (2010).
- [218] N. M. Kronenberg et al., *Chem. Commun.* , 6489 (2008).
- [219] F. Würthner, **1999**, 2103 (1999).
- [220] H. Bürckstümmer et al., *J. Mater. Chem.* **20**, 240 (2009).
- [221] A. Mishra and P. Bauerle, *Angewandte Chemie International Edition* **51**, 2020 (2012).
- [222] V. Steinmann et al., *Advanced Energy Materials* **1**, 888 (2011).
- [223] W. Stampor, *Chemical Physics* **256**, 351 (2000).
- [224] Q. Fu, J. Chen, C. Shi, and D. Ma, *ACS Appl. Mater. Interfaces* **4**, 6579 (2012).
- [225] M. Riede et al., *Advanced Functional Materials* **21**, 3019 (2011).
- [226] J. Meiss et al., *Applied Physics Letters* **99**, 043301 (2011).
- [227] R. Pandey and R. J. Holmes, *Advanced Materials* **22**, 5301 (2010).
- [228] B. E. Lassiter et al., *Applied Physics Letters* **98**, 243307 (2011).
- [229] K. J. Bergemann and S. R. Forrest, *Applied Physics Letters* **99**, 243303 (2011).
- [230] S. Pfuetzner, J. Meiss, A. Petrich, M. Riede, and K. Leo, *Applied Physics Letters* **94**, 223307 (2009).
- [231] M. C. Barr, R. M. Howden, R. R. Lunt, V. Bulovic, and K. K. Gleason, *Advanced Energy Materials* **2**, 1404 (2012).
- [232] M. C. Barr, C. Carbonera, R. Po, V. Bulovic, and K. K. Gleason, *Applied Physics Letters* **100**, 183301 (2012).
- [233] H. Park et al., *ACS Nano* **6**, 6370 (2012).
- [234] Z. Wang et al., *Energy & Environmental Science* **6**, 249 (2012).
- [235] D. Fujishima et al., *Solar Energy Materials and Solar Cells* **93**, 1029 (2009).
- [236] M. Hirade and C. Adachi, *Applied Physics Letters* **99**, 153302 (2011).
- [237] J. A. Macko et al., *Physical Chemistry Chemical Physics* **14**, 14548 (2012).

- [238] J. Y. Kim et al., *Science* **317**, 222 (2007).
- [239] S. K. Hau, H.-L. Yip, K.-S. Chen, J. Zou, and A. K. Y. Jen, *Applied Physics Letters* **97**, 253307 (2010).
- [240] X. Guo, F. Liu, B. Meng, Z. Xie, and L. Wang, *Organic Electronics* **11**, 1230 (2010).
- [241] B. E. Lassiter, J. D. Zimmerman, A. Panda, X. Xiao, and S. R. Forrest, *Applied Physics Letters* **101**, 063303 (2012).
- [242] K.-A. Kim et al., *Journal of Applied Polymer Science* **46**, 1â€š (1992).
- [243] J. Liu, Y. Shi, and Y. Yang, *Advanced Functional Materials* **11**, 420 (2001).
- [244] T. Ishikawa, M. Nakamura, K. Fujita, and T. Tsutsui, *Applied Physics Letters* **84**, 2424 (2004).
- [245] T. M. Letcher, U. Domanska, A. Goldon, and E. M. Mwenesongole, *South African Journal of Chemistry-Suid-Afrikaanse Tydskrif Vir Chemie* **50**, 51 (1997), WOS:A1997XF24700009.
- [246] P. P. Kulkarni and C. T. Jafvert, *Environmental Science & Technology* **42**, 845 (2008).
- [247] R. S. Ruoff, D. S. Tse, R. Malhotra, and D. C. Lorents, *The Journal of Physical Chemistry* **97**, 3379 (1993).
- [248] V. Shrotriya, G. Li, Y. Yao, C.-W. Chu, and Y. Yang, *Applied Physics Letters* **88**, 073508 (2006).
- [249] F.-C. Chen, J.-L. Wu, K.-H. Hsieh, W.-C. Chen, and S.-W. Lee, *Organic Electronics* **9**, 1132 (2008).
- [250] R. Koeppe et al., *ChemSusChem* **2**, 309 (2009).
- [251] J. Ajuria et al., *Energy Environ. Sci.* **4**, 453 (2010).
- [252] C. Tao et al., *Applied Physics Letters* **95**, 053303 (2009).
- [253] G.-M. Ng et al., *Applied Physics Letters* **90**, 103505 (2007).
- [254] H. Schmidt et al., *Applied Physics Letters* **94**, 243302 (2009).
- [255] S. K. Hau, H. L. Yip, J. Zou, and A. K. Jen, *Organic Electronics* **10**, 1401 (2009).



- [256] R. F. Bailey-Salzman, B. P. Rand, and S. R. Forrest, *Applied Physics Letters* **88**, 233502 (2006).
- [257] M. Kroger et al., *Applied Physics Letters* **95**, 123301 (2009).
- [258] N. Li, B. E. Lassiter, R. R. Lunt, G. Wei, and S. R. Forrest, *Applied Physics Letters* **94**, 023307 (2009).
- [259] F. Liu, S. Shao, X. Guo, Y. Zhao, and Z. Xie, *Solar Energy Materials and Solar Cells* **94**, 842 (2010).
- [260] X. W. Sun et al., *Applied Physics Letters* **97**, 053303 (2010).
- [261] M. Pfeiffer, A. Beyer, T. Fritz, and K. Leo, *Applied Physics Letters* **73**, 3202 (1998).
- [262] W. Gao and A. Kahn, *Applied Physics Letters* **79**, 4040 (2001).
- [263] J. Blochwitz, M. Pfeiffer, T. Fritz, and K. Leo, *Applied Physics Letters* **73**, 729 (1998).
- [264] H. Kanno, R. J. Holmes, Y. Sun, S. Kena-Cohen, and S. R. Forrest, **18**, 339 (2006).
- [265] X. Qi, N. Li, and S. R. Forrest, *Journal of Applied Physics* **107**, 014514 (2010).
- [266] W. A. Luhman and R. J. Holmes, *Applied Physics Letters* **94**, 153304 (2009).